

7-3-2012

Heterostructure engineering of quantum dots-in-a-well infrared photodetectors

Ajit Barve

Follow this and additional works at: https://digitalrepository.unm.edu/ece_etds

Recommended Citation

Barve, Ajit. "Heterostructure engineering of quantum dots-in-a-well infrared photodetectors." (2012).
https://digitalrepository.unm.edu/ece_etds/28

This Dissertation is brought to you for free and open access by the Engineering ETDs at UNM Digital Repository. It has been accepted for inclusion in Electrical and Computer Engineering ETDs by an authorized administrator of UNM Digital Repository. For more information, please contact disc@unm.edu.

Candidate

Department

This dissertation is approved, and it is acceptable in quality and form for publication:

Approved by the Dissertation Committee:

_____, Chairperson

Heterostructure Engineering of Quantum Dots-in-a-Well Infrared Photodetectors

by

AJIT VIJAY BARVE

**B.E, UNIVERSITY OF MUMBAI, 2005
M. TECH, INDIAN INSTITUTE OF TECHNOLOGY, KANPUR, 2007**

COMMITTEE CHAIR: PROF. SANJAY KRISHNA

DISSERTATION

Submitted in Partial Fulfillment of the
Requirements for the Degree of

**DOCTOR OF PHILOSOPHY
ENGINEERING**

The University of New Mexico
Albuquerque, New Mexico

May 2012

© Ajit Vijay Barve, 2012.

Dedicated to Three Women in My Life,

Mother, Daughter and Wife!

Acknowledgments

I would like to thank my advisor, Prof. Sanjay Krishna, for his support and guidance throughout this work! The amount of freedom he offered, in all the aspects of research, shows his confidence in his students and his care for them. His cheerful and positive attitude and incredible sense of 'right way to move forward' makes his inputs invaluable. Thanks also for so many group lunches and for providing one of the best offices at UNM with our own couch! I would like to sincerely thank my committee members, Prof. Steven R. J. Brueck, Prof. Luke F. Lester and Prof. Kevin J. Malloy, for their time and constructive inputs at various stages of this work. Special thanks to Prof. Dawson, for his teaching, guidance and support throughout this work.

Many thanks to all my group members, for their help in the lab and for making my stay always enjoyable. All those discussions, long coffee breaks, food, snowboarding, tennis and ping pong events will be badly missed! Thanks to Rajeev, Dr. Yagya Sharma, Dr. Sang Jun Lee, Jun Oh, Nina, Eric, Maya and Ha Sul Kim for helping me learn the ropes for growth, processing and characterization. Thanks to Stephen for endless hours in the cleanroom, as a 'buddy'. It was great fun to pick on him all these years! Thanks John for help with flipchip bonding, polishing, dry etching with RIE, whenever I needed! Thanks to the FPA characterization team of Eric, Sebastian and Glauco for testing all the FPAs. Thanks Brianna for RIE etching and help with 'dicing' for substrate removal. Thanks to Ali and Marziyeh for helping with polishing. Many thanks to Dr. Thomas Vandervelde and Jiayi for growing some of my early samples. Jiayi also helped with TEM images and polarized spectral response. Many thanks to Prof. Gunny's group in my office for making the place lively. No one can graduate from MBE lab without thanking Dr. Thomas Rotter for his dedicated care and guidance with anything MBE. I would also like to thank Dr. Alex Albrecht for letting me use the PL setup.

I have been lucky to have smart and dedicated summer interns working with me every year. Thanks to Shreyas, Krit, Megan for helping me with measurements! Special thanks to Srujan for helping me with, and continuing the work on modeling of quantum dots. Working with summer interns is always interesting and fun filled because of the new perspective they share. I would also like to acknowledge visiting researchers Saumya

Sengupta for helping me with MBE growth and device characterization and Sourav Adhikary for the help with processing.

CHTM has the best run facilities I have worked in. This would not be possible without the dedicated team led by Rick Bradley and Dan Bryant. I would also like to thank all the cleanroom staff, for making sure that all the equipments are available as much as possible. Thanks to all the office staff in CHTM, for taking care of all the paperwork promptly and keeping the office a lively, fun-filled place with all the potlucks and Christmas decorations. My heartfelt thanks to Ms Elmyra Grelle from ECE for making my transition to UNM easy and taking good care of every student who comes to ECE.

I would also like to take this opportunity to thank Vincent Chow, for not only letting me work for his company Vega Tech & Systems as an intern, but also sharing with me his vast knowledge of cleanroom processing, dicing, electron microscopy and characterization! I learned quite a bit not just from research point of view, but also about the power of motivation, dedication and persistence! He gave me one important tip, that helped me during all the critical steps "Murphy has all the weapons, all you have against him is time. Use it wisely".

Many thanks to the team of SK Infrared (skinfrared), especially Dr. Sanchita Krishna and Prof. Sanjay Krishna for letting me work on the exciting area of skin cancer research, for applying my research to help real dermatology patients. I learned a lot from this exposure. Thanks also for frequent 'lunch meetings'!

I cannot even begin to thank my friend, colleague and wife Nutan. She inspired me to go into research and provided me with motivation all along. Thanks for being there with me, bearing with me, (taking care of paperwork and food), and for endless discussions on everything related to research. Thanks for teaching me XRD, Hall measurement, polishing and various aspects of growth; not very many wives can do that! Special thanks to my daughter, Anvesha. She has been as patient with me as a seven month old can be! And finally, my love for my family, my aai, baba and Apurva, without whom, none of this would be possible...

Heterostructure Engineering of Quantum Dots-in-a-Well Infrared Photodetectors

by

Ajit Vijay Barve

Master of Technology, Indian Institute of Technology,

Kanpur, India, 2007

PhD, Engineering, University of New Mexico, 2012.

Abstract

Three of the most important characteristics of third-generation imaging systems are, high-operating temperature, multispectral operation, and large format arrays. The quantum dot infrared photodetector technology, owing to the three-dimensional confinement of carriers, the richness of the electronic spectra in quantum dots, and the mature III-V based fabrication technology, satisfy these requirements. This work focuses on quantum dots-in-a-well (DWELL) detectors in which InAs quantum dots are embedded in a compressively strained InGaAs-GaAs quantum well. Barriers separating two stacks of quantum dots can be GaAs, AlGaAs or a combination of different materials, with 'smart barriers'.

Motivation for this work is to improve the understanding and the performance of DWELL detectors to achieve high temperature operation and high signal to noise ratio for these detectors for given wavelength requirements, at applied biases compatible with CMOS

technology. This aim has been pursued on three fronts: barrier designs, device designs and material systems. *Smart* barriers, such as resonant tunneling barriers have been demonstrated to improve the signal to noise ratio of the detector by reducing the dark current significantly, while keeping the photocurrent constant. A systematic experimental study has been conducted for understanding the effect of different types of transitions on the properties of DWELL detectors, which showed that bound to quasibound (B-Q) type of transitions optimize the device performance at moderate bias levels. The performance of B-Q type of architectures has been substantially improved by the use of confinement enhancing (CE) barriers that combine the advantages of high energy barriers, such as low dark current and high signal to noise ratio, with those of low energy barriers, such as high responsivity and longer peak wavelengths at low bias operation.

A new type of detector, a quantum dot based quantum cascade detector, has been proposed and implemented. QD-QCD exhibits a strong photovoltaic action, leading to strong performance at zero bias, by the virtue of internal electric field generated by the quantum cascade action in the barrier. The zero bias operation, combined with record low photoconductive gains for any quantum dot detectors, makes QD QCD very attractive for focal plane array applications.

For improved understanding, theoretical modeling of quantum dot strain, based on atomistic valence force field method as well as transport simulations of general heterostructure detectors with drift-diffusion model have been developed. The transport simulation results indicate the presence of a strong space charge region forming between the highly n-doped contact regions and non-intentionally doped barrier regions, which makes the internal electric field highly

nonlinear in space. This has been verified by systematic experiments, in which effects of this electric field nonlinearity on the device parameters have been studied.

This work would enable a device designer to *choose* different device parameters such as spectral response position and shape, photoconductive gain, response, signal to noise ratio, dark current levels, activation energies etc. This knowledge has been utilized in demonstrating highly sensitive FPAs, as well as high operating temperature imaging (at 140K) with DWELL detectors. State of the art performance has been obtained from different devices at different wavelengths, such as such as a detectivity of $4 \times 10^{11} \text{ cm.Hz}^{1/2}\text{W}^{-1}$ at 77K in a bound to quasibound device with a cutoff wavelength of 8.5 μm , which is higher than that obtained from state of the art QWIPs. Although the dark current levels are substantially lower than standard QWIPs, and background limited photodetection is at much higher temperature, the focal plane array sensitivities are lower than those of the state of the art QWIPs, by around 10 mK, due to lower quantum efficiency (a factor of 2-3) and higher photoconductive gain. This difference can be eliminated by the use of gratings or shape engineering through the use of submonolayer quantum dots and with smaller photoconductive gains with DWELL detectors.

Contents

List of Figures	xiii
List of Tables	xxv
1 Introduction.....	1
1.1 Infrared Detectors: Requirements and Types.....	2
1.2 Comparison between QDIP and QWIP	4
1.3 DWELL Detectors	8
1.4 Motivation and Approach	10
1.5 Outline of the Dissertation	13
2. Building Blocks	15
2.1 Epitaxial Growth.....	15
2.1.1 Introduction to MBE.....	15
2.1.2 Stranski-Krastanov growth mode.....	18
2.1.3 Optimizing the growth parameters.....	19
2.2 Device Fabrication	21
2.3 Characterization	23
2.3.1 Material Characterization.....	23
2.3.2 Device Characterization.....	25
2.4 Device Designs	33
3 Electronic Band Structure Modeling of Quantum Dots.....	39
3.1 Introduction and Motivation	39
3.2 Challenges for Accurate QD Modeling	40
3.3 Strain Calculations	42
3.3.1 Strain Tensor	42
3.3.2 Methods.....	43
3.3.3 Results for Strain Calculations on Quantum Dots	48
3.3.4 Results for Strain Calculations for DWELL Structures	51
3.4 Electronic Structure Computation.....	52
3.5 Conclusion and Discussions	55
4 Resonant Tunneling Barriers	58
4.1 Introduction.....	59

4.2	Mathematical Justification for RT-DWELL	61
4.2.1	Tunneling	62
4.2.2	Density of States Calculations	67
4.2.3	Simulation Considerations and Results.....	69
4.3	RT-DWELL Devices	70
4.3.1	Designs.....	72
4.3.2	Results.....	73
4.4	RT-DDWELL	78
4.4.1	Designs.....	78
4.4.2	Results.....	83
4.5	Conclusions.....	89
5	Confinement Enhanced DWELL Detectors.....	90
5.1	Different Transitions in DWELL Detectors.....	90
5.1.1	Introduction.....	90
5.1.2	Device Designs	91
5.1.3	Results.....	92
5.1.4	High Temperature Operation	97
5.2	Confinement Enhanced DWELL Detectors.....	101
5.3	Effect of Different Barrier Configurations on DWELLs	109
5.3.1	Motivation.....	109
5.3.2	Device Designs	111
6	Quantum Dot Quantum Cascade Detectors	124
6.1	Introduction.....	124
6.2	Design Considerations	127
6.3	Discussions	134
7	Transport in Quantum Intersubband Photodetectors.....	137
7.1	Introduction.....	137
7.2	Motivation.....	139
7.3	Drift Diffusion Model	141
7.3.1	Theoretical Background.....	141
7.3.2	Algorithm:.....	144
7.3.3	Solution to Poisson equation:.....	146
7.3.4	Results.....	148

7.4	Experimental Work.....	149
7.5	Comparison with Theoretical Results	154
8	Discussions and Future Directions.....	158
8.1	Conclusions.....	158
8.2	Discussions and Future Work	163
8.2.1	RT DWELL Devices.....	163
8.2.2	CE DWELL Devices.....	164
8.2.3	QD QCD Devices	165
8.2.4	Higher Normal Incidence Absorption.....	168
8.2.5	Transport Modeling	169
	Appendix A: Growth.....	172
	Appendix B: Processing.....	175
	References.....	183

List of Figures

Fig. 1.1 : Spectral photon radiance as a function of wavelength for different blackbody temperatures.....	2
Fig. 1.2: Schematics, density of states, and the carrier distribution for (A) bulk, (B) quantum wells, (C) quantum wires, and (D) quantum dots. Note that the quantum dot density of states is independent of temperature. Because the carrier distribution in quantum dots is discrete in energy, thermal transitions between the states require absorption of one or multiple phonons of the energy equal to the energy spacing, unlike the continuous distribution in the case of quantum well. This leads to lower dark current in QDIPs.....	7
Fig. 1.3: (a) Conduction band diagram of a typical DWELL detector, showing a quantum dot embedded in a quantum well. Infrared transition is from the ground state of the quantum dot to the excited state in the quantum well. (b) A TEM image of a DWELL detector (measured by P. Rotella), (c) Schematics of a typical DWELL test pixel and biasing scheme. (c) Band diagram of a multicolor bias tunable DWELL, showing multiple excited energy levels giving rise to different wavelength at different bias ranges.	9
Fig. 1.4: Overview of different aspects of this work. Overall research is broadly divided in three sections.....	11

Fig. 2.1: The device research cycle.....	15
Fig. 2.2 Schematics of MBE reactor	16
Fig. 2.3: Growth rate vs source temperature Arrhenius plot measured on P-MBE system	17
Fig. 2.4: PL spectrum for different nominal QD deposition thicknesses, showing a shift from small QD size to large QD size, through a bimodal distribution (b) Effect of growth temperature on PL spectrum.	20
Fig. 2.5: Effect of doping density on (a) PL (b) Responsivity and (d) Detectivity	21
Fig. 2.6 (a) Room temperature PL spectrum with low power HeNe laser and high power Ar^{++} laser, clearly showing the quantum dot excited state transition. (b) This excited state transition cannot be observed at low temperatures	24
Fig. 2.7: Measured photoconductive gain for different well widths in DWELL detectors, as a function of electric field	30
Fig. 2.8: Overview of the device design process.	34
Fig. 2.9: Different transitions in a bias tunable, multicolor DWELL detector.	35
Fig. 2.10: (a) PL and (b) Spectral response comparison between two detector with identical device designs and different QD nominal depositions.....	36
Fig. 2.11: (a) PL and (b) Spectral response comparison between two detector with identical device designs and different QD compositions.....	37
 Fig. 3.1 One unitcell of zinc blende (ZnS) type FCC lattice (two extra atoms are also shown.) . For the simulations, 8 atoms are assigned to each cubic grid as marked. 1 to 4 are As atoms while 5-8 are group III (Ga or In) atoms.....	45

Fig. 3.2: (a) Geometry of QD showing various crystal directions (b) Plot of total change in atomic position in each iteration against number of iterations, showing rapid convergence.	49
Fig. 3.3 (a) Strain profile for hydrostatic and biaxial strains along [001] direction, which is the growth direction. These are defined as $\epsilon_{\text{hyd}} = \epsilon_{xx} + \epsilon_{yy} + \epsilon_{zz}$ and $\epsilon_{\text{biax}} = 2\epsilon_{zz} - \epsilon_{xx} - \epsilon_{yy}$, respectively. (b) Hydrostatic and biaxial strain profiles along [001] direction for the same geometry, calculated by Jiang et al, showing excellent agreement between the two results.	50
Fig. 3.4: A 2D plot of ϵ_{xx} , ϵ_{zz} and ϵ_{hyd} in xz cross section showing non uniform distribution of strain components inside the quantum dot.....	50
Fig. 3.5: (a) DWELL structure assumed in simulations (b) Calculated strain coefficients in [001] direction, showing the effect of QW.	51
Fig. 3.6: (a) 2D cross sections of strain profiles for (a) E_{zz} , (b) E_{xx} (c) Hydrostatic strain and (d) Biaxial strain for DWELL structures.	52
Fig. 3.7: Computed electronic structure showing two confined energy levels in the CB. The first excited state is composed of two degenerate states of opposite symmetry. The VB ground state is also shown for completeness.(b) The results from a single band effective mass calculation of the CB. (c) Electronic structure for the same structure from Jiang et als for validation.	54
Fig. 3.8: Probability amplitudes of the envelope wavefunctions corresponding to the energy levels shown in a horizontal cross-section of the heterostructure. The QD boundary is shown for reference.....	55

Fig 4.1 (a) Tunneling probability as a function of energy, near barrier height. (b) Tunneling probability as a function of applied voltage, near the barrier height.....	64
Fig 4.2: Schematics of resonant tunneling barrier.	65
Fig 4.3: (a) Effect of barrier thickness on resonant tunneling probability. (b) Effect of well-width on the resonant tunneling probability.	67
Fig 4.4: Calculated density of state functions for quantum dots, quantum well, bulk and total.	68
Fig 4.5: Dark current characteristics for DWELL structure, for the conventional barrier and resonant tunneling barrier.	70
Fig 4.6: Schematic of the control sample: (a) Structure of the device with various energy states (b) Measured spectral response for two biases.	71
Fig 4.7: (a) Calculated energy eigenvalues and wavefunctions for RT-DWELL-2. (b) Calculated Tunneling Probabilities for the two RT-DWELL designs.....	73
Fig 4.8: Spectral response for (a) RT-DWELL 1: Prominent LWIR response for all biases (b) RT-DWELL 2: Prominent MWIR response for lower biases.....	74
Fig 4.9: Normalized spectral response of (a) Control sample (b) RT-DWELL sample, at 30K, 60K, 90K. Note that at 90K maximum operating bias of the device, the spectral response from the RT-DWELL is much stronger than that of the control sample.	75
Fig 4.10: (a) Comparison of dark current density for three devices at 90K showing 2-3 orders of magnitude reduction in dark current. (b) Arrhenius plot of dark current, showing reduction in dark current at all the temperatures. (c) Comparison of dark currents in control and RT-DWELL1 devices at 90K with the theoretical calculations. (d) Activation energies for the three devices.....	76

Fig 4.11: Comparison of (a) responsivity and (b) specific detectivity between RT-DWELL samples and control sample at 77K	77
Fig 4.12: (a) Schematic of DDWELL control sample. The calculated energy levels for various transitions are marked. (b) Measured spectral response for DDWELL control sample at 77 K, clearly showing four distinct peaks which can be individually tuned by the application of different biases	80
Fig 4.13: (a) Schematic of RT-DDWELL Structure. The calculated energy levels for various transitions and resonant tunneling barrier are marked. (b) Measured spectral response for RT-DDWELL sample at 77 K.	80
Fig 4.14: HRTEM image of RT-DDWELL sample, showing quantum dot, quantum well and resonant tunneling barrier. Lines are guide to eye.	81
Fig 4.15: (a) Schematic of RT-Split barrier structure. The calculated energy levels for various transitions and resonant tunneling barrier are marked. (b) Measured spectral response for RT-Split barrier sample at 77 K, clearly showing exclusively longwave in the positive bias. The negative bias shows all the three peaks from the DDWELL control sample.	83
Fig 4.16: (a) Comparison between dark current densities for RT-DDWELL samples with control sample, at 77 K (b) Arrhenius plots comparing RT-DDWELL device dark current with the control sample at +1 V (open symbols) and +4 V (filled symbols). Close to order of magnitude reduction is apparent.	84
Fig 4.17: Comparison of activation energy for all the devices.	85
Fig 4.18: Comparison of (a) responsivity and (b) specific detectivity between RT-DDWELL, RT-Split barrier and DDWELL control samples at 77 K. (c) Comparison of	

peak detectivities (open symbols) and detectivity at +3 V (filled symbols) between DDWELL control sample and RT-DDWELL sample, showing improvement in the device performance even at higher temperatures..... 87

Fig 4.19: Noise PSDs at (a) 77 K and (b) 100 K compared for RT-DDWELL and DDWELL control sample 88

Fig. 5.1 (a) Schematics of the designed structures. The strain bed thickness is varied to tune the excited energy level (b) Band diagram of individual DWELL section for B-C device. (c) Schematics of the types of transitions describing the relative advantages and disadvantages 94

Fig. 5.2: Normalized spectral responses obtained from all the four devices, showing FWHM getting smaller for increasing well width. 94

Fig. 5.3: (a) Measured responsivity at 77K for all the devices. Note that the responsivity for B-C device is highest at lower electric field, while at higher electric fields, the responsivity of B-B device is highest. (b) Measured detectivities for various samples at 77 K, plotted for $f/2$ optics. 95

Fig. 5.4: (a) Photoconductive gain comparison for various devices at 77K (b) Photoconductive gain for B-Q2 at different temperatures, showing an increase in PC gain. 96

Fig. 5.5: (a) Absorption QE comparison for various devices at 77K (b) Absorption QE for B-Q2 at different temperatures. 97

Fig. 5.6: Measured responsivity at higher operating temperatures and corresponding conversion efficiency at the peak wavelengths..... 98

Fig. 5.7: Measured peak detectivities for various samples at higher operating temperatures at $f/2$ optics, showing high detectivity values even at 200K.	99
Fig. 5.8: (a) Comparison of the measured dark current density with estimated photocurrent density to estimate the BLIP temperature for B-Q2 device. (b) Comparison of noise current spectral density (CSD) for different field of views at various temperatures, to estimate the BLIP temperature for B-B device.	100
Fig. 5.9: Infrared image taken at 80K, 85K, 90K and 95K using 320×256 FPA fabricated from B-C device.....	101
Fig. 5.10: Schematics of CE DWELL 1 and the DWELL control device active region, showing the influence of CE barrier (dashed) on the excited energy level, pushing it towards the continuum energy.	103
Fig. 5.11: RHEED patterns during the growth of different layers. (a) Chevron pattern after the quantum dot growth, (b) spotty pattern during the capping layer growth indicating partially capped quantum dots (c) streak pattern during the GaAs capping layer growth, indicating that the quantum dots are completely covered and the surface is flat.	104
Fig. 5.12: TEM images of CE DWELL 1 (a) All seven stacks showing excellent material quality and dot uniformity (b) Flat top pyramidal quantum dot in a compressively strain InGaAs quantum well. Bright layers above and below the quantum well are attributed to CE barriers.	105
Fig. 5.13 (a) Spectral response comparison between CE DWELL 1 and the DWELL control device at 77K; showing broadening of the peak near 6.2 μm and elimination of the bound to bound type peak at 10.2 μm in CE DWELL 1 as compared to the DWELL	

control sample. Inset shows the schematics of participating transitions. (b) Spectral response from CE DWELL 1 at various temperatures, showing the ratio of peaks at 7.5 μm and 6.2 μm increases with temperature. 106

Fig. 5.14 (a) Measured responsivity comparison between CE DWELL 1 and the DWELL control device at 77K, showing a factor of 7 increase in responsivity for CE DWELL 1 at lower bias. (b) Measured detectivity of CE DWELL 1 device showing more than a factor of 10 increase in D^* over the DWELL control device, at 77K, $f/2$ optics..... 107

Fig. 5.15 (a) Effect of QW thickness on the spectral response of CE DWELL structure, showing a redshift in the response due to 0.9 nm increase in the QW thickness for CE DWELL 2 device. (b) Effect of QD nominal coverage, showing a blueshift in the spectral response in CE DWELL 3, which has 2.3ML QD, as compared to 2.0ML QDs in CE DWELL 2. B-B nature of transitions is clear from the small spectral width. Inset shows the comparison of PL spectrum for two devices..... 108

Fig. 5.16 : Comparison of detectivities for all the CE DWELL devices with the control device. 109

Fig. 5.17: Schematic conduction band diagram of the four devices, showing the thicknesses, composition of various materials used and approximate position of the ground state and excited state energies. The diagrams are not to scale..... 112

Fig. 5.18: (a) Normalized PL spectra of all four devices measured using He Ne laser at room temperature. Reduction in the peak wavelength is attributed to lowering of interdiffusion due to mechanical barrier action of Al. Device C has lower PL peak wavelength due to lower strain cap thickness above the quantum dot. (b) Un-normalized spectrum to compare the PL intensities. 113

- Fig. 5.19: Spectral response from the four devices at 77K. The 10-10.5 μm peak present in device A and B is absent in device C and D due to the presence of $\text{Al}_{0.22}\text{Ga}_{0.78}\text{As}$ barrier, which blocks long wavelength carriers 115
- Fig. 5.20: (a) Effect of proximity barrier on the responsivity. Device A, B and D have same remote barrier. It is clear that as the proximity barrier energy increases, the responsivity increases due to better confinement in the excited state leading to a higher wavefunction overlap with the ground state. (b) Effect of remote barrier on the responsivity is much more drastic, with several orders of magnitude reduction in the responsivity due to blocking of both photocarriers and dark current carriers by the large barrier..... 117
- Fig. 5.21: Dark current density comparison between all devices at 100K, showing several orders of magnitude reduction in the dark current for device C due to tall remote barrier. Device D also has more than an order of magnitude lower dark current as compared to device A and B due to the action of CE barriers..... 118
- Fig. 5.22: Dark current density and photocurrent comparison for all the devices to estimate the BLIP temperature..... 120
- Fig. 5.23: Activation energy for the four devices confirming a small effect of the proximity barrier on the activation energy while large effect of remote barrier on the same. 120
- Fig. 5.24: Comparison of detectivities of all the four devices at 77K. This clearly shows that the increase in proximity barrier energy increases the detectivity due to increase in signal and decrease in noise. This does not add to the operating bias for maximum

detectivity. Device C, due to presence of large remote barrier has high detectivity due to low dark current, but it needs large bias voltage for optimum performance. 121

Fig. 5.25: (a) Images for a solder iron on a stand at various temperatures at $V = 0.5V$ (b) Image at 60K for 2.7V of applied bias (c) Image at 80K at 2.3V applied bias. Two point non uniformity correction (NUC) was performed on the images. 122

Fig. 6.1: Pictorial representation of a cascade action. Analogy between a reservoir of water and QD conduction band ground state, pump and photon, water cascade and electron cascade is apparent. 125

Fig. 6.2: Energy band diagram of single stack of QD-QCD in flatband condition. Calculated energies and wavefunctions of energy levels in cascade barrier are shown. Energy levels in DWELL region ($E_0 - E_2$), shown with dashed lines are estimated based on CE DWELL data. 130

Fig. 6.3: Measured spectral response from the QD-QCD device, showing broad response from $5\mu m$ to $9\mu m$, at 90K, showing a strong zero bias response. 131

Fig. 6.4: (a) Comparison of current voltage characteristics at various temperatures for dark and glowbar illuminated conditions. (b) Activation energy as calculated from dark current data, shows two distinct regions at high and low temperatures. 132

Fig. 6.5: (a): Measured responsivity for the QD QCD at 77K, showing 0V responsivity of 10mA/W. The ripple at 0.45V is possibly from a leakage path in the cascade region. Inset shows the differential conductivity at two different temperatures, showing similar dips. (b) Measured detectivity for $f/2$ optics at 77K, showing no operation in negative bias. 133

Fig. 6.6: Estimated photoconductive gain and measured noise at 77K. PC gain at low bias is overestimated, due to system noise limited operation.....	134
Fig. 6.7: (a) Comparison of normalized PL intensity between CE DWELL 1 and QD QCD device, showing the effect of QCD strain profile on the growth of the quantum dot. (b) Comparison between spectral response from two devices, showing slight blue shift in the spectral response and a dominant midwave peak in QD QCD.	135
Fig. 7.1: (a) Schematics of the simulated structure (b)-(f) Contour plots of absolute electric fields at different temperatures.....	148
Fig. 7.2: Charge density plot for the structure in Fig. 7.1 at 0.1V	149
Fig. 7.3: Schematics of structures used for experimental study. Active regions are same as those used in CE DWELL 1 device. (a) 'Bottom Spacer' device (b) 'Top Spacer' device (c) Control device.	150
Fig. 7.4: Comparison of dark currents between (a) Bottom Spacer and the control device, showing same dark current levels in positive bias and a bias and temperature dependent reduction for the spacer device in negative bias. (b) Top Spacer device and the control device, showing the same trend in other bias polarity.	152
Fig. 7.5: (a) Ratio of dark current between the control device and bottom spacer device, showing huge reduction in the dark current, which reduces with reduction in negative bias and increase in temperature. (b) Comparison of activation energy between the three devices showing similar activation energy for top spacer and control device in the negative bias and bottom spacer and control device in the positive bias.....	153

Fig. 7.6: Comparison of responsivity for all the three devices showing similar responsivity between the control device and bottom spacer device in positive bias, while reduced responsivity for spacer device in the negative bias. Same trend is observed for top spacer for the other bias polarity. It is to be noted that this reduction in responsivity is much smaller than the reduction in dark current. 154

Fig. 7.7: Simulated electric field for top spacer and control device for different bias polarities. In positive bias, increasing electric field drops across the top spacer, while in the negative bias, the field drop across the spacer region is small. 156

Fig. 7.8 (a): Band diagram for top spacer structure for +1V and -1V, showing higher band bending for first QW in positive bias. (b) Charge density as a function of distance, showing that the spacer charge regions near the contact regions are much bigger than those near the individual quantum well regions. 157

Fig. 8.1: (a) QD QCD design for same wavelengths as in QD QCD 1, but with 4 quantum wells in the cascade region. (b) QD QCD design with $\text{In}_{0.7}\text{Al}_{0.3}\text{As}$ quantum dots, for LWIR detection..... 167

Fig. 8.2: Polarization dependent spectral response for (a) B-Q2 device (measurements by Dr. Jiayi Shao) and (b) CE DWELL 1 device (measurements by Dr. Jun Oh Kim) showing 21% s/p' polarization ratio..... 168

List of Tables

Table 3.1: Values of material parameters used in this work.....45

Table 5.1: Strain bed thickness (d_1), Al composition in the barrier, peak wavelength and full width half maximum (FWHM) of the spectral response measured at 77K.....93

Table 7.1: List of input and output variables for the drift diffusion model138

1 Introduction

Every object above absolute zero temperatures emits photons. The spectrum of these photons is governed by Planck's law [1] ,

$$L_e = \frac{2hc^2}{\lambda^5} \frac{1}{e^{\frac{hc}{\lambda k_B T}} - 1} \left(\frac{W}{cm^2 sr \mu m} \right) \quad (1.1)$$

Where L_e is the spectral radiance, λ is the wavelength of light, h is Planck's constant, c is the velocity of light in vacuum, and k_B is Boltzmann's constant. This has been plotted in Fig. 1.1, after scaling to a more appropriate form of photon radiance (L_q) (photons/cm².s.sr.μm) for photon detectors.

The infrared regime covers wavelengths from 0.7 μm to 1000 μm. It is often divided into different bands of interest, such as near infrared (NIR) from 0.7 μm to 1 μm, shortwave infrared (SWIR) from 1 μm to 3 μm, midwave infrared (MWIR) from 3 μm to 5 μm, longwave infrared (LWIR) from 8 μm to 14 μm, very longwave infrared (VLWIR) from 14 μm to 30 μm and terahertz (THz) or far infrared (FIR) from 30 μm all the way up to 1000 μm. MWIR and LWIR bands are of special interest as the objects with temperatures within the range of 100K to 1000K have highest radiance in these bands, as can be seen from Fig. 1.1, making them useful for various applications such as defense and security, surveillance, medical imaging, night vision, industrial hot-spot monitoring etc. These bands also have high transparency through atmosphere. It is to be noted that the curves shown in Fig. 1.1 are for perfect blackbody objects. For real objects, which are typically 'gray' these curves are scaled depending on the spectrum of emissivity (ϵ). For 300K

objects, the peak of the radiance spectrum is near $10\ \mu\text{m}$, making the LWIR bands more sensitive, and hence more important for imaging applications. In this work, we will focus on the MWIR and LWIR bands, however the concepts developed can be scaled to VLWIR bands as well.

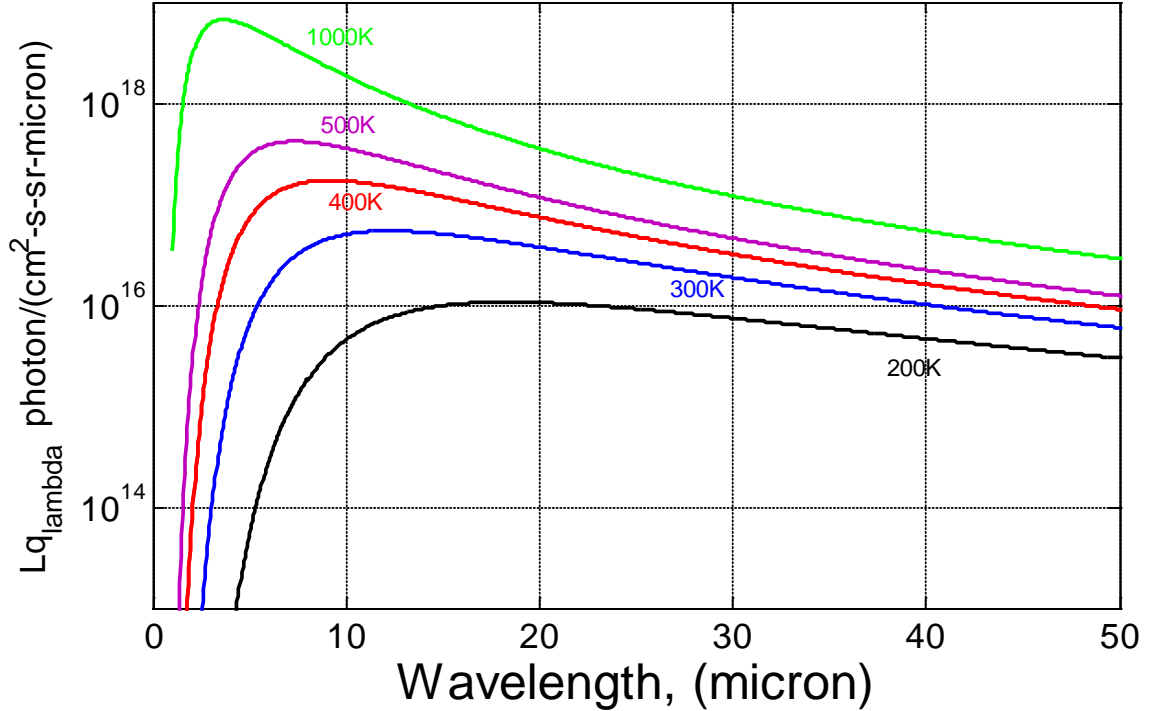


Fig. 1.1 : Spectral photon radiance as a function of wavelength for different blackbody temperatures.

1.1 Infrared Detectors: Requirements and Types

Infrared detectors can be generally classified in two broad categories [2, 3], thermal detectors and photon detectors. Thermal detectors, such as Si microbolometers, pyrometers, thermocouples, Golay cells, superconductors etc detect the integrated power of incoming infrared radiation as 'heat'. These typically have a broadband spectrum with room temperature operation, low sensitivity and are low cost, with the exception of

superconductors (eg. superconducting nanowires [4]). Photon detectors, on the other hand, respond to the infrared radiation by changing the electrical properties, such as conductance or voltage drop by incremental increase for every photon absorbed. Popular materials for photon detectors are III-V and II-VI semiconductors with direct bandgap, which is equal to the energy of photon bands of interest. These are called band to band detectors, which typically have large quantum efficiency. Examples of these include HgCdTe, InSb, InAs/GaSb based strained layer superlattices etc. An other type of photon detectors, namely intersubband detectors utilize the energy spacing, typically result of quantum confinement, in one of the bands, such as conduction band. Quantum well infrared photodetectors (QWIP) and quantum dot infrared photodetectors [5] (QDIP) are examples of intersubband detectors. These typically have lower absorption quantum efficiency as compared to band to band detectors. In this work, we will be focusing on a hybrid between QWIP and QDIP, called quantum dots-in-a-well (DWELL) photodetectors, using InAs quantum dots in InGaAs-GaAs-AlGaAs quantum wells.

Infrared photodetectors have diverse design requirements placed on their performance parameters, such as the required sensitivity, spectral selectivity, operating temperature, peak wavelength and cost, depending upon the application [3]. In low volume high cost applications, such astronomical applications, where highly sensitive and extremely low noise detectors are required, HgCdTe-based (MCT) detectors are currently the dominant technology in the longwave infrared regime [6]. Large area non-uniformity, cost and lack of availability of substrates are some of the critical problems associated with HgCdTe detectors, which makes research on detectors based on mature III-V epitaxial material systems attractive. Other important interband infrared detector technologies are based on

InSb for mid-infrared applications and Si:As impurity band conductors (IBCs) [7] for very-long-wave infrared applications. These detectors require cryogenic operating temperatures and the cutoff wavelength drifts with changes in operating temperature. An emerging interband technology is type II strained layer superlattices (SLs) [8, 9] based on the InAs-(In-Ga)Sb material systems. These detectors are promising alternatives for HgCdTe-based detectors because of high quantum efficiency and low dark currents [10]. Excellent comparisons of the technologies mentioned above can be found in [3, 11-13].

1.2 Comparison between QDIP and QWIP

Quantum intersubband detectors, such as QWIP, QDIP and DWELL detectors, consist of several stacks of quantum wells/quantum dots separated by thick barrier materials. This active layer is sandwiched between highly n-doped top and bottom contact layers, forming an n-i-n photoconductive structure. Infrared detection takes place due to transition of electrons from the ground state of the quantum well or quantum dot to one of the excited states in the conduction band by absorption of photon. Carriers drift towards to contact regions by the application of electric field. In this section, we compare the operating principles and the performance of QWIPs with QDIPs and DWELL. This is important because these technologies belong to a class of intermediate volume intermediate cost applications. They have similar market requirements, and similar cost per pixel associated with them, making them competing technologies for this niche. Hence we will use QWIPs a performance benchmark for QDIPs.

Typical characteristics of the third-generation imaging systems are high-operating temperature, multispectral operation, and large format arrays. The quantum dot infrared

photodetector technology, owing to the three-dimensional confinement of carriers, the richness of electronic spectra in the quantum dots, and the mature III-V based fabrication technology, suit these requirements. In QDIP devices, the infrared absorption is a result of intersubband transitions from the quantum dot ground state to various excited states in the conduction band.

The QDIP technology has seen rapid progress [5, 14-17] over the last decade, making it a competitive technology for a third-generation imaging system. Quantum dot infrared detectors have already demonstrated high operating temperature imaging [18, 19] room temperature operation at midwave infrared [19] and longwave infrared and very longwave infrared [20] regimes, excellent characteristics in far-infrared and terahertz [21] detection and excellent imaging with large format arrays [22] in LWIR regime. However, QD-based detectors currently suffer from lower absorption quantum efficiency as compared with the band-to-band photodetectors. Nevertheless, for the photon-rich terrestrial applications, the focal plane array performance is usually limited by the charge capacity of the readout circuit. In this regime, QDIP detectors can achieve similar performance as band-to-band photodetectors because of the ultralow dark current levels in QDIPs.

Quantum well infrared photodetectors [23-26], using intersubband absorption in quantum wells, are well-established as a technology and are commercially available in large format focal plane arrays [24], due to a mature and relatively inexpensive III-V epitaxial growth and fabrication processes. QWIPs are technologically important for LWIR photon-rich systems such as medical imaging, gas sensors, and surveillance applications. However, they suffer from low quantum efficiency, higher dark current, absence of

normal incidence absorption, and required cryogenic temperature of operation. Quantum dot infrared photodetectors are generically similar to QWIPs but promise to solve these problems by the virtue of zero-dimensional quantum confinement. Some of the potential advantages of QDIPs over QWIPs include the following:

1. Ability to absorb normally incident light because of three-dimensional confinement, thereby eliminating the need of special light coupling techniques such as gratings.
2. Reduced dependence of the carrier distribution on the temperature.
3. Carrier lifetimes 10–100 times longer than QWIPs, giving rise to a lower dark current.

The latter two advantages can be explained qualitatively by reference to Fig. 1.2. In a perfect zero-dimensional system, the density of states is represented by a series of delta-functions in energy. This eliminates the dependence of the density of states on the temperature, leading to a greatly reduced dependence of carrier distribution on the temperature. Because the carriers are confined in all the three dimensions, if the energy separation between the two states is higher than longitudinal optical (LO) phonon energies, carriers need multiphonon process at the same time, in order to get to the excited state. This reduces the efficiency of the scattering mechanisms and hence reduces the dark current significantly, as compared with the QWIP devices, by increasing the carrier lifetimes in the excited state of the quantum dot. Theory and experiments confirmed that electrons in quantum dots have much higher carrier lifetimes, up to of 100 ps [27] as compared to bulk or quantum wells that are limited to about 1–5 ps [28].

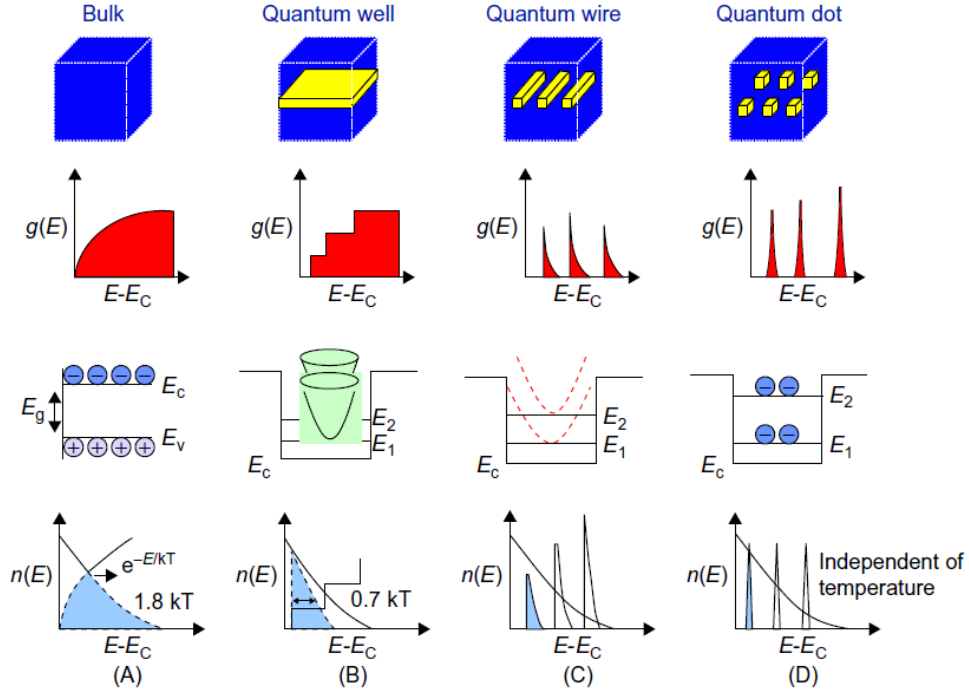


Fig. 1.2: Schematics, density of states, and the carrier distribution for (A) bulk, (B) quantum wells, (C) quantum wires, and (D) quantum dots. Note that the quantum dot density of states is independent of temperature. Because the carrier distribution in quantum dots is discrete in energy, thermal transitions between the states require absorption of one or multiple phonons of the energy equal to the energy spacing, unlike the continuous distribution in the case of quantum well. This leads to lower dark current in QDIPs.

Although the advantages of an ideal zero-dimensional system in optoelectronic devices were predicted much earlier [29, 30], it was only after the repeatable and controllable epitaxial growth of self-organized quantum dots in Stranski-Krastanov (SK) mode that researchers began to probe into quantum dot physics by growth optimization [31-33], spectroscopy [34, 35] (Drexler et al., 1994; Heitz et al., 1997), band structure modeling [36, 37] and device-related studies. Because of the interesting physical properties and the relative ease of fabrication, researchers were attracted toward QDIPs.

Berryman et al. [38] was among the first groups to demonstrate MWIR photoresponse in 1997. QDIPs in the LWIR [39, 40] and VLWIR [41] wavelengths were also demonstrated. It has been predicted [14, 42, 43] that QDIPs will significantly outperform QWIPs and emerge as an important technology for infrared detection. Currently various research groups from around the world are working toward realizing the theoretically predicted advantages of QDIPs. After about a decade of research, QDIPs are beginning to outperform QWIPs by demonstrating lower dark current and higher operating temperature [44-46]. Various groups have been working on methods to improve the structural and optical properties of quantum dots [47-52] to increase the carrier lifetime, as well as to increase the quantum dot density. Dark current levels have been significantly reduced by using various barriers, such as AlGaAs current blocking layers [53, 54] on GaAs-based QDIPs.

1.3 DWELL Detectors

In quantum dots-in-a-well or DWELL detectors, typically, InAs or InGaAs quantum dots are embedded in InGaAs-GaAs quantum well or InGaAs-GaAs-AlGaAs double quantum well. The presence of compressively strained InGaAs surrounding compressively strained InAs quantum dots increases the optical quality of the quantum dots by strain relaxation and optimized growth temperatures of the matrix materials, along with increased dot densities. DWELL designs [55-57] have attracted a lot of researchers as they allow superior control of peak wavelength of operation, improved optical properties of quantum dots, and reduced dark currents [58-64]. The infrared absorption is from the quantum dot ground state to one of the eigenstates of the quantum well. Multiple peaks arise from

transitions to different final states and can be efficiently selected by changing the bias voltage. Schematics of DWELL Detectors, transmission electron microscope (TEM) image of a typical DWELL detector and a schematics of a bias tunable multicolor DWELL detector and the corresponding biasing scheme is depicted in Fig. 1.3. Recently, band-structure engineering approaches to reduce dark current levels and improve transport properties have been demonstrated. Some of the approaches include resonant tunneling QDIPs [20, 65-67] and superlattice based QDIPs [68].

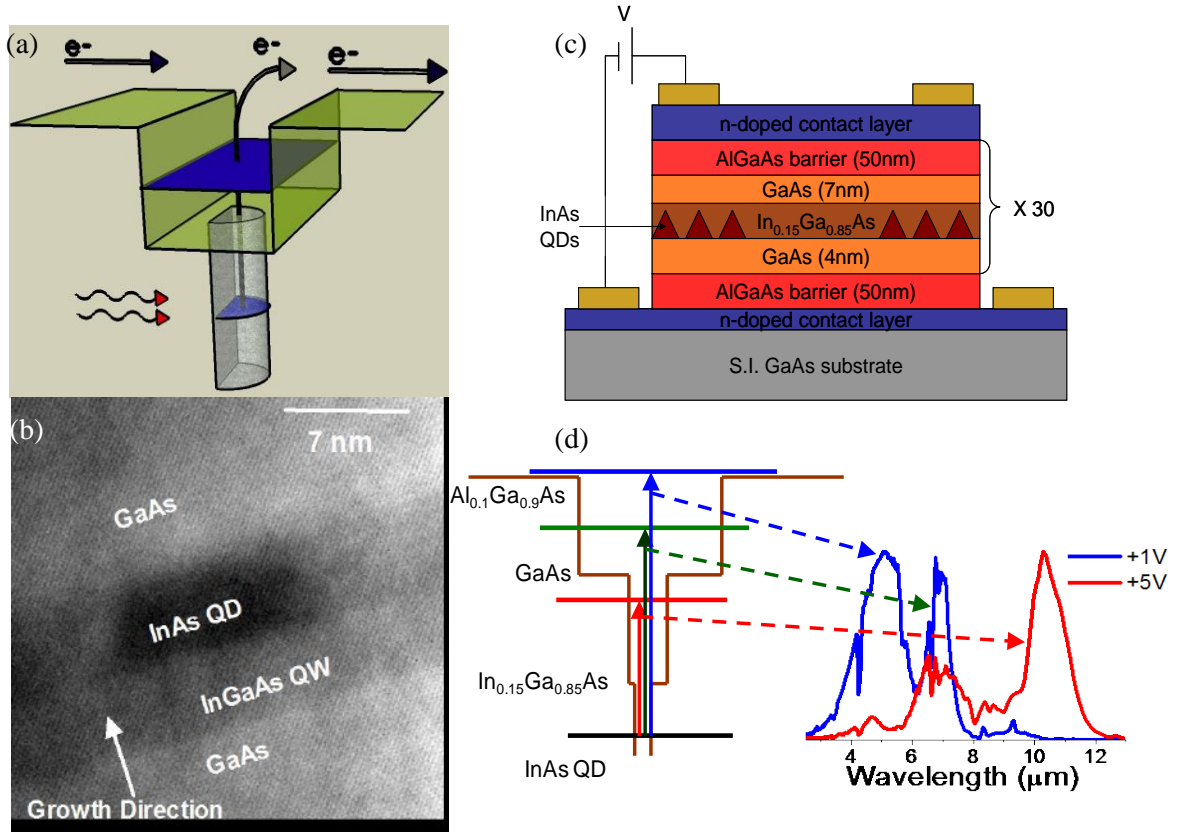


Fig. 1.3: (a) Conduction band diagram of a typical DWELL detector, showing a quantum dot embedded in a quantum well. Infrared transition is from the ground state of the quantum dot to the excited state in the quantum well. (b) A TEM image of a DWELL detector (measured by P. Rotella), (c) Schematics of a typical DWELL test pixel and biasing scheme. (d) Band diagram of a multicolor bias tunable DWELL, showing multiple excited energy levels giving rise to different wavelengths at different bias ranges.

Theoretical modeling of quantum dots [36, 69-71] has been carried out to analyze and predict the quantum dot characteristics measured from photoluminescence (PL), photoluminescence excitation [72], spectral response, and absorption studies. Most popular methods include atomistic pseudopotential approach [73]; eight-band k.p analysis [36, 71] based on valence force field method for strain calculations; and numerical simulations based on finite volume methods [74]. Various groups around the world have successfully demonstrated good-quality infrared imaging [18, 75-77] with QDIP-based focal plane arrays. There are excellent articles that review the physics of QDIPs [40, 69, 78, 79] and discuss the fundamental advantages and device characteristics, as well as the state-of-the-art reviews [14, 16, 17, 80].

1.4 Motivation and Approach

Although QDIPs and DWELL detectors have shown much potential for replacing QWIPs as a dominant technology for the intermediate volume intermediate cost, tactile applications, in reality the technology has not yet been commercially successful. In this work, we identify key areas of improvement which could lead to successful demonstration of DWELL focal plane arrays at high operating temperature. Huge improvement in terms of better designs and improved material quality can be achieved through understanding of the physics of carrier transport and carrier confinement in these detectors. This work is aimed at making the DWELL technology suitable towards making successful FPAs. This includes reduction in dark current, increase in quantum efficiency, understanding and reducing the photoconductive gain, better understanding of carrier

transport and electronic bandstructure and low bias operation. The approach can be divided in three broad areas as summarized in Fig. 1.4.

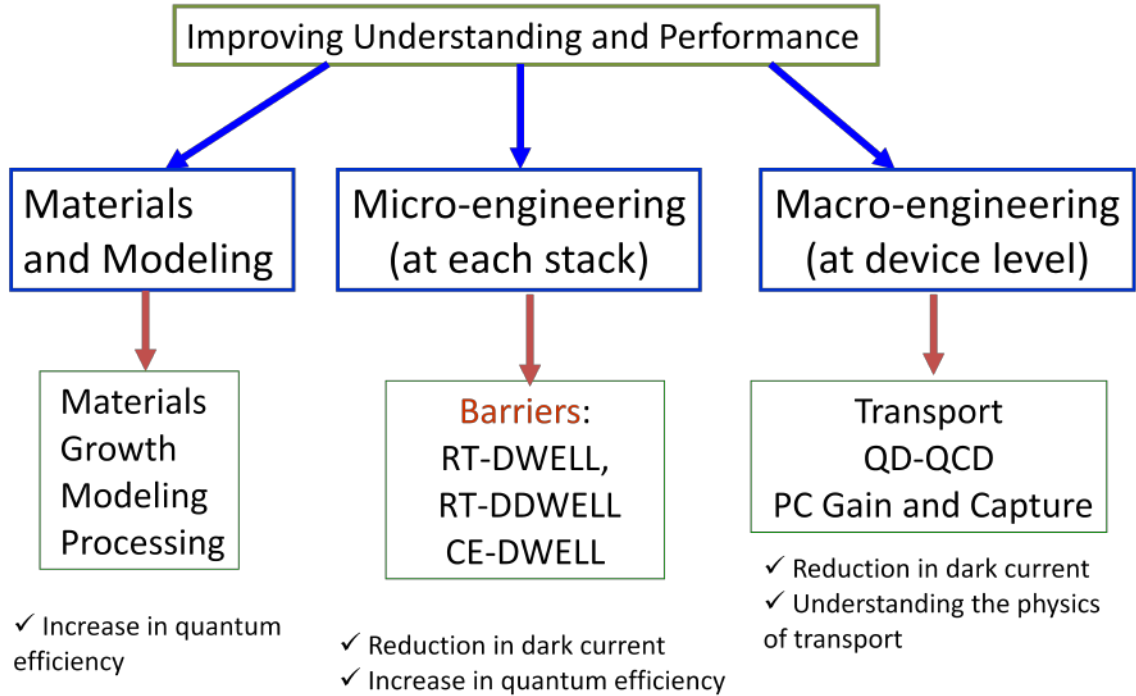


Fig. 1.4: Overview of different aspects of this work. Overall research is broadly divided in three sections.

Micro-engineering refers to understanding and improving the barrier designs for DWELL detectors in order to reduce the dark current without compromising the photocurrent. Effect of different parameters such as barrier compositions, widths, distance from the quantum dots, well designs, etc on device properties such as the peak wavelength, spectral width, dark current, responsivity, photoconductive and detectivity have been studied. It is found that just by controlling the excited state in the quantum well with respect to the barrier, different types of transitions such bound to bound (B-B), bound to continuum (B-C) and bound to quasibound (B-Q) can be achieved. This gives the device designer precise control over the above mentioned properties. Lower operating bias for

maximum detectivity, which is important from a FPA point of view, can be achieved by going towards B-C and B-Q types of transitions. The optimized B-Q transition based structures can be further improved by the introduction of confinement enhancing (CE) barriers around the DWELL region. *Smart* barriers, which selectively block the dark current while allowing the photocurrents of the desired wavelengths to pass have been designed. An example to this are resonant tunneling (RT) barriers. Use of these barriers to drastically reduce the dark current and improve the operating temperature and also to select the wavelength band of interest out of a broad control spectrum has been demonstrated on both DWELL and quantum dots in a double well (DDWELL) structures.

Macro-engineering refers to study of the electric transport in the DWELL detectors both experimentally and theoretically to understand the behavior of electric field, space charge region, emission and capture into the DWELL region etc across the entire device. A simple model based on the solution of Poisson's equation coupled with the current continuity equations has been utilized to qualitatively explain the experimental behavior of DWELL detectors, such as the variation of activation energy with the number of stacks, effect of spacer layers between the active region and contacts on the dark current, etc.

A novel quantum dot quantum cascade detector (QD-QCD) design has been proposed and fabricated, which has a photovoltaic response with n-i-n architecture. In QD QCD, the photoexcited electrons are swept away by the internal electric field generated by quantum cascade action, which couples the electron back into the quantum dot of the next stack. The prime advantages of this structure are zero bias operation and low photoconductive gain, both highly desirable for FPA implementation.

No device can be successful without optimized material properties. In this work, we optimize the quantum dot growth parameters such as growth temperatures, growth rates, doping, matrix materials and the quantum dot materials to achieve better material as well as device results. However, it will be shown that higher photoluminescence (PL) intensity does not necessarily indicate higher signal to noise ratio for the detector. In order to understand the properties of quantum dot to design better devices, electronic structure simulations, along with strain modeling with valence force field method [36] have been carried out.

1.5 Outline of the Dissertation

The dissertation is organized into three sections. The first section is 'Building Blocks' of the DWELL infrared detectors. In chapter 2, different steps in the detector fabrication such as epitaxial growth, material processing, material and device characterization techniques are discussed. Detector design process using a semi-empirical approach, which has been successfully used in different barrier design configurations, will be discussed. Issues related to the detector designs, such as effect of barriers, doping, quantum dot and quantum well dimensions etc are highlighted. In chapter 3, a rigorous quantum dot electronic bandstructure modeling approach is discussed. Procedure and results for strain modeling and k.p simulations of the quantum dots are presented.

Section II, chapter 4 and 5, focus on the 'micro-engineering' approach. Chapter 4 presents the tradeoff involved in traditional barrier design and the use of resonant tunneling barriers to circumvent this tradeoff. Detailed discussion on design and characterization of RT-DWELL detectors on unoptimized DWELL and optimized DDWELL structures are

included. In chapter 5, a systematic study of different transitions leading to high operating temperature and high performance DWELL detectors with desired properties is presented. Designs and results related to confinement enhanced DWELL (CE-DWELL) architectures will be discussed. This chapter will also include a discussion about the effect of various components of the barrier on the detector parameters such as dark current, responsivity and activation energy, in order to shed light on barrier design process.

Section III, which includes chapter 6 and 7 focuses on 'macro-engineering'. Chapter 6 introduces the QD-QCD device motivation, designs and results. Theoretical and experimental investigation of the nature of electric field and space charge regions in the DWELL structures are discussed in chapter 7. Finally, chapter 8 are devoted to discussions about conclusions from this work and identifying the key areas for the future work.

Two appendices have been added to supplement the text without disturbing the flow. Appendix A gives detailed growth recipe for a typical DWELL design and discusses the fine details of growth such as temperature changes, interruptions etc. Appendix B gives a process flow for the cleanroom fabrication of focal plane arrays. Hybridization and substrate removal process are discussed briefly.

2. Building Blocks

This chapter will give an overview of the methods used in this work. Research in QDIPs can generally be divided in four sections. These are summarized in Fig. 2.1 below. Each section contains several steps, detours and unknowns, which make the research challenging and exciting. In this work, we have sought improvements in all the four aspects of research, in order to improve the understanding and performance of QDIPs. In this chapter, these aspects and the steps involved in them will be briefly discussed.

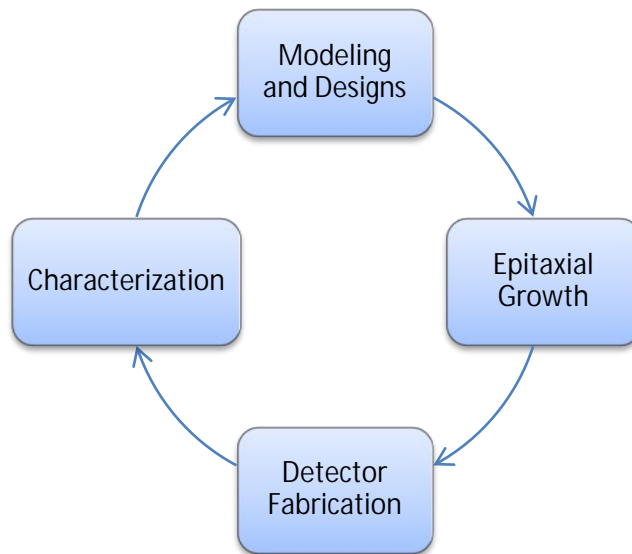


Fig. 2.1: The device research cycle

2.1 Epitaxial Growth

2.1.1 Introduction to MBE

Epitaxial growth of QDIPs is typically done using molecular beam epitaxy (MBE) or metal organic chemical vapor deposition (MOCVD). In this work, all the material growth

has been done with an elemental source V80 MBE machine by VG Semicon, tagged as P-MBE to distinguish from other MBE systems. The schematic of the MBE machine is shown in Fig. 2.2. The source panel in this MBE system contains two dopant cells, Si for n-type and Be for p-type doping on GaAs, group III sources such as two Ga sources, Al and In sources and group V sources such as Arsenic and Phosphorus sources equipped with a valved cracker. The system is always maintained under ultra high vacuum (UHV) in order to reduce the defect density and the background doping concentration in the growth epilayers. For this, the growth chamber needs to be thoroughly baked at elevated temperatures for extended time frame after it has been exposed to the atmosphere, to evaporate all the organic impurities and water contents from the chamber.

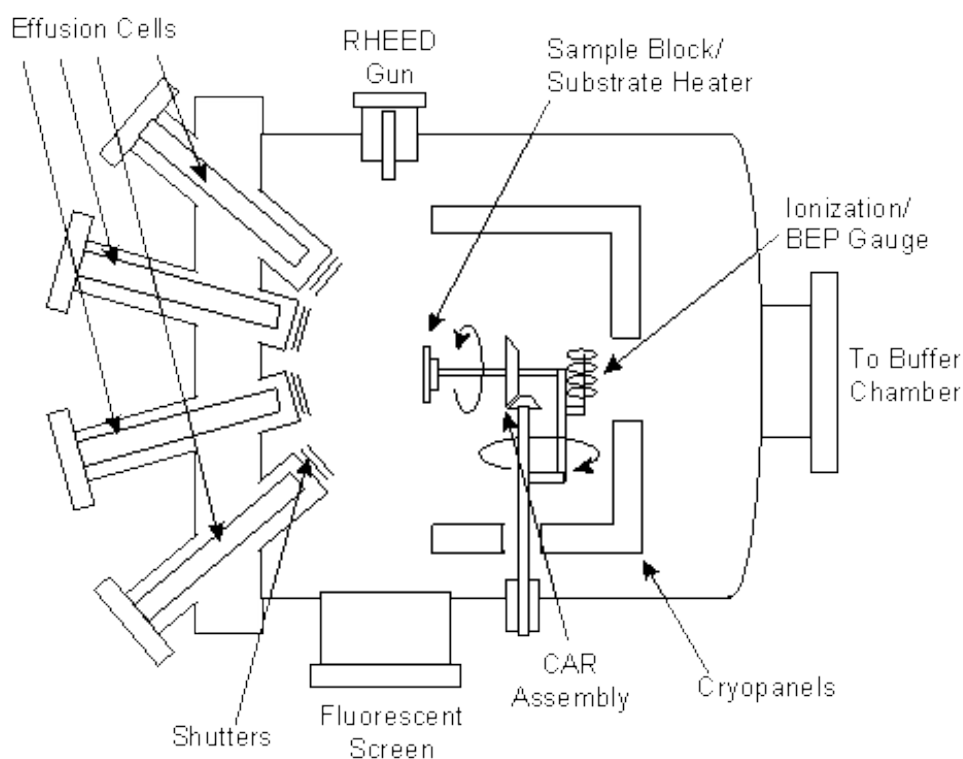


Fig. 2.2 Schematics of MBE reactor

Prior to growth, various system parameters need to be calibrated. This includes growth rates, doping densities, pyrometer temperatures etc. For growth rate calibrations, reflection high energy electron diffraction (RHEED) intensity oscillations [81] are used. For this, a small sample (typically 3-4 mm side squares) are mounted on a molybdenum plates. The RHEED pattern is obtained after oxide desorption. The intensity oscillations are observed after both group III and V shutters are open. During the two readings, surface is recovered under group V flux. This procedure is repeated several times (4-5 times) at every source temperature and then it is repeated for 4-5 different source temperatures. A line fit through the Arrhenius plot of log of growth rate in monolayers/s against $1/T$ gives the equation for growth rate at different source temperatures under those conditions. A typical Arrhenius plot of growth rate against $1000/\text{source temperature}$, obtained from P-MBE is shown in Fig. 2.3. The absolute value of source temperature for the given growth rate depends on the source design and material characteristics. X-ray diffraction (XRD) calibration samples may be grown after this to verify the growth rates.

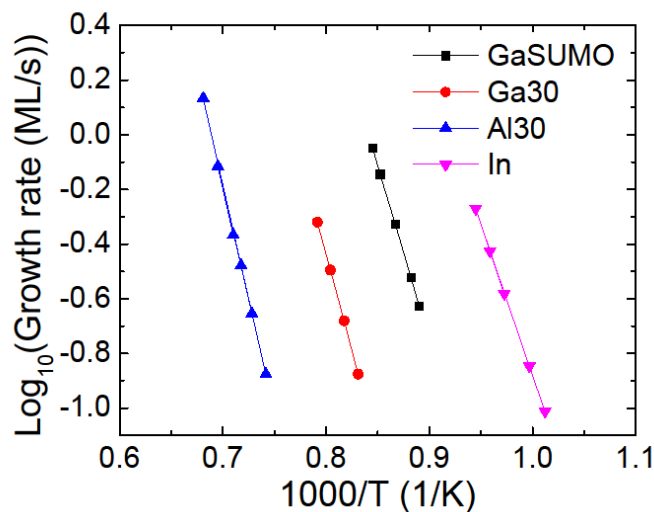


Fig. 2.3: Growth rate vs source temperature Arrhenius plot measured on P-MBE system

For doping calibrations, thick GaAs layers (typically 3 μm) are grown with doping at different dopant source temperatures. Hall measurement in Van der Pauw configurations are carried out to measure the doping density. A linear fit in the data gives doping density for different dopant temperatures for a given growth rate, which can be scaled to different growth rates.

2.1.2 Stranski-Krastanov growth mode

For the growth of strained epilayer on the substrate, the three well known growth modes [82] are Frank-van der Merwe, Stranski–Krastanov, and Volmer-Weber, depending on the interface and surface energies. Formation of the epitaxial, self-assembled quantum dots, Stranski–Krastanov (SK) growth mode is by far the most popular and widely studied growth mechanism for the growth of coherently strained, dense, self-assembled arrays of quantum dots. In the Stranski–Krastanov growth mode, the strained layer undergoes a transition from the planar growth mode to 3D island formation after a critical thickness has been grown. This reduces the total free energy of the system, which is a sum of interface, bulk, and surface energies. The abrupt 2D–3D transition occurs within 0.2 monolayers (ML) after the critical thickness, showing rapid rise of the density of the quantum dots. This strain mediated formation of quantum dots on a planar, strained “wetting layer” is observed across different strained material systems such as InAs/GaAs, InGaAs/GaAs, InAs/InP, Ge/Si, and so on. Although observed across a wide variety of materials and conditions, the driving kinetic mechanisms for these processes are highly dependent on the material conditions, such as orientation, flatness, and growth conditions such as growth temperature, growth interruptions, growth rate and III-V flux ratios.

Comprehensive studies of these transitions have been published [31, 82-84] in the literature.

2.1.3 Optimizing the growth parameters

For optimized device designs, the understanding of optimum growth parameters is crucial. These parameters include, growth temperatures for quantum dots, quantum wells, and barriers, growth rates, interruption time, doping densities in each layers, and nominal quantum dot thicknesses. In this subsection we will discuss effect of these parameters on the detector performance. A sample growth recipe and temperature programs have been detailed in appendix A.

Growth temperature, nominal deposition and growth rate of quantum dots

The most important parameters in the growth optimization of quantum dots are the growth temperature of the quantum dots and surrounding matrix material, and quantum dot nominal deposition. For higher growth temperatures, the adatom mobility increases, thereby increasing the size of the dot. This, in turn, leads to a red shift in the PL wavelength. At lower growth temperatures, the dot sizes are smaller because of the reduced surface mobility. However, the PL intensity decreases at low growth temperatures as a result of higher size variation. Typical growth temperatures for the MBE growth of InAs QD are from 450 to 510°C. The growth optimization involves finding the optimum temperature with high dot density and smaller size variation. As the nominal deposition thickness of QD increases, the size of quantum dot gets larger, leading to a redshift in PL wavelength. Typically, the PL intensity also increases, before it saturates at some value. Fig. 2.4 shows the effect of nominal deposition thickness of QD and growth temperature variation on the PL intensity and wavelength. It is to be

noted that these results were obtained during the optimization process and not under optimum growth conditions. For higher rate of QD deposition, the effect is similar to the reduction in growth temperature as it increases the dot density and reduces the dot size. However, it is difficult to precisely control the deposition at very-high rate. Typically, deposition rates of 0.05–0.2 ML/s are used for InAs QD growth, as is the case in this work.

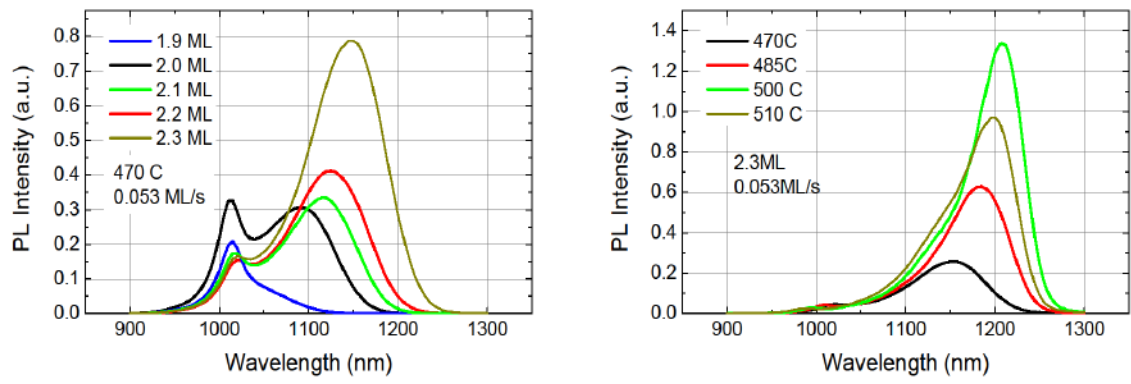


Fig. 2.4: PL spectrum for different nominal QD deposition thicknesses, showing a shift from small QD size to large QD size, through a bimodal distribution (b) Effect of growth temperature on PL spectrum.

Doping Optimization

Doping optimization involves estimation of optimum doping density in quantum dots, for highest detectivity. As the doping increases, the absorption efficiency increases, increasing the responsivity. PL intensity is also increased proportional to the amount of doping. However, the dark current increases as well, suggesting that there exists an optimum doping density. Typically, this is 1-2 electron per dot [85, 86], where the dot density is estimated by atomic force microscopy (AFM). For example, Fig. 2.5 shows the variation of PL, responsivity and detectivity for three devices with identical growth

conditions and different doping in QDs. Density of QD was assumed to be $8 \times 10^{10} \text{ cm}^{-2}$. It has been shown previously [85] that for undoped quantum dots, the detectivity decreases.

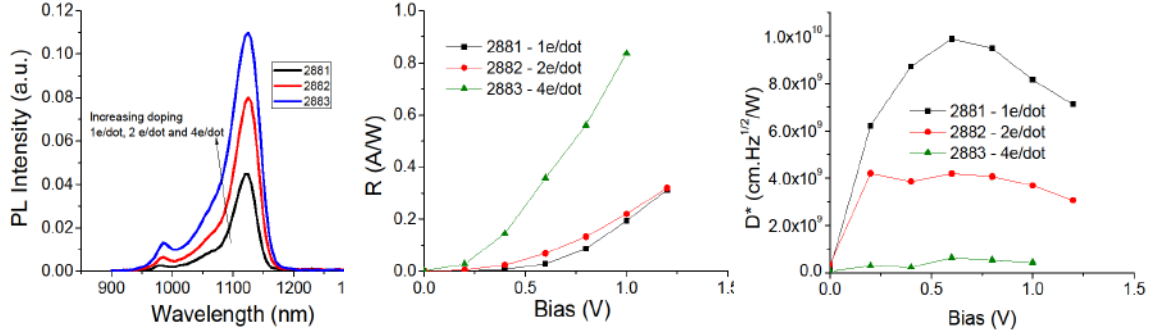


Fig. 2.5: Effect of doping density on (a) PL (b) Responsivity and (d) Detectivity

Although a higher PL peak intensity for the given growth conditions corresponds to better optical quality of quantum dots, it does not imply a better detector performance, contrary to the popular belief. In this work, it has been repeatedly observed that PL intensity cannot be compared across different device structures and doping profiles. Instead, a more important parameter is the PL peak wavelength, which governs the wavelengths of spectral response. This fact will be highlighted in section 2.4 for designing DWELL detectors.

2.2 Device Fabrication

Once grown, the material is processed into an array of single pixel detectors. This process involves the following steps which are performed in the cleanroom. Contact lithography is used to define the patterns in photoresist for every step. The details of processing steps are given in Appendix B.

1. Mesa etching: This is the first step, which involves inductively coupled plasma (ICP) etching for vertical sidewalls. The sidewalls may be further smoothed by wet chemical etching to reduce the surface roughness.
2. Contact metallization: For n-i-n devices, since both the contacts are n-type doped, common metal can be used. Ge/Au/Ni/Au metal has been used in all the devices to form Ohmic contacts.
3. Passivation (optional): Si_3N_4 can be used for protecting sidewalls from further oxidation to increase the lifetime of the devices. For single pixel processing, this step is usually skipped.
4. Rapid thermal annealing (RTA): Metal contacts are annealed at high temperature (350 °C to 400 °C) for one minute to form an eutectic alloy between Ge and Au metals, to form delta doping which creates Ohmic contacts.

If the material performance is satisfactory, it can be processed into a focal plane array for imaging applications. FPA process flow involves following steps:

1. Mesa etching
2. Si_3N_4 deposition
3. Si_3N_4 etching
4. Contact metal deposition
5. RTA
6. Under-bump metal deposition (Ti-Ni-Au)
7. Indium deposition
8. Dicing.

9. Indium reflow
10. Hybridization with ROIC
11. Underfil epoxy and baking
12. Substrate removal

All the above mentioned steps can be now performed in Center for High Technology Material (CHTM) laboratories.

2.3 Characterization

Several characterization techniques have been used in the course of this work. These can be broadly classified as material characterization and device characterization. References are given for various characterization techniques.

2.3.1 Material Characterization

Material characterization is critically important as a feedback during epitaxial growth optimization. Most frequent methods [81] for this work were photoluminescence, hall measurement, X-ray diffraction and transmission electron microscopy. Sample surface topology can be also analyzed by scanning electron microscopy (SEM), dark field phase contrast microscopy and Normarski microscopy.

Photoluminescence

PL is extremely powerful, yet relatively simple technique for the active region characterization. The PL setup in CHTM has great flexibility in PL measurement, such that it can measure 10K to room temperature PL, with different laser system such as low power HeNe lasers to high power Argon (Ar^{++}) ion laser. Wavelength range is also

variable from 800 nm to mid-infrared wavelengths ($\sim 5.5 \mu\text{m}$) allowed by different detectors and grating monochromator.

After every epitaxial growth, a room temperature PL measurement with a HeNe laser is done, in order to verify the quantum dot growth. A good QD, due to three dimensional confinement, emits intense PL radiation, which corresponds to the transition between the ground states of the conduction band and valence band. At higher energies, different excited levels can be observed, especially at low temperatures and higher excitation powers. A way to distinguish between bimodal distribution (that is, existence QD ensembles with two different sizes) and excited state in QD is to vary the excitation power and observing the change in the ratio of the peaks. For example, in Fig. 2.6 shows the room temperature and 20K PL data for the same device. At room temperature, the ratio of ground state peak and excited state peak changes dramatically between low power HeNe and 2W Ar^{++} lasers, indicating that it is indeed an excited state in the QD. However, these states are not observed at 20K, probably because of low state filling, due to absence of thermal transitions.

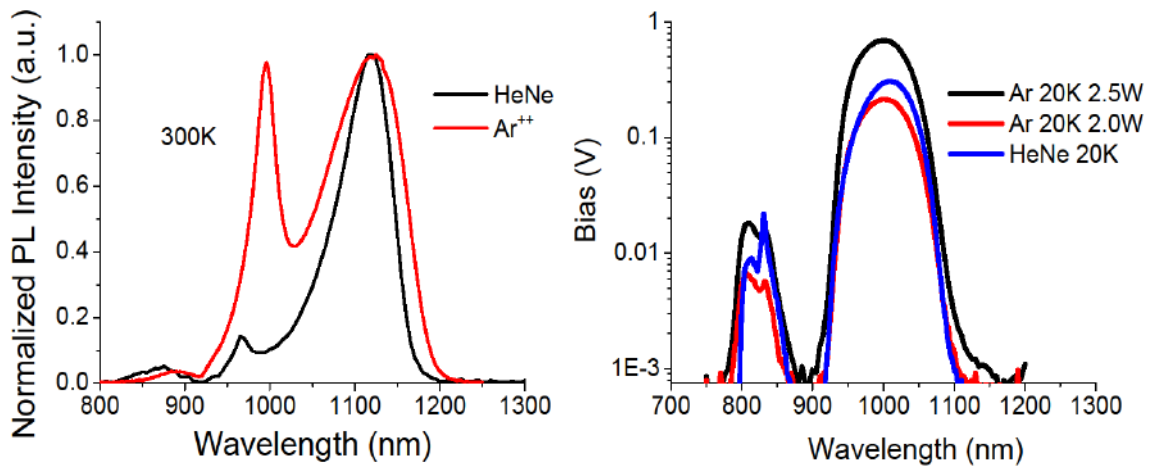


Fig. 2.6 (a) Room temperature PL spectrum with low power HeNe laser and high power Ar^{++} laser, clearly showing the quantum dot excited state transition. (b) This excited state transition cannot be observed at low temperatures .

Hall Measurement

Hall measurement is primarily used to determine the doping density of the device, in order to calibrate the dopant source. For reliable measurements, especially at low doping densities, thick ($>3 \mu\text{m}$) doped layers are desired. Sample preparation involves cleaving the sample in small squares, reflowing indium bumps on four corners. Indium is usually annealed to form ohmic contacts. Gold wires are then attached to Indium bumps which are used to pass the current through the device in Van der Pauw configuration. The measurement gives an estimate of sheet doping density, type of dopant and mobility of the sample. This measurement can also be used for monitoring the background doping in the sample, which gives an idea about the cleanliness of the MBE growth chamber. For this purpose, a standard high electron mobility transistor (HEMT) structure can be grown for improved sensitivity or a very thick GaAs epilayer can be grown for background doping.

2.3.2 Device Characterization

After the device is processed, the detector characteristics are measured. In this subsection, various detector figures of merit, such as dark current, responsivity, photoconductive gain, detectivity and noise equivalent temperature difference (NETD) will be discussed, with respect to their relation with better FPA imaging [5].

Dark current

Dark current is the current which flows through the detector in absence of any photon flux. It is usually measured in a variable temperature cryostat with a cold shield (made of Al) in front of the device and cold finger cooling the device from the back side. This

arrangement, however, has some error depending on the cold shield temperatures which cannot be at absolute zero.

From a system design perspective, the dark current of the detector is one of the key figures of merit. Dark current determines the maximum operating temperature for the detector for a given signal-to-noise ratio (SNR). In QDIPs, the prime source of dark current is the thermionic emission of carriers from the quantum dots, while field-assisted tunneling, interdot tunneling [87], sequential resonant tunneling through defects [88], and thermal generation of carriers in barrier regions are other important sources. Detailed modeling of dark current and transport in QDIPs [43, 89-92] are available. Dark current can be reduced by lowering the operating temperature or by increasing the energy barrier by changing the composition in the barrier material. The latter makes it difficult to extract the higher wavelength carriers out of quantum dots. Hence, in a typical QDIP design, there is a trade-off between longer peak wavelength and lower dark current. Because the density of states in quantum dots should be “atom-like,” the dark current is expected to be lower for similar wavelengths, as compared with QWIPs. This is because carriers confined in the quantum dot ground state do not contribute to the bulk dark current, unlike the case of quantum wells, where, due to the continuous density of state even the quantum well ground state contributes to the dark current.

Doping concentrations inside quantum dots have to be carefully controlled and optimized in order to have minimum dark current with high photocurrent levels. The dark current can also be reduced by designing resonant tunneling barriers that block the continuum energies contributing to the dark current while allowing the energy levels of interest to pass through. This allows the dark current to be selectively reduced, while maintaining

the same photocurrent. This has enabled far-infrared detection with QDIPs with moderately low dark current levels.

By comparing the dark current density with photocurrent density, the background limited infrared photodetection (BLIP) temperature regime can be estimated. BLIP temperature is the temperature, for a given bias, at which the photocurrent is higher (typically, by a factor of 4) than the dark current.

Responsivity and photoconductive gain

Responsivity is defined as the amount of photocurrent flowing through the external circuit per watt of optical power incident on the detector. It is typically measured with a calibrated blackbody source radiating photons in the detector response range, which can be calculated by using Planck's law (equation 1.1). Using basic radiometric calculations [1] the number of photons per second falling on the detector can be calculated for the given parameters such as blackbody temperature, aperture size, distance from the detector, detector optical area and the wavelength range of interest. Using these factors, following formula for responsivity can be derived:

$$R = \frac{I_o}{\int_{\lambda_1}^{\lambda_2} \frac{R(\lambda)}{R(\lambda_c)} L_e(\lambda, T) \frac{A_s A_p A_d}{r_1^2 r_2^2} t_1 t_2 F_F d\lambda} \quad (2.1)$$

where $\frac{R(\lambda)}{R(\lambda_c)}$ is the normalized spectrum of the detector, $L_e(\lambda, T)$ is the radiance,

$\frac{A_s A_p A_d}{r_1^2 r_2^2}$ is the solid angle subtended from blackbody onto the detector, in extended

source extended detector configuration (A_s , A_p and A_d are the area of blackbody aperture,

blackbody slit and detector respectively, while r_1 and r_2 are the distances from the blackbody aperture to the slit and blackbody slit to the detector, respectively). I_0 is the measured photocurrent from a detector. Photocurrent is taken out from the detector and amplified in a low noise preamplifier and measured using a spectrum analyzer. The chopper frequency is used as a trigger for the SRS760 fast Fourier transform (FFT) spectrum analyzer. t_1 and t_2 are transmission of windows and any other optics used, and F_F is the form factor which can be calibrated with a detector with known responsivity (such as InGaAs detector at 77K). This includes chopper loss and any other optical scattering losses.

Photoconductive (PC) gain is the number of electrons flowing through the external circuit for each photon absorbed. The physical origin of photoconductive gain arises from charge neutrality condition in the quantum dot due to positively charged donor ions left behind after photo-excitation of electrons from the quantum dot.

Increased carrier lifetime in the QDIPs as compared with QWIPs, because of the phonon bottleneck, has significant implications. Because the excited states of quantum dots are long-lived, it is easier to extract the carriers out, by the application of an electric field, before they relax back to the ground state, thereby increasing the quantum efficiency. Longer carrier lifetime also implies higher photoconductive gain. Photoconductive gain, which is inversely proportional to the capture probability, from 0.1 to 10,000 has been observed in the literature [89, 93, 94] for QDIPs. Photoconductive gain originates from the requirement of charge neutrality of the quantum dots after photoexcitation (or thermal excitation) of an electron from the quantum dot. If p_c is the capture probability of the quantum dot, $1/p_c$ carriers are needed for one electron to get captured in the

quantum dot. If there are N stacks in the active region, approximately, average of $g = 1/Np_c$ electrons have to be injected from the contact for each photon absorbed. Note that this formula is highly approximate, as it assumes uniform capture probability (hence uniform electric field) in all the stacks and also neglects the relative position of the stack with respect to the contact and carrier re-excitation from the quantum dots. Experimentally, the photoconductive gain can be estimated from the measured noise and I-V curves [95],

$$g = \frac{i_n^2}{4qI_{dark} \Delta f} + \frac{1}{2N} \quad (2.2)$$

In QDIPs, the last term is negligible as the gain is usually higher than unity because of the low capture probability of quantum dots. The equation is valid only when the dark current is mainly generation–recombination (g–r) dominated. In DWELL designs, the photoconductive gain is also affected by the efficiency of carrier capture by the quantum well [93], as can be seen in Fig. 2.7. The quantum dots in all the three structures have been grown in identical conditions, while the thickness of the quantum well in the DWELL region is varied such that the excited state energy is tuned with respect to the barrier energy, leading to different transitions such as bound to continuum (B–C), bound to quasibound (B–Q) and bound to bound (B–B). In B–B devices, the excited energy level is deep inside the barrier, thus has greater carrier capture efficiency, as compared with B–C designs, where the excited energy level falls in the continuum band, preventing electrons from getting captured in the quantum well. These schemes enable the designer to control the photoconductive gain of the detector as a “knob” to control the charge flow into the charge well in the readout integrated circuit (ROIC).

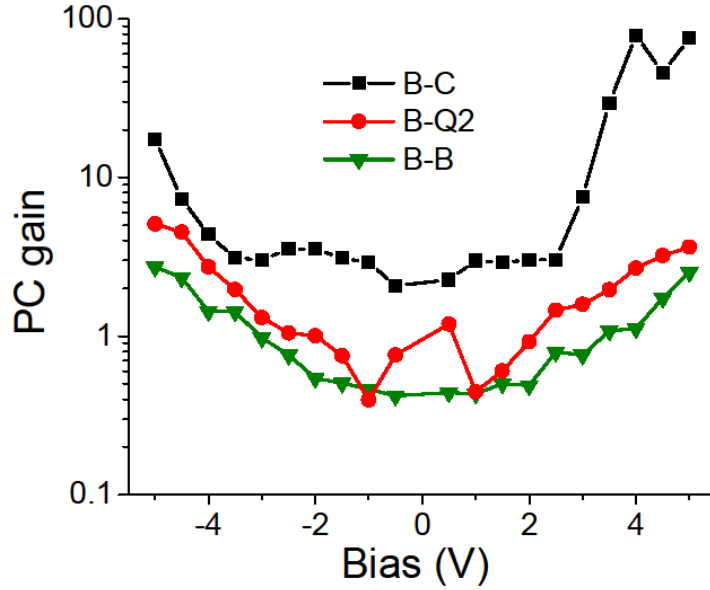


Fig. 2.7: Measured photoconductive gain for different well widths in DWELL detectors, as a function of electric field .

Photoconductive gain increases the extraction quantum efficiency and hence the responsivity as many electrons flow in the external circuit for a single photon absorbed in the quantum dot. However, the absorption quantum efficiency (η_{abs}) is not affected by the photoconductive gain. Absorption quantum efficiency of quantum dots tends to be lower than that for quantum wells because of the reduced fill factor and lower absorption coefficient because of size variation of quantum dots. Because both signal and noise currents are amplified by the photoconductive gain, the signal-to-noise ratio remains constant.

From responsivity measurements and PC gain measurements, η_{abs} of the detector can be estimated as below:

$$\eta_{\text{conv}} = R * \frac{\left(\frac{hc}{q}\right)}{\lambda_{\text{peak}}} \quad (3.3)$$

$$\eta_{conv} = \eta_{abs} \mathcal{G}$$

where η_{conv} is the conversion QE.

Detectivity and noise equivalent temperature difference

Specific detectivity (D^*) is a widely used figure of merit for describing the signal-to-noise ratio of a detector, normalized with respect to the detector area (A_d) and measurement bandwidth (Δf). It is defined as,

$$D^*(\lambda) = \frac{R(\lambda)\sqrt{A_d\Delta f}}{i_n} \quad (3.4)$$

where, i_n is the root mean square (RMS) noise current. For $\lambda = \lambda_{peak}$, $D^*(\lambda)$ is referred to as peak-specific detectivity, which is often quoted as the figure of merit for a single-pixel detector.

Primary components of noise current in QDIPs are shot noise because of dark current and photocurrent, and the thermal noise. The expression for the root mean square (RMS) noise current is,

$$i_n = \sqrt{i_{Background}^2 + i_{Signal}^2 + i_{Dark}^2 + i_{th}^2} \quad (3.5)$$

where

$$i_{Background} = 4qgI_{Backgorund} \Delta f (A_{rms})$$

$$i_{Signal} = \sqrt{4qgI_{Signal} \Delta f} (A_{rms})$$

$$i_{Dark} = \sqrt{4qgI_{Dark} \Delta f} (A_{rms})$$

$$i_{th} = \sqrt{\frac{4kT}{R}} (A_{rms})$$

where q is the electronic charge, g is the photoconductive gain, I_{dark} and I_{signal} are the dark current and photocurrents, respectively, k is the Boltzmann constant, T is the absolute temperature, and R_d is the differential resistance of the device. The last term i_{th} is the thermal noise current, also called Johnson noise, is usually negligible compared with the shot noise.

For detectivity calculations, the noise is usually measured with a FFT spectrum analyzer. The device is exposed to 300K background (2π field of view (FOV)). The spectrum of noise is analyzed. The noise in g-r limit is measured by rms averaging of noise over a certain bandwidth. At low frequencies, typically lower than 400Hz for QDIP, the noise is dominated by $1/f$ noise, which is important for FPA applications. From 400Hz to typically 5000Hz, the white noise from generation recombination dominates. After the detector cutoff, only Johnson noise (i_{th}) is present. For detectivity measurements, noise is usually measured at 2000Hz, with a long integration time. Care must be taken to operate the preamplifier at highest possible gain without overloading, in order to maximize the sensitivity (reduce the noise floor) of the measurement.

Noise equivalent temperature difference (NETD) is a useful figure of merit for the performance of a FPA, which depends on the SNR of the detector as well as properties of the electronics associated with the ROIC. It determines the minimum temperature difference the detector can distinguish for a given bias, input irradiance, and temperature.

In the charge capacity limited regime, NETD scales as $\sqrt{2g/N_w}$ where N_w is the storage

capacity, in terms of the number of electrons in the storage well, for the readout circuit. Hence, in a charge capacity limited regime, it is better to have lower photoconductive gain. NETD values as low as 5–7mK have been reported for QWIP FPAs, partly because of much lower photoconductive gain. However, if the dark current is very low, then it is possible to be in storage capacity limited regime only for high irradiance or higher operating temperatures. Because QDIPs can have very-low dark currents, they can demonstrate high temperature operation, or low NETD at lower temperature.

2.4 Device Designs

Depending on the application requirements, various parameters of the devices need to be adjusted. In this work, we follow a semi-empirical design approach, which involves understanding the effect of various device parameters on device characteristics and modifying the parameters accordingly. The device design process can be summarized as shown in Fig. 2.8. As we will discuss later, there are several problems with modeling the QDIP or DWELL devices from first principles, in order to predict the response. In this work, we combine the data measured on previous devices, such as photoluminescence, spectral response with a one-dimensional Schrodinger equation solution to modify the response accordingly. However, in order to be able to make conclusions about the band diagram from the measured spectral response, understanding of the properties of different transitions involved is critical.

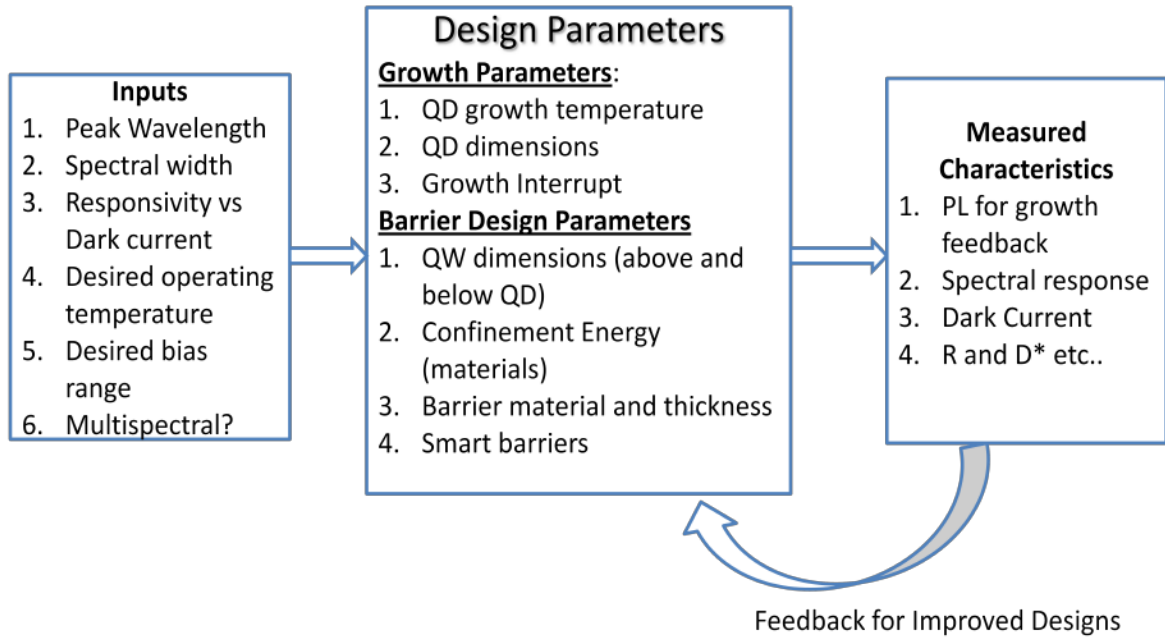


Fig. 2.8: Overview of the device design process.

Depending on the placement of excited energy level, the transitions can be labeled as bound to continuum, bound to bound and bound to quasi bound. Bound to continuum transitions have broad spectrum with $\Delta\lambda/\lambda$ typically over 25%. For bound to bound transitions, on the other hand $\Delta\lambda/\lambda$ is typically lower than 12%. From the difference between wavelengths of bound to continuum transition and bound to bound transitions, the energy depth of the excited energy with respect to continuum can be calculated.

Another way of estimating the energy level is to combine the information about QD ground state from PL, difference between the ground and excited state from the spectral response, with known conduction band offsets (CBO). Both these techniques have been used in this work. However, since there is a lot of variation in the values for CBOs of strained materials in the literature, the latter approach is somewhat uncertain.

For B-C transitions, since the photoexcited electrons are already above the continuum, very small electric field is required to collect the photocarriers. The opposite is true for B-B types of transitions. In a multicolor detector, where both types of transitions are present, this effect can be used to get different bands with different bias values and bias polarities. For example, one such detector is shown in Fig. 2.9. As can be seen, there is a broad peak at around 5 μm , which comes from B-C transitions, and narrow peaks at 8.8 μm and 10.5 μm , in negative and positive biases, respectively, which result from bound to bound transitions, as shown in the conduction band diagram. The peak at 6.8 μm is attributed to another energy level in the quantum well. It can be seen that MWIR B-C transitions dominate at low biases, and LWIR B-B transitions dominate at higher bias. The difference between the peak wavelength in negative and positive bias is attributed to the asymmetry of quantum dots and quantum well designs. It is obvious a well designed DDWELL structure provides several opportunities for multicolor, bias tunable device designs, which can be utilized in several applications. This does not add to fabrication complexities as this is still a two contact device.

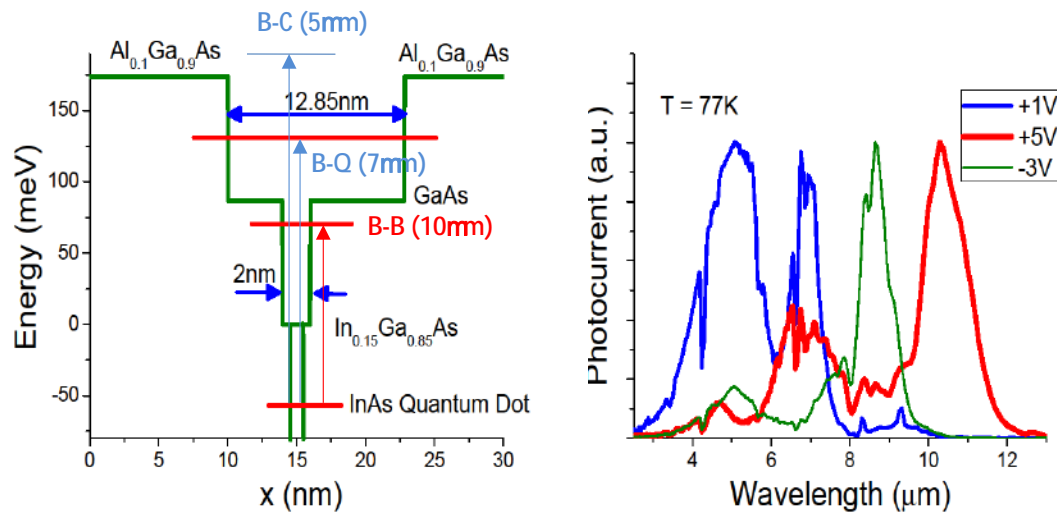


Fig. 2.9: Different transitions in a bias tunable, multicolor DDWELL detector.

As shown in Fig. 2.8, growth parameters as well as device designs can be changed to achieve the desired characteristics. The effect of growth parameters is usually larger on the spectral response of the detector, while barrier design make bigger difference with respect to other figures of merit such as dark current, responsivity, photoconductive gain etc. An example of controlling the spectral transitions with change in QD thickness or material is shown in Fig. 2.10. Fig. 2.10 (a) shows the PL comparison for two devices with identical structures but different QD deposition thicknesses. These devices are in fact confinement enhanced DWELL (CE-DWELL) detectors, as discussed later. For 2.3 ML QD, the PL is red-shifted, as expected, due to increase in the QD size. PL intensity is also increased due to better optical quality of QDs. Fig. 2.10 (b) shows the dramatic impact it has on the device spectral response characteristics, by just 0.3ML change in QD deposition! In 2.3ML device, the transitions are B-B while in 2.0ML device they are B-C due to difference in QD energy depth.

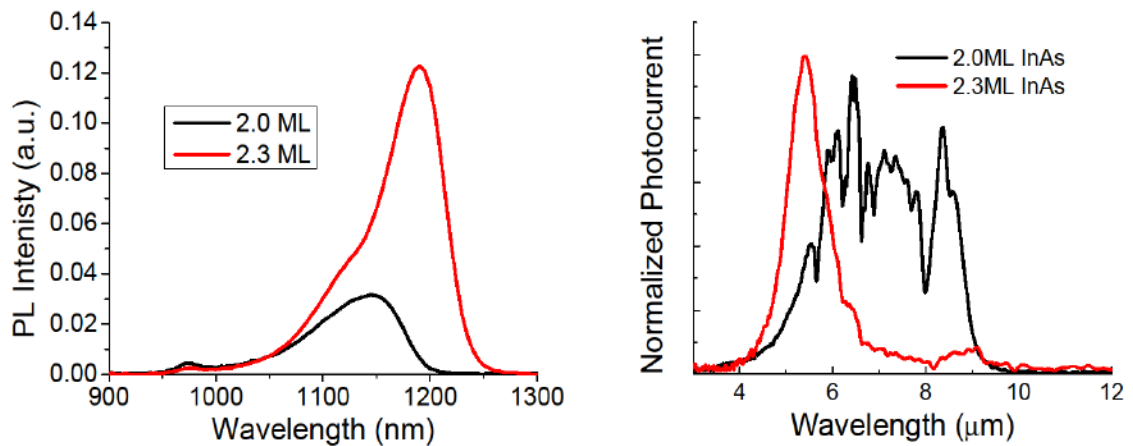


Fig. 2.10: (a) PL and (b) Spectral response comparison between two detector with identical device designs and different QD nominal depositions.

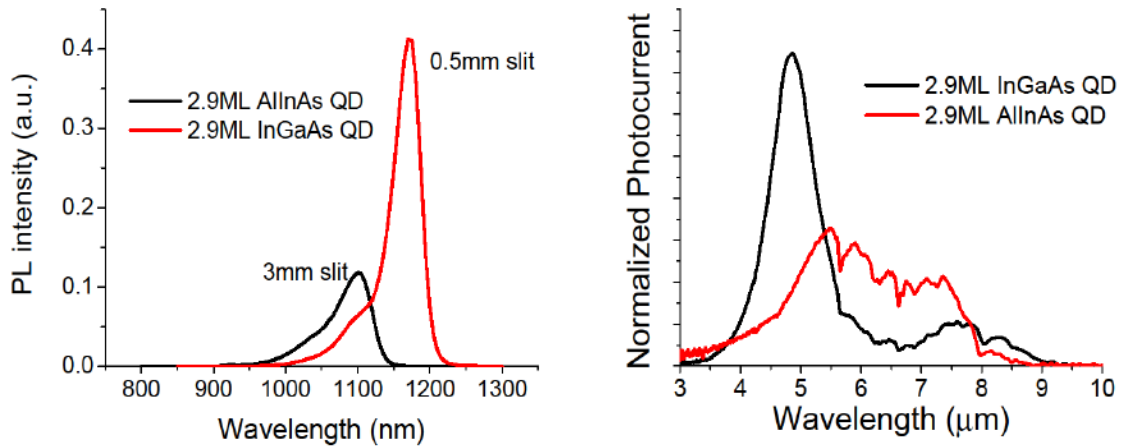


Fig. 2.11: (a) PL and (b) Spectral response comparison between two detector with identical device designs and different QD compositions.

Similar effect can be achieved by changing the QD composition. Fig. 2.11 (a) shows the PL spectrum for 2.9ML $\text{Al}_{0.15}\text{In}_{0.85}\text{As}$ QD and 2.9ML $\text{In}_{0.85}\text{Ga}_{0.15}\text{As}$ QDs with identical device design. The device design is different than that for the device in Fig. 2.10. Similar effect can be observed in Fig. 2.11 (b). In fact, the spectral ranges are also similar to those in Fig. 2.10, despite of different designs, due to similarity of PL wavelengths. These results illustrate the importance of precise control over the growth parameters for achieving the desired results.

Barrier Design Considerations

Effect of barriers on the response of DWELL detectors is twofold. The barriers not only affect the dark current, spectral properties, responsivity etc for the detector, but also affect the growth of QD. For example, in CE DWELL detectors, PL wavelengths is affected by confinement enhancing barrier due to reduced intermixing and higher confinement. However, this effect is hard to predict. We will focus our attention on the trade-off between the peak wavelength, dark current and responsivity of the detector.

This will be explained in more detail in the 'effect of barrier' section in chapter 5. In traditional DWELL designs, as the barrier energy increases, it becomes harder to extract long wavelength transitions, due to higher barrier. However, increase in barrier height blocks both dark current and photocurrent in different proportion, so that improvements in signal to noise ratio are possible. Typically, barriers can be adjusted to choose between 'low dark current low photocurrent' and 'high dark current high photocurrent' configurations. The first configuration is suitable for high temperature imaging with reduced sensitivity, while the second configuration is more suitable for low temperature but highly sensitive imaging. The noise in the imager comes from several other factors (readout noise, non uniformity noise, temperature fluctuations etc), which negates the advantage of low noise in the 'low dark current low photocurrent' configuration. However, since the charge wells are not saturated, high temperature imaging is possible.

3 Electronic Band Structure Modeling of Quantum Dots

The field of electronic band structure modeling of quantum structures is vast and involved. This chapter covers the motivation and challenges involved in QD modeling, strain field calculations using valence force field (VFF) approach and some basics of k.p modeling for calculating the energy and wavefunctions in various bands. No attempt will be made to explain the theory in detail, as several references cited have a detailed account of multiband k.p theory.

3.1 Introduction and Motivation

For predictive device designs and optimizing the performance of devices, the electronic band structure of quantum dots needs to be well understood. However, even though several groups have made excellent progress on device designs and fabrications, modeling the electronic band structure and transport through the QDIPs is in its infancy. There are several challenges associated with QD band structure modeling, which we will discuss in the next section. The sheer complexity of problem of solving three dimensional Schrödinger equation for a complex geometry of a self assembled quantum dots, or DWELL detectors prevent any easy approach to modeling. Also, unlike QWIPs or quantum well quantum cascade detectors, the electronic transport through the device and band structure calculations are two separate problems in the case of QDIPs and

DWELLs, which prevents complete TCAD based solutions for the system. On the other hand, thorough and accurate models are simple to obtain for band structure of QWIPs due to one dimensional and well defined problem.

The general approach for QD band structure calculations [36, 69-71] is to approximate the exact solution of Schrödinger equation by envelope function techniques, such as single band effective mass approach and multiband k.p approach [36, 71, 96-101], or atomistic techniques such as atomistic pseudopotential approach [73], or spectral techniques [55]. These models require different calculations such as strain calculations [102], piezoelectric corrections etc. Band structure modeling techniques, their physical origin and implementation details are reviewed in several textbooks [103, 104].

For this work, the modeling of quantum dots for computing strain profiles across the quantum dot and DWELL regions and k.p calculations of electronic band structures are undertaken not only to model and predict the device designs, but also to gain important physical understanding of crystal structures, strain profiles and the effect of various parameters on the electronic levels of DWELL structures. It is understood that various challenges associated with QD modeling, discussed in next section imply that it is nearly impossible for successful predictive modeling of quantum dots, nevertheless, the insights gained by this modeling process is key towards improving the semiempirical approach followed in this work, which was described in chapter 2.

3.2 Challenges for Accurate QD Modeling

1. Size and shape of the quantum dots is variable, depending on the growth conditions, because of the presence of intermixing. Even for the same growth conditions, the size and

shape of quantum dots vary significantly in the ensemble. For a physical model, the size of the quantum dots has to be guessed from the TEM data, which may not give correct representation of the average size in the ensemble. Large area techniques, such as AFM cannot be used for predicting the size, as the size and shape distribution are significantly altered, during the capping of the quantum dots. In practice, the quantum dots have to be approximated to ideal shapes, such as pyramids, hemispheres, and so on.

2. As a result of segregation and intermixing of group III elements, the composition inside the quantum dots is not uniform and is not fully known.
3. Physical size of self-assembled quantum dots is large, which makes atomistic simulations computationally demanding.
4. Large-scale effects such as vertical and lateral coupling between the quantum dots are extremely difficult to model because of the random distribution of the quantum dots.
5. Effect of doping is extremely difficult to model because of random placement of doping, band bending, coulombic interactions between the dopants, and so on.
6. Values of several important variables such as the band offsets and deformation potentials are either unknown or highly uncertain, which prevent models from being accurate.

3.3 Strain Calculations

3.3.1 Strain Tensor

For crystalline semiconductors, strain modifies the bandgap, the effective masses, mobility and various other electronic and optical properties. The incorporation of strain is now routinely used as a technique to modify these properties in strained layer heteroepitaxy, in various optoelectronic devices such as quantum well lasers at long wavelengths, infrared detectors, modulators etc. Strain is a measure of deformation in the crystal. It can be defined as the amount of deformation with respect to the original unstrained length. It should be clear that the strain needs to be expressed in terms of a 3×3 tensor, due to three orthonormal directions in the crystal. Strain tensor can be defined from following equations in terms of three orthonormal unit vectors ($\hat{x}, \hat{y}, \hat{z}$):

$$\begin{aligned} x' &= (1 + \epsilon_{xx}) \hat{x} + \epsilon_{xy} \hat{y} + \epsilon_{xz} \hat{z} \\ y' &= \epsilon_{yx} \hat{x} + (1 + \epsilon_{yy}) \hat{y} + \epsilon_{yz} \hat{z} \\ z' &= \epsilon_{zx} \hat{x} + \epsilon_{zy} \hat{y} + (1 + \epsilon_{zz}) \hat{z} \end{aligned} \quad (3.1)$$

where (x', y', z') are the coordinates of a point with respect to the origin after uniform deformation of the crystal. Coordinates of the same point in unstrained crystal are (x, y, z) .

Thus, a vector $\bar{r} = x \hat{x} + y \hat{y} + z \hat{z}$ in unstrained crystal gets displaced by R where

$$\bar{R} = \bar{r}' - \bar{r}$$

$$R = (x \epsilon_{xx} + y \epsilon_{yx} + z \epsilon_{zx})\hat{x} + (x \epsilon_{xy} + y \epsilon_{yy} + z \epsilon_{zy})\hat{y} + (x \epsilon_{xz} + y \epsilon_{yz} + z \epsilon_{zz})\hat{z} \quad (3.2)$$

From this equation 3.2, using the position of a point in unstrained crystal , and its displacement, we can calculate all the 9 components of the strain tensor.

3.3.2 Methods

Two of the most popular methods for strain calculations are continuum elasticity [105] (CE) method (also called continuum mechanical (CM) model) and valence force field method (VFF). These methods have been compared in Steir et al [71] and Pryor et al [106]. Both of these methods are based on minimizing the total strain energy of the system iteratively to find the minimum energy configurations of nodes. Once this is found, based on unstrained values of node positions, the strain tensor can be calculated. In this work VFF method has been used for obtaining the strain results with a conjugate gradient minimization approach, as described below.

Continuum Elasticity:

This approach is not atomistic, so one can work with cubic grid placement. Here, one uses classical elasticity. For a cubic system, the strain energy per atom, E_{CE} , is

$$E_{CE} = \frac{V}{2} C_{11} (\epsilon_{xx}^2 + \epsilon_{yy}^2 + \epsilon_{zz}^2) + \frac{V}{2} C_{44} (\epsilon_{xy}^2 + \epsilon_{yz}^2 + \epsilon_{zx}^2) + V C_{12} (\epsilon_{xx} \epsilon_{zz} + \epsilon_{xx} \epsilon_{yy} + \epsilon_{yy} \epsilon_{zz}) \quad (3.3)$$

where V is the equilibrium volume, C_{ij} are the elasticity constants. For total energy, equation 3.3 is summed over all the nodes. E_{CE} is minimized to obtained strain tensor

based on the definition. Typically, conjugate gradient minimization is used for the minimization problem over a finite difference method grid.

Valence Force Field Method

Valence force field approach was developed by Keating [101] and Martin [107]. Since this method involves atomistic calculations, it is also valid in atomically thin layer limits (such as wetting layer), unlike continuum elasticity theory, and is generally more accurate than CE near the boundaries of strained regions. This theory calculates the strain energy stored in bond stretching and bond bending interactions between the atom and its nearest neighbors. We follow the equation in Singh et al [36], for the total strain energy (V) of the system:

$$V = \frac{1}{4} \sum_{ij} \frac{\frac{3}{4} \alpha_{ij} (d_{ij}^2 - d_{0ij}^2)}{d_{0ij}^2} + \frac{1}{2} \sum_i \sum_{j \neq k} \frac{\frac{3}{4} \beta_{ijk} \left(\mathbf{d}_{ij} \cdot \mathbf{d}_{ik} + \frac{d_{0ij} d_{0ik}}{3} \right)^2}{d_{0ij} d_{0ik}} \quad (3.4)$$

where i runs over all the atomic sites, j and k run over the nearest neighbors of i , \mathbf{d}_{ij} is the vector joining i and j atoms, d_{ij} is the length of the vector, d_{0ij} is the unstrained bond length between i and j . First term in the equation is from bond stretching, with α_{ij} as bond stretching parameter and β_{ijk} is the bond bending parameter. For bond bending parameter of In-As-Ga bond, the harmonic average of β is taken. Values of parameters used in this work are given in table Table 3.1

Material	E_c	E_v	γ_1	γ_2	γ_3	E_p	Δ	α	β
	(eV)	(eV)				(eV)	(eV)	(N/m)	(N/m)
GaAs	1.519	0	6.85	2.10	2.90	22.71	0.341	41.19	8.95
InAs	0.758	0.360	19.7	8.4	9.29	20.2	0.38	35.18	5.5

Table 3.1: Values of material parameters used in this work.

For calculation of the strain tensor at each atom, it is clear that a minimization problem involves minimization over $3N$ variables, where N is number of atoms in the entire grid. Typically, a $30 \times 30 \times 20 \text{ nm}^3$ grid would have around 100,000 atoms, so the dimensionality of the minimization problem is $\sim 300,000$, which makes it prohibitively difficult to solve by a direct approach. Hence, in this work, a popular approach of iterative solution which solves minimization problem for each individual atom (over 3 spatial variables) and scan through all the atoms and then repeat the procedure has been used. For large grids, a large number of iterations (~ 2500) are necessary for convergence.

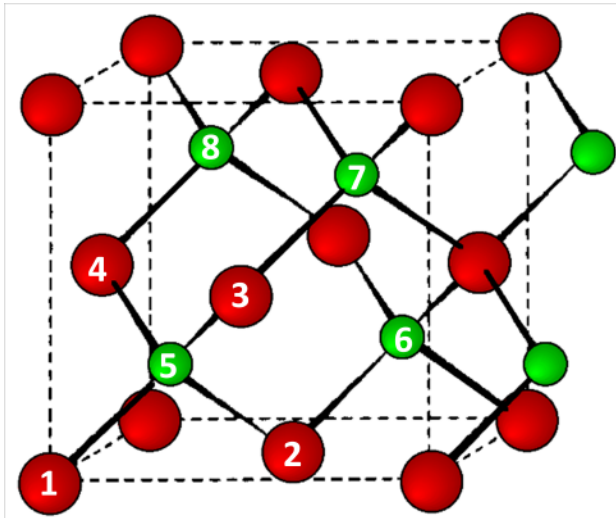


Fig. 3.1 One unitcell of zinc blende (ZnS) type FCC lattice (two extra atoms are also shown.) . For the simulations, 8 atoms are assigned to each cubic grid as marked. 1 to 4 are As atoms while 5-8 are group III (Ga or In) atoms.

The implementation of the code was done in MATLAB. Parallel computing was implemented to speed up the process on multicore computers and also to make it compatible to run on a UNM supercomputer. The algorithm overview is as follows:

Algorithm

1. At the start of simulation, all the atoms are placed on GaAs face centered cubic (FCC) grid. This configuration has been used by several authors and is known to lead to faster convergence. The atoms are numbered as shown in Fig. 3.1 and only 8 atoms (4 cations and 4 anions) are assigned to the unit cell. The reference to atom is made in a 5 dimensional matrix, as (unit cell number, atom number, three dimensions of coordinates of atom). The unit cell number covers all the unit cells indexed serially, atom number goes from 1 to 8 and coordinates cover x, y, z position (called R_x , R_y and R_z for that atom).
2. Geometry of the quantum dot, capping material, wetting layer etc is defined in Cartesian coordinates. Material properties are assigned to each **bond**. This is important at the boundary of the two materials. For example, if an Indium atom is inside the pyramidal QD and Arsenic atom is outside, the bond gets assigned properties of InAs, while if Ga is outside and As is inside the QD, bond is assigned properties of GaAs. This is obvious but can be easily overlooked.
3. Identify and store the location of boundary atoms. Note that not all the atoms in the unit cell at a boundary are boundary atoms. For example, for $x = 0$ boundary, only atoms 1 and 4 would be at the boundary. This would be important for periodic boundary conditions.

4. Identify and store the location of 4 nearest neighbors (NN) for all the atoms. Note that all the 4 NNs are not in the same unit cell, so neighboring unit cells also needs to be considered. Assign various parameters such as α , β and d_0 to each bond.

5. Main Iteration Starts

Run following steps for 3000 iterations

Run following steps for all the atoms in all the unit cells.

- i) Slice the data for parallel processing
- ii) Implement periodic boundary conditions in x and y directions (z directions has Dirichlet boundaries). For this, nearest neighbors of nearest neighbors are required to be calculated.
- iii) Calculate and store current distances between atoms and nearest neighbors, so that this doesn't have to be done during minimization. (saves time)
- iv) Conjugate gradient minimization of $V(R_x, R_y, R_z)$ to find (R_x, R_y, R_z) . (this needs to be appropriately modified for parallel implementation, since this is the most time consuming step. Excellent reference for conjugate gradient minimization, detailing the algorithms used, is Shewchuk et al [108]. In particular nonlinear conjugate gradients with Newton-Raphson and Fletcher-Reeves were used.
- v) Store new position of current atom and proceed to next atom.

6. Interpret the strain tensor from displacements of each atoms [106]. We modify the scheme given in Pryor et al, to solve the over-determined system of 12 equations for 9 variables using least square approach.

7. Interpolate to suit the cubic grid used in k.p calculations. While our strain calculation method is atomistic, we carry out electronic structure computation in the envelope approximation, wherein the potentials and wavefunctions we deal with are essentially in the continuum. This would require us to interpolate the values of strain at atomistic sites into the continuum. We do so by assigning a bulk strain tensor to each unit cell in the lattice. The bulk strain tensor is calculated by a linear (gradient) interpolation of the strain at each atom in the unit cell towards the center of the unit cell, followed by an average over these atoms.

3.3.3 Results for Strain Calculations on Quantum Dots

Fig. 3.2 (a) shows schematics of QD, showing different crystal directions. For DWELL structures, QW is added above and below the QD, while for QD-only simulations, GaAs substrate is added. Fig. 3.2 (b) shows a typical convergence plot with respect to the number of iterations. Change per iteration is defined as a sum of squares of net displacements of all the atoms on the calculation grid, with respect to the previous iteration. As can be seen, the asymptotic limit is not reached even after 2500 iterations, even though the change in atomic positions is negligible. It is to be noted that for large grid sizes, such as $30 \times 30 \times 25 \text{ nm}^3$, it takes around 10 minutes per iteration while running on all the four cores of Intel i7 processor and a 16GB random access memory in 64-bit configuration. Thus, 2500 iterations take ~13 to 14 days (amount of time per iteration decreases as convergence gets better)! Hence in all the simulations, calculations were run

for maximum of 2500 iterations. It is also to be noted that it takes fewer number of iterations, as well as smaller time per iteration for smaller grids, but the strain profiles change abruptly near boundaries, which creates an artificial potential for the subsequent k.p calculations.

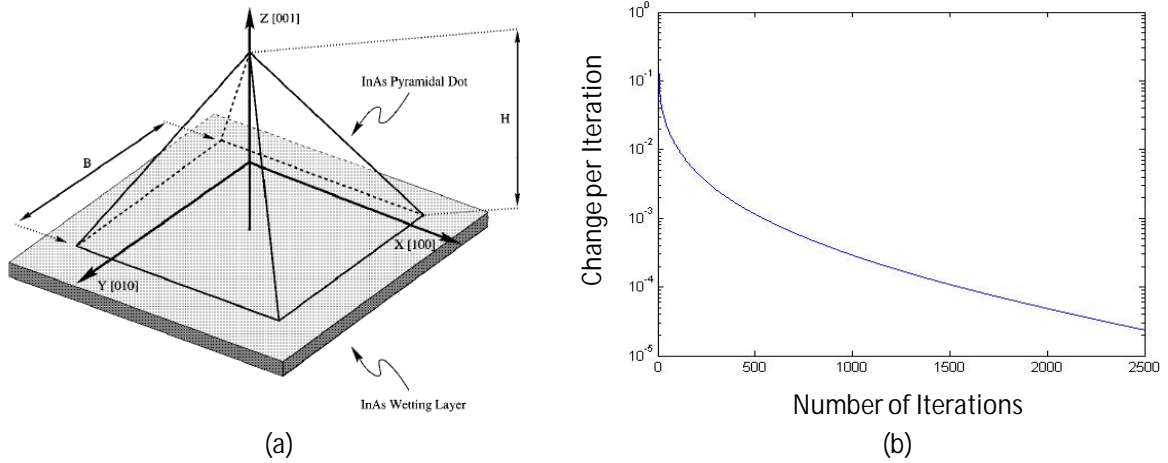


Fig. 3.2: (a) Geometry of QD showing various crystal directions (b) Plot of total change in atomic position in each iteration against number of iterations, showing rapid convergence.

The strain profile for a quantum dot calculated by valance force field method with 2000 iterations is shown in Fig. 3.3 (a). The geometry is same as structure used by Jiang et al [103], whose results are shown in Fig. 3.3 (b). Excellent agreement between the two validates the strain calculations here. The small difference at the quantum dot tip is due to different grid positions with respect to the quantum dot tip.

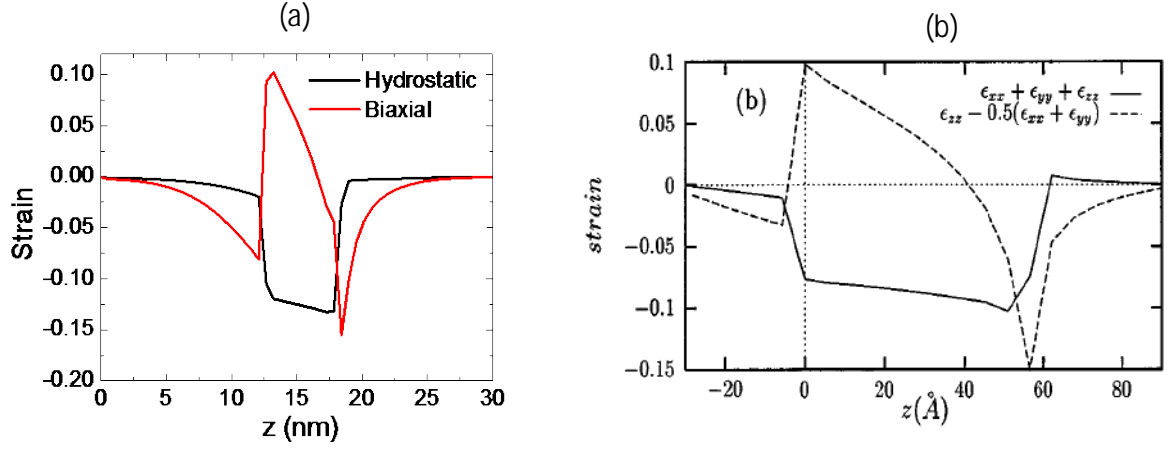


Fig. 3.3 (a) Strain profile for hydrostatic and biaxial strains along [001] direction, which is the growth direction. These are defined as $\epsilon_{\text{hyd}} = \epsilon_{xx} + \epsilon_{yy} + \epsilon_{zz}$ and $\epsilon_{\text{biax}} = 2\epsilon_{zz} - \epsilon_{xx} - \epsilon_{yy}$, respectively. (b) Hydrostatic and biaxial strain profiles along [001] direction for the same geometry, calculated by Jiang et al, showing excellent agreement between the two results.

To get an idea about strain distribution within and around the quantum dot, ϵ_{xx} , ϵ_{zz} and ϵ_{hyd} in xz cross section are shown in Fig. 3.4. As can be seen, the strain profile inside the quantum dot is highly non uniform, leading to interesting confinement related effects in the device characterization.

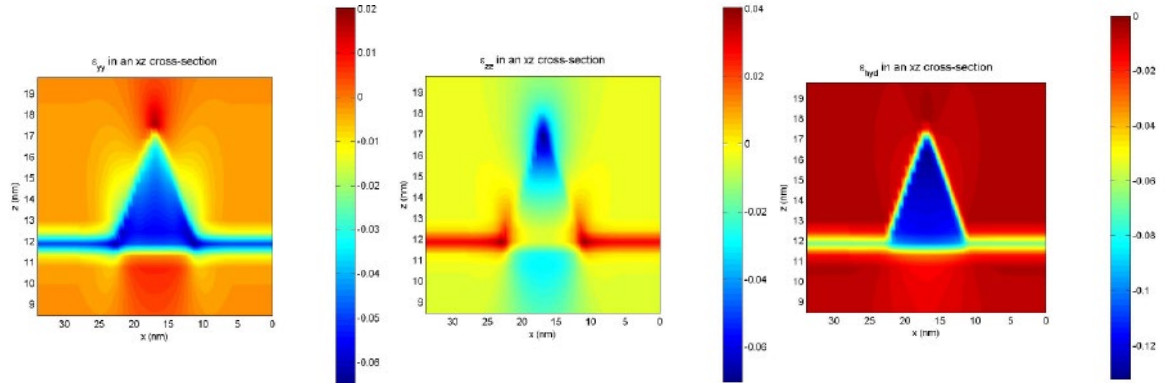


Fig. 3.4: A 2D plot of ϵ_{xx} , ϵ_{zz} and ϵ_{hyd} in xz cross section showing non uniform distribution of strain components inside the quantum dot

3.3.4 Results for Strain Calculations for DWELL Structures

For DWELLs, structural parameters were chosen from TEM images for CE DWELL 1 structure explained in chapter 5. The assumed structure is shown in Fig. 3.5 (a). InGaAs was assumed to be a binary material with corresponding material properties interpolated from InAs and GaAs. This is done to avoid random placement of atoms, which poses a great challenge for boundary value problems. Note that these are first strain simulations on DWELL detectors. Calculated strain profiles for this structure, in [001] direction are shown in Fig. 3.5 (b). Calculated strain profiles for E_{zz} and E_{xx} are shown in Fig. 3.6 (a) and (b) in two dimensional plots. Plots for hydrostatic and biaxial strains, are shown in Fig. 3.6 (c) and (d), respectively.

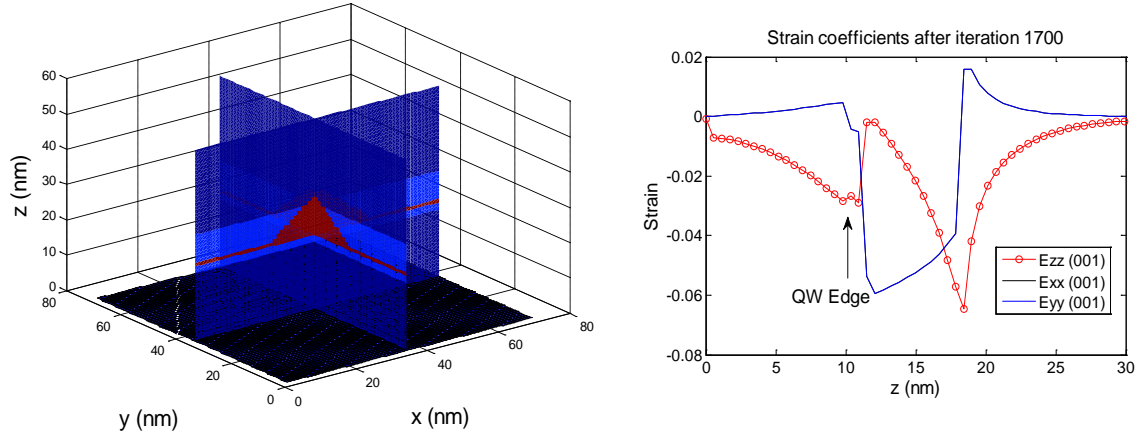


Fig. 3.5: (a) DWELL structure assumed in simulations (b) Calculated strain coefficients in [001] direction, showing the effect of QW.

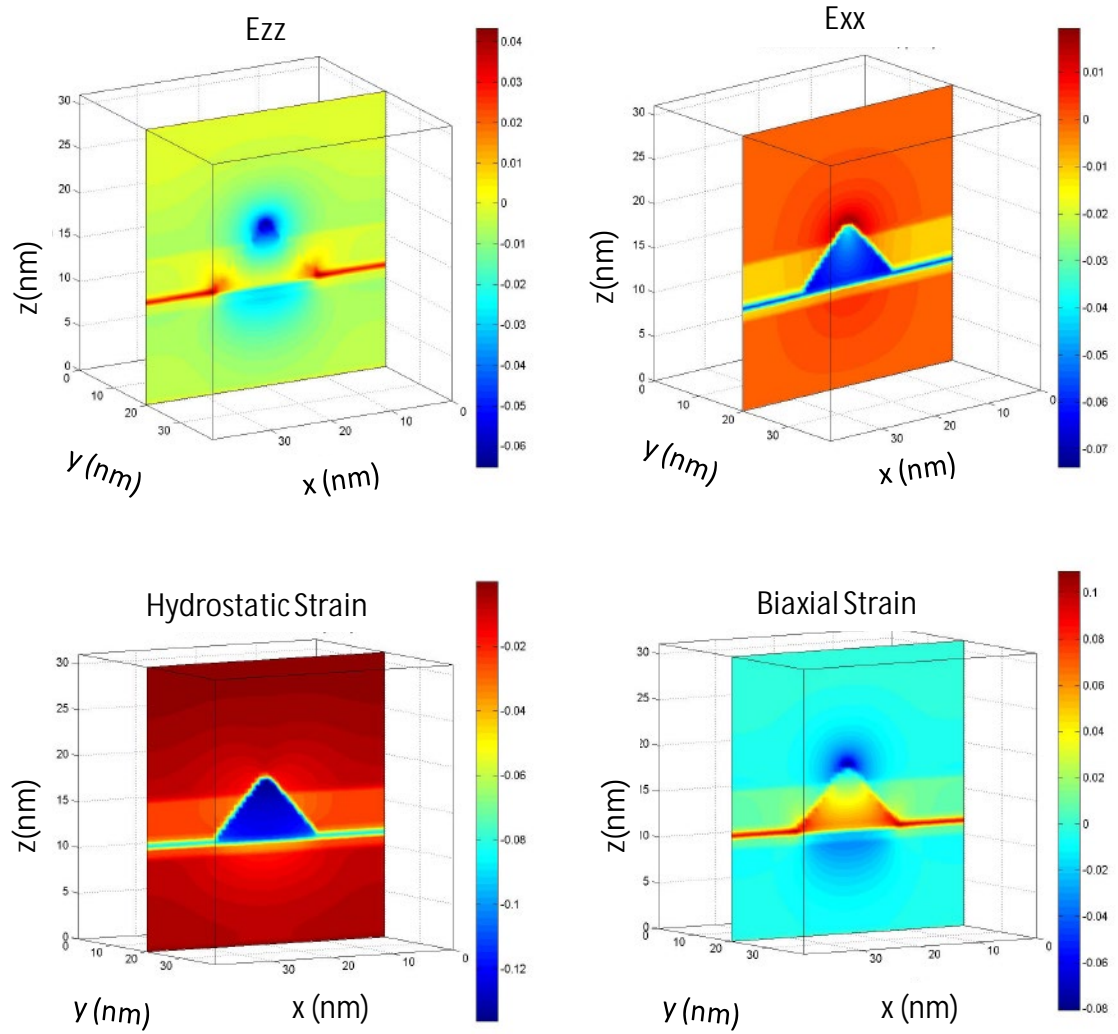


Fig. 3.6: (a) 2D cross sections of strain profiles for (a) E_{zz} , (b) E_{xx} (c) Hydrostatic strain and (d) Biaxial strain for DWELL structures.

3.4 Electronic Structure Computation

Note: This part of the simulation is currently being pursued by Srujan Meesala for his undergraduate research, the codes developed and partial results obtained are from his ongoing work. They have been included here for the completeness of the chapter. The overview of formulation used and software implementation is detailed in Meesala *et al* [109].

It is now known that the simple effective mass approach to calculate the band structure of decoupled conduction band and k.p for valence bands leads to some serious errors, especially for self-assembled quantum dot simulations. This is because (1) the band gap of bulk InAs is 0.4 eV, while the effective gap of the dot is close to 1.0 eV; (2) the nature of the strain tensor is such that there is a strong spatial variation in strain; and (3) the strain components are very large, and the resultant splitting in the bands are comparable with the interband separations in the bulk material [36]. A popular approach to model the quantum dot energy spectrum is eight-band k.p, which includes the influence of remote bands on conduction band and valence band.

In the eight-band k.p analysis, 8×8 Hamiltonian acts on eight envelope functions corresponding to conduction band and the three valence bands (heavy holes, light holes, and split off bands) and their time-reversed conjugates. These envelope functions are linear combinations of band edge Bloch functions. The exact form of 8×8 k.p Hamiltonian is given in the study of Jiang and Singh [36], and the formalism is explained in more detail in the study of Bimberg et al. [82], Enders et al. [110] and Gershoni et al. [111]. Implementation details for k.p formulation are given in Stier *et al.* [71, 112].

The problem statement for k.p solution is to solve the 8×8 Hamiltonian, given in [36] for eigenvalues (energies) and eigenfunctions (wavefunctions). Since there are 8 envelope functions, each of the dimensionality N^3 , where N is the number of nodes on a cubic grid, the dimensionality of Hamiltonian is $8N^3 \times 8N^3$. N needs to be sufficiently large to make sure that the wavefunctions vanish near the edges, thus allowing for the application of Dirichlet boundary conditions. In order to be able to find the eigenvalues of such a large matrix, the sparse nature of the matrix needs to be exploited. Another important thing is,

instead of solving for *all* the eigenvalues of the matrix, only a few eigenvalues, which are close to the rough estimate of energy level, are calculated, which considerably saves time for code execution. It is also needed to ensure that the Hamiltonian is Hermitian, for faster eigenvalue calculations.

The results of k.p calculation for the quantum dot geometry which is similar to the one used in Jiang et al [36], are shown in Fig. 3.7 (a). Three bound states were obtained in the conduction band, with two excited states being degenerate. The occurrence of two bound energies is perhaps the most essential prediction of the k.p approach. Fig. 3.7 (b) shows the results from a simple effective mass treatment, in which the Schrödinger equation is solved for conduction band only, which incorrectly predicts only one bound state. We validate our results by comparison with the results from [36], which are shown in Fig. 3.7 (c).

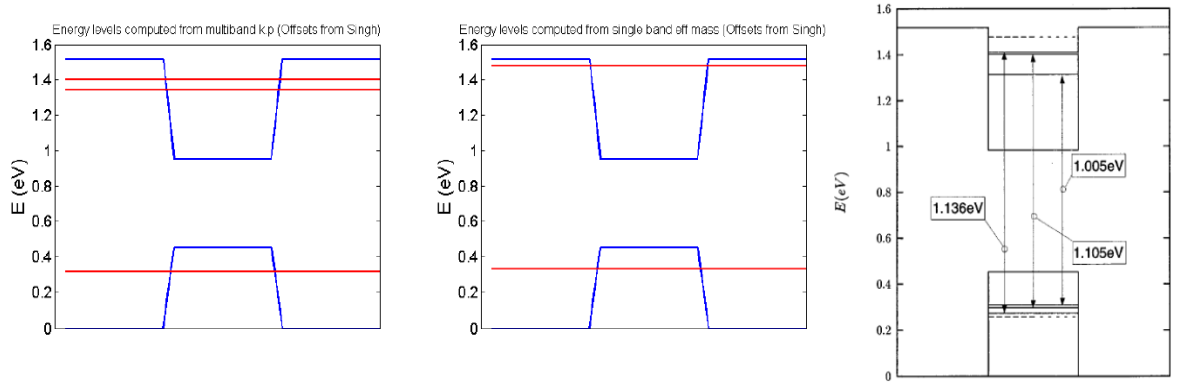


Fig. 3.7: Computed electronic structure showing two confined energy levels in the CB. The first excited state is composed of two degenerate states of opposite symmetry. The VB ground state is also shown for completeness. (b) The results from a single band effective mass calculation of the CB. (c) Electronic structure for the same structure from Jiang et al for validation.

The probability amplitudes, which are the square of wavefunctions of the three confined states in the conduction band and a heavy hole state in valence band are shown in Fig.

3.8. Light hole and split off band energy levels have not been included in calculations.

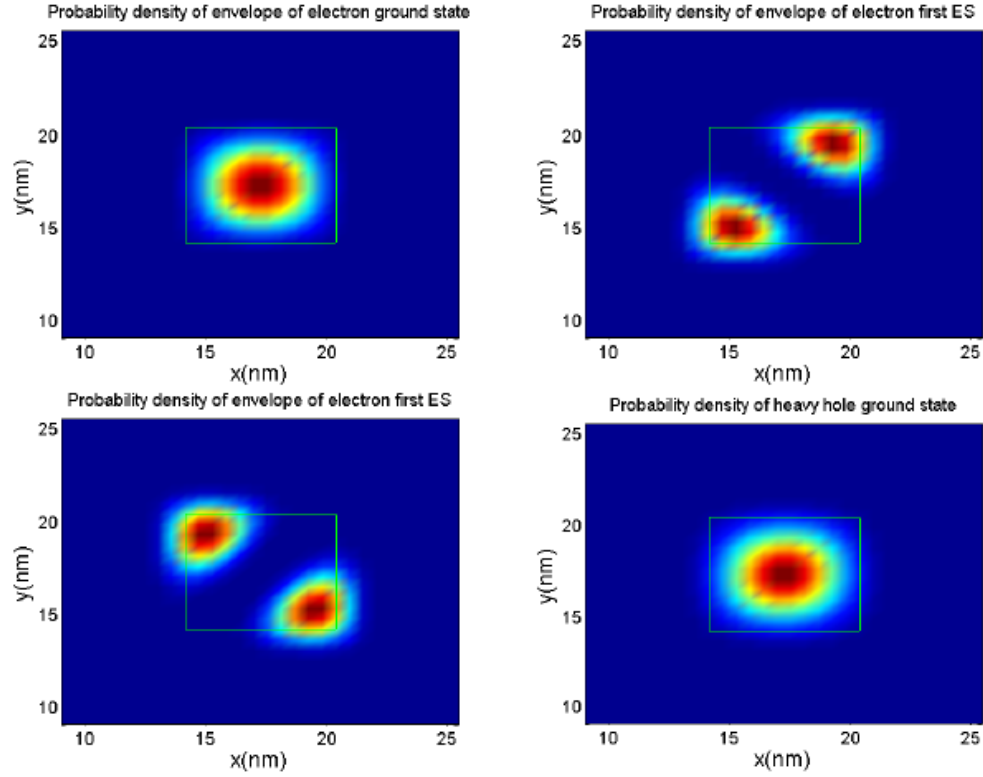


Fig. 3.8: Probability amplitudes of the envelope wavefunctions corresponding to the energy levels E_0 , E_1 and E_2 in the conduction band and HH_1 in the valence band, shown in a horizontal cross-section of the heterostructure. The QD boundary is shown for reference.

3.5 Conclusion and Discussions

In conclusion, a highly involved procedure is required for modeling the electronic structure of simple pyramidal quantum dots. This process is complicated by problems associated with estimating the exact parameters used in simulations, such as the quantum dot geometry, ensemble distribution, various band offsets and deformation potentials etc. These inaccuracies in input parameters make prediction of the exact energy values of the

system impossible. However, the process of calculation of the electronic structure not only is satisfying but also gives important physical insights of working of quantum dot heterostructures. This gives important pointers for designing different configurations for detection. Hence, in this work, emphasis was placed to model the quantum dot heterostructure with local MATLAB codes, without using the *blackbox* approach of available TCAD based simulators (such as NextNano, or Nemo 3D). Several assumptions and approximations involved in the simulations could not have been known without this approach.

Even after the solution of 8×8 k.p equation, for the calculation of absorption coefficient, Fermi golden rule needs to be used with the calculated wavefunctions and density of states information. This process is extremely complicated, in the presence of applied bias, which is necessary for device operation. Hence, instead of solving the exact three dimensional Schrödinger equation for device designs, more predictable semi-empirical approach which involves coupling the information obtained from PL and spectral response of existing device to a one dimensional Schrodinger equation solution to *estimate* the device design. This needs iterative process for optimizing device performance.

The future work:

1. Development of a fully functional multiband k.p model.
2. Application of this on known DWELL heterostructures
3. Comparison with experiments for different barrier designs

4. The ultimate goal would be to combine this modeling with the transport simulations in order to predict the properties of QDIPs and DWELL detectors under different biasing conditions. This, however, may be rendered to a mere academic exercise due to various challenges discussed earlier and due to sheer complexity of the problem, combined with the variability of device growth conditions.

4 Resonant Tunneling Barriers

In this chapter, we will discuss the use of 'smart' resonant tunneling (RT) barriers which have the ability to selectively block the dark current carriers while allowing photocurrent carriers to pass. We will start with mathematical modeling of dark current to compare the dark current through conventional DWELL detectors with that in RT-DWELL detector. This will be followed by experimental results. In the first generation RT-DWELL detectors, design and implementation of RT barriers on unoptimized simple DWELL designs, which reduced the dark current by 2-3 orders of magnitude will be presented. Since the responsivity is reduced only by a factor of 5, this results in significant improvement in overall signal to noise ratio and the operating temperature of these devices. Control device with identical structure and absence of RT barriers has been used to compare the performance. By varying the passband of RT barriers, it is possible to extract different wavelength peaks from the same parent structure.

In the second generation RT-DWELL detectors, use of RT-barriers has been demonstrated to improve the performance of optimized quantum dots-in a double well (DDWELL) detectors. These detectors have InAs QDs embedded in a double quantum well of InGaAs-GaAs-AlGaAs. In order to avoid confusion, we will refer to as these detectors as DDWELL detectors and corresponding RT-barrier devices as RT-DDWELL detector. Extremely low dark current levels and record high detectivity values have been obtained for LWIR RT DDWELL detectors. Ability to extract long wavelength response,

even at low bias has been demonstrated with RT-Split barriers, which will be discussed in detail.

4.1 Introduction

DWELL offers additional advantages such as superior optical quality of the quantum dots due to strain relaxation [48, 67, 113] in the InGaAs QW and optimum growth temperature for capping layer materials. Barrier material can also be changed to obtain desired device performance. For example, if the Al mole fraction in AlGaAs barrier is increased, the dark current decreases, while the peak wavelength that can be extracted out of the active region by the application of electric field, also decreases. Thus, in a traditional detector design with triangular barriers, there is always a trade-off between increasing the peak wavelength and reduction in the dark current. This trade-off can be broken by the use of resonant tunneling filters in barriers, which can selectively extract the energy levels corresponding to the excited states of the QW in DWELLs, while blocking carriers with energies different than the resonant energies. RT filters have sharp transmission peaks at the resonant energies where the transmission is near unity, while transmission probability for other energies is very small. Since the dark current is generated by the thermally generated carriers with a continuum of energy distribution, it is significantly reduced [65] by the application of RT-barrier. However, the photocurrent is primarily generated from the carriers excited to the bound state of the QW in DWELL structure. Hence the photocurrent level remains comparable to the control device, as the RT-barriers have near unity transmission at those energies. This results in significant increase in the signal to noise ratio (SNR) of the detector. Resonant tunneling filters can

be designed to extract different bound states of the DWELL detectors, leading to the ability to shape the spectral response of the detector for selective extraction of the designed wavelengths. Resonant tunneling barriers have been previously used for QDIPs, demonstrating room temperature operation with very long wavelength response [20, 65] and even in the THz range [21, 114]. Bias tunable multicolor operation for tunneling QDIP have been demonstrated [115]. More recently, the resonant tunneling barriers have been used with quantum ring detectors [116] for THz detection.

It is to be noted that for high temperature imaging applications, the SNR in the focal plane arrays is limited by the storage capacity of the charge well in the readout integration circuit. In this limit, the reduction in dark current is very important for operating at higher temperature, even for the same signal to noise ratio of the detector. The increase in SNR, while reducing the dark current thus makes RT-DWELL detectors very attractive candidate for high temperature imaging applications.

In section 4.2, a simple mathematical model for the dark current of DWELL and RT DWELL detectors, based on emission capture model will be presented, to justify the need for RT barrier. In section 4.3, RT barriers on unoptimized DWELL detectors will be presented. They not only improve the signal to noise ratio and the dark currents, but also allow for selective extraction of different bands. Further improvement in D^* with very low dark current levels has been demonstrated with an optimized DDWELL structure, which will be discussed in section 4.4. A resonant tunneling barrier with a special “split barrier” configuration to selectively extract only the longwave peak from a bias tunable spectral response of the parent structure has been designed and implemented. The design motivations and methodology will be clearly discussed. Results have been analyzed by

calculating the activation energies for all the devices to explain the details of the designs and various results. In section 4.4 we will discuss the design, analysis and results for RT-DWELL devices [66] .

4.2 Mathematical Justification for RT-DWELL

Dark current in the QDIPs has been extensively modeled in the literature [65, 117]. Here, a simple model described in Su et al [65] has been followed and suitably modified for DWELL geometries. The key point in this model is the calculation of number of electrons excited out of QDs which are able to cross the barrier, by tunneling or thermionic emission, to be collected at the electrodes. The dark current is given by

$$I_D = ev_d(V)n_{em}(V)A \quad (4.1)$$

where, A is the detector area, n_{em} is the concentration of electrons excited out of quantum dots by thermionic emission or tunneling, v_d is the drift velocity, given as a function of applied voltage V , by,

$$v_d(V) = \frac{\mu F(V)}{\sqrt{1 + \left(\frac{\mu F(V)}{v_s}\right)^2}} \quad (4.2)$$

where μ is the mobility of electron in the bulk, F is the electric field and v_s is the saturation velocity of electron in GaAs. n_{em} is given by

$$n_{em}(V) = \int_{-\infty}^{\infty} N(E)f(E)T(E,V)dE \quad (4.3)$$

where, $f(E)$ is the Fermi-Dirac distribution function, T is the tunneling probability, as a function of energy and applied voltage, and $N(E)$ is the density of state (DOS) in the active region.

4.2.1 Tunneling

In the conventional design, the tunneling barrier is rectangular at zero bias, which essentially blocks all the electrons (dark current contribution as well as photo-response contribution) below a particular energy level. This situation is improved by having a resonant tunneling barrier, which has a near-unity transmission coefficient at the designed peak wavelength, while small probability of tunneling away from the peak. This structure, thus, can allow the designed wavelengths to pass, while block other wavelengths, which effectively block the dark current electrons, which have continuous spectrum. This is also rightfully called “tunneling filter”, as it filters out the bulk of the dark current electrons. For the comparison point of view, both kinds of tunneling barriers have been modeled in this work, and the models are presented below:

Triangular Barrier

The tunnel probability has been derived from the time independent Schrödinger equation:

$$-\frac{\hbar^2}{2m} \frac{d^2Y}{dx^2} + V(x)Y = EY \quad (4.4)$$

which can be rewritten as

$$\frac{d^2Y}{dx^2} = \frac{2m^*(V - E)}{\hbar^2} Y \quad (4.5)$$

Assuming that $V(x)-E$ is independent of position in a section between x and $x+dx$, the solution is,

$$Y(x+dx) = Y(x) \exp(-kdx) \quad (4.6)$$

where $k = \sqrt{\frac{2m^*(V - E)}{\hbar^2}}$

The minus sign is chosen since the particle is moving from left to right. For a slowly varying potential the amplitude of the wave function at $x = L$ can be related to the wave function at $x = 0$

$$\Psi(L) = \Psi(0) \exp\left[-\frac{i}{\hbar} \int_0^L \sqrt{2m^*(V(x) - E)} dx\right] \quad (4.7)$$

This equation is referred to as the WKB (Wigner, Kramers, Brillouin) approximation.

From this the tunneling probability, T , can be calculated for a triangular barrier for which

$$V(x) - E = q\phi_B \left(1 - \frac{x}{L}\right) \quad (4.8)$$

$$T = \frac{\Psi(L)\Psi^*(L)}{\Psi(0)\Psi^*(0)} = \exp\left[-\frac{2}{\hbar} \int_0^L \sqrt{2m^* \left(q\phi_B \left(1 - \frac{x}{L}\right)\right)} dx\right] \quad (4.9)$$

The tunneling probability then becomes,

$$T = \exp\left[-\frac{4}{3} \frac{\sqrt{2mq^*}}{\hbar} \phi_B L\right] \quad (4.10)$$

This is popularly known as Fowler-Nordheim tunneling.

Based on this formulation, the tunneling barrier was simulated, and the variation of tunneling probability as a function of electron energy is plotted in Fig 4.1 (a). Here, E_{Barrier} is the barrier energy with respect to the reference energy. Note that the x-axis has a magnified scale, to see the variation near the barrier height. In the ‘big picture’ the tunneling probability will be zero for the energies less than barrier height, and near unity for the energies greater than the barrier height. Variation of tunneling probability with applied voltage is plotted in Fig 4.1 (b), again for the energies close to barrier height at no bias.

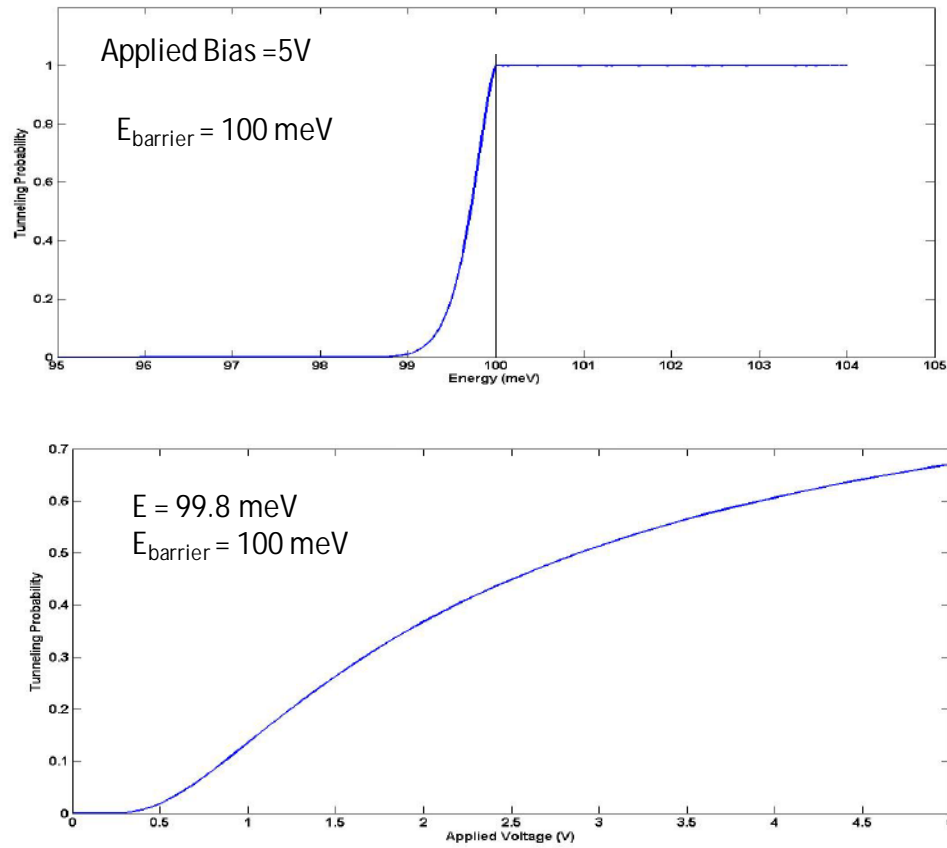


Fig 4.1 (a) Tunneling probability as a function of energy, near barrier height. (b) Tunneling probability as a function of applied voltage, near the barrier height.

Resonant Tunneling

As stated earlier, the resonant tunneling occurs when two barriers are separated by a quantum well, to form a symmetric double barrier. When the energy of an incoming electron is same as the bound state energy of the quantum well; the transmission probability of the double barrier approaches unity. This resonant behavior cannot be accurately analyzed by the WKB method, as the method only considers the barriers, and not the resonance effects. Transfer matrix methods have been developed to calculate the tunneling probability of arbitrarily shaped barriers with resonant tunneling [118]. In this

work, the transfer matrix method was replaced by a specific method for double rectangular barrier resonant tunneling system, based on **scattering matrices**. The method, described next, also allows modeling the effect of applied bias and changes in dimensions.

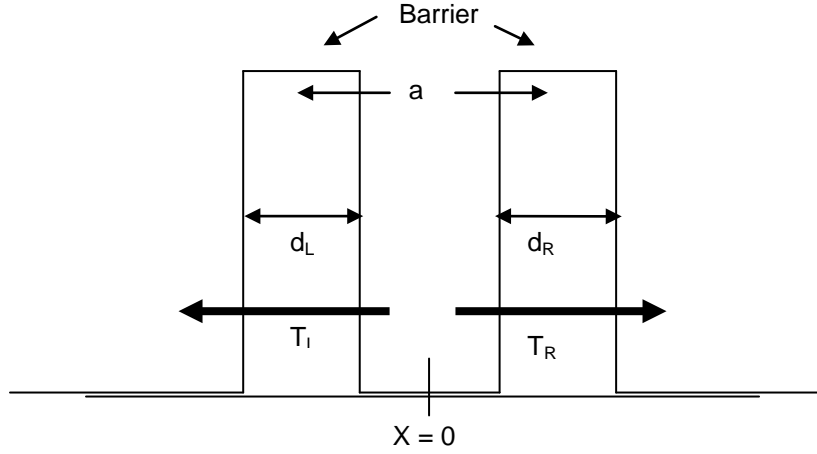


Fig 4.2: Schematics of resonant tunneling barrier.

The final expression for the tunneling probability through the double barrier is given by [119]

$$T = t^* t = \frac{T_L T_R}{1 + R_L R_R - 2\sqrt{R_L R_R} \cos(2ka + r_L + p_R)} = \frac{T_L T_R}{(1 - \sqrt{R_L R_R})^2 + 4\sqrt{R_L R_R} \sin^2 \frac{1}{2} f} \quad (4.11)$$

where $T_{L,R} = t_{L,R}^* t_{L,R}$ and $R_{L,R} = r_{L,R}^* r_{L,R}$ are the transitivity and reflectivity of each barrier, in the direction shown in Fig 4.2

$j = 2ka + r_L + r_R = 2n\rho$ is the phase factor,

$$\text{where } r_L = |r_L| \exp(ir_L), \quad r_R = |r_R| \exp(ir_R) \quad (4.12)$$

here, $r_{L(R)}$ and $t_{L(R)}$ are the complex reflection and transmission coefficients for the left (right) barrier, respectively, from the origin (which is located at the center of the well).

Note that a is sum of well width and half of the total width of two barriers. k is the wavenumber, given by,

$k_i = \sqrt{\frac{2m_i^*}{\hbar^2}(E - V_i)}$ where, $i = 1$ to 5 is the section index, as shown. m_i^* is the effective mass of i^{th} layer and V_i is the potential in i^{th} section. Note that we can include the effect of different material parameters and applied voltage by suitably modifying m_i^* and V_i .

Parameters t and r , for the left and right barriers are calculated as

$t = \frac{T_{11}T_{22} - T_{12}T_{21}}{T_{22}}$ and $r = -\frac{T_{21}}{T_{22}}$, where T_{ij} are the elements of **total transfer matrix** of

the barrier (this includes barrier effect and the effect of phase shift).

$$t_L = \frac{2k_3k_2e^{-ik_3d_L}}{2k_3k_2\cos k_2d_L - i(k_3^2 + k_2^2)\sin k_2d_L} \quad (4.13)$$

$$t_R = \frac{2k_3k_4e^{-ik_3d_R}}{2k_3k_4\cos k_2d_R - i(k_3^2 + k_4^2)\sin k_4d_R} \quad (4.14)$$

$$r_L = \frac{i(k_3^2 - k_2^2)\sin k_2d_L}{2k_3k_2\cos k_2d_L - i(k_3^2 + k_2^2)\sin k_2d_L}e^{-ik_1d_L} \quad (4.15)$$

$$r_R = \frac{i(k_3^2 - k_4^2)\sin k_4d_R}{2k_3k_4\cos k_4d_R - i(k_3^2 + k_4^2)\sin k_4d_R}e^{-ik_3d_R} \quad (4.16)$$

where $d_{L(R)}$ is the thickness of left (right) barrier, as shown in Fig 4.2. The above equations come from combining the scattering matrices for the two back to back shifted barriers.

The results of the simulation are shown in Fig 4.3, where the resonance peaks are clearly visible. Note that at the peak, the tunneling probability is near unity. The sharpness of peak increases with increase in the difference between the barrier height and electron

energy. Also, as seen from Fig 4.3 (a), the peak becomes sharper for thicker barrier, which is intuitive! These peaks correspond to the allowed energy levels in the quantum well between the tunneling barrier. This can be seen from Fig 4.3 (b), where the effect of widening the well is a decrease in the resonant energies.

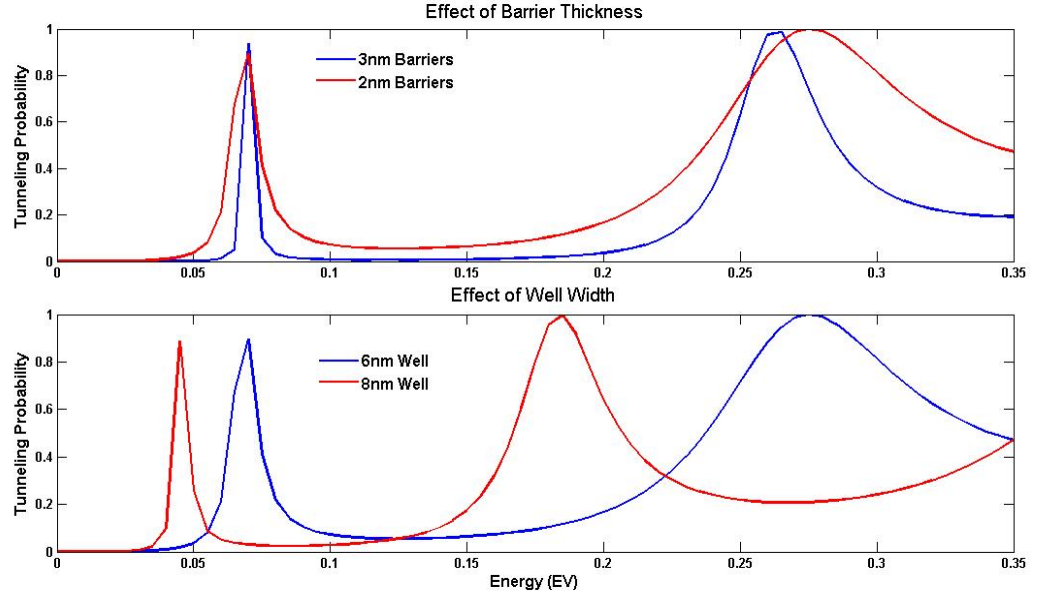


Fig 4.3: (a) Effect of barrier thickness on resonant tunneling probability. (b) Effect of well-width on the resonant tunneling probability.

4.2.2 Density of States Calculations

The total density of states in active region is approximately:

$$N(E) = \frac{2N_d}{L_p} \frac{1}{\sqrt{2ps}} \exp\left[-\frac{(E - E_i)^2}{2s^2}\right] + \frac{4pm^*}{L_p h^2} H(E - E_{w_j}) + \frac{8\sqrt{2}pm^{*(3/2)}}{h^3} \sqrt{E - E_c} H(E - E_c) \quad (4.17)$$

where, N_d is quantum dot surface density, L_p is the width of quantum well for DWELL structure and width of wetting layer for conventional QDIP structure, s is the

inhomogeneous broadening of quantum dot energies, E_i are quantum dot energy levels, m^* is the effective mass of electrons in conduction band, E_{w_j} are the quantum well energy levels, H is Heaviside step function.

Clearly, the density of state function is approximated as the sum of densities of states in quantum dots, quantum well (or the wetting layer) and the bulk. This function is calculated in the active region. For the case of conventional QDIP design, wetting layer width is very small, so it is assumed that there is only one energy state in it. However, for quantum well, in a DWELL design, the energy levels are calculated [120] using 3 point finite difference method (FDM), using non-uniform grid, to enhance the computation speed [121]. The calculated density of states functions for various layers are shown in Fig 4.4. Note that the quantum dot DOS is very small compared to the other two.

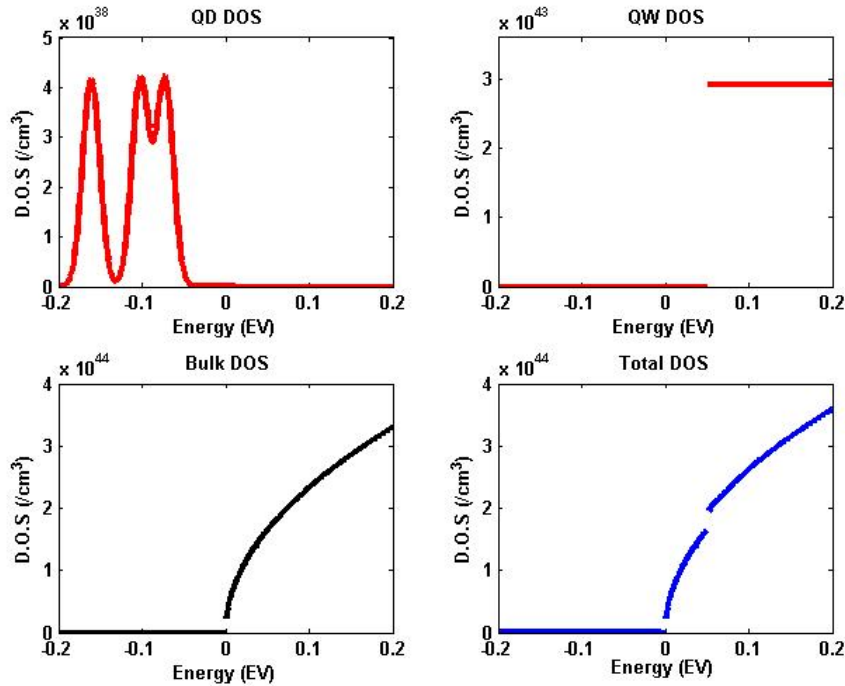


Fig 4.4: Calculated density of state functions for quantum dots, quantum well, bulk and total.

4.2.3 Simulation Considerations and Results

The simulation, based on the theoretical model described was carried out in MATLAB.

The total dark current density was obtained by assuming the typical device geometry.

Dimensions of the resonant tunneling barriers are:

Barrier width = 2nm, Well width = 6nm.

The composition of barriers is $\text{Al}_{0.3}\text{Ga}_{0.7}\text{As}$, while the well is of $\text{Al}_{0.1}\text{Ga}_{0.9}\text{As}$. The energy levels in the quantum dots have been assumed, the Fermi level is assumed to be placed at the lowest level of the quantum dot.

The effect of applied bias and the operating temperature was calculated, and the results are presented in Fig 4.5. It can be seen that the dark current is reduced by at least an order of magnitude for all the temperatures. Another point to be noted, which is not apparent from this work is that, even though the tunneling is sharply peaked, the photoresponse does not show peaked nature, in general. This is probably due to phonon assisted coupling from various states into a resonant tunneling state.

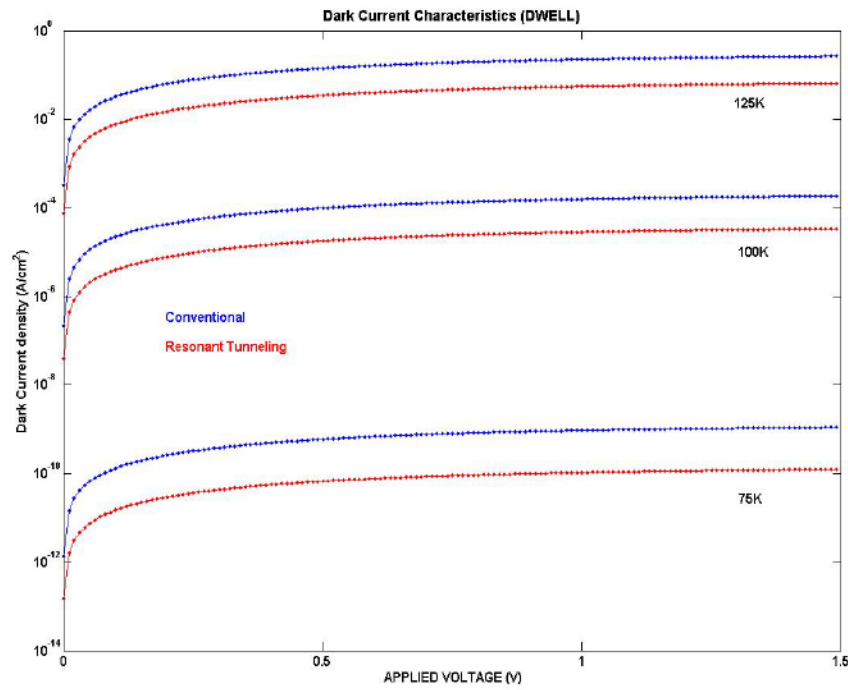


Fig 4.5: Dark current characteristics for DWELL structure, for the conventional barrier and resonant tunneling barrier.

4.3 RT-DWELL Devices

In this section, we will discuss the first generation RT DWELL designs, fabrication, simulations and experimental results.

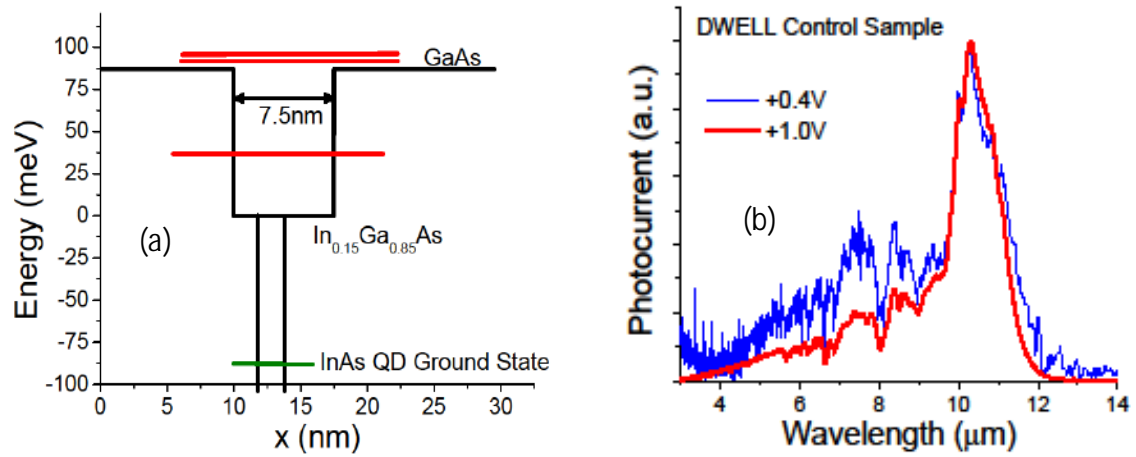


Fig 4.6: Schematic of the control sample: (a) Structure of the device with various energy states (b) Measured spectral response for two biases.

The structure of simple DWELL detectors, used as a control sample, is shown in Fig 4.6 (a). The InAs quantum dots are embedded in 7.5nm In_{0.15}Ga_{0.85}As quantum well. The In_{0.15}Ga_{0.85}As well serves dual purpose of contributing to the infrared absorption and improving the optical properties of InAs quantum dots by allowing optimal growth temperature as well as strain distribution as a capping layer. The prominent longwave transition, shown in Fig 4.6 (b) is from the ground state of the quantum dot to the bound state in the quantum well, while the weak midwave component is the transition to the continuum. The peak wavelength in these structures can be effectively tuned [80] by simply changing the thickness of In_{0.15}Ga_{0.85}As layer. The bound state energy level for QW shown in Fig. 4.6 (a) has been calculated from solving the one-dimensional Schrödinger equation by a three point finite difference method, using the band parameters taken from [122]. The conduction band offsets were calculated from [123]. The values used for conduction band offsets for In_{0.15}Ga_{0.85}As/GaAs and Al_xGa_{1-x}As/GaAs are 87meV and 870x meV, respectively, while the effective masses have been interpolated

from their binary values. The quantum dot energy level was estimated by semi-empirical approach, from photoluminescence and spectral response data.

4.3.1 Designs

As a proof-of-the-concept, two RT-DWELL designs were developed based on the aforementioned structure. All the samples were grown by V-80 solid source molecular beam epitaxy, with $\text{In}_{0.15}\text{Ga}_{0.85}\text{As}$ layers grown at 470°C , while GaAs and $\text{Al}_{0.3}\text{Ga}_{0.7}\text{As}$ layers were grown at 590°C . The resonant tunneling barriers consist of 2 nm GaAs spacer - 2 nm $\text{Al}_{0.3}\text{Ga}_{0.7}\text{As}$ - d nm $\text{In}_{0.15}\text{Ga}_{0.85}\text{As}$ - 2 nm $\text{Al}_{0.3}\text{Ga}_{0.7}\text{As}$ - 50 nm GaAs layers on the top of the DWELL structure, where d can be varied to change the passband of the RT-barrier. $\text{Al}_{0.3}\text{Ga}_{0.7}\text{As}$ was chosen in the resonant tunneling barriers, assuming that it will block most of the thermally generated carriers, while $\text{In}_{0.15}\text{Ga}_{0.85}\text{As}$ was chosen to extract energy levels lying below the conduction band edge of GaAs. There are 10 such stacks constituting the active region. The barrier is undoped while the quantum dots are n-doped with Si at approximately 2 electrons per dot. The top and bottom contact layers are n-doped with the doping concentration of $2 \times 10^{18} \text{ cm}^{-3}$.

First structure, RT-DWELL 1 was designed to extract the longwave peak of the response by aligning the resonant level of the barrier with the bound state of the quantum dot, by setting $d = 5.5$ nm. The second structure was designed to extract the midwave component of the spectral response at the lower bias (Bias < 0.6V). In this sample, the passband of the RT-barrier has been aligned with the conduction band of GaAs, by setting $d = 5$ nm, to extract the continuum energy levels. Calculated energy eigenvalues and wavefunctions for RT-DWELL 2 are shown in Fig 4.7 (a), while the tunneling probabilities as a function of energy for the two RT-barriers are shown in Fig 4.7 (b). Tunneling probabilities have

been calculated by transmission matrix method. Wavefunctions and energy eigenvalues calculated from FDM and TMM are in excellent agreement, to within 1%. It is to be noted that the simulations are only qualitative as they do not take into account the perturbation due to presence of quantum dots. The 2 nm GaAs spacer layer is provided to minimize the effect of coupling between RT barrier and DWELL. The calculated resonance level with and without the presence of the quantum well are only separated by 4 meV.

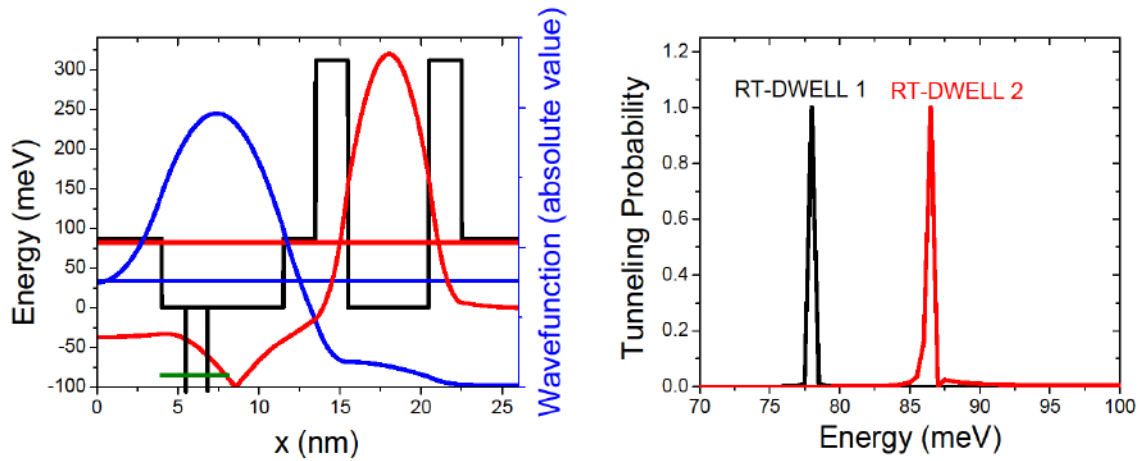


Fig 4.7: (a) Calculated energy eigenvalues and wavefunctions for RT-DWELL-2. (b) Calculated Tunneling Probabilities for the two RT-DWELL designs.

4.3.2 Results

The spectral response for the fabricated samples was measured using standard Fourier transform infrared spectroscopy (FTIR) analysis. The spectral response for the two RT-DWELL samples at 30K is shown in Fig 4.8. Here, positive bias is defined as positive voltage applied on the top contact. Clearly, RT-DWELL 1 response is dominantly LWIR, for all the biases, as designed. RT-DWELL 2 device, on the other hand is dominantly MWIR for lower biases, which is a clear indication of the effect of resonant tunneling

barrier. The resonant tunneling action also results, in a significant decrease in the dark current, resulting in higher operating temperature. Fig 4.9 compares the spectral response at different temperatures from the control sample and RT DWELL 1. It is clear that RT-DWELL 1 operates better than the control device at higher temperatures.

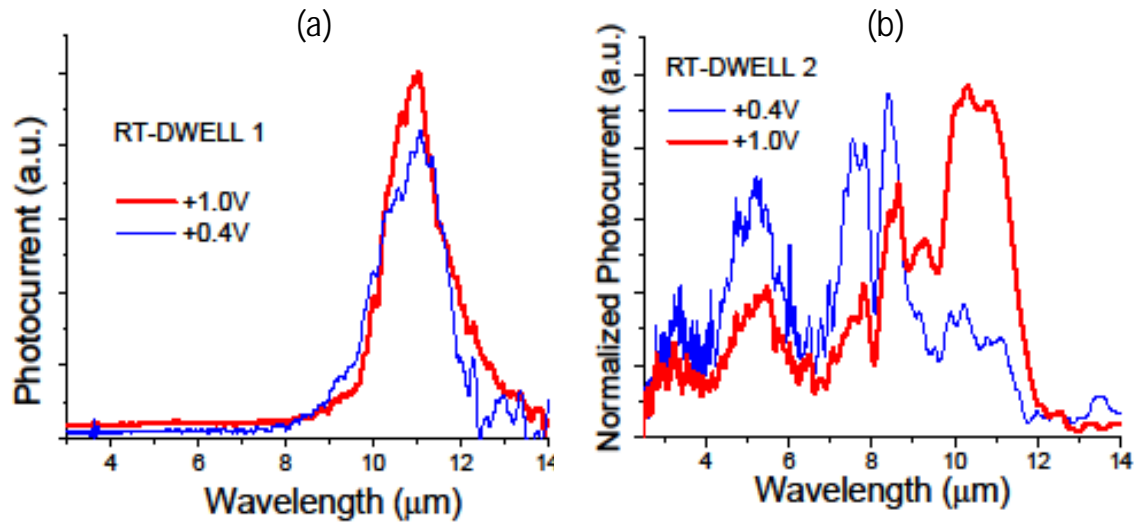


Fig 4.8: Spectral response for (a) RT-DWELL 1: Prominent LWIR response for all biases (b) RT-DWELL 2: Prominent MWIR response for lower biases

Fig 4.10 (a) shows comparison of dark current levels for the three samples at 90K. The reduction in the dark current is present at all the temperatures, as shown in Fig 4.10 (b). The dark current is lower in the positive bias for RT-DWELL samples, as the resonant tunneling barrier is located on positive bias side of the DWELL structure. Fig 4.10 (c) shows the comparison of the theoretically predicted dark current with the measured dark current for the two devices at 90K. It can be seen that although the results match well for RT-DWELL devices, the measured dark current is higher than that predicted theoretically in the control sample. This is presumably because of the simplicity of the model, which ignores thermionic emission from the ground state of quantum dot. Fermi energy was

assumed to be just above the QD ground state energy in the conduction band. This model underestimates the dark current at higher biases and cannot predict dark currents at different temperatures accurately.

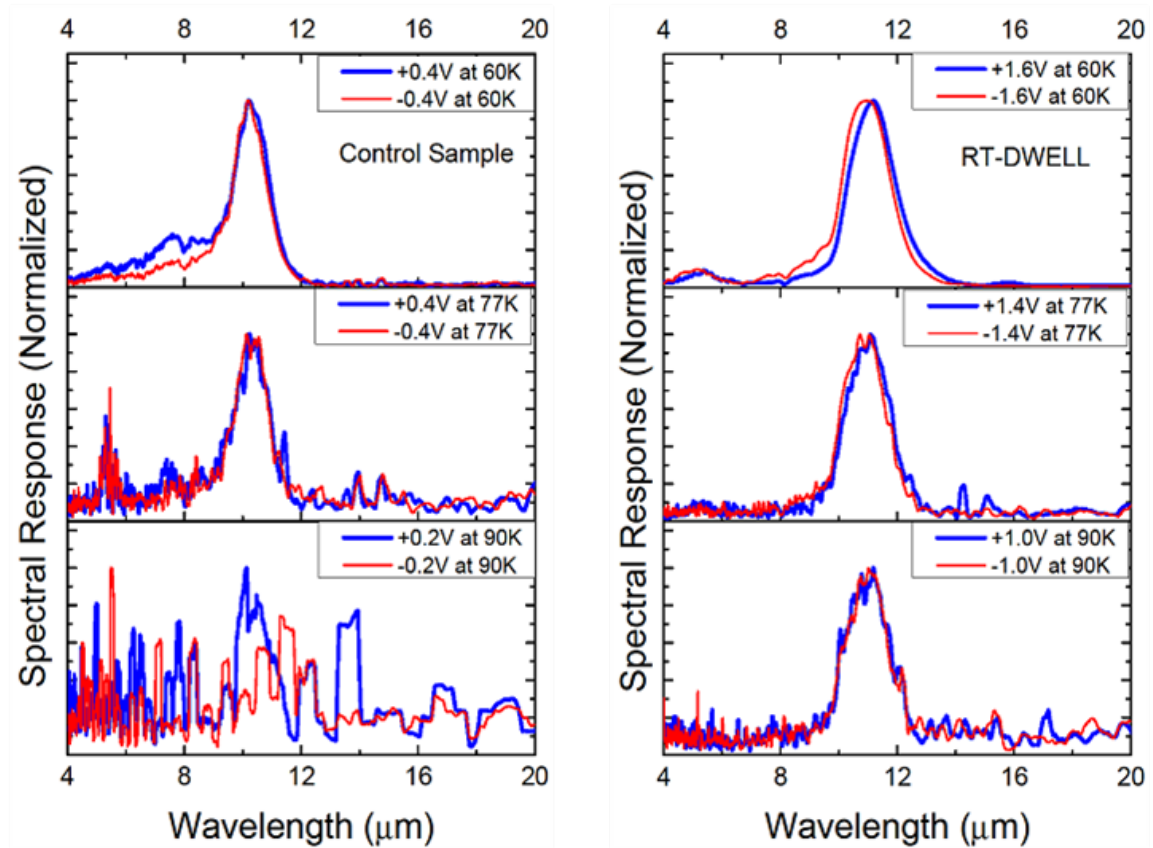


Fig 4.9: Normalized spectral response of (a) Control sample (b) RT-DWELL sample, at 30K, 60K, 90K. Note, that at 90K maximum operating bias of the device, the spectral response from the RT-DWELL is much stronger than that of the control sample.

Another interesting feature is that the dark current in RT-DWELL 2 sample is lower for the positive bias than that for RT-DWELL 1 sample, while in the negative bias they are comparable. This can be explained by Fig 4.7 (b), which shows the passband of RT-DWELL 2 sample at higher energy than that for RT-DWELL 1 sample. This should

result in higher activation energy for this device, which results in lowering of the dark current. This is indeed true, as shown in Fig 4.10 (d), which clearly shows higher activation energy for RT-DWELL 2 sample in the positive bias. Activation energies were calculated from the slopes of the Arrhenius plots at various biases. This effect is not observed in the negative bias, as expected.

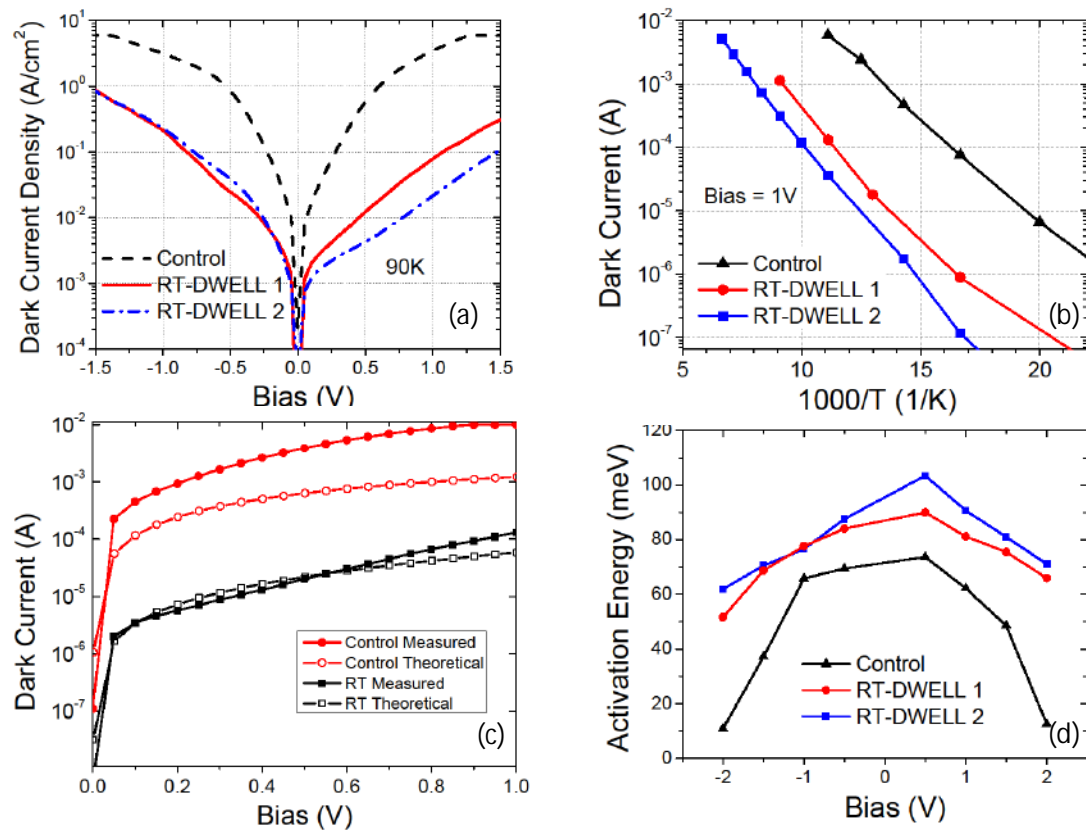


Fig 4.10: (a) Comparison of dark current density for three devices at 90K showing 2-3 orders of magnitude reduction in dark current. (b) Arrhenius plot of dark current, showing reduction in dark current at all the temperatures. (c) Comparison of dark currents in control and RT-DWELL1 devices at 90K with the theoretical calculations. (d) Activation energies for the three devices.

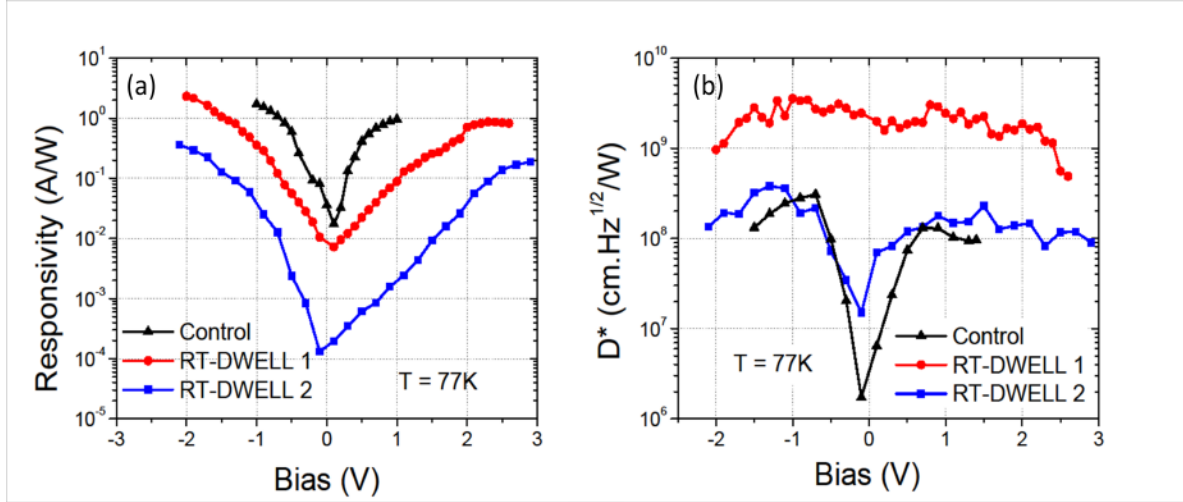


Fig 4.11: Comparison of (a) responsivity and (b) specific detectivity between RT-DWELL samples and control sample at 77K

Radiometric measurements were carried out in a pour filled dewar, at 77K using a calibrated blackbody source. Measured values of responsivity and D^* of the RT-DWELL samples are compared with the control sample in Fig 4.11 (a) and (b), respectively. As can be seen from Fig 4.11 (a), the responsivity for the RT-DWELL samples is lower than that of the control for the same bias. This is possibly due to non-unity transmission probability through the RT barriers. Responsivity of RT-DWELL 2 sample is further lower than that of the RT-DWELL 1 sample, as it is designed to extract midwave, which is the weaker component of the spectral response. This reduction in responsivity is more than compensated by the reduction in the noise, so D^* for RT-DWELL 2 is slightly higher than the control sample, while that for RT-DWELL 1 is factor of 10 higher. This is a significant improvement in the device performance.

4.4 RT-DDWELL

Although significant improvements in the performance parameters of DWELL detectors have been made by the application of RT barriers, further improvements are possible by selecting more optimized parent structures. The control sample used in Section 4.3 has a 7.5-nm $\text{In}_{0.15}\text{Ga}_{0.85}\text{As}$ quantum well with an additional 5 nm of $\text{In}_{0.15}\text{Ga}_{0.85}\text{As}$ in the resonant tunneling barrier. As $\text{In}_{0.15}\text{Ga}_{0.85}\text{As}$ is compressively strained on GaAs substrate, the cumulative strain added by each stack degrades the performance of upper quantum dot layers, thus restricting the number of stacks that can be grown with minimum defects. Another important factor, as seen from Fig 4.10 (c), is that the activation energies of these simple DWELL detectors are very low, leading to higher dark current. These problems can be solved by placing the $\text{In}_{0.15}\text{Ga}_{0.85}\text{As}$ - GaAs quantum well inside a GaAs - $\text{Al}_{0.1}\text{Ga}_{0.9}\text{As}$ quantum well. This allows reduction in the thickness of $\text{In}_{0.15}\text{Ga}_{0.85}\text{As}$ layer in DWELL structure to a very low value, thus reducing the cumulative compressive strain per stack. The additional $\text{Al}_{0.1}\text{Ga}_{0.9}\text{As}$ barrier also serves as a current blocking layer, thus increasing the activation energy. It is to be noted that the control samples used here have previously been used [77] to fabricate focal plane arrays with excellent imaging performance. In this section, we discuss the performance enhancement of these optimized quantum dots in double quantum well detectors by the application of resonant tunneling filters.

4.4.1 Designs

The schematic of the parent structure used for the purpose of comparison with the RT-DDWELL designs is shown in Fig 4.12 (a). The structure consists of InAs QDs

embedded in a double quantum well formed by $\text{Al}_{0.1}\text{Ga}_{0.9}\text{As}$ - 4 nm GaAs - 2 nm $\text{In}_{0.15}\text{Ga}_{0.85}\text{As}$ - 6.85 nm GaAs- $\text{Al}_{0.1}\text{Ga}_{0.9}\text{As}$ layers. The active region of the detector consists of 15 such stacks, separated by 50 nm $\text{Al}_{0.1}\text{Ga}_{0.9}\text{As}$ barriers. Fig 4.12 (b) shows the spectral response obtained from this structure at 77 K at three different biases. The multicolor response has three prominent peaks at 4.8, 7, and 10.5 μm , respectively, in the positive bias and at 5 and 8.7 μm in the negative bias. The longwave peaks are dominant at higher biases, as they are believed to originate from the transition from quantum dot ground state to a bound state in $\text{In}_{0.15}\text{Ga}_{0.85}\text{As}$ - GaAs quantum well, thus requiring higher applied bias for extraction. On the other hand, the broad midwave peak is a result of a transition from quantum dot ground state to the continuum, thus can easily be extracted even at lower applied biases. It is believed that there are two bound states in the quantum wells, as marked in the Fig 4.12 (b), at 70 and 130 meV from $\text{In}_{0.15}\text{Ga}_{0.85}\text{As}$ conduction band edge, responsible for responses at 10.5 μm and 7 μm respectively. Note that the energy values are approximate as they have been calculated from a one-dimensional analysis, while the quantum dot ground state has been calculated by a semi-empirical approach.

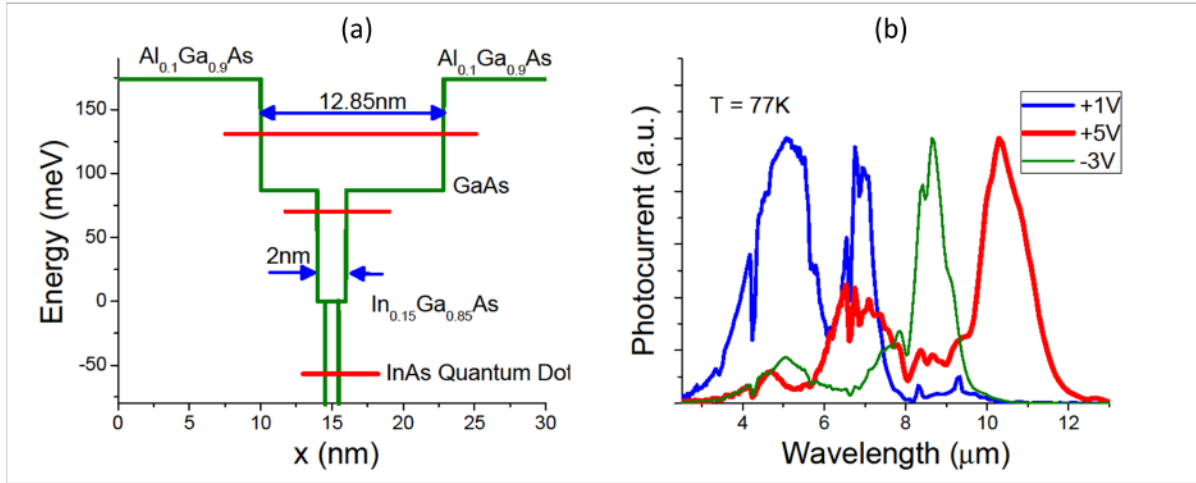


Fig 4.12: (a) Schematic of DDWELL control sample. The calculated energy levels for various transitions are marked. (b) Measured spectral response for DDWELL control sample at 77 K, clearly showing four distinct peaks which can be individually tuned by the application of different biases

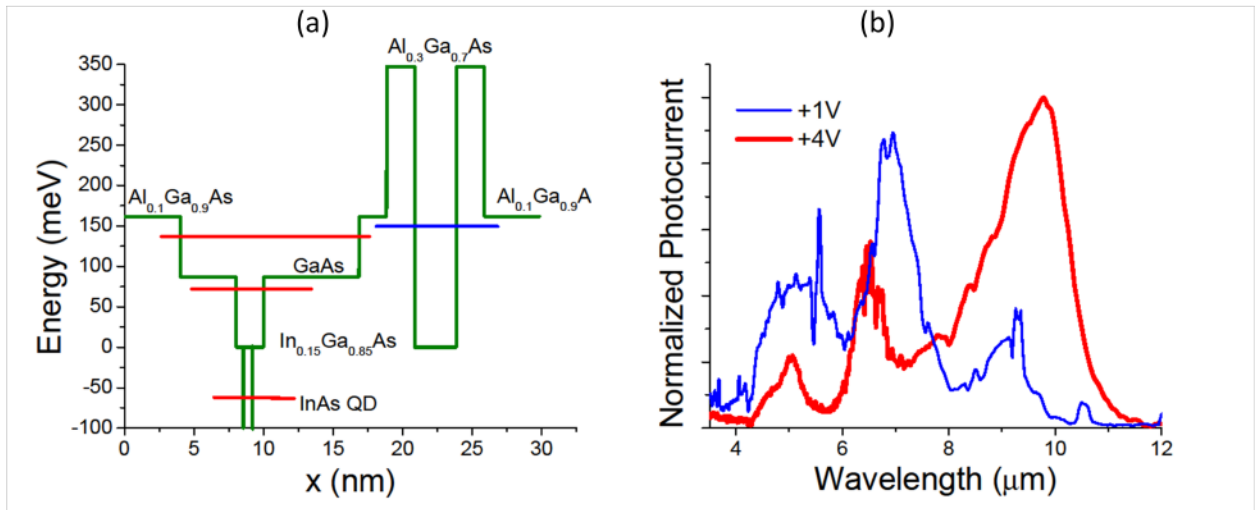


Fig 4.13: (a) Schematic of RT-DDWELL Structure. The calculated energy levels for various transitions and resonant tunneling barrier are marked. (b) Measured spectral response for RT-DDWELL sample at 77 K.

Two resonant tunneling barrier structures were designed for the aforementioned DDWELL structure as the parent sample. Schematic of the first RT-DDWELL device is shown in Fig 4.13 (a). The energy levels calculated for both DDWELL and resonant

tunneling barrier are shown. The resonant energy of the RT- barrier has been aligned with the second excited state in the DDWELL structure, as shown in the figure. The RT barrier consists of a 2 nm $\text{Al}_{0.1}\text{Ga}_{0.9}\text{As}$ spacer - 2 nm $\text{Al}_{0.3}\text{Ga}_{0.7}\text{As}$ - 3 nm $\text{In}_{0.15}\text{Ga}_{0.85}\text{As}$ - 2 nm $\text{Al}_{0.3}\text{Ga}_{0.7}\text{As}$ followed by 50 nm of $\text{Al}_{0.1}\text{Ga}_{0.9}\text{As}$ barrier. The DDWELL structure has been kept same as the parent sample, for comparison.

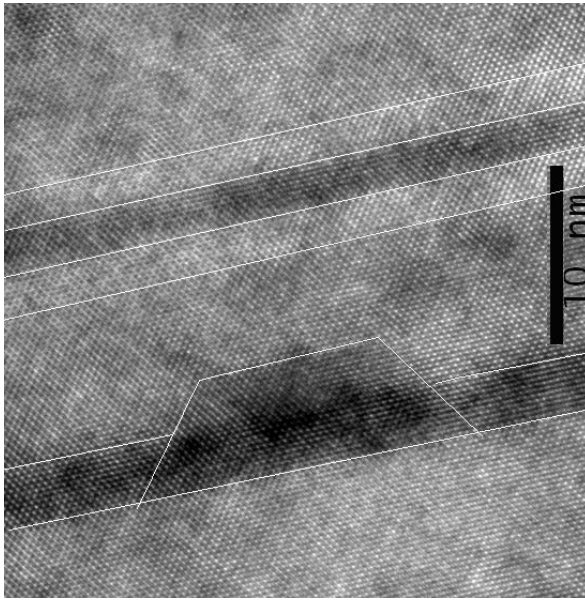


Fig 4.14: HRTEM image of RT-DDWELL sample, showing quantum dot, quantum well and resonant tunneling barrier. Lines are guide to eye.

A high-resolution transmission electron microscope (HRTEM) image of an RT-DDWELL sample is shown in Fig 4.14, clearly showing quantum dot, $\text{In}_{0.15}\text{Ga}_{0.85}\text{As}$ quantum well, and resonant tunneling barrier. The spectral response obtained from this device for two different biases in the positive bias at 77 K is shown in Fig 4.13 (b). As can be seen, the peak at 7 μm has been enhanced and narrowed, so it is reasonable to assume that the resonant band is aligned to the second excited state in the quantum well part of the DWELL structure, as expected. However, at higher bias, the longwave peak at 10 μm is still dominant.

Aligning the resonant tunneling passband with the longwave peak is much more challenging. For extracting the first excited level in $\text{In}_{0.15}\text{Ga}_{0.85}\text{As}$ quantum well, the resonant energy of the RT barrier needs to be lowered, by increasing the thickness of the $\text{In}_{0.15}\text{Ga}_{0.85}\text{As}$ layer in RT barrier. This lowering of resonant energy pushes it well below $\text{Al}_{0.1}\text{Ga}_{0.9}\text{As}$ conduction band, and hence the extraction probability drastically reduces. To solve this problem, some region of $\text{Al}_{0.1}\text{Ga}_{0.9}\text{As}$ adjacent to RT barrier has been replaced by GaAs layer. GaAs layer is followed by $\text{Al}_{0.1}\text{Ga}_{0.9}\text{As}$ layer to ensure the quantum confinement in the next DDWELL stack. The schematic of the structure of this device with a “split-barrier configuration” is shown in Fig 4.15 (a). The thickness of $\text{In}_{0.15}\text{Ga}_{0.85}\text{As}$ layer in RT barrier required for the extraction of LW peak is 5 nm. There are various considerations for fixing the width of GaAs layer thickness in the split barrier. The GaAs layer should be thick enough so that the carriers tunneling out of RT barrier acquire enough kinetic energy from the applied electric field to pass over the $\text{Al}_{0.1}\text{Ga}_{0.9}\text{As}$ layer, while it should be thin enough such that the carriers do not thermalize before they reach $\text{Al}_{0.1}\text{Ga}_{0.9}\text{As}$ layer. Another factor that limits the thickness is that the $\text{Al}_{0.1}\text{Ga}_{0.9}\text{As}$ layer should be far away from the RT barrier, such that it does not quantum mechanically perturb the resonant tunneling extraction. The thickness of GaAs was chosen to be 20 nm, which satisfies all the above constraints. The spectral response from this resonant tunneling split barrier (RT-Split) configuration sample is shown in Fig 4.15 (b), in both positive and negative bias, at 77 K. As designed, in the positive bias exclusively longwave response is observed, while in negative bias, all the three peaks are clearly visible. This clearly indicates successful resonant tunneling action in the positive bias.

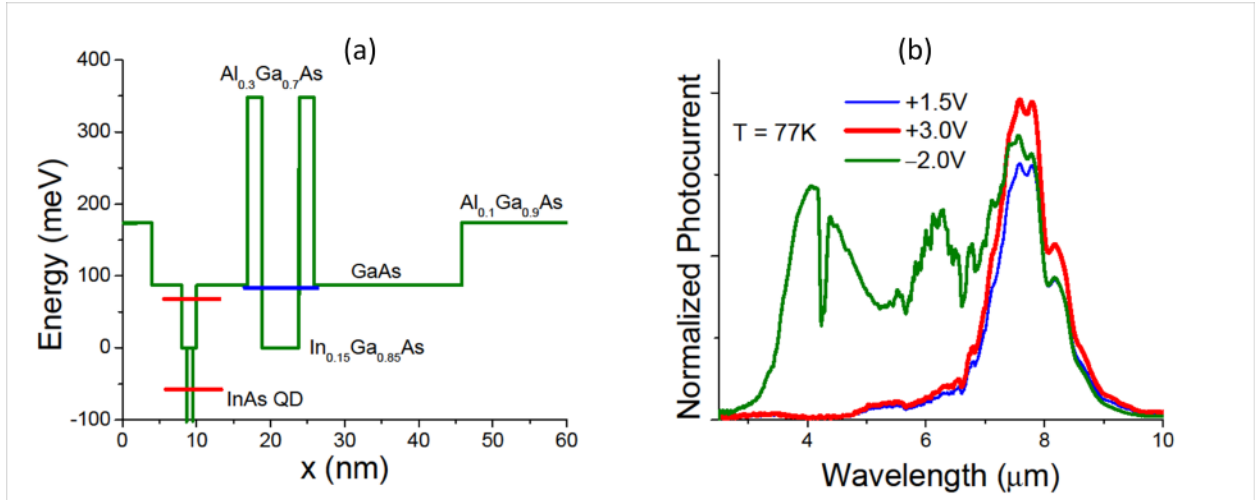


Fig 4.15: (a) Schematic of RT-Split barrier structure. The calculated energy levels for various transitions and resonant tunneling barrier are marked. (b) Measured spectral response for RT-Split barrier sample at 77 K, clearly showing exclusively longwave in the positive bias. The negative bias shows all the three peaks from the DDWELL control sample.

4.4.2 Results

Since the barrier region in DDWELL devices consists of Al_{0.1}Ga_{0.9}As, the dark current levels are significantly lower than those in DWELLs, at the cost of increase in the electric field required to extract the longwave response. This can be a problem in focal plane arrays where maximum operating bias is limited by the readout circuit designs. Special designs such as RT-Split barrier configuration allows effective extraction of the longwave response even at lower biases in the positive bias, at the cost of slightly higher dark current density. This increase in the dark current can be nullified by operating the device at lower bias, while still being able to extract the longwave carriers.

RT-DDWELL detectors further reduce the dark current density, as compared with the DDWELL control sample, resulting in very low dark current densities. Measured values of dark current densities at 77 K are compared in Fig 4.16 (a). The reduction in the dark current for RT-DDWELL device is significant for increasing the operating temperature

further. The Arrhenius plot in Fig 4.16 (b) shows that the reduction in the dark current is significant at all the temperatures. Dark current is also reduced in negative bias because of additional current barriers provided by the resonant tunneling barriers for the next stack.

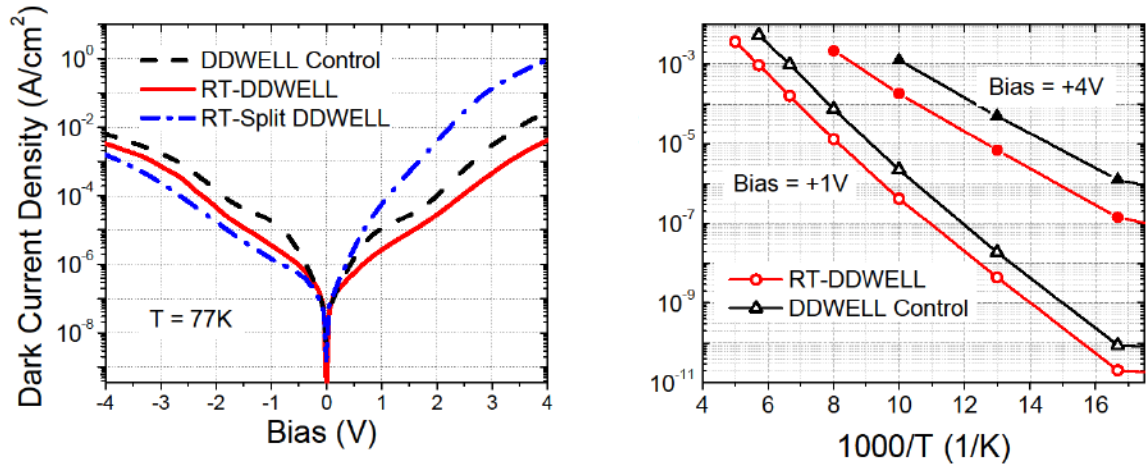


Fig 4.16: (a) Comparison between dark current densities for RT-DDWELL samples with control sample, at 77 K (b) Arrhenius plots comparing RT-DDWELL device dark current with the control sample at +1 V (open symbols) and +4 V (filled symbols). Close to order of magnitude reduction is apparent.

For RT-DDWELL device, as observed before for RT-DWELL devices, the dark current is close to one order of magnitude lower in the positive bias. Note that the dark current levels for DDWELL devices are much lower than simple DWELL devices, resulting in better SNR and higher operating temperature. It is to be noted that the dark current for RT-DDWELL devices is lower than the state-of-the-art QWIP devices used for imaging applications, and have been compared in the review paper [16] by Barve et al. For RT-Split barrier configuration, the activation energies are vastly different in the two bias polarities, due to the height of the barrier on two sides. The positive bias has reduced activation energy as Al_{0.1}Ga_{0.9}As layer adjacent to RT barrier has been replaced by GaAs

layer. This reduction is reflected in the activation energies for various biases calculated from the slope of Arrhenius plots, plotted in Fig 4.17. Activation energies for previous three samples have also been plotted for comparison. It can be seen that activation energies for RT-DDWELL and DDWELL control sample are similar in the negative bias, as expected, with slight increase in activation energy for RT-DDWELL sample in the positive bias. The activation energies for RT-Split barrier configuration are intermediate to that for DWELL and DDWELL samples in the positive bias, while it is slightly higher than DDWELL samples in the negative bias. This increase in the negative bias is attributed to the redshift in quantum dot PL.

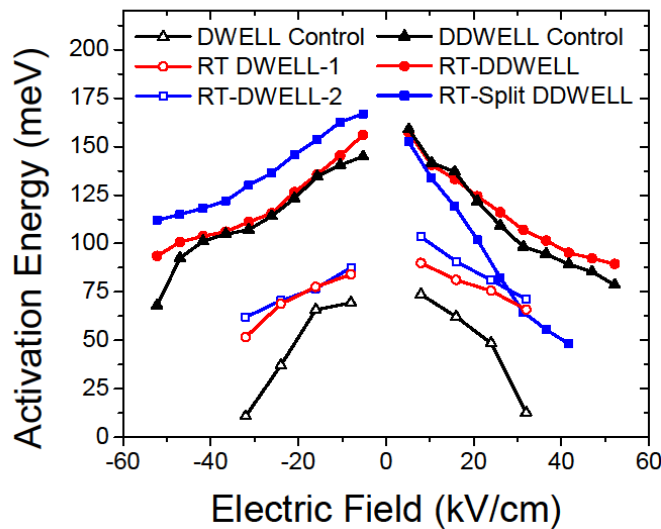


Fig 4.17: Comparison of activation energy for all the devices.

Fig 4.18 (a) and (b) shows measured values of responsivity and detectivity, respectively, compared between RT-DDWELL samples and the control sample. The responsivity measurements were carried out in the same setup described before, and the results were normalized to $f/2$ optics for fair comparison. Scaling the detectivities is justified because,

as seen later (see Fig 4.19 (a)) the devices are background limited at 77 K. The responsivity for RT-DDWELL sample is lower than that for DDWELL control sample by a factor of 4–5 in the positive bias. However, due to significant reduction in the noise in the positive bias, the signal to noise ratio is actually improved, as can be seen in Fig 4.18 (b), which shows an order of magnitude improvement in the detectivity in the positive bias for RT-DDWELL. For RT-Split barrier sample, the noise is not suppressed as in RT-DDWELL device due to increase in the dark current. Hence the detectivity is similar in the positive bias. However, detectivity is higher in the negative bias, for all the three samples, as a result of higher responsivity. Peak detectivity for RT-DDWELL, RT-Split barrier and DDWELL control samples are $2.9 \times 10^{10} \text{ cm.Hz}^{1/2}/\text{W}$ (8.8 μm), $2.1 \times 10^{10} \text{ cm.Hz}^{1/2}/\text{W}$ (7.8 μm), and $1.4 \times 10^{10} \text{ cm.Hz}^{1/2}/\text{W}$ (8.7 μm), respectively. The detectivity enhancement is significant even at higher operating temperatures, as compared in Fig 4.18 (c), due to reduction in the noise.

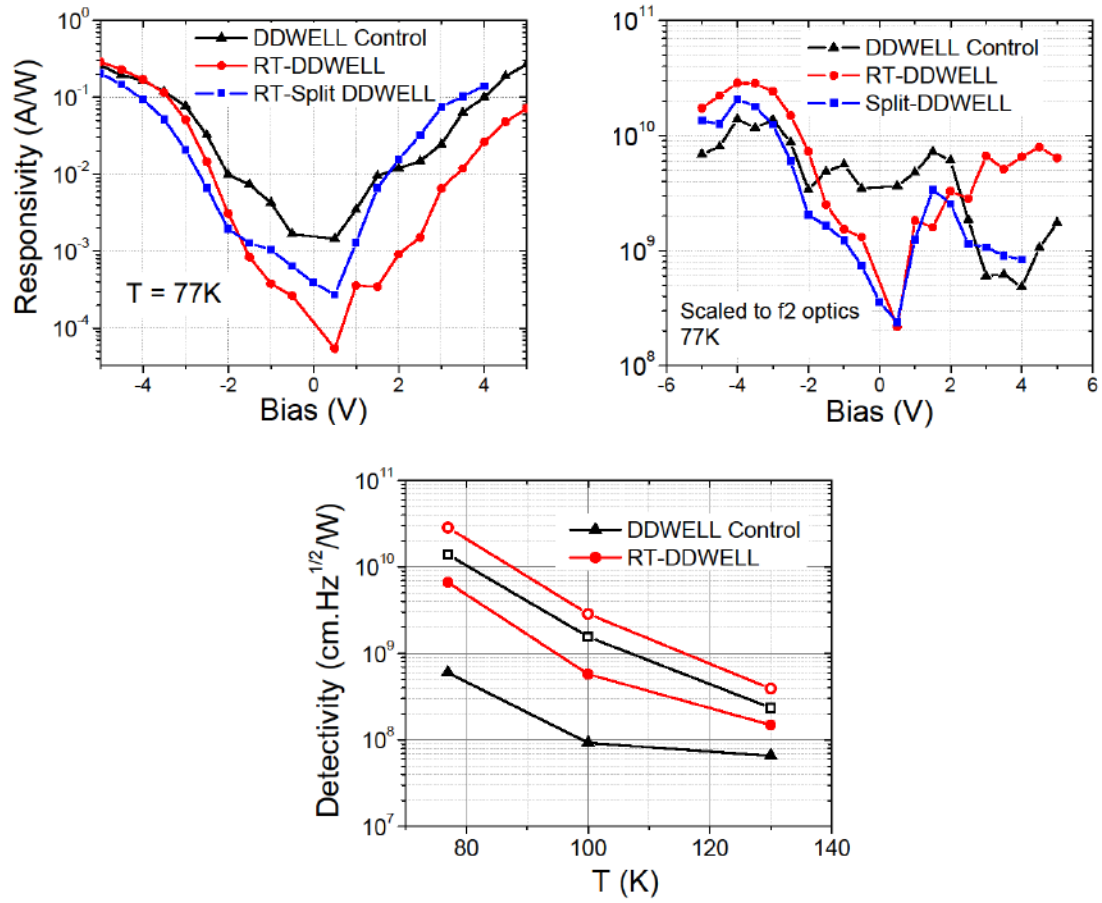


Fig 4.18: Comparison of (a) responsivity and (b) specific detectivity between RT-DDWELL, RT-Split barrier and DDWELL control samples at 77 K. (c) Comparison of peak detectivities (open symbols) and detectivity at +3 V (filled symbols) between DDWELL control sample and RT-DDWELL sample, showing improvement in the device performance even at higher temperatures.

To get further insights into device noise performance, the device noise under different conditions has been measured. The measurement setup consists of a variable temperature dewar with a cold finger on the backside of the sample. The two conditions used were with and without cold shield for 0 and field of view (FOV), respectively. The noise power spectral density (PSD) measurements were carried out in these two conditions. Noise measurements were carried out away from $1/f$ noise regime, so that the primary noise mechanism are the fluctuations in the emission and capture processes in the active

region, similar to generation- recombination (G-R) noise in the band to band photoconductors.

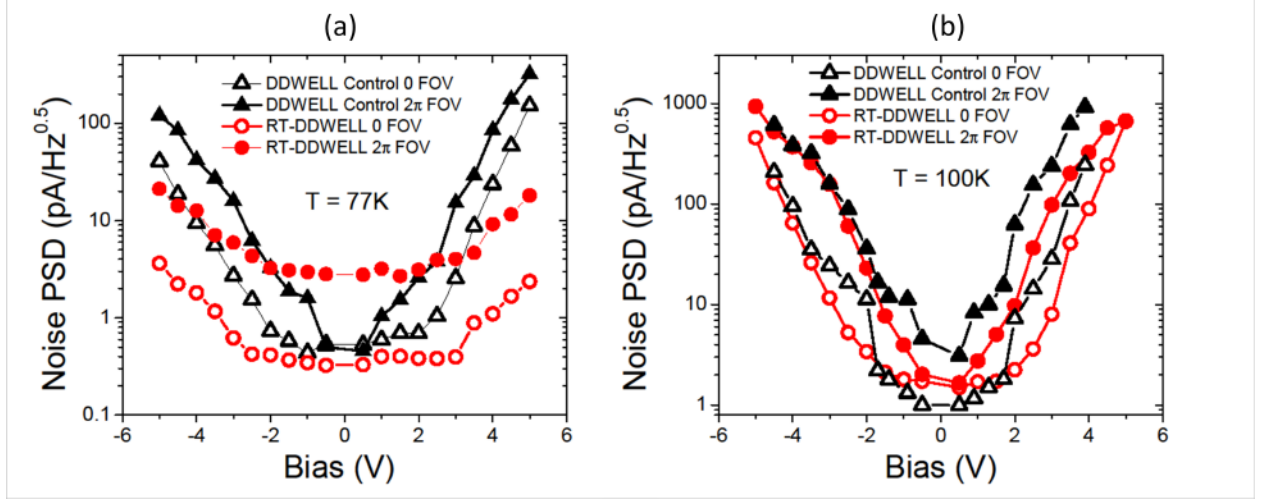


Fig 4.19: Noise PSDs at (a) 77 K and (b) 100 K compared for RT-DDWELL and DDWELL control sample

The noise PSD at 77 K has been plotted in Fig 4.19 (a), shows a flat region at lower biases for dark settings. This is due to system noise limited operation. Thus, it can be expected that in the Johnson-noise limited regime (JOLI), the detectivity value would be higher than $2.9 \times 10^{10} \text{ cm.Hz}^{1/2}/\text{W}$, which is for $f/2$ optics. Hence, to avoid system noise limited operation in order to calculate photoconductive gain, measurements were repeated at higher temperatures so that the noise is above system noise limit. Measured values of noise PSD are shown in Fig 4.19 (b), at 100 K for RT-DDWELL and DDWELL control sample. Noise PSDs with 2π FOV are also plotted for comparison. It is clear that the devices are background limited at 77 K as well as 100 K, as the noise PSD with 2π FOV is much higher than the noise PSD in dark settings. It is also apparent that RT-DDWELL device has superior noise performance as compared to the DDWELL control sample, even at elevated temperatures.

4.5 Conclusions

Resonant tunneling barriers can be effectively used for suppression of dark current, enhancement in signal-to-noise ratio and selective extraction of different wavelength response on a common parent sample. We present a detailed account of design of RT barriers on simple DWELL devices as well as optimized DDWELL devices. Mathematical modeling of dark current with a simple emission capture model has been used to compare the dark currents of resonant tunneling barrier and classic triangular barrier configurations. Two RT-DWELL devices for extraction of LWIR and MWIR components of spectral response of DWELL parent samples are reported. The dark current has been reduced by 2–3 orders of magnitude, with an increase in the detectivity values by a factor of 5–10. We also present RT-DDWELL device which shows performance enhancement over optimized parent sample. Superior performance has been obtained with detectivity of $2.9 \times 10^{10} \text{ cm.Hz}^{1/2}/\text{W}$ in LWIR. Specialized design with split barrier configuration is presented for extracting exclusively LWIR response from a multicolor parent sample.

5 Confinement Enhanced DWELL Detectors

In chapter 2 we discussed the different types of DWELL transitions, such as bound to continuum, bound to bound and bound to quasibound transitions and their characteristics. In this chapter we will compare various characteristics such as spectral response, dark current, responsivity, detectivity, photoconductive gain, absorption QE etc systematically between these transitions. It will be demonstrated that B-Q types of transitions optimize the performance at moderate bias levels required for FPA applications. We will further optimize the B-Q types of transitions by accommodating a confinement enhancing (CE) barrier in the design, which increases the absorption QE while simultaneously reducing the dark current. High performance imaging is shown at elevated temperatures. In the last section of this chapter, we will talk about the effect of barrier systematically by analyzing the effect of barrier close to the DWELL region and far away from the DWELL region.

5.1 Different Transitions in DWELL Detectors

5.1.1 Introduction

The ability to independently tune the ground state energy, which is dominated by the quantum dot properties, and the excited energy state, which is a function of quantum well and barrier properties offers unique advantage to DWELL detectors over both QWIP and QDIP type of devices. Systematic study of different transitions in QWIPs have been previously reported [23], however no such study has been reported on QDIPs as it is hard to control the energy levels in the quantum dots. In this study, the excited state in the

quantum well of the DWELL structure has been tuned with respect to the barrier to obtain different types of transitions [76, 93], such as bound to bound, bound to quasi-bound (2 devices) and bound to bound . The full width half maximum (FWHM) of the spectral response decreases progressively from B-C to B-B transitions. The measured responsivity shows that at lower biases, the responsivity decreases with decreasing FWHM (going from B-C to B-B), while at higher biases the exact reversal of the trend is observed. B-C transitions have unity escape probability for photoexcited electrons hence show high responsivity at lower bias. On the other hand, B-B transitions have the best absorption coefficient due to better wavefunction overlap between the two states, but poor escape probability at lower biases. These designs allow optimizing the detector performance for the required spectral width, wavelength, photoconductive gain and absorption quantum efficiency. In this study, very high detectivities of $\sim 4 \times 10^{11}$ cm.Hz^{1/2}/W at 77K and $\sim 4 \times 10^8$ cm.Hz^{1/2}/W at 220K for *f*/2 optics have been obtained. The measured background limited performance (BLIP) temperature for B-Q device is ~ 100 K for 300K background with 2π field of view (FOV). High performance focal plane arrays (FPA) have been fabricated using these devices, which have average noise equivalent temperature difference (NETD) of 44mK at 80K operating temperature, for *f*/2.3 optics.

5.1.2 Device Designs

Four DWELL devices with varying quantum well thicknesses were fabricated and characterized. The B-C, B-Q2 and B-B samples consist of 20 stacks of InAs quantum dots placed in In_{0.15}Ga_{0.85}As quantum wells, each separated with 50nm of Al_{0.08}Ga_{0.92}As barriers. B-Q1 device has only 5 stacks in the active region. Devices B-Q2 and B-B have

an additional 50nm of $\text{Al}_{0.08}\text{Ga}_{0.92}\text{As}$ barriers near the top and bottom contact, which serve as current reducing layers. The schematics of all the four samples are shown in Fig. 5.1 (a). The strain bed thickness (d_1) was 1.5 nm, 3.5 nm, 4 nm and 4.5 nm, respectively, for B-C, B-Q1, B-Q2 and B-B samples. These structures were chosen such that for B-C structure, the excited energy level will be aligned with the continuum band at the barrier conduction band, while for B-Q and B-B structures; the energy level will be progressively lowered. Schematic of energy structure of B-C device is shown in Fig. 5.1 (b). Fig. 5.1 (c) shows cartoons of conduction bands for different transitions and their properties. In all the samples, the capping $\text{Al}_{0.08}\text{Ga}_{0.92}\text{As}$ layer was kept 2.5 nm so that the dot shape and size does not alter significantly, which was confirmed with similar photoluminescence (PL) data obtained from all the samples. The peak of PL at room temperature was between 1055 nm to 1060 nm for all the samples. The height of quantum dot is approximately 5nm and base diameter is 15 nm, as interpreted from TEM data. The measured spectral response obtained from all the devices is shown in Fig. 5.2, which shows full width half maximum of 35%, 15.8%, 12.2% and 8.8% of the peak wavelengths, respectively. Summary of the device results obtained from these structures is given in Table 5.1.

5.1.3 Results

The radiometric measurements were performed to calculate the responsivity and detectivity of the structure. The responsivity, plotted in Fig. 5.3 (a) for all the samples, shows that at low electric fields, the B-C sample has largest responsivity, which decreases with decreasing FWHM. This trend reverses at higher electric field, owing to higher absorption in B-B structures. At lower electric fields, the extraction probability of

electrons below the barrier is very small, which results in lower responsivity for B-B transitions, while B-C device has highest responsivity due to unity extraction probability. At higher electric fields, most of the photoexcited carriers can be collected by the field assisted tunneling, resulting in higher responsivity for B-B devices, which have higher absorption coefficients. The responsivity values increase with increasing temperature due to the increase in the photoconductive gain. The detectivities, measured with noise measurements and scaled to $f/2$ optics, have been plotted in Fig. 5.3 (b), show similar trends, with the detectivity roll-off electric field progressively increasing from B-C to B-B samples. Very high values of detectivities confirm excellent signal to noise ratio for these samples. For example, in B-Q2 device, detectivities of $\sim 4 \times 10^{11} \text{ cm.Hz}^{1/2}/\text{W}$ at 77K and $\sim 4 \times 10^8 \text{ cm.Hz}^{1/2}/\text{W}$ at 220K for $f/2$ optics have been obtained.

d1 (nm)	x (%)	λ (μm)	$\Delta\lambda/\lambda$ (%)	Type
1.5	8	6.1	35	B-C
3.5	8	7.1	16	B-Q(1)
4.0	6	7.5	12	B-Q(2)
4.5	8	7.4	9	B-B

Table 5.1: Strain bed thickness (d_1), Al composition in the barrier, peak wavelength and full width half maximum (FWHM) of the spectral response measured at 77K.

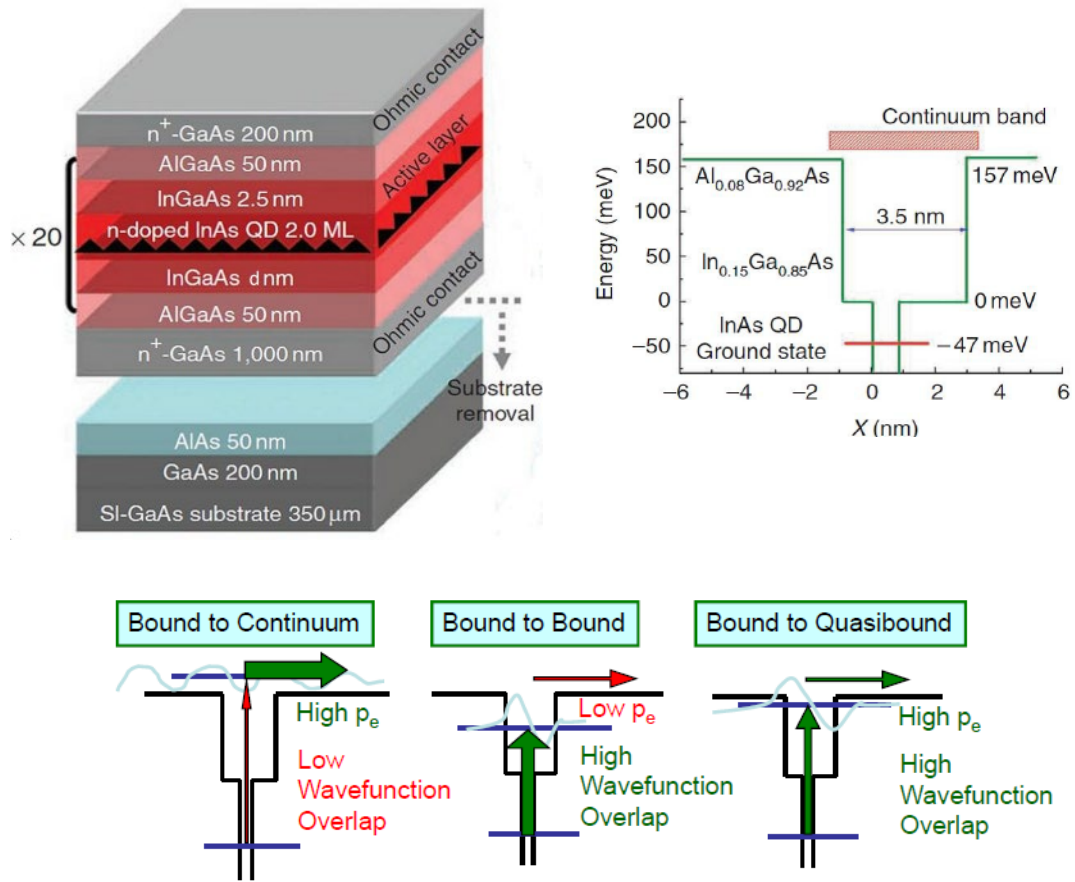


Fig. 5.1 (a) Schematics of the designed structures. The strain bed thickness is varied to tune the excited energy level (b) Band diagram of individual DWELL section for B-C device. (c) Schematics of the types of transitions describing the relative advantages and disadvantages

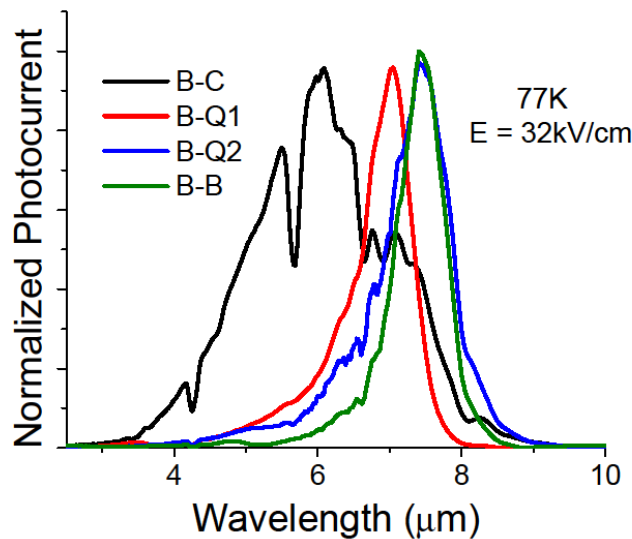


Fig. 5.2: Normalized spectral responses obtained from all the four devices, showing FWHM decreasing for increasing well width.

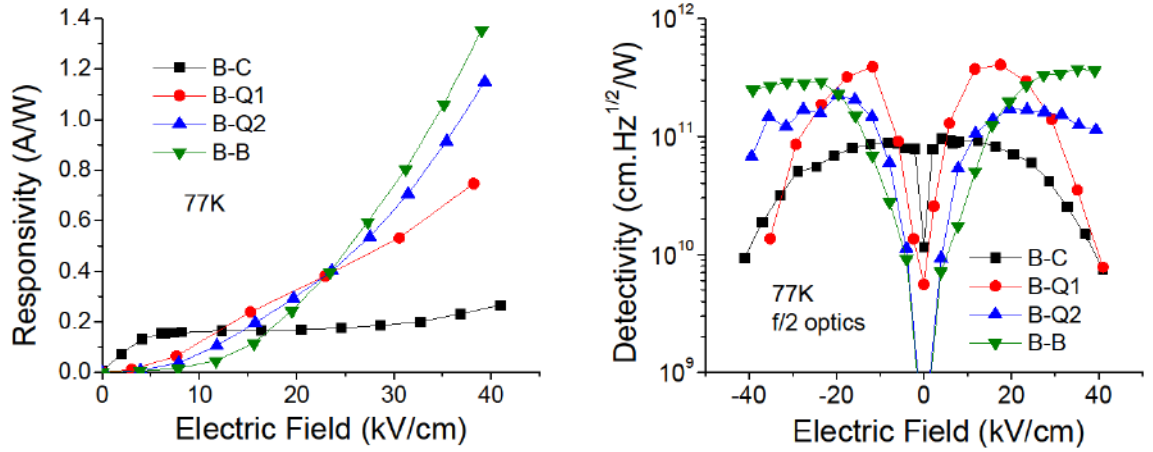


Fig. 5.3: (a) Measured responsivity at 77K for all the devices. Note that the responsivity for B-C device is highest at lower electric field, while at higher electric fields, the responsivity of B-B device is highest. (b) Measured detectivities for various samples at 77 K, plotted for $f/2$ optics.

To get further insights into the device transport physics, PC gains were measured to estimate the absorption quantum efficiency in all devices. To measure the PC gain, the devices were irradiated with a blackbody at 900 K, to force the shot noise due to photogenerated carriers to be much higher than the shot noise due to dark current. In such conditions, the PC gain (G_{ph}) can be estimated by

$$G_{ph} = \frac{i_n^2}{4q\Delta f I_{ph}} \quad (5.1)$$

where, i_n is the measured noise current, q is the electronic charge Δf is the noise bandwidth of the measurement system, and I_{ph} is the measured photocurrent under these conditions. The estimated PC gain, which is inversely proportional to the capture probability, has been shown in Fig. 5.4 (a). It can be seen that the B-C device has highest PC gain which decreases progressively for the B-Q and B-B devices. This is due to the fact that the B-C transitions have the least capture probability as there is no excited energy level to trap the electrons. Similar measurements were carried out at 100K and

130K, where an increase in PC gain with increasing temperature was observed, plotted in Fig. 5.4 (b) for B-Q2 device. The increase in PC gain is due to increase in thermal velocity of carriers, which reduces the capture probability at higher temperatures.

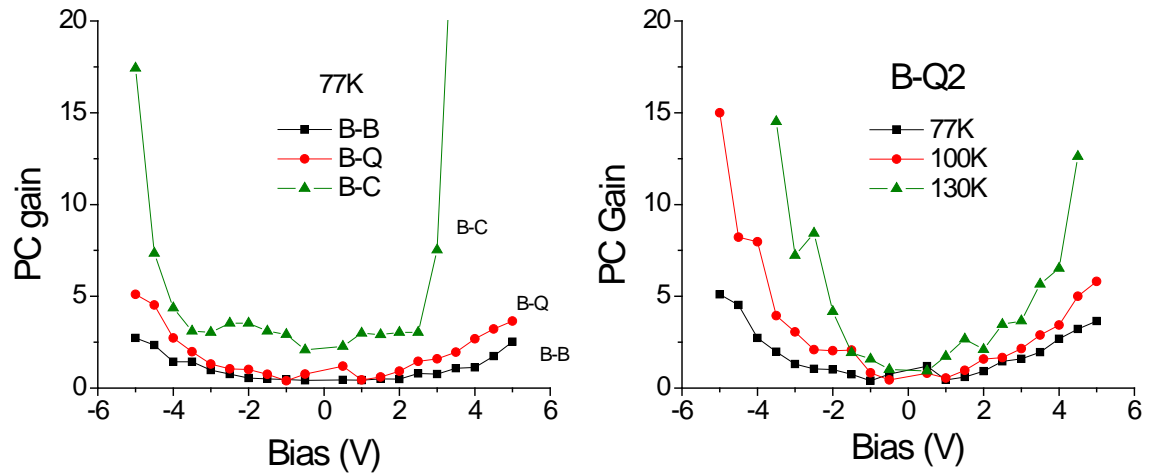


Fig. 5.4: (a) Photoconductive gain comparison for various devices at 77K (b) Photoconductive gain for B-Q2 at different temperatures, showing an increase in PC gain.

The absorption QE, plotted in Fig. 5.5 (a), was calculated from the measured responsivity and the calculated values of PC gains. Clearly, the B-B transitions have the highest absorption QE at higher biases, due to the strongest wave function overlap between the two states. This absorption QE decreases progressively for the B-Q and B-C transitions. The 12% absorption QE for the B-B device is one of the highest reported absorption QE for QDIPs. The absorption QE decreases at higher temperatures as plotted in Fig. 5.5 (b) for B-Q2 device. Similar trends were observed in other devices as well. It is to be noted that this measurement does not account for substrate scattering, which is known to increase the absorption QE by a factor between 2-3.

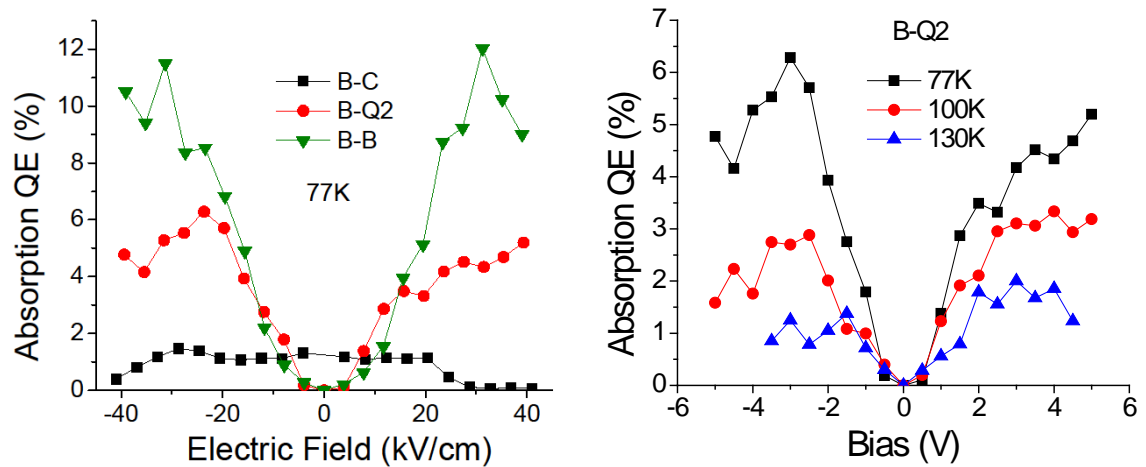


Fig. 5.5: (a) Absorption QE comparison for various devices at 77K (b) Absorption QE for B-Q2 at different temperatures.

5.1.4 High Temperature Operation

Radiometric measurements at different operating temperatures show that the signal remains relatively constant at higher temperatures, while the noise becomes higher. Fig. 5.6 (a)-(d) show the responsivities of all the four devices measured at higher operating temperatures. Notice that the trends observed at 77K are still valid at higher operating temperatures. The slight increase in the responsivity as the temperature increases is because of increased photoconductive gain at higher temperatures, as will be discussed later. Fig. 5.6 also shows the respective conversion efficiencies for all the devices. The conversion efficiency is defined as total number of electrons flowing in the external circuit for each incident photon. These values are calculated from responsivity data and are equal to the product of the absorption quantum efficiency and the photoconductive gain. Notice that the conversion efficiencies of these devices are high, and the value of conversion efficiency follow similar trends as the responsivity values. At lower electric

fields, the conversion efficiency for B-C device is highest ($\sim 3.5\%$) while at higher electric fields, the B-B device has higher conversion efficiency ($\sim 25\%$).

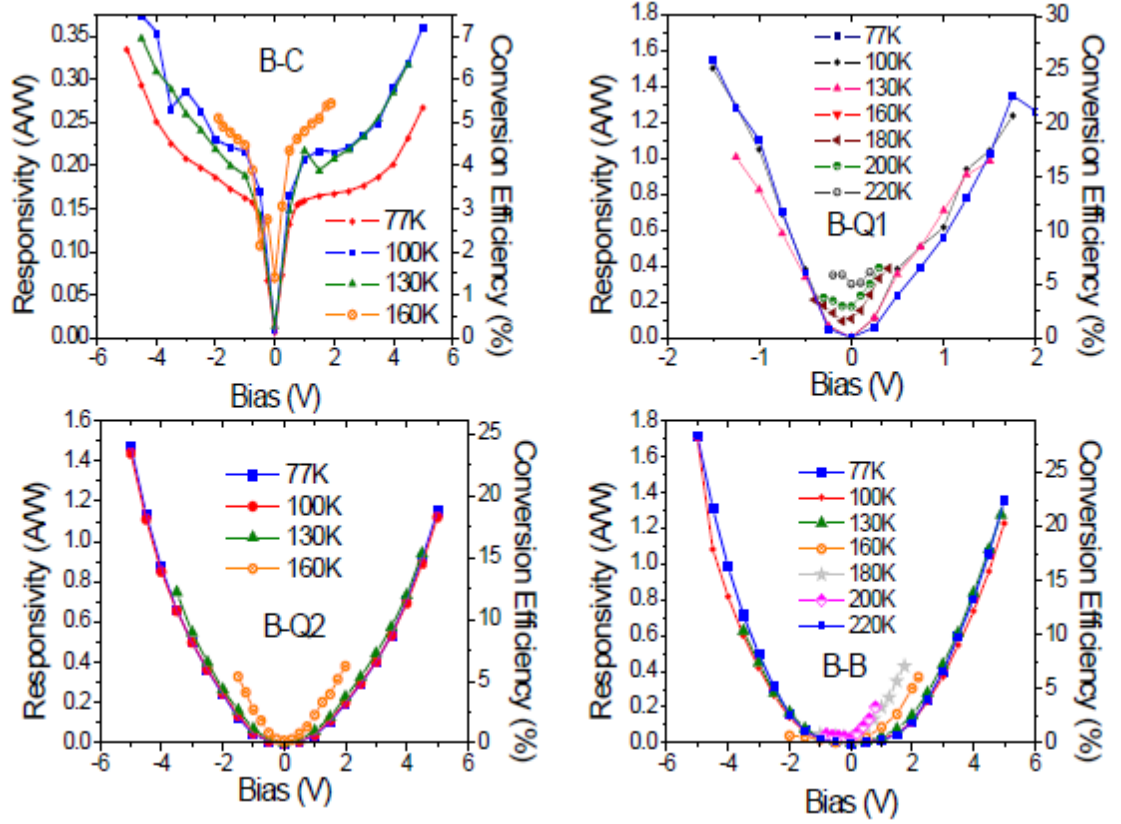


Fig. 5.6: Measured responsivity at higher operating temperatures and corresponding conversion efficiency at the peak wavelengths.

Fig. 5.7 shows the measured peak detectivities of all the four devices as a function of temperature and compares it with QWIP. As can be seen, high values of detectivities can be obtained even at higher temperatures. The slow decrease in detectivities as a function of temperatures, as compared to QWIPs is attributed to the phonon bottleneck which reduces the temperature dependence of the carrier distribution in the quantum dot.

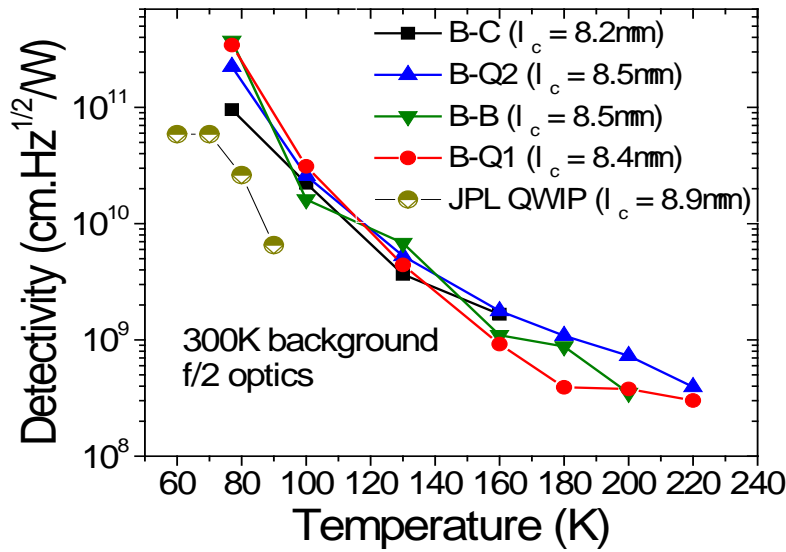


Fig. 5.7: Measured peak detectivities for various samples at higher operating temperatures at $f/2$ optics, showing high detectivity values even at 200K.

It is clear that these devices have excellent response at high operating temperature. To estimate background limited infrared photodetection (BLIP) temperature, two separate techniques were used. In first, a photocurrent, estimated by multiplying conversion efficiency calculated from responsivity, by the number of photons incident from 300K blackbody on the detector, is compared with dark current. In second measurement, noise is compared between 0 field of view and 2π field of view conditions to find the temperature at which noise from 2π FOV is comparable to that of 0 FOV. Both these techniques resulted in BLIP temperature of $\sim 100\text{K}$, which is reasonably high. These measurements are shown in Fig. 5.8 (a) and (b), respectively.

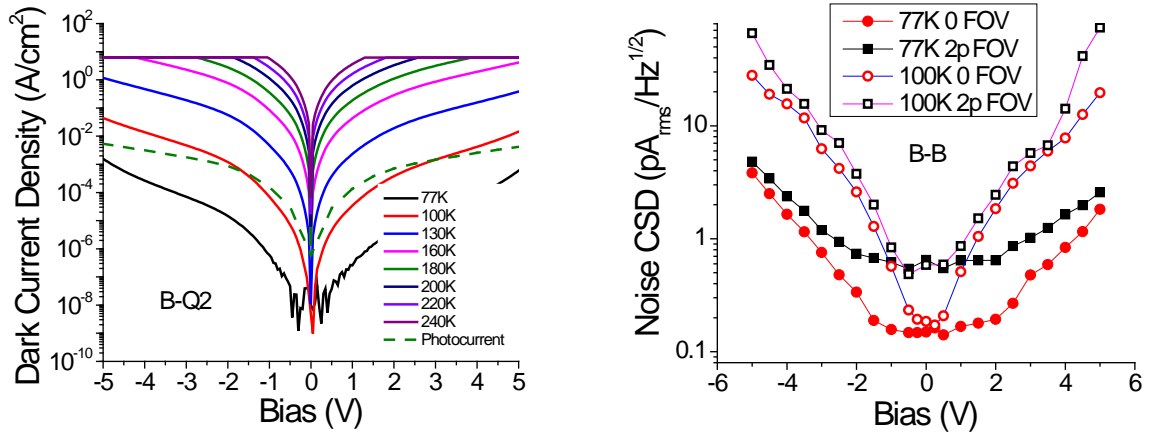


Fig. 5.8: (a) Comparison of the measured dark current density with estimated photocurrent density to estimate the BLIP temperature for B-Q2 device. (b) Comparison of noise current spectral density (CSD) for different field of views at various temperatures, to estimate the BLIP temperature for B-B device.

For demonstration of higher operating temperature for the actual focal plane array, 320×256 pixel FPAs were fabricated from B-C device. The characterization of this FPA shows excellent imaging quality at 80K, with NETD of 44mK, for f/2 optics. The imaging quality degrades rapidly with increase in the operating temperature, as seen in Fig. 5.9. It is apparent that imaging 300K human body is possible even at 95K, which is one of the highest operating temperatures for a LWIR FPA. Measured NETD is 44mK at 80K.

It is to be noted that the right side of the image, which shows substantially higher non uniformity at higher temperature has surface plasma array [124] on the backside. Since this was designed only for a narrow wavelength out of the broad overall response, the image quality (hence NETD) actually is lower for surface plasma enhanced side. However, temporal NETD at the resonance peak is higher than the left side without surface plasma. The surface plasma is used to couple the normally incident light into a

surface wave, which increases the propagation length for photons within the active region. This, combined with higher p-polarization absorption in QDs, lead to an increase in absorption for the resonance wavelength. In this particular device, the resonance wavelength was chosen to be $6.2\text{ }\mu\text{m}$.

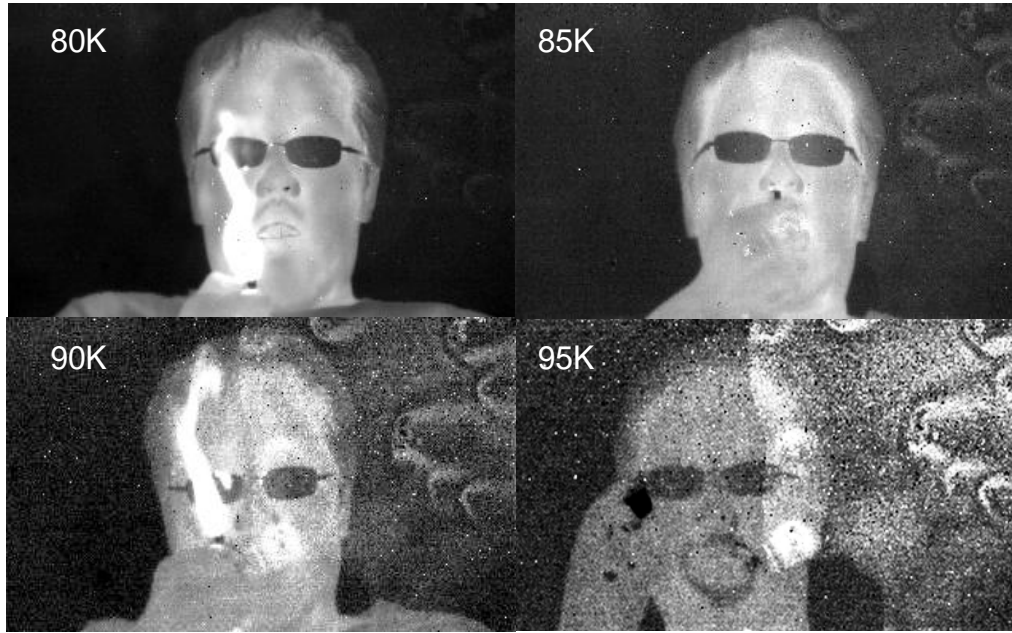


Fig. 5.9: Infrared image taken at 80K, 85K, 90K and 95K using 320×256 FPA fabricated from B-C device

5.2 Confinement Enhanced DWELL Detectors

From the previous section, it is clear that B-Q types of transitions are optimized for the best performance in the intermediate bias range, in order to combine the best of B-C and B-B types of transitions. However, at low bias they still suffer from poor escape probability leading to low responsivity. In this section, we discuss further optimization of B-Q types of transitions by the use confinement enhancing AlGaAs barriers, to increase the absorption coefficient, and the escape probability. Using these structure, the device is

able to function very close to zero bias due to B-C types of transitions (leading to a broad spectral response) while maintaining high wavefunction overlap.

The CE barriers are designed such that the excited energy in the QW is close to the continuum energy level, such that photoexcited electrons can easily escape. A similar concept was first demonstrated for quantum well infrared photodetectors (QWIP), both theoretically [125] and experimentally [23]. DWELL structures, where the quantum dot ground state and the quantum well excited state can be controlled independently, are ideal for designing architectures for B-Q transitions for a given wavelength, without reducing the barrier energy. The use of thin AlGaAs barriers around the DWELL region was previously reported [17] for the reduction in the dark current, but not for B-Q transitions. Ling et al [54] suggested using a thin AlGaAs layer directly after the QD growth to confine the carriers in the lateral direction. However, the AlGaAs layer does not conform to the QD, due to the preferential growth of the AlGaAs layer away from InAs quantum dots. Thus the barrier is presented only in the lateral direction, which does not result in decrease in the dark current. In the present architecture, CE barriers are grown such that they surround the entire DWELL structure, without altering the QD ground state energy. This results in reduced dark current due to the presence of a barrier in the transport direction. Due to the increase in the escape probability, this does not reduce the responsivity, even at low bias operation.

Fig. 5.10 shows the heterostructure schematic of the CE DWELL 1 device and the DWELL control device, which has the same structure without CE barriers. The active region consists of 7 DWELL layers, separated by 50nm $\text{Al}_{0.07}\text{Ga}_{0.93}\text{As}$ barriers. The DWELL region consists of $\text{Al}_{0.2}\text{Ga}_{0.8}\text{As}$ (2nm) – GaAs (1nm) – $\text{In}_{0.15}\text{Ga}_{0.85}\text{As}$ (1nm) –

InAs QD (2.0ML) – $\text{In}_{0.15}\text{Ga}_{0.85}\text{As}$ (4.2nm) – GaAs (1nm) – $\text{Al}_{0.2}\text{Ga}_{0.8}\text{As}$ (2nm) layers for the CE DWELL-1 device. Material composition and thicknesses of each layer were chosen such that the excited energy is close to the continuum energy for optimum B-Q operation. To ensure a conformal coverage of CE barriers around the DWELL region, the following growth scheme was adopted: First the barrier and CE barrier was grown and capped with 1nm GaAs layer at 590 °C, before reducing the temperature to 500 °C to grow the $\text{In}_{0.15}\text{Ga}_{0.85}\text{As}$ QW and 2ML InAs QD doped with Si. After the QW growth, the structure was capped with 1nm GaAs before changing the substrate temperature to 590 °C. This results in evaporation of excess InAs not capped by GaAs, thus forming a truncated pyramid. The substrate temperature was changed during a growth interrupt of 180 seconds. It is to be noted that the designs and growth parameters for these devices are different than those discussed in the previous section, and hence the detectivity values cannot be compared between these structures.

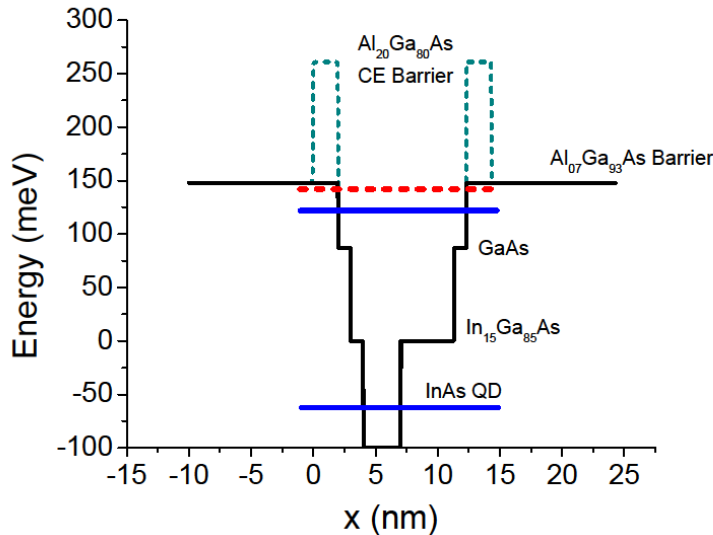


Fig. 5.10: Schematics of CE DWELL 1 and the DWELL control device active region, showing the influence of CE barrier (dashed) on the excited energy level, pushing it towards the continuum energy.

Fig. 5.11 (a) shows the chevron-type RHEED pattern, typical of SK quantum dots. Fig. 5.11 (b) shows spotty RHEED pattern during the InGaAs capping, indicating that the quantum dots are not yet fully covered, which changes to a streak pattern during the GaAs capping layer growth. After this capping layer, during the temperature ramping, the pattern shows sharp lines, thus indicating that the excess Indium has been evaporated. This insures that the CE-barriers are grown over the quantum dots. The conformal coverage of the CE barriers over the quantum dots was also confirmed with transmission electron microscopy (TEM). Fig. 5.12 shows TEM images obtained with CE DWELL 1. Fig. 5.12 (a) shows all the seven stacks with quantum dots. Excellent material quality with no visible defect can be observed. The quantum dot density is almost constant in all the seven layers. Fig. 5.12 (b) shows an expanded view of one of the quantum dots. A flat-top pyramidal quantum dot, with a base width of 16-18 nm and the height of 7 nm, along with a compressively strained $\text{In}_{0.15}\text{Ga}_{0.85}\text{As}$ quantum well is clearly visible. CE-barriers can be seen above and below the quantum well as bright stripes, although the contrast between $\text{Al}_{0.07}\text{Ga}_{0.93}\text{As}$ and $\text{Al}_{0.22}\text{Ga}_{0.78}\text{As}$ layers in this strain field map is low. Strain fields from the quantum dots above and below the quantum dots are visible.

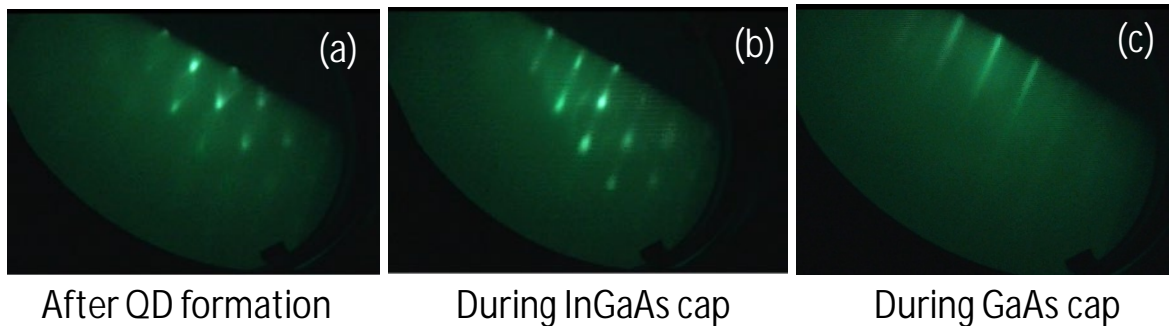


Fig. 5.11: RHEED patterns during the growth of different layers. (a) Chevron pattern after the quantum dot growth, (b) spotty pattern during the capping layer growth indicating partially capped quantum dots (c) streak pattern during the GaAs capping layer growth, indicating that the quantum dots are completely covered and the surface is flat.

The devices were processed into $410 \times 410 \text{ } \mu\text{m}^2$ square detectors for the detector characterization. Fig. 5.13 (a) compares the spectral response obtained from CE DWELL 1 device and the DWELL control device. Some of the dips in spectra are due to atmospheric absorption. The peak near $6.5 \text{ } \mu\text{m}$ is broader in CE DWELL 1 device as compared to the control device. The $10.2 \text{ } \mu\text{m}$ peak present in the control device is completely blocked by the CE barrier, as it is bound deep inside the QW. Fig. 5.13 (b) shows the spectral response obtained from the CE DWELL 1 device at different temperatures, indicating that the ratio of the photocurrent at $6 \text{ } \mu\text{m}$ and $7.5 \text{ } \mu\text{m}$ decreases at higher temperatures. This indicates that the peak at $7.5 \text{ } \mu\text{m}$ probably results from the second excited state of the QD to the excited state in the QW.

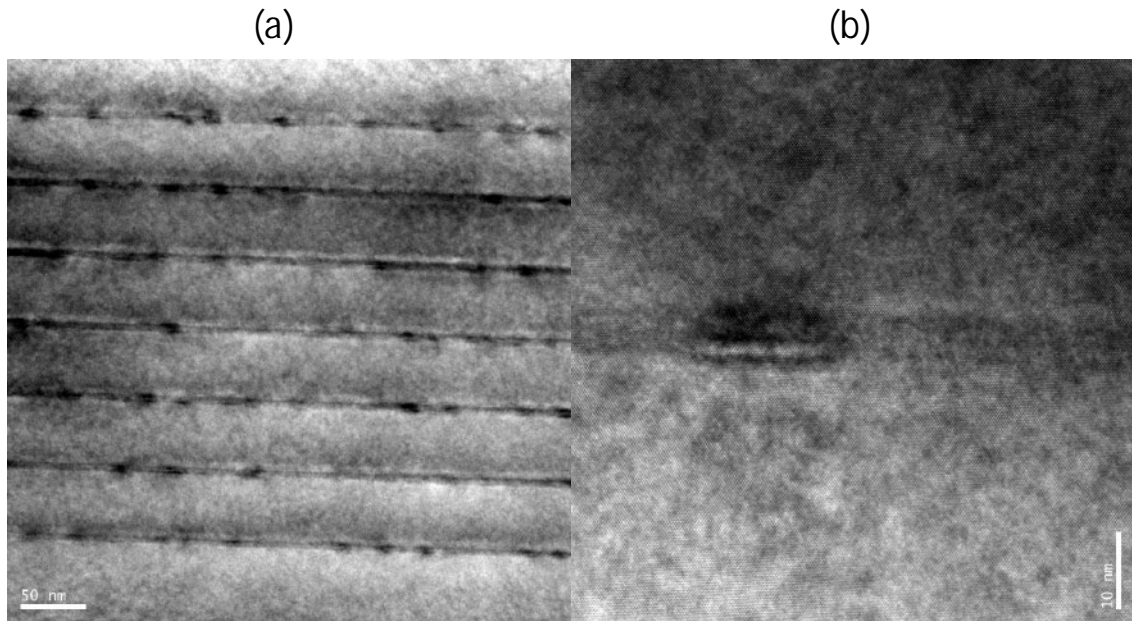


Fig. 5.12: TEM images of CE DWELL 1 (a) All seven stacks showing excellent material quality and dot uniformity (b) Flat top pyramidal quantum dot in a compressively strain InGaAs quantum well. Bright layers above and below the quantum well are attributed to CE barriers.

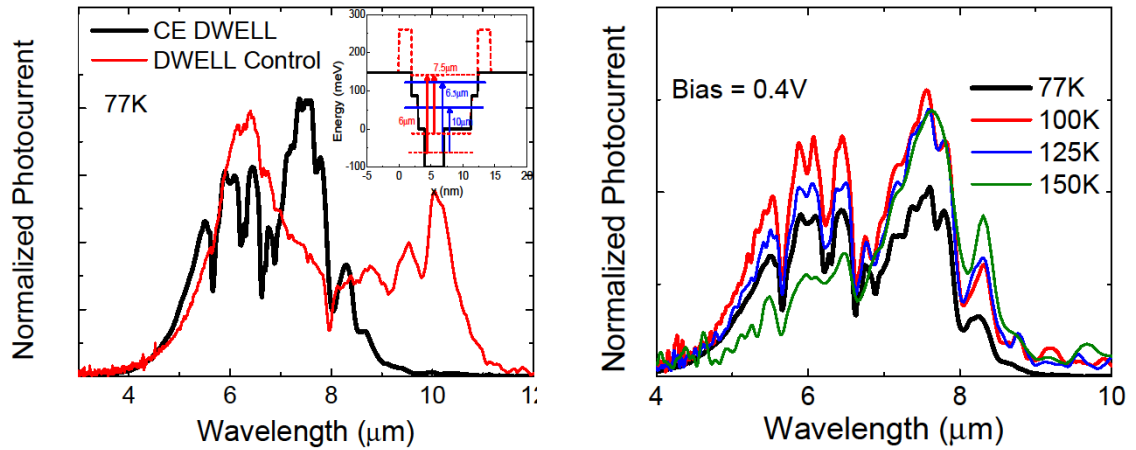


Fig. 5.13 (a) Spectral response comparison between CE DWELL 1 and the DWELL control device at 77K; showing broadening of the peak near 6.2 μm and elimination of the bound to bound type peak at 10.2 μm in CE DWELL 1 as compared to the DWELL control sample. Inset shows the schematics of participating transitions. (b) Spectral response from CE DWELL 1 at various temperatures, showing the ratio of peaks at 7.5 μm and 6.2 μm increases with temperature.

The measured responsivity for the two devices, measured using a calibrated blackbody setup in a liquid nitrogen cooled dewar has been compared in Fig. 5.14 (a). It is to be noted that for low bias, the responsivity is higher in CE DWELL 1 device as compared to the control DWELL device, despite the addition of barriers. This indicates higher absorption efficiency and escape probability for the photoexcited electrons, even near zero bias. The CE barriers also reduce the dark current in the device by close to a factor of 10 at 77K. This increase in the signal and reduction in the dark current results in a factor of 10 improvement in the detectivity for CE DWELL, as compared to the DWELL control device at 77K, as shown in Fig. 5.14 (b). Note that very high values of detectivities are obtained, even at zero bias. The detectivity is underestimated at zero bias due to the system noise in the noise measurement setup.

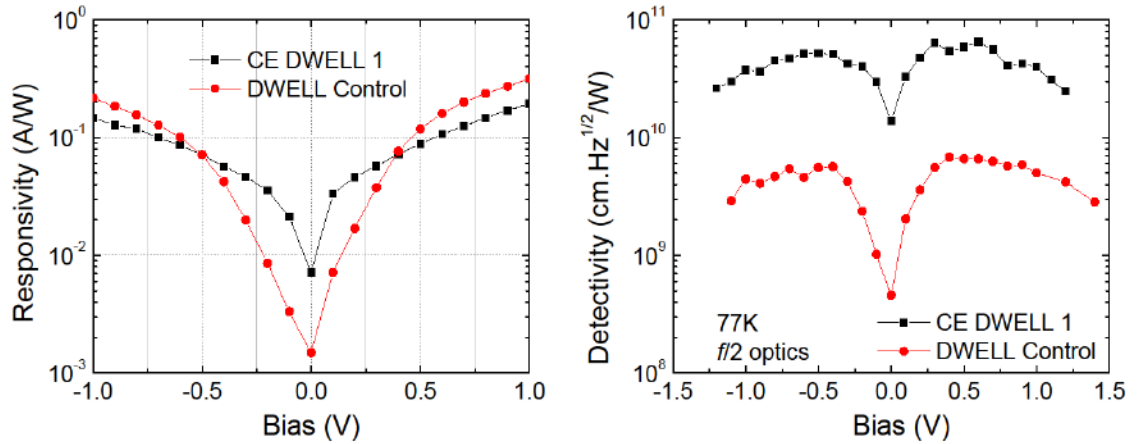


Fig. 5.14 (a) Measured responsivity comparison between CE DWELL 1 and the DWELL control device at 77K, showing a factor of 7 increase in responsivity for CE DWELL 1 at lower bias. (b) Measured detectivity of CE DWELL 1 device showing more than a factor of 10 increase in D^* over the DWELL control device, at 77K, $f/2$ optics.

By changing the quantum well thickness or the quantum dot size, it is possible to change the response wavelength of the CE DWELL detectors. Fig. 5.15 (a) and Fig. 5.15 (b) show the effect of change in QW thickness and QD size, respectively. CE DWELL 2 has 5.1 nm InGaAs QW capping instead of 4.2 nm in CE DWELL 1. This decreases the excited state energy by approximately 10 meV, as seen by the redshift in spectral response wavelength, as compared to CE DWELL 1, as shown in Fig. 5.15 (a). CE DWELL 3 has a same structure as CE DWELL 2 except for the 2.3ML nominal deposition of InAs QD instead of 2.0ML used in the other structures. Formation of larger quantum dots, indicated by a redshift in PL by $\sim 45\text{meV}$ as shown in inset of Fig. 5.15 (b), lowers the quantum dot ground state energy and the excited state energy in the quantum well. This results in bound to bound transitions, with a blueshift in spectral response, as shown in Fig. 5.15 (b). It is to be noted that all the structures with CE barriers completely suppress the B-B type peak at $10.2 \mu\text{m}$, which is present in the control sample.

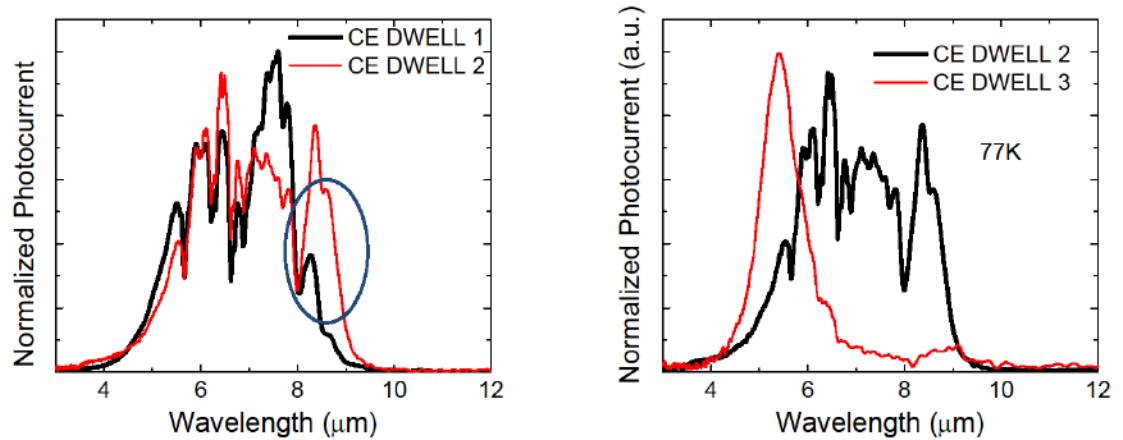


Fig. 5.15 (a) Effect of QW thickness on the spectral response of CE DWELL structure, showing a redshift in the response due to 0.9 nm increase in the QW thickness for CE DWELL 2 device. (b) Effect of QD nominal coverage, showing a blueshift in the spectral response in CE DWELL 3, which has 2.3ML QD, as compared to 2.0ML QDs in CE DWELL 2. B-B nature of transitions is clear from the small spectral width. Inset shows the comparison of PL spectrum for two devices.

Although it is possible to alter the response wavelength by only changing the QW or the QD properties, this does not result in an excited state in QW close to the continuum energy. Thus, these devices fail to completely utilize the potential of confinement enhancing barriers, which results in a lower responsivity in these structures. However, due to the dark current reduction by the CE barriers, the noise is also reduced, which compensates for the reduction in the responsivity. The measured peak detectivity is $2 \times 10^{10} \text{ cm.Hz}^{1/2}/\text{W}$ for CE DWELL 2 device and $1.8 \times 10^{10} \text{ cm.Hz}^{1/2}/\text{W}$ for CE DWELL 3 device, which is still a factor of 3 higher than that of the DWELL control device, but lower than that of CE DWELL 1 device, primarily because of the reduction in the responsivity. The detectivity of all the four devices is compared in Fig. 5.16.

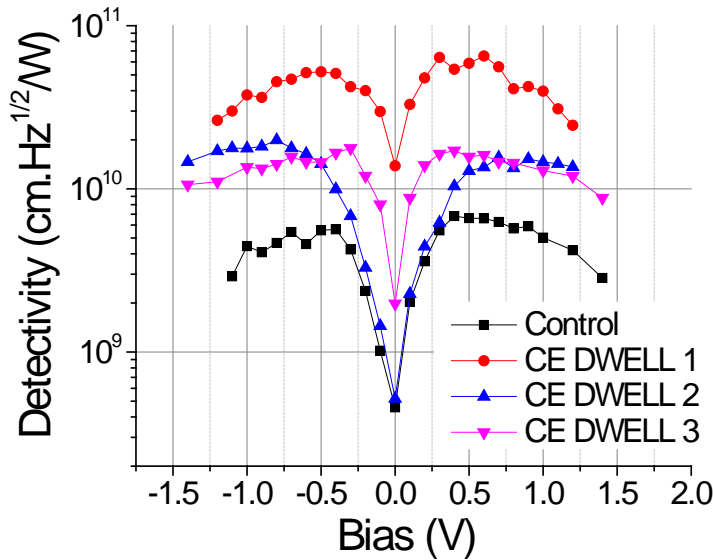


Fig. 5.16 : Comparison of detectivities for all the CE DWELL devices with the control device.

5.3 Effect of Different Barrier Configurations on DWELLs

5.3.1 Motivation

Key requirements for the third generation infrared focal plane arrays are multicolor operation, high operating temperatures and large format arrays. DWELL detectors with AlGaAs barriers provide several excited states in the conduction band, leading to a bias tunable multicolor operation [67, 75, 77]. For high operating temperatures, the most important requirement is low dark current, such that charge wells in readout integrated circuits are not saturated. In traditional DWELL designs, however, there is a tradeoff between the dark current level, responsivity and the peak wavelength. For example, if the AlGaAs barrier energy increases, the dark current level drops exponentially, but the escape probability of the photoexcited, bound electrons also decreases, leading to decrease in the responsivity. Since the energies corresponding to the long wave infrared transitions are bound deep inside, they cannot escape at low bias levels, thus limiting the

maximum detection wavelength. Other effect is increase in the optimal operating bias [17, 63, 67, 126], with the addition of AlGaAs barrier. Since typical ROIC bias levels are limited to low values, these designs are not well suited for FPA imaging.

We have now established that bound to quasibound transitions optimize the detectivity at moderate bias, leading to high operating temperatures [76]. Confinement enhanced DWELL detectors [127] have been demonstrated to increase the responsivity and decrease the noise, simultaneously, for a low bias operation, thus increasing the signal to noise ratio. There are several design parameters in the design of DWELL devices for FPA applications, such as the absolute values of dark current and responsivity, the spectral range, detectivities and the optimum operating bias. In this section, we discuss a series of systematic experiments in order to understand the tradeoffs associated with different barrier configurations for these parameters. We will compare the characteristics of CE DWELL detectors with different traditional barrier compositions and spacing to examine the device design rules for optimizing the signal to noise ratio at lower bias. Four devices are designed and fabricated with different 'proximity barriers', which are barriers adjacent to the DWELL region and 'remote barriers' which are thick barriers separating the two DWELL regions to avoid strain coupling and inter-dot tunneling. Two of these four devices are DWELL Control device and CE DWELL 1 device, which were described earlier in last section. However, for brevity, we will refer to these four devices as A, B, C and D. CE DWELL designs have been shown to optimize the SNR at lower bias amongst the four devices.

5.3.2 Device Designs

Fig. 5.17 (a)-(d) shows the schematics of four devices (A, B, C and D) discussed in this study. In all the devices, InAs quantum dots with a nominal 2 monolayer thickness are embedded in $\text{In}_{0.15}\text{Ga}_{0.85}\text{As}$ quantum well. Quantum dots are doped such that there are approximately 2 electrons per dot. Quantum wells and quantum dots are grown at 500 °C and barrier regions are grown at 590 °C. All the devices have 7 stacks of DWELL, each separated by 50 nm thick barrier regions and sandwiched between n-doped contact regions. In device A, B (previously referred to as DWELL Control) and D (previously referred to as CE DWELL 1), the 50 nm thick barrier separating the DWELL regions, here onwards called 'remote barrier' is $\text{Al}_{0.07}\text{Ga}_{0.93}\text{As}$, while in device C this barrier is composed of $\text{Al}_{0.22}\text{Ga}_{0.78}\text{As}$. In device A, B and D, $\text{In}_{0.15}\text{Ga}_{0.85}\text{As}$ quantum well thickness is 1nm below the quantum dot (strain bed) and 4.3 nm above the quantum dot (strain cap). In device C, the strain cap thickness was lowered to 3.5 nm in order to increase the escape probability of the electrons due to increase in the excited state energy.

Growth temperature changes are facilitated by growing 1 nm GaAs layer after the growth of remote barrier at high temperature and growing 1 nm GaAs after the strain cap at 500 C, to avoid Indium desorption from the quantum well. We define the term 'proximity barrier' as the 2 nm region directly after the growth of 1 nm GaAs layer after the quantum well. Thus, in Device A, the proximity barrier is GaAs, in Device B, the proximity barrier is composed of $\text{Al}_{0.07}\text{Ga}_{0.93}\text{As}$, while in Device C and D it is $\text{Al}_{0.22}\text{Ga}_{0.78}\text{As}$. In device D, the proximity barrier serves as confinement enhancing barrier

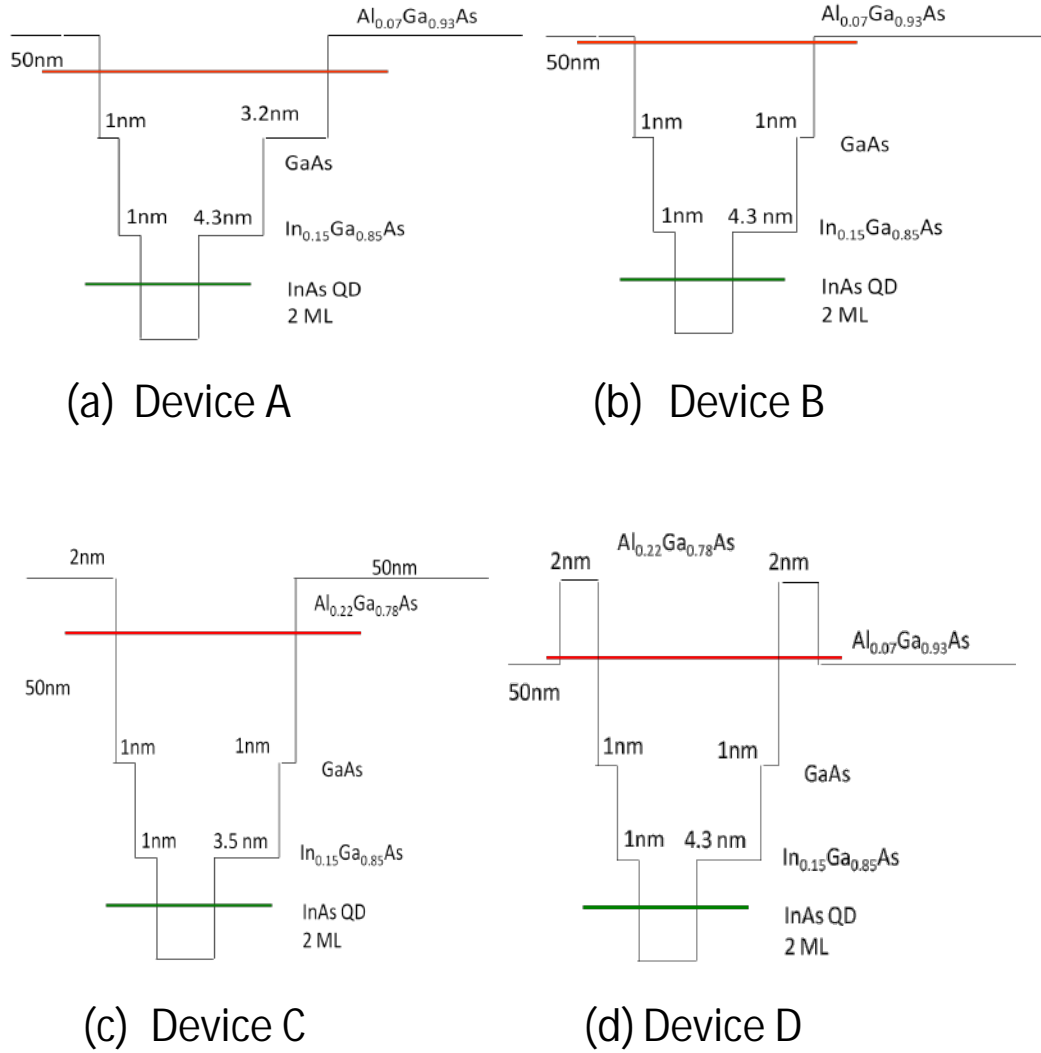


Fig. 5.17: Schematic conduction band diagram of the four devices, showing the thicknesses, composition of various materials used and approximate position of the ground state and excited state energies. The diagrams are not to scale.

After MBE growth, photoluminescence measurement were carried out with He-Ne laser at room temperature. Fig. 5.18 (a) shows the normalized PL from all four devices. The peak of PL was found at 1154 nm (Device A), 1142 nm (Device B), 1076 nm (Device C) and 1118 nm (Device D). Clearly, as the Al concentration in the proximity barrier increase, e.g. GaAs for device A, $\text{Al}_{0.07}\text{Ga}_{0.93}\text{As}$ for device B and $\text{Al}_{0.22}\text{Ga}_{0.78}\text{As}$ in device C and D, the PL wavelength is blue-shifted. This is not only because of the increase in

confinement due to barrier action, but also because Aluminum acts as a mechanical diffusion barrier, reducing the loss of confinement due to In to Ga interdiffusion, resulting in smaller quantum dots. Between device C and D, device C has lower PL peak wavelength due to smaller strain cap thickness, resulting in smaller quantum dots. Interestingly, the PL intensity follows same trend as PL wavelength, as it highest for device A and lowest for device C, as shown in Fig. 5.18 (b). This is due to interfacial defects caused by the presence of Aluminum, and is believed to be growth system dependent.

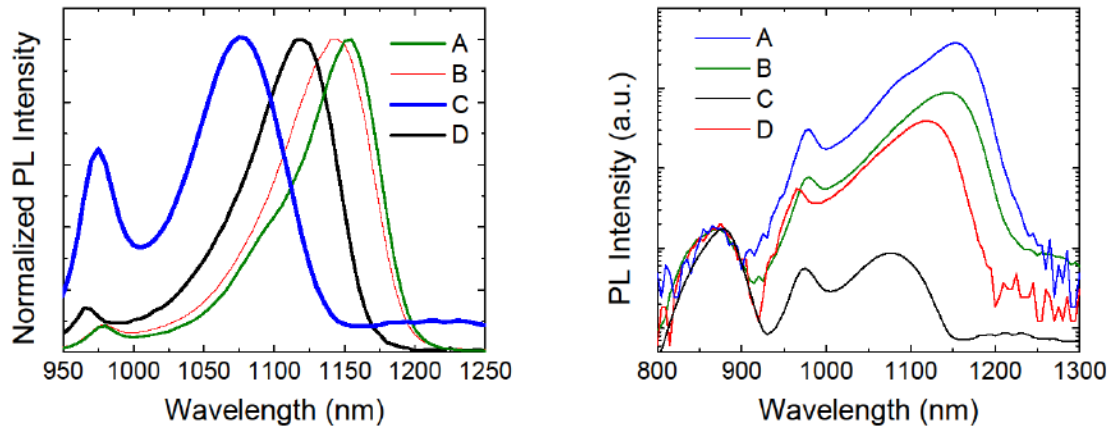


Fig. 5.18: (a) Normalized PL spectra of all four devices measured using He Ne laser at room temperature. Reduction in the peak wavelength is attributed to lowering of interdiffusion due to mechanical barrier action of Al. Device C has lower PL peak wavelength due to lower strain cap thickness above the quantum dot. (b) Un-normalized spectrum to compare the PL intensities.

The material was processed into $410 \times 410 \mu\text{m}^2$ single pixel devices for top illumination. The mesa patterns were etched with inductively coupled plasma etching, followed by a wet chemical etching. Ge/Au/Ni/Au contact metal was deposited and annealed to form ohmic contacts. These detectors were characterized in identical conditions for comparison. Fig. 5.19 shows the spectral response comparison between all four devices.

As it can be seen from the schematics in Fig. 5.17 (b) and (c), with the increase in the barrier energy, the excited level in the quantum well becomes more tightly confined. Due to enhanced confinement, the energy separation between the two states also increases, which results in blue-shifting of the spectral response in device C. Due to larger energy step, long wavelength photoexcited electrons have poor escape probability. This results in blocking of longwave carriers. This explains the spectral differences between device B and C. In device A, due to weaker confinement in the excited state, the broad midwave response, which results from bound to continuum type of transitions dominates the longwave response. LWIR response at $10.5\ \mu\text{m}$ is observable in device A and B, but with addition of $\text{Al}_{0.22}\text{Ga}_{0.78}\text{As}$ in the proximity barrier that peak is absent from device C and D. Device C spectral response is blue shifted with respect to device D due to increase in the energy spacing between the ground state and excited state due to the smaller quantum well.

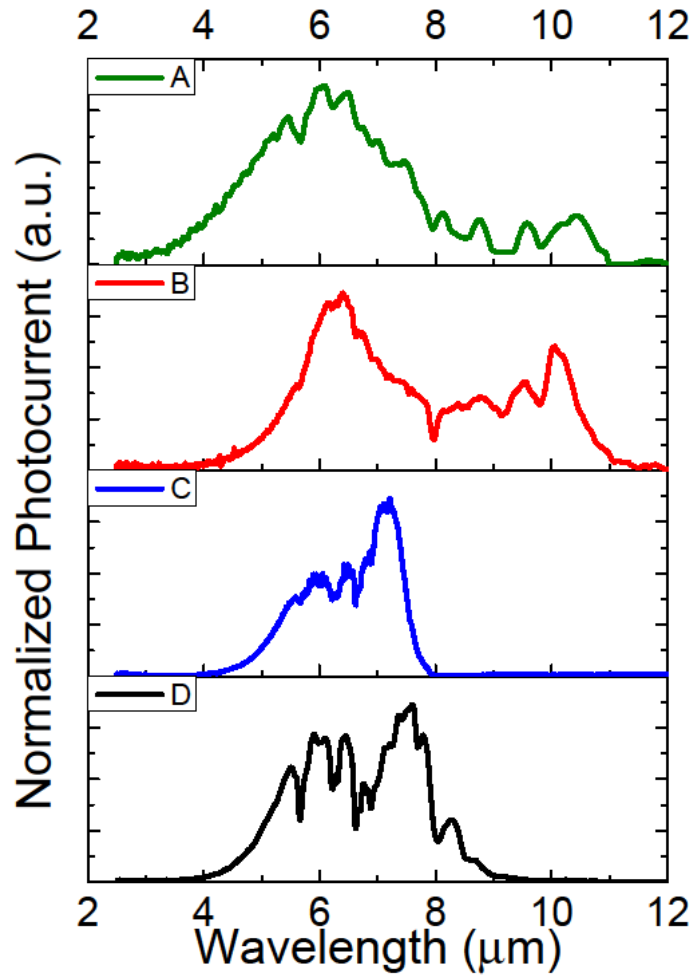


Fig. 5.19: Spectral response from the four devices at 77K. The 10-10.5 μm peak present in device A and B is absent in device C and D due to the presence of $\text{Al}_{0.22}\text{Ga}_{0.78}\text{As}$ barrier, which blocks long wavelength carriers

Radiometric measurements were performed in liquid nitrogen cooled dewar with a calibrated blackbody setup. Fig. 5.20 (a) and (b) shows the responsivity for different proximity barriers (device A, B and D) and different remote barriers (device B and D), respectively, measured at 77K. Comparison between the responsivity of device A and B reveals that the responsivity of device A is lower than device B by close to an order of magnitude. For example, at a bias of 0.5V, the responsivity of device A is 13 mA/W

while that of device B is 110 mA/W. This increase in responsivity, for a same remote barrier and a similar spectral range is attributed to the reduction in confinement due to low energy proximity barrier. This trend continues, at lower biases, between device B and D, which have same remote barrier but different proximity barriers. Due to confinement enhancing action of $\text{Al}_{0.22}\text{Ga}_{0.78}\text{As}$ CE-barriers, the responsivity is higher than device B, at low bias. At higher bias, however, the device D starts saturating before device B, due to closeness of excited level in device D with respect to the remote barrier, as shown in Fig. 5.17. Fig. 5.20 (b) reveals the effect of remote barrier on the responsivity, as both device C and D have same proximity barrier but different remote barriers. Device C has lowest responsivity at a given bias, but the bias range is much higher than other devices. The bias range in these measurements was limited by saturation of the preamplifier used to collect the current output. The lower responsivity, by a few orders of magnitude, in device C is a result of large energetic barrier provided by thick $\text{Al}_{0.22}\text{Ga}_{0.78}\text{As}$ remote barrier. This barrier blocks photocurrent carriers as well as dark current carriers, resulting in low responsivity as well as low dark current, as we shall see later. These comparisons clearly indicate that the increase in the energy of the proximity barrier increases the responsivity, before it starts saturating at higher biases, while increase in the remote barrier drastically reduces the responsivity, and increases the operating bias range.

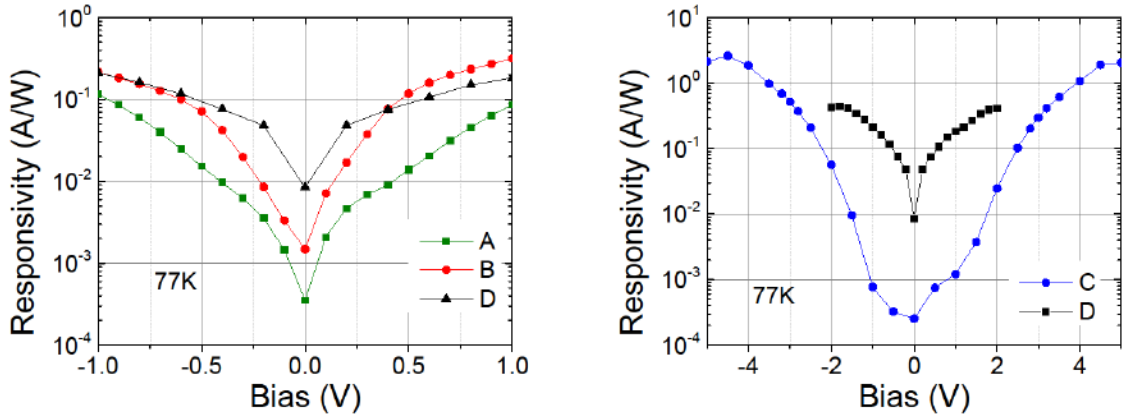


Fig. 5.20: (a) Effect of proximity barrier on the responsivity. Device A, B and D have same remote barrier. It is clear that as the proximity barrier energy increases, the responsivity increases due to better confinement in the excited state leading to a higher wavefunction overlap with the ground state. (b) Effect of remote barrier on the responsivity is much more drastic, with several orders of magnitude reduction in the responsivity due to blocking of both photocarriers and dark current carriers by the large barrier.

Fig. 5.21 compares the dark current densities obtained from all the four devices at 100K. As can be clearly seen, device C has more than five orders of magnitude lower dark current than device D, which has a same proximity barrier but different remote barrier. This reduction is more than the reduction in the responsivity, as seen before, thus the overall signal to noise ratio is maintained high. Comparison between dark current density of device A and B reveals that the effect of increase in the barrier height for the proximity barrier on the dark current levels is negligible. However, device D has more than an order of magnitude lower dark current as compared to device A and B, as the proximity barrier is above the remote barrier, which blocks some of the dark current carriers. Thus, the effect of CE barrier is to increase the responsivity while simultaneously lowering the dark current, thus increasing the overall signal to noise ratio.

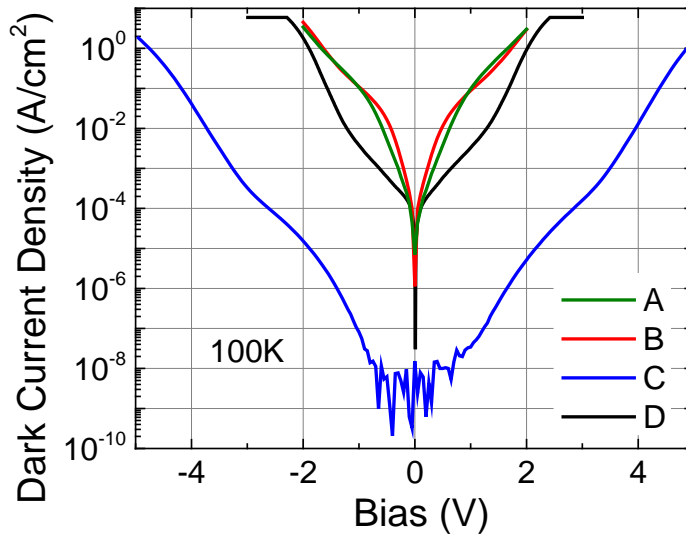


Fig. 5.21: Dark current density comparison between all devices at 100K, showing several orders of magnitude reduction in the dark current for device C due to tall remote barrier. Device D also has more than an order of magnitude lower dark current as compared to device A and B due to the action of CE barriers.

Comparison of the dark current densities and photocurrent densities for all the samples at different temperatures is shown in Fig. 5.22 (a)-(d). The photocurrent density was calculated by multiplying incident number of photons per second on the detector with the conversion efficiency of the detector, calculated from the measured responsivity. Responsivity value at 77K was used, as the change in responsivity with the increase in temperature is small. Comparison reveals that the BLIP condition is satisfied below 80K in device A, 90K for device B, 100K for device C and device D, at the optimum operating bias. The activation energies calculated from this data is plotted in Fig. 5.23. It shows that the activation energy is only weakly dependent on the composition of the proximity barrier, while is a strong function of the remote barrier energy. By changing the remote barrier to $\text{Al}_{0.22}\text{Ga}_{0.78}\text{As}$ from $\text{Al}_{0.07}\text{Ga}_{0.93}\text{As}$, the activation energy is increased by approximately 150 meV (bias dependent), which corresponds to increase in the barrier

height. This is to be expected as the activation energy is approximately the difference between the barrier energy and the Fermi energy. The dependence of activation energy on different barriers can be further highlighted by looking at Fig 4.17 which shows that the activation energy for the RT-Split detector is similar to DDWELL detectors (with $\text{Al}_{0.1}\text{Ga}_{0.9}\text{As}$ barriers) for smaller biases while it becomes comparable to DWELL devices (with GaAs barriers) at higher bias. This is because at higher biases, the band bending due to electric field prevents carrier from seeing the taller $\text{Al}_{0.1}\text{Ga}_{0.9}\text{As}$ barriers, which is as designed.

The most important figure of merit from the detector operation point of view is specific detectivity. Fig. 5.24 compares the detectivity of all the four devices at 77K for $f/2$ optics. It is to be noted that the detectivities are underestimated at low bias in device C (from -2V to 2V) and D (from -0.4V to 4V) due to the system noise limit on the noise measurement. As expected, the detectivity increases from device A to device B, due to increase in responsivity. Device C has much higher detectivity as compared to device B, an order of magnitude increase. However, the peak detectivity is at -3V, which is too large bias for the FPA operation, due to limitations of typical ROICs. Device D, however, combines the best of both the worlds, with high detectivity at a low bias.

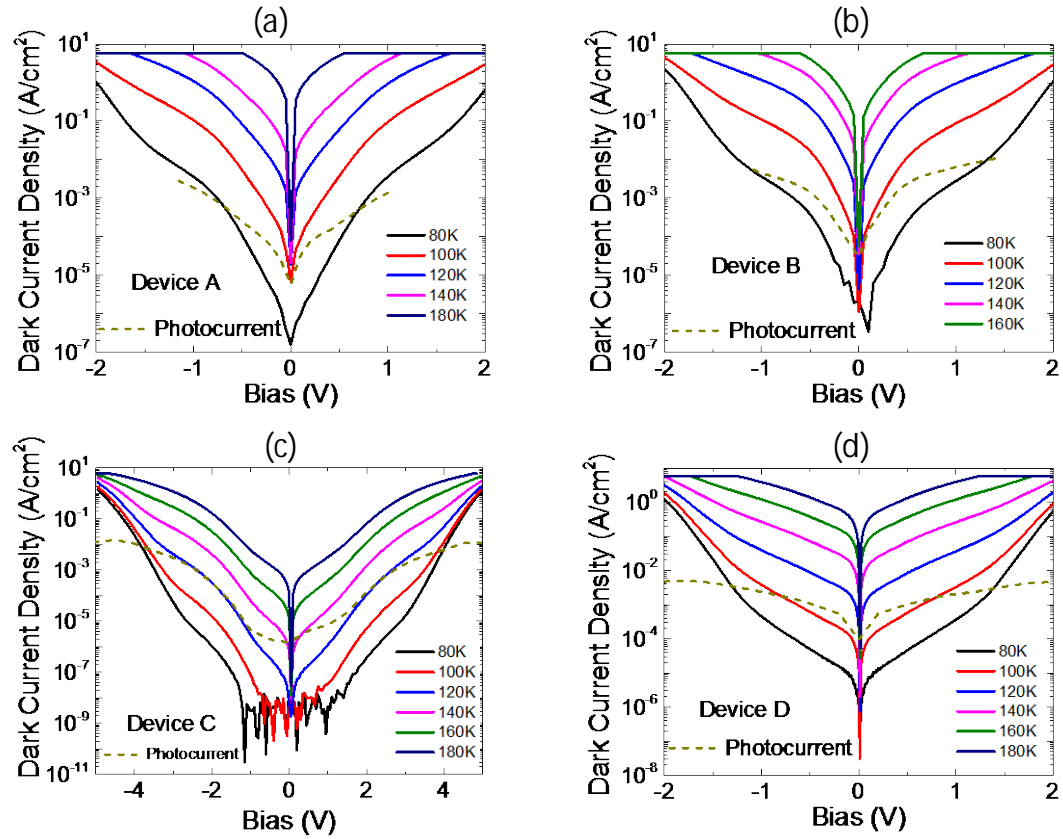


Fig. 5.22: Dark current density and photocurrent comparison for all the devices to estimate the BLIP temperature.

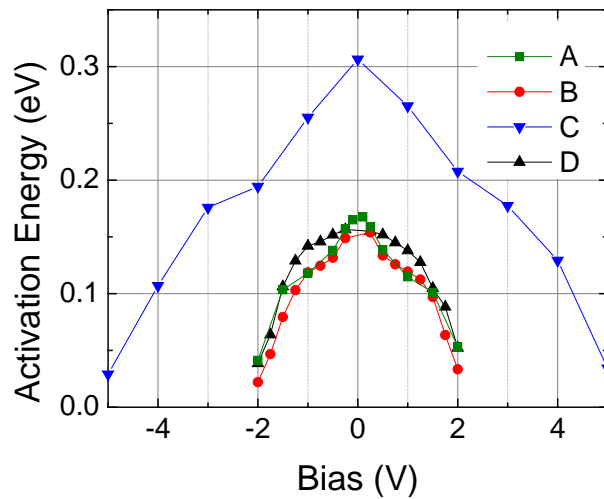


Fig. 5.23: Activation energy for the four devices confirming a small effect of the proximity barrier on the activation energy while large effect of remote barrier on the same.

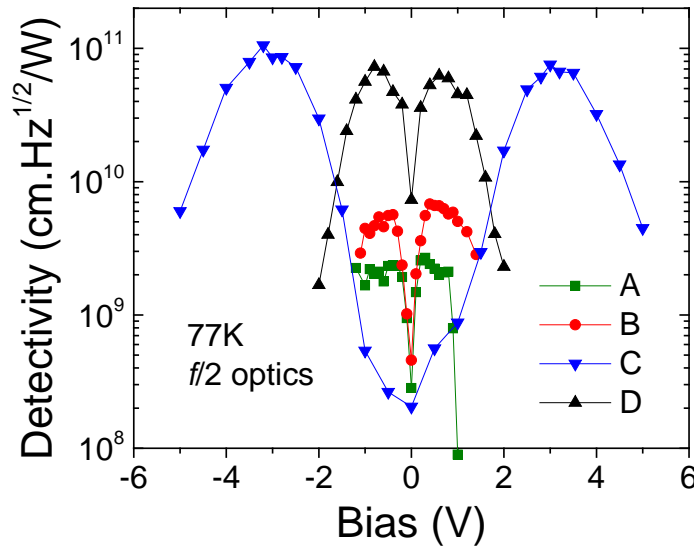


Fig. 5.24: Comparison of detectivities of all the four devices at 77K. This clearly shows that the increase in proximity barrier energy increases the detectivity due to increase in signal and decrease in noise. This does not add to the operating bias for maximum detectivity. Device C, due to presence of large remote barrier has high detectivity due to low dark current, but it needs large bias voltage for optimum performance.

As discussed before, the device C, due to very low dark current densities, is suitable for FPA imaging at high temperature. Fig. 5.25 (a) shows FPA images obtained from device C for several different temperatures for a same scene. It is clear that the infrared imaging is possible at high temperatures, which was observed to be 140K. It is to be noted that the signal strength is very weak, as the images were taken at 0.5V, which is not the optimum bias for this device. This highlights the conclusion that even if the SNR is high for device C, it cannot be used optimally for FPA imaging scenario, as the noise is dominated by system noise (such as ROIC read out noise, non uniformity noise, temperature fluctuations etc). Fig. 5.25 (b, c) shows the images obtained at 60K and 80K at higher biases, showing good material quality. The lines on the image are from the cracks developed during the substrate removal process.

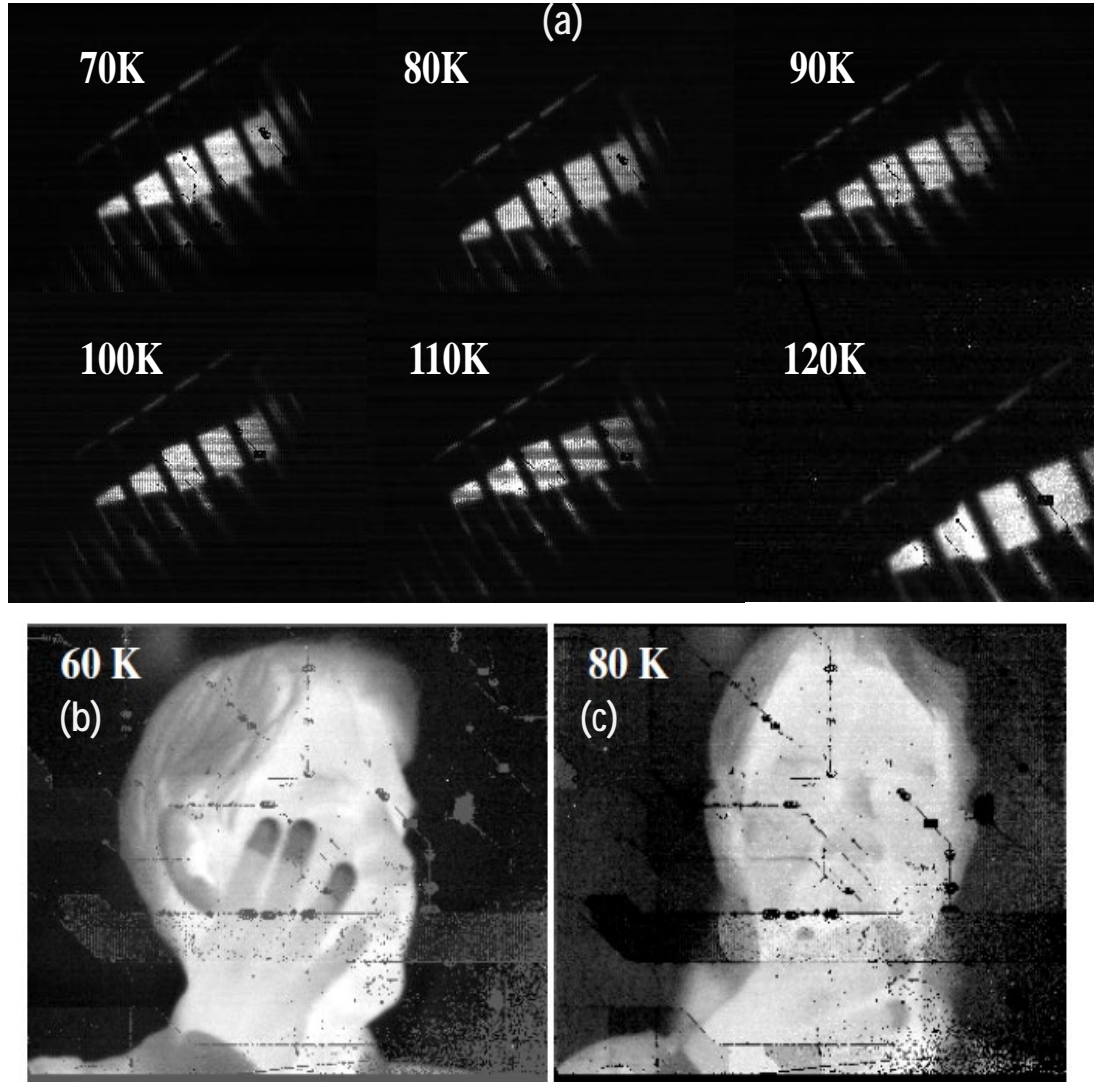


Fig. 5.25: (a) Images for a solder iron on a stand at various temperatures at $V = 0.5V$ (b) Image at 60K for 2.7V of applied bias (c) Image at 80K at 2.3V applied bias. Two point non uniformity correction (NUC) was performed on the images.

In conclusion, effects of proximity barrier and remote barrier on the device performance are very different in nature. As the proximity barrier energy increases, the confinement in the excited state of DWELL region increases, which leads to an increase in the wavefunction overlap with the ground state, thus increasing the responsivity, before it starts saturating at higher bias for large proximity barrier. The growth mechanism assures that the confinement enhancing barriers have been grown conformally over the quantum

dot regions, as confirmed by RHEED and TEM images. Proximity barrier higher than the remote barrier, such as in device D, also leads to reduction in dark current. The activation energy only weakly depends on the proximity barrier. On the contrary, as the remote barrier energy increases, both signal and dark currents are drastically reduced, the peak wavelength is blueshifted, and the activation energy is proportionally increased. This leads to high detectivities, but the optimum operating bias is also increased. Thus, with high detectivity, high responsivity, lower dark current, excellent optical quality of quantum dots and operation at low bias voltage suitable for focal plane array applications, device D, with CE-DWELL configuration optimizes the performance as it combines the advantages of large proximity barrier and small remote barrier.

6 Quantum Dot Quantum Cascade

Detectors

6.1 Introduction

In chapter 4 and 5, we examined different barrier configurations for improving the performance of photoconductive device. The emphasis was on improving the performance at higher operating temperature and lower bias range, suitable for application in focal plane arrays. However, other successful and emerging technologies, such as HgCdTe based detectors, InSb detectors, InAs/GaSb strain layer superlattice detectors etc, typically employ a photovoltaic architecture. The photovoltaic architecture has some intrinsic advantages over photoconductors, such as zero bias operation due to diffusion limited operation, a $\sqrt{2}$ improvement in signal to noise ratio [1] etc. In this chapter, we look at a novel photovoltaic detector based on n-i-n photoconductive architecture based on quantum mechanical tunneling. The quantum cascade detector barrier is arranged such that it generates an energy ladder (or cascade) for electrons to relax back to the ground state. This creates an effect which is similar to applying electric field across the active region. This internal electric field allows for a zero bias operation. The concept of quantum cascade detection is pictorially represented in Fig. 6.1. The key stages are, a reservoir which supplies electrons, in this case it is n-doped QD ground state, a pump to excite electrons to the excited state, for example photons of appropriate energies, and a cascade region to relax the carriers back to the reservoir.

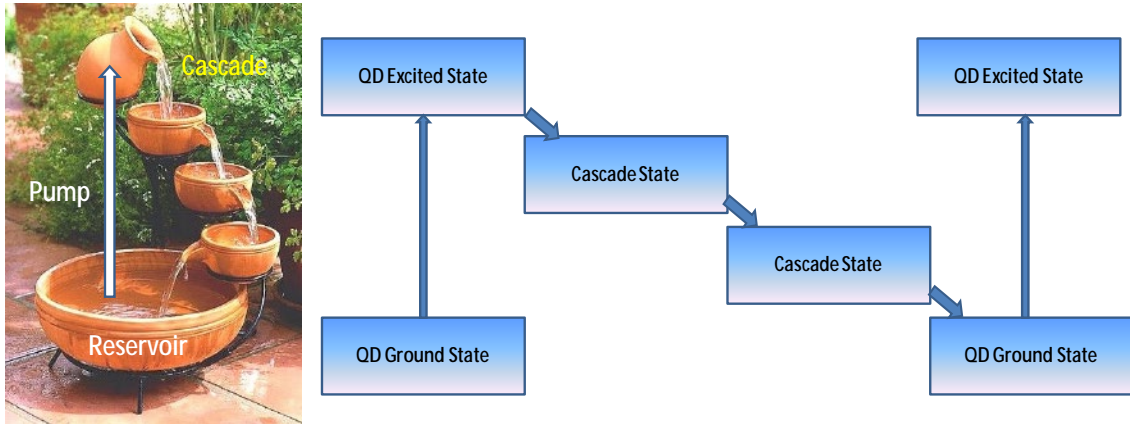


Fig. 6.1: Pictorial representation of a cascade action. Analogy between a reservoir of water and QD conduction band ground state, pump and photon, water cascade and electron cascade is apparent.

Even though excellent imaging performance has been obtained from QDIP and DWELL detectors, intrinsically high photoconductive gain [17, 94], due to small capture probability, increases the noise equivalent temperature difference (NETD) for focal plane arrays in the charge capacity limited regime [26]. In the present design, we use quantum cascade barriers have been inserted between the quantum dot layers to effectively capture the carriers into the quantum dot from a quantum well. The energy separation between the cascade states is designed to be comparable to the longitudinal optical (LO) phonon energy. The internal electric field provided by the quantum cascade in the barrier, results in zero bias operation and a photovoltaic type of response. Reduction in photoconductive gain and zero bias operation are extremely desirable properties for FPAs for high temperature operation and small NETD.

Photovoltaic type of detection with QWIP [128] and QDIP [129, 130] structures has been previously reported, with zero bias operation. Due to small photoconductive gain and zero bias photovoltaic operation, very low NETD values have been achieved for the QW

devices [131, 132]. Quantum well based quantum cascade detectors (QW-QCD) have also been previously demonstrated [133] with excellent characteristics for near infrared [134] (NIR), MWIR [135, 136], LWIR [136], VLWI [137, 138] and THz [139] regime. In a QW-QCD device, the extraction of photoexcited electron through the quantum cascade barrier competes with fast relaxation of the carrier back to the ground state. On the other hand, in quantum dots, the carrier capture time is much longer than that in quantum wells [140, 141], making the transport through quantum cascade potentially more efficient. However, to date, there has been no report of a quantum dot QCD detector.

QW-QCD devices can be designed and simulated very accurately due to purely one dimensional current transport. This one dimensional transport also results in low dark currents. To summarize, the advantages of QW-QCD devices over traditional QWIP photoconductive designs are:

- Zero bias operation
- Very low photoconductive gain (Near unity capture probability)
- No bulk (3D) component of dark current

For QD-QCD devices, the advantages over QW-QCD devices are:

- Phonon bottleneck in QD increases efficiency of extraction of the excited electron.
- Normal incidence operation
- Higher absorption theoretically possible

6.2 Design Considerations

Although it is clear that QD QCD has several important advantages over traditional photoconductive detectors, designing QD QCD devices is much more challenging due to:

1. Band structure of QDs is hard to obtain.
2. Since quantum dot ground state is much deeper with respect to the barrier energy, and since it is highly compressively strained, it cannot be accessed easily. In fact, in order to make the energy separation between the injecting QW and the QD ground state comparable to LO phonon energy, the QW needs to be very thick and compressively strained. This results in a large cumulative compressive strain per stack, preventing a large number of stacks.

For obtaining band structure of QD, a semi-empirical approach is again used. Since we already know the characteristics of CE-DWELL 1 device discussed in last chapter in great detail, including the possible positions of QD energy states with respect to the barrier, the DWELL region of CE DWELL 1 device has been used for the QD-QCD active region. It is assumed that the quantum cascade region will not significantly affect the band structure, for this first iteration.

Solution to point two, about coupling the electron back into the quantum dot can have two solutions. First is to grow high energy QD with InAlAs, instead of InAs. Several devices to optimize the PL intensity and wavelength for InAlAs quantum dots were grown. However, it was found that due to MBE growth chamber conditions, inclusion of Al in QDs would substantially degrade the material quality, thus reducing PL intensity.

Due to mechanical barrier action of Al, it is advised to grow large QDs (e.g. 2.9 ML) , and give a long growth interruption (e.g. 20s) after the growth of QD. Best result obtained with $\text{In}_{0.86}\text{Al}_{0.14}\text{As}$ QD PL is shown in Fig. 2.11 (a) in chapter 2. It is obvious that the PL intensity is much weaker than corresponding $\text{In}_{0.86}\text{Ga}_{0.14}\text{As}$ QDs. Since the PL wavelength is still comparable to InAs QDs, these QDs were not used in this first generation QD-QCD devices. However, in future, especially for going towards LWIR and VLWIR QD-QCDs, InAlAs QDs with higher Al concentrations can be exploited.

To solve the problem of electron injection in QDs, the solution employed here was to couple to the first excited state in the QD, rather than the ground state of the quantum dot. This allows for a design with only two QWs with $\text{In}_{0.15}\text{Ga}_{0.85}\text{As}$ for injection, as the excited state energy in QD is only 5-10meV lower than $\text{In}_{0.15}\text{Ga}_{0.85}\text{As}$ conduction band, estimated from CE-DWELL 1 data. Two designs were made, one with 3 wells in the barrier region for cascade action, and energy separation between the QW to be close to LO phonon energy of 36 meV for GaAs. This energy was chosen for efficient phonon scattering of electrons to make the cascade action efficient. The second design consisted of 4 quantum wells for cascade action, with energies of QW separated by lower than 36 meV, for improved design tolerance, as the scattering time increases rapidly [141] above 36 meV due to multiphonon processes involved. Unfortunately, only the first structure could be successfully grown due to a vacuum related problem with MBE growth chamber. This structure is detailed in chapter 8.

The designed structure consists of 5 stacks of n-doped InAs quantum dots in $\text{In}_{0.15}\text{Ga}_{0.85}\text{As}$ - GaAs - $\text{Al}_{0.2}\text{Ga}_{0.8}\text{As}$ quantum well, forming quantum dots-in-a-well structure, separated by a quantum cascade barrier. The DWELL design utilizes same

structure as confinement enhanced DWELL detectors. Only 5 stacks were grown to keep the strain-thickness product low enough to not cause strain relaxation through defects. Strain relaxation for a DDWELL detector with 2 nm $\text{In}_{0.15}\text{Ga}_{0.85}\text{As}$ quantum wells and 2 ML InAs quantum dots was previously observed after the growth of 50 stacks. The quantum dots have been doped 1-2 electrons per dot. In order to couple the electron from the barrier into the quantum dot efficiently, compressively strained $\text{In}_{0.15}\text{Ga}_{0.85}\text{As}$ - $\text{Al}_{0.2}\text{Ga}_{0.8}\text{As}$ quantum wells have been used. In order to minimize the cumulative compressive strain build-up, first the QW is formed with GaAs - $\text{Al}_{0.2}\text{Ga}_{0.8}\text{As}$, with 2nm thick $\text{Al}_{0.2}\text{Ga}_{0.8}\text{As}$ barriers. The three quantum wells in the quantum cascade region are formed with 10nm GaAs, 4nm $\text{In}_{0.15}\text{Ga}_{0.85}\text{As}$ and 10nm $\text{In}_{0.15}\text{Ga}_{0.85}\text{As}$, respectively, with 2nm thick $\text{Al}_{0.2}\text{Ga}_{0.8}\text{As}$ barriers separating them. Thin GaAs capping layers are grown on top of $\text{Al}_{0.2}\text{Ga}_{0.8}\text{As}$ and $\text{In}_{0.15}\text{Ga}_{0.85}\text{As}$ layers to facilitate the change in growth temperatures and to minimize Indium desorption from the surface. 50nm $\text{Al}_{0.07}\text{Ga}_{0.93}\text{As}$ barriers are grown between the active region and n-doped top and bottom contacts to eliminate the tunneling injection of electrons into the quantum dots from the contacts. All Indium containing layers were grown at 500°C and AlGaAs barriers were grown at 590°C. The energy levels in the three quantum wells are chosen such that their separation equals LO phonon energies in the barrier. Calculated energy levels and their corresponding wavefunctions are shown in Fig. 6.2. These have been calculated using a one-dimensional Schrödinger equation, without considering the perturbation from the quantum dot. The energy levels in the DWELL structure (shown with dashed lines) have been estimated based on photoluminescence and spectral response data from the CE DWELL 1 [127] structure. The ground state energy of final quantum well in the cascade

region is chosen such that it couples the electron into the excited state (E_1) of the quantum dot. In lightly doped quantum dots, these electrons relax back to the ground state E_0 . Higher energy levels E_6 and E_7 are also shown in Fig. 6.2. They do not contribute to the desired electronic transport.

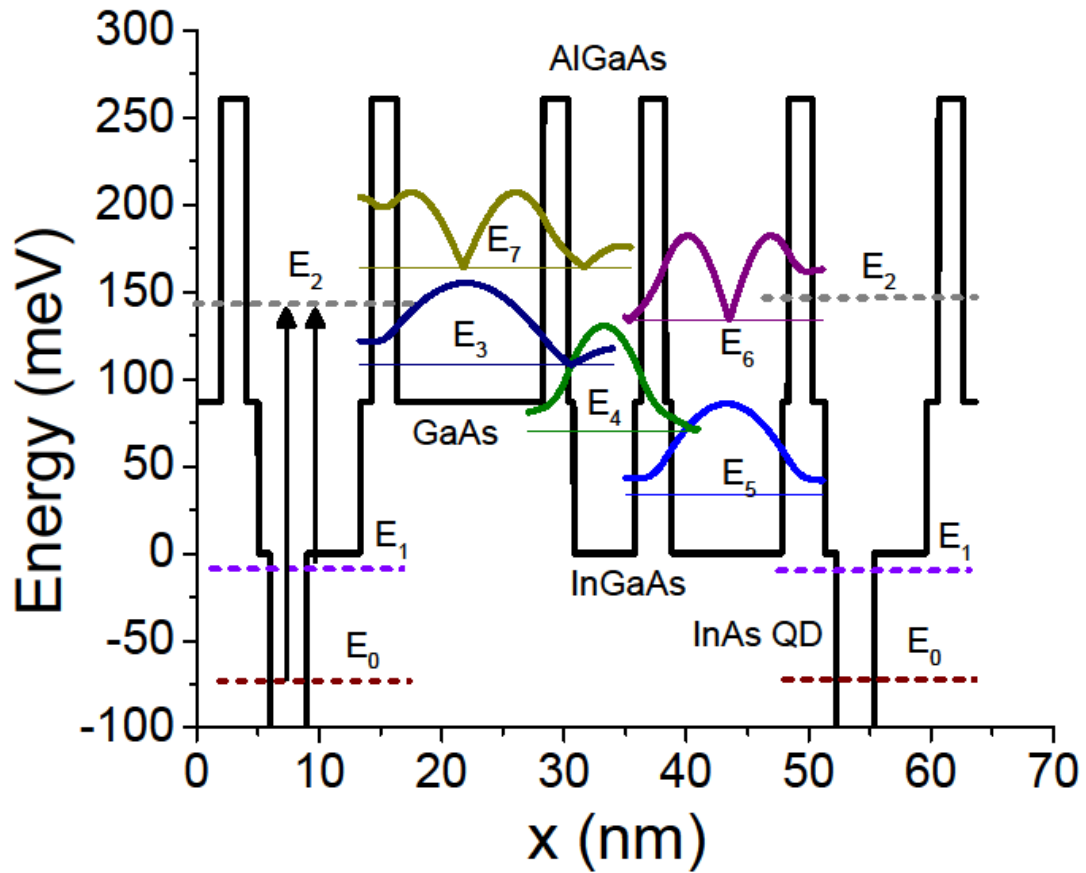


Fig. 6.2: Energy band diagram of single stack of QD-QCD in flatband condition. Calculated energies and wavefunctions of energy levels in cascade barrier are shown. Energy levels in DWELL region ($E_0 - E_2$), shown with dashed lines are estimated based on CE DWELL data.

Spectral response measured from these detectors at 90K at two different bias values is shown in Fig. 6.3. Three distinct peaks are clearly observed. The peak at $\sim 5.5\mu\text{m}$ and $\sim 7.5\mu\text{m}$ are attributed to transitions from E_0 to E_2 and E_1 to E_2 , respectively, based on the

measurements on the parent CE-DWELL structure [127]. It is expected that with increased doping in the quantum dots, and with increased operating temperature, the ratio between peaks at $7.5\ \mu\text{m}$ and $5.5\ \mu\text{m}$ will increase. It is believed that carriers are relaxing to E_0 level, from E_1 level, leading to a stronger response at $5.5\ \mu\text{m}$.

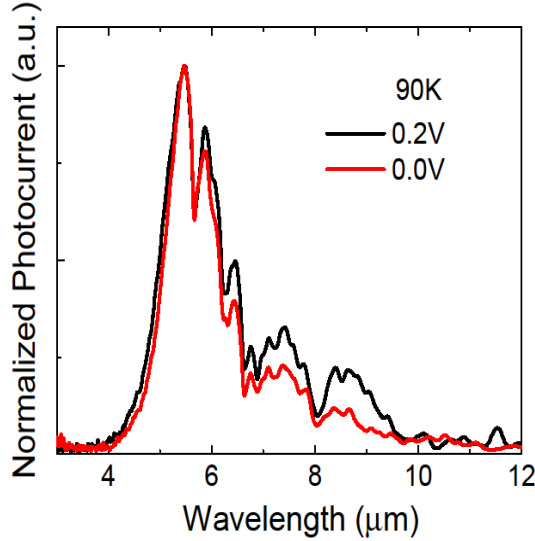


Fig. 6.3: Measured spectral response from the QD-QCD device, showing broad response from $5\ \mu\text{m}$ to $9\ \mu\text{m}$, at 90K, showing a strong zero bias response.

Fig. 6.4 (a) shows the dark current density as a function of bias at various temperatures, compared with the current under illumination with a glowbar source. Strong photovoltaic response, with 2 orders of magnitude increase in the current density at low bias is apparent under the glowbar illumination. Background limited infrared photodetection temperature is close to 80K for 2π field of view. Small photovoltaic shift in the dark current at 30K is attributed to imperfections in the cold shield used for the measurement. At low temperatures, ripples are visible for the dark current at various positive bias steps, showing regions with negative differential resistance. These ripples flatten out at higher temperatures, although they are still observed in the differential conductivity plots. Origin

of these ripples have been previously observed and analyzed [142] for QW-QCDs, and have been attributed to long range resonant tunneling between various levels in the quantum cascade structure. It can also be seen that at higher temperatures, the dark current levels are close to each other, leading to low activation energies of ~ 20 meV. At moderate temperatures, the activation energy close to zero bias is ~ 110 meV, as shown in Fig. 6.4 (b) A detailed transport model is needed in order to understand these effects.

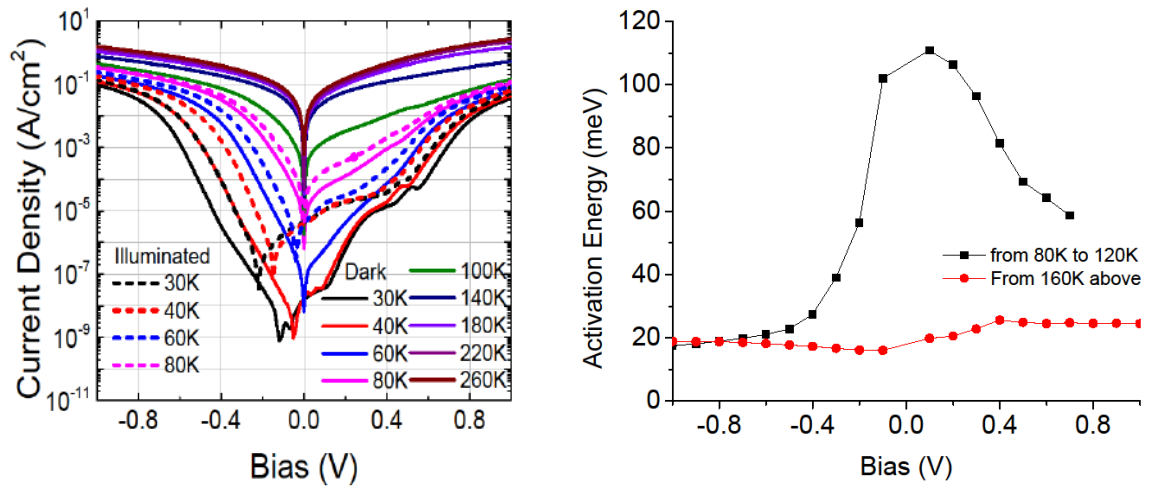


Fig. 6.4: (a) Comparison of current voltage characteristics at various temperatures for dark and glowbar illuminated conditions. (b) Activation energy as calculated from dark current data, shows two distinct regions at high and low temperatures.

Measured responsivity and detectivity values at 77K are plotted in Fig. 6.5 (a) and (b), respectively. At zero bias, the responsivity of 10 mA/W is obtained, with 23 mA/W at 0.5V. Care was taken to substantially reduce the effect of substrate scattering. Ripples near 0.55V at 77K is possibly due to alignment between E_3 and E_6 , which provides a leakage path to carriers. Note that there are similar dips in the differential conductivity, calculated from the I-V curve, around this bias, as shown in the inset of Fig. 6.5 (a). At

zero bias, detectivity of $9 \times 10^9 \text{ cm.Hz}^{1/2}\text{W}^{-1}$ is measured for $f/2$ optics, at 77K. It is to be noted that the measured noise is at system noise level at low biases, thus underestimating detectivities. The values of responsivity and detectivity are comparable or higher than the reported QW-QCDs [135, 136] working at similar wavelengths. As expected, the detectivity decreases monotonically in the negative bias, as the quantum cascade action occurs only in the positive bias. At higher positive bias, the dark current noise is much higher due to several leakage paths provided by excited levels of the quantum wells in the barrier, as well as the field assisted tunneling. This also reduces the photocurrent, as the electrons are not efficiently captured by the next DWELL region.

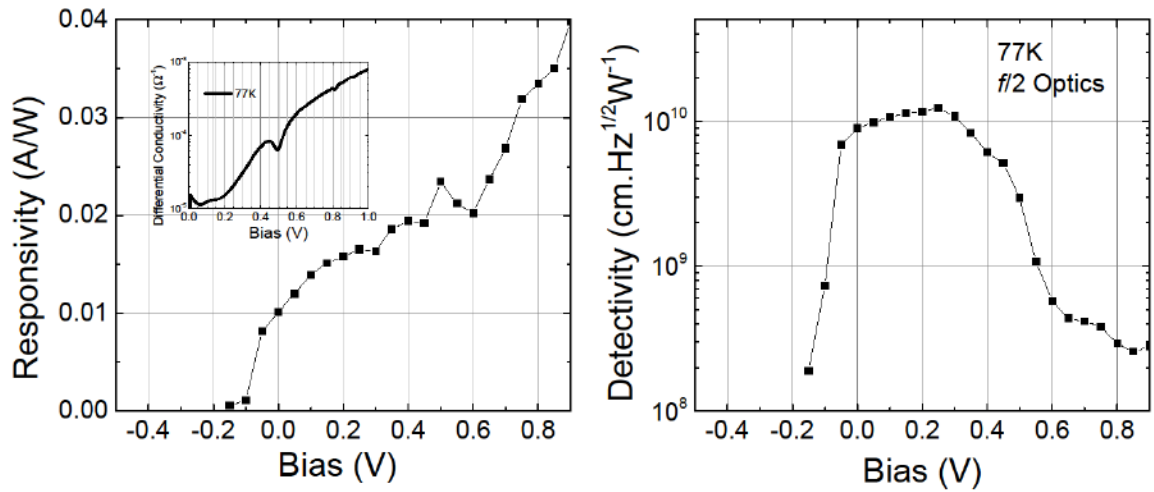


Fig. 6.5: (a): Measured responsivity for the QD QCD at 77K, showing 0V responsivity of 10mA/W. The ripple at 0.45V is possibly from a leakage path in the cascade region. Inset shows the differential conductivity at two different temperatures, showing similar dips. (b) Measured detectivity for $f/2$ optics at 77K, showing no operation in negative bias.

As can be seen in Fig. 6.6, the photoconductive (PC) gain is less than unity at low bias values, while it increases above 0.4V. However, the measured noise at low bias values is system noise limited due to low dark current levels. This results in overestimation of PC

gain. Measured PC gain at 0.25V is 0.38, which indicates efficient electron capture in the quantum dots through the quantum cascade mechanism, as the PC gain for typical QDIPs are much higher than unity [94] due to low capture probability in the quantum dots.

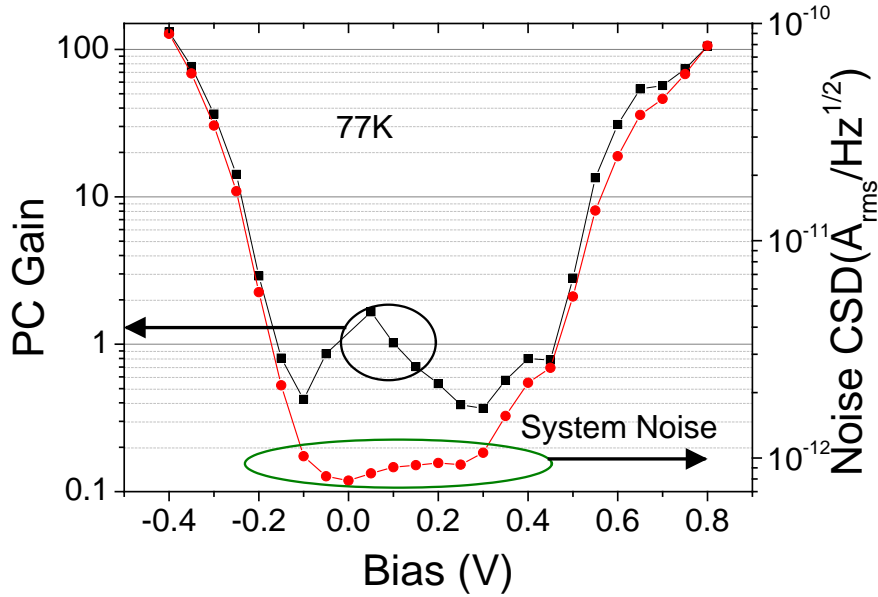


Fig. 6.6: Estimated photoconductive gain and measured noise at 77K. PC gain at low bias is overestimated, due to system noise limited operation.

6.3 Discussions

It is clear from the encouraging results obtained from the first iteration of QD QCD design that this architecture has immense potential from the point of view of high operating temperature imaging. Key points to be noted are

1. Low dark currents at 0V operation
2. Slow increase in dark current as the temperature increases (low activation energy).
3. Strong photovoltaic shift, especially at low temperatures, thus showing photovoltaic operation in majority carrier n-i-n architecture!

4. Low photoconductive gain, lower than unity!

However, it is also clear that there is a lot of scope of improvement over the current design. Since the design was made without a priori knowledge of the bandstructure of the DWELL region, the design is slightly off from expectation. This is because the presence of $\text{In}_{0.15}\text{Ga}_{0.85}\text{As}$ QW below the quantum dot layer affects the strain field of QD, thus changing PL wavelength. Fig. 6.7 (a) shows the comparison between the PL obtained by QD-QCD and CE DWELL 1 device. PL intensity has been normalized, but it is clear that QD-QCD has much higher intensity, looking at the intensity of GaAs peak. It can be seen that the PL peak wavelength (hence the QD ground state energy) is red-shifted. This resulted in blue-shifted spectral response as compared to CE DWELL 1 device, as shown in Fig. 6.7 (b)

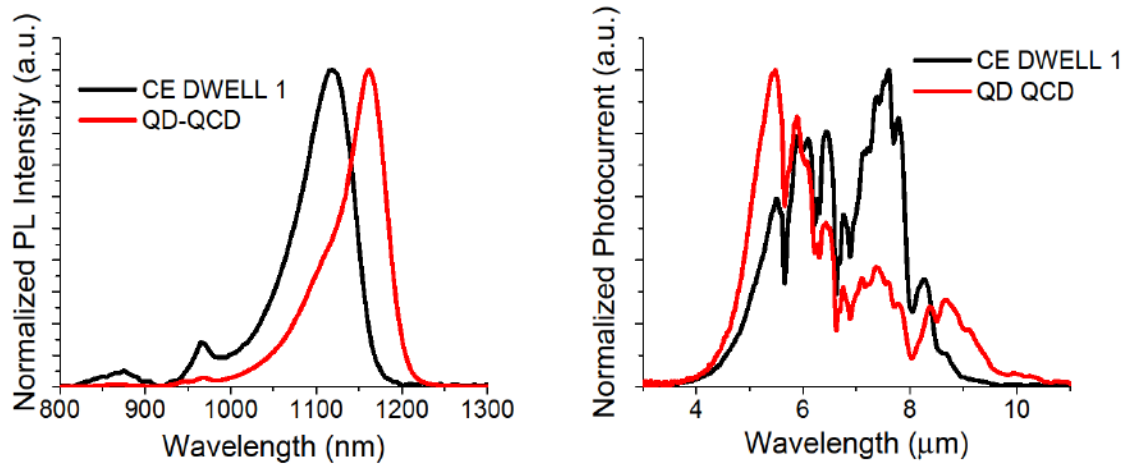


Fig. 6.7: (a) Comparison of normalized PL intensity between CE DWELL 1 and QD QCD device, showing the effect of QCD strain profile on the growth of the quantum dot. (b) Comparison between spectral response from two devices, showing slight blue shift in the spectral response and a dominant midwave peak in QD QCD.

Another point to be noted is even though the quantum cascade action takes place between the excited state in the DWELL structure and excited state in QD, the peak at 5.5 μm is

more prominent. Since this peak results from QD ground state to excited state, it is clear that the electrons are relaxing back to QD ground state, before being excited by photons. To avoid this, the doping inside the QD can be increased to populate the state E_1 . Although this would increase the dark current, it would also increase the responsivity. Thirdly, the $\text{Al}_{0.2}\text{Ga}_{0.8}\text{As}$ barriers used in CE and quantum cascade regions are only 2 nm thick. This allows for leakage of carriers and efficient long range resonant tunneling providing further leakage paths. The coupling between the quantum wells has not been optimized. By increasing the thickness or energy of barrier layers, it is possible to reduce the dark current further, which would compensate from the dark current increase from increased doping in QD, resulting in net increase in SNR.

In conclusion, a strong photovoltaic response with zero bias operation with a quantum dot - quantum cascade detector has been demonstrated. This is a first demonstration of QD based quantum cascade detector. One dimensional transport in QC barrier reduces the dark current densities, which, coupled with a zero bias response and low photoconductive gain, are attractive for high operating temperature operation of FPA. Dark current density of $6.5 \times 10^{-7} \text{ A.cm}^{-2}$, at 80K and at zero bias, has been observed. The responsivity and detectivity values for the detector are 10 mA/W and $9 \times 10^9 \text{ cm.Hz}^{1/2}\text{W}^{-1}$ at 77K for zero bias operation, which are comparable or higher than QW-QCD devices [135, 136] working at similar wavelengths. Several improvements over this unoptimized structure are possible, such as, the use of thicker barriers to minimize the leakage paths and thermionic emission at higher temperatures, optimized doping in quantum dots, increasing the number of stacks by additional strain compensating layers as barriers.

7 Transport in Quantum Intersubband Photodetectors

7.1 Introduction

In this chapter, macroscopic transport in the active region of quantum intersubband photoconductive detectors will be discussed with theoretical modeling as well as experimental insights. Although the models have been developed for one dimensional intersubband detectors without considering any particular active region element such as a quantum dot or a well, the conclusions drawn from theory and experiments are applicable to a broader class of quantum intersubband detectors.

In particular, the drift-diffusion formulation has been used to model the transport inside the active region, by solving the nonlinear Poisson equation coupled with electron and hole current continuity equation. Specialized Scharfetter-Gummel discretization scheme has been used for the solution of continuity equations. Although the technique can be extended for 2D or 3D transport, due to a linear geometry of these devices, simple one dimensional solution is adequate. This is a very powerful technique, originally developed for modeling the transport inside transistors, that gives the following variables as a function of bias and/or depth as an output:

Inputs	Outputs
<ul style="list-style-type: none"> Material profile (with material parameters) Doping Profile 	<ul style="list-style-type: none"> Non-equilibrium carrier densities Electric field Conduction and valence band diagrams Current-voltage profile Capacitance-voltage profile.

Table 7.1: List of input and output variables for the drift diffusion model

For the development of this model, first a simple model for homogenous medium at equilibrium was developed, which was later extended to homogeneous non-equilibrium, heterogeneous equilibrium and finally heterogeneous non-equilibrium media. Details of the model will be presented in section 7.3. The model, in its current form can accept arbitrary heterostructure profiles with arbitrary shallow doping profile. This model has been used to simulate quantum well based n-i-n photoconductive detectors.

In this work, we use asymmetrically placed spacer layers, with the same composition as barrier regions to experimentally study the behavior of DWELL detectors. Simple coupled Poisson equation with drift diffusion model [143] solution has been presented to qualitatively understand the effect of the non-uniform electric field due to the space charge region formed near the contact regions. By studying the dark current, photocurrent and activation energy as a function of bias with and without the spacer layer, we have been able to verify the presence of large field drop across the PN junctions formed near the top and bottom contacts.

7.2 Motivation

This work highlights the importance of considering the background doping in epitaxially grown semiconductor layers for modeling the transport. The formation of the space charge region due to the non-zero non-intentional doping is often neglected even in highly sophisticated transport models. Several models have been developed to shed insight into various operating parameters of these detectors, such as the dark current, photocurrent, carrier capture and emission etc. A popular assumption used in early models [144] and designs for QWIPs is a uniform electric field. Although these models predict the dark current behavior at low bias, they underestimate the dark current at higher electric fields and higher temperatures. Emission-capture models also fail to explain the variation of activation energies with change in the number of stacks in the system, as observed experimentally [145]. For example, in Asano et al [145], it is observed that the activation energy increases rapidly as the number of stacks for DWELL regions are reduced. This cannot be explained with simple emission capture models. Several models that do not assume uniform electric field also do not consider the effect of background doping in non-intentionally doped (nid) barrier regions. However, the barrier regions, typically composed of GaAs or AlGaAs, have significant non-intentional doping, which tends to be p-type. In molecular beam epitaxially grown GaAs layers, typical acceptor concentration is $\sim 10^{14} \text{ cm}^{-3}$, while for AlGaAs layers, it tends to be higher [146, 147]. This results in formation of n^+p^- junctions near both top and bottom contact metals, leading to a formation of a significant spacer charge regions near both the contacts. This effect is more prominent in lightly doped quantum wells and quantum dots, due to the

higher band bending. Although the band bending has been predicted for undoped quantum dots [145], no systematic study has been done to verify its existence.

These high electric field regions have serious implications for the understanding and modeling of these devices. Although, some models discuss the effect of this space charge region [145, 148][90, 149] most of them focus on the space charge region formed within the quantum well, which is, in fact, much smaller in comparison. There has been no experimental study to verify the effect of this space charge region on the device characteristics. This study is important because understanding the charge density distribution and the electric field distribution across the active region is important for developing novel devices. For example, electric field modeling in non-homogeneous materials at higher bias is important for designing avalanche detectors [150] , or barrier designs in band to band devices such as PbIbN structures for strained layer superlattices [151] (to minimize the field drop across a small bandgap active region) etc. Carrier density profiles are important for predicting and tuning the capacitance voltage (C-V) characteristics of a heterostructure, which would also play an important role in bias tunable surface plasmonic devices.

It is to be noted that for transport simulations with commercial TCAD solvers, thanks to the advances in modeling for designing MOSFETs and other transistor structures, are quite mature and readily available. However, using TCAD solvers as a 'black box' for modeling the devices prevents detailed understanding of the transport phenomenon and the intricacies involved. Commercial TCAD simulators also tend to be slower and more tedious to use than personalized codes, such as the MATLAB codes developed in this work. This is because these simulators generally require 2D simulations with specific

finite element grids. The advantage of these simulators is, however, the level of physical phenomena that can be incorporated in the simulations, such as detailed mobility models, thermodynamic effects, etc. However, for the purpose of this work, all these details are not needed and the simple model with limited number of features proved to be sufficient. Number of possible addendums to the model will be suggested at the end of next section.

7.3 Drift Diffusion Model

7.3.1 Theoretical Background

Drift diffusion model is an approximation of Boltzmann transport equation, which is quite accurate for describing some of the important transport properties in semiconductors. The model consists of coupled differential equations with Poisson equation and two current continuity equations, which can be described completely using three variables. The three variables of choice can be $(\phi, n$ and $p)$ where ϕ is the electrostatic potential, n is the electron density and p is the hole density. Alternately, other forms of equations can involve quasi-Fermi energy levels F_n and F_p or Slotboom variables, which are exponentials of quasi-Fermi levels, as we shall see later.

For homojunctions under non-equilibrium conditions, these equations are [104]

$$\frac{dn}{dt} = \frac{1}{q} \nabla \cdot J_n + G_n - R_n \quad (7.1)$$

$$\frac{dp}{dt} = -\frac{1}{q} \nabla \cdot J_p + G_p - R_p \quad (7.2)$$

$$\nabla \cdot \epsilon \nabla \phi = -q(p - n + N_D^+ - N_A^-) \quad (7.3)$$

where, J_p and J_n are the hole and electron current densities, given by sum of drift and diffusion components, as follows:

$$J_n = qn(x)\mu_n E(x) + qD_n \left(\frac{dn}{dx} \right) \quad (7.4)$$

$$J_p = qp(x)\mu_p E(x) - qD_p \left(\frac{dp}{dx} \right) \quad (7.5)$$

μ_n and μ_p are electron and hole mobilities, respectively, D_n and D_p are the diffusion constants for electrons and holes in the given material, related to the temperature and mobility through Einstein's relationships. G_n and R_n are the generation and recombination rates per unit volume for the material. N_D^+ and N_A^- are the ionized donor and acceptor densities, respectively.

Here, carrier densities are a function of potential, as

$$n = n_i \exp\left(-\frac{F_n - E_i}{kT}\right)$$

$$p = n_i \exp\left(-\frac{E_i - F_p}{kT}\right) \quad (7.5)$$

where

$$E_i = -q\phi + E_r \quad (7.6)$$

$$F_n = -q\phi_n + E_r \quad (7.7)$$

$$F_p = -q\phi_p + E_r \quad (7.8)$$

Thus, expressions for n and p become,

$$n = n_i \exp\left(-\frac{q(\phi_n - \phi)}{kT}\right) \quad (7.9)$$

$$p = n_i \exp\left(-\frac{q(\phi - \phi_p)}{kT}\right) \quad (7.10)$$

In terms of Slotboom variables Ψ_n and Ψ_p , which are used to write the Poisson equation in linear fashion,

$$n = \Psi_n \exp\left(\frac{q\phi}{kT}\right) \quad (7.11)$$

$$p = \Psi_p \exp\left(-\frac{q\phi}{kT}\right) \quad (7.12)$$

where Slotboom variables are defined as

$$\Psi_n = n_i \exp\left(-\frac{q\phi_n}{kT}\right) \quad (7.13)$$

$$\Psi_p = n_i \exp\left(\frac{q\phi_p}{kT}\right) \quad (7.14)$$

Equations (7.1) to (7.14) are true for homojunctions under equilibrium. For heterojunctions, the band-lineup needs to be expressed, with respect to a reference energy, using electron affinities (χ). Even though this is not valid for strained materials, the electron affinities can be 'tweaked' to use known band lineup. These material parameters can be concisely expressed [143] in terms of two potential parameters V_n and V_p in order to express the modified Poisson equation and band gap narrowing effects (not considered here) in an equation similar to that for homojunctions. Following equations have been taken from reference [143].

Poisson equation:

$$\frac{d}{dx} \left(\epsilon(x) \frac{dV}{dx} \right) = -q \left[n_i \exp\left(-\frac{q(\phi - V_p - \phi_p)}{kT}\right) - n_i \exp\left(+\frac{q(\phi + V_n - \phi_n)}{kT}\right) + N_D^+ - N_A^- \right] \quad (7.15)$$

Current equations are

$$J_n = -qn(x)\mu_n\nabla(\phi + V_n) + qD_n\left(\frac{dn}{dx}\right) \quad (7.16)$$

$$J_p = -qp(x)\mu_p\nabla(\phi - V_p) - qD_p\left(\frac{dp}{dx}\right) \quad (7.17)$$

Material parameters are defined as,

$$qV_n = \chi(x) - \chi_r + kT\log\left[\frac{N_C(x)}{N_{C_r}}\right] + kT\log\left[\frac{\mathcal{F}_1(\eta_c)}{e^{\eta_c}}\right] \quad (7.18)$$

$$qV_p = -(\chi(x) - \chi_r) - (E_G(x) - E_{G_r}) + kT\log\left[\frac{N_V(x)}{N_{V_r}}\right] + kT\log\left[\frac{\mathcal{F}_1(\eta_v)}{e^{\eta_v}}\right] \quad (7.19)$$

$$\text{where } \eta_c = \frac{(F_n - E_c)}{kT} \text{ and } \eta_v = \frac{(E_v - F_p)}{kT} \quad (7.20)$$

Last terms in equation (7.18) and (7.19) are only for the case of Fermi-Dirac distribution and reduce to zero for using Boltzmann approximation. $\mathcal{F}_{\frac{1}{2}}(x)$ is the half order Fermi-Dirac integral. The algorithm for the solution of nonlinear transport equations for heterojunction under non-equilibrium conditions for the case of Boltzmann approximation is as follows. In the case of Fermi Dirac distribution, the only change is that parameters V_n and V_p are needed to be approximated at every iteration, as they depend on the carrier densities.

7.3.2 Algorithm:

1. Initialize the material parameters, structural parameters, simulation grid etc.
2. Calculate the potential and the material parameters V_n and V_p for the initial guess. For Boltzmann approximation, parameters V_n and V_p do not need to be 'guessed'.

Approximation for the potential is typically chosen as a charge neutrality approximation, calculated from dopant densities ($D = N_D^+ - N_A^-$) as

$$\phi = \frac{V_p - V_n}{2} + \text{sgn}(D) \frac{kT}{q} \cdot \log \left[\left| \frac{D}{2} \right| \exp \left(-\frac{q(V_p - V_n)}{2kT} \right) + \sqrt{\frac{1}{4} D^2 \exp \left(\frac{q(V_p - V_n)}{2kT} \right) + 1} \right] \quad (7.21)$$

3. Solve the Poisson equation (7.15) for equilibrium conditions $\phi_n = \phi_p = 0$ to get ϕ .

4. Add the bias. Bias should be chosen as smaller than the thermal voltage $V_T = \frac{kT}{q}$ (V) in order to achieve better convergence. The bias is applied as a boundary condition on ϕ , as

$$\phi^v(1) = \phi^{v-1}(1) + \frac{\Delta Bias}{2} \text{ and } \phi^v(N) = \phi^{v-1}(N) + \frac{\Delta Bias}{2} \quad (7.22)$$

5. Solve continuity equations for the potential calculated above, to get n and p (ϕ_n and ϕ_p), using Scharfetter-Gummel discretization method [152], as described later.

6. Solve Poisson equation for this ϕ_n and ϕ_p .

7. If does not converge, go to step 5, otherwise go to step 4. (Convergence is defined as the condition when largest potential change in the last iteration is less than a certain value (chosen here as 10^{-7} V).

8. Analyze and plot the results.

To solve the continuity equations using Scharfetter-Gummel discretization method, we solve the following system of equations. These equations can be derived from equation (7.4) and (7.5) after a lot of algebraic manipulations [153, 154],

$$\frac{D_{i-\frac{1}{2}}^n}{\Delta^2} B\left(\frac{V_{i-1}-V_i}{V_T}\right) n_{i-1} - \left[\frac{D_{i+\frac{1}{2}}^n}{\Delta^2} B\left(\frac{V_i-V_{i+1}}{V_T}\right) + \frac{D_{i-\frac{1}{2}}^n}{\Delta^2} B\left(\frac{V_i-V_{i-1}}{V_T}\right) \right] n_i + \frac{D_{i+\frac{1}{2}}^n}{\Delta^2} B\left(\frac{V_{i+1}-V_i}{V_T}\right) n_{i+1} =$$

$$U_i \quad (7.23)$$

$$\frac{D_{i-\frac{1}{2}}^n}{\Delta^2} B\left(\frac{V_i-V_{i-1}}{V_T}\right) p_{i-1} - \left[\frac{D_{i+\frac{1}{2}}^n}{\Delta^2} B\left(\frac{V_{i+1}-V_i}{V_T}\right) + \frac{D_{i-\frac{1}{2}}^n}{\Delta^2} B\left(\frac{V_i-V_{i-1}}{V_T}\right) \right] p_i + \frac{D_{i+\frac{1}{2}}^n}{\Delta^2} B\left(\frac{V_i-V_{i+1}}{V_T}\right) p_{i+1} =$$

$$U_i \quad (7.24)$$

where $B(x) = \frac{x}{e^x - 1}$ is Bernoulli function.

This formulation is useful for robust and rapid convergence because the exponential dependence of n and p is buried in very stable Bernoulli function. Equation (7.23) and (7.24) can be solved as a tridiagonal matrix algorithm using back-substitution [155].

To solve Poisson's equation we use a scheme similar to that used in Mayergoyz et al [156], which solves nonlinear differential equation by Newton's method.

7.3.3 Solution to Poisson equation:

$$\frac{d}{dx} \left(\epsilon(x) \frac{dV}{dx} \right) = -q \left[n_i \exp \left(-\frac{q(\phi - V_p - \phi_p)}{kT} \right) - n_i \exp \left(+\frac{q(\phi + V_n - \phi_n)}{kT} \right) + N_D^+ - N_A^- \right]$$

$$(7.25)$$

Converting in finite difference method

$$\epsilon_{i+1} \phi_{i+1} + \epsilon_{(i-1)} \phi_{i-1} - (\epsilon_{i+1} + \epsilon_{i-1}) \phi_i =$$

$$-q(\Delta x)^2 \left[N_D^+ - N_A^- + n_i \exp \left(\frac{q(V_p + \phi_p)}{kT} \right) \exp \left(-\frac{\phi}{V_T} \right) - n_i \exp \left(\frac{q(V_n - \phi_n)}{kT} \right) \exp \left(+\frac{\phi}{V_T} \right) \right]$$

$$(7.26)$$

writing as

$$\alpha_{i+1}\phi_{i+1} + \alpha_{i-1}\phi_{i-1} - 2\alpha_i\phi_i - \beta_1 \exp(\phi/V_T) - \beta_2 \exp(-\phi/V_T) = f_i \quad (7.27)$$

where

$$\alpha = \epsilon_s$$

$$\beta_1 = q(\Delta x)^2 n_i \exp\left(\frac{q(V_n - \phi_n)}{kT}\right)$$

$$\beta_2 = -q(\Delta x)^2 n_i \exp\left(\frac{q(V_p + \phi_p)}{kT}\right)$$

$$f_i = q(\Delta x)^2 n_i (N_D^+ - N_A^-) \quad (7.28)$$

Solving by Newton Rhapsion method:

$$2\alpha_i\phi_i + \beta_1 \exp\left(\frac{\phi}{V_T}\right) + \beta_2 \exp\left(-\frac{\phi}{V_T}\right) - F_i = 0 \quad (7.29)$$

$$F_i = \alpha_{i+1}\phi_{i+1} + \alpha_{i-1}\phi_{i-1} - f_i$$

Inner loop

$$f(\phi_i) = 2\alpha_i\phi_i + \beta_1 \exp\left(\frac{\phi}{V_T}\right) + \beta_2 \exp\left(-\frac{\phi}{V_T}\right) - F_i \quad (7.30)$$

$$\phi_i^{(v+1)} = \phi_i^{(v)} + \chi^{(v)}$$

where

$$\chi^v = -\frac{f(\phi_i^v)}{f'(\phi_i^v)}$$

$$f'(\phi_i^v) = 2\alpha_i + \frac{\beta_1}{V_T} \exp\left(\frac{\phi}{V_T}\right) - \frac{\beta_2}{V_T} \exp\left(-\frac{\phi}{V_T}\right) \quad (7.31)$$

7.3.4 Results

A simple N-P-N structure with GaAs, shown in Fig. 7.1 (a), simulated using the above procedure, shows the development of spacer charge regions leading to high electric fields near the contact and P region interfaces. Fig. 7.1(b)-(f) show the absolute value of electric field calculated at several different biases. These results agree closely with those obtained by a commercial Sentaurus TCAD simulator.

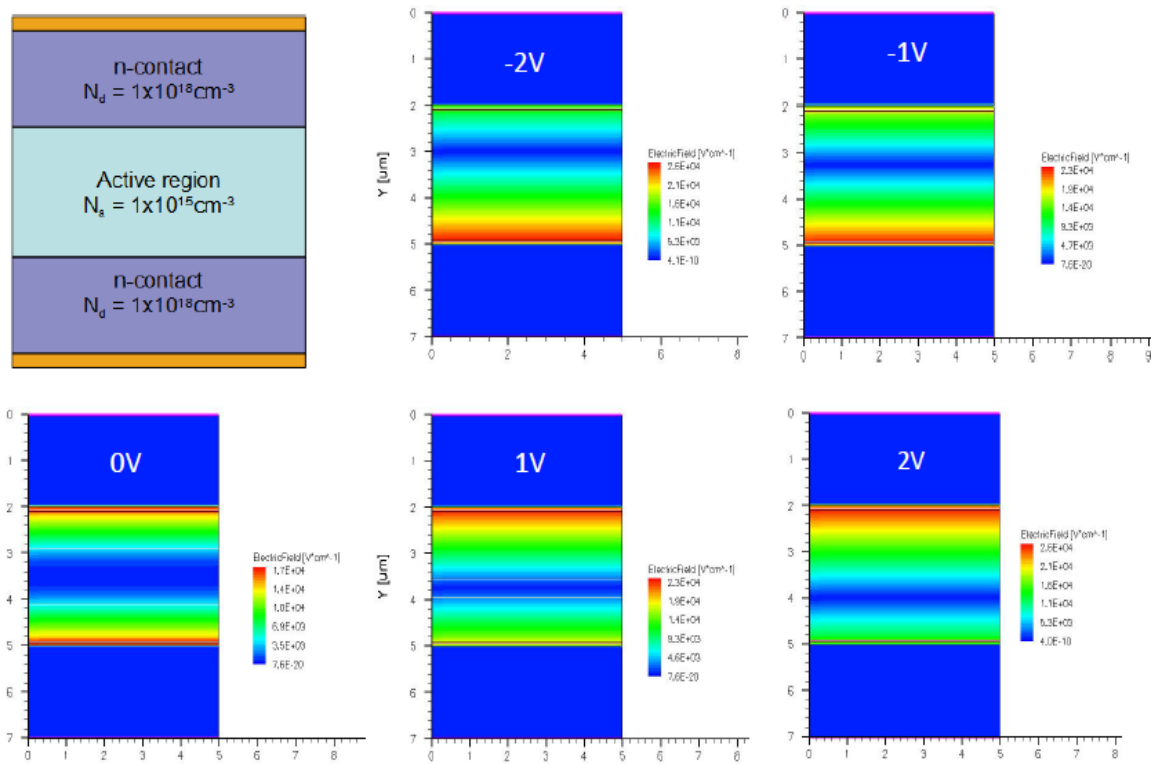


Fig. 7.1: (a) Schematics of the simulated structure (b)-(f) Contour plots of absolute electric fields at different temperatures.

The simulated structure has a similar form as a typical n-i-n detector without the doping in the quantum wells. It is clear from Fig. 7.1 that the effect of p^- background doping for barrier regions results in the formation of high electric fields near the contacts, due to back to back p-n junctions. Formation of space charge regions is shown in Fig. 7.2. The

electric field dropping across the p-n junction depletion near the bottom contact, for example, decreases as the positive bias increases. For active regions with quantum well and n-type quantum well doping, the behavior of the electric field is similar to this, as shown later. We will revisit the device simulations after discussing the experimental results.

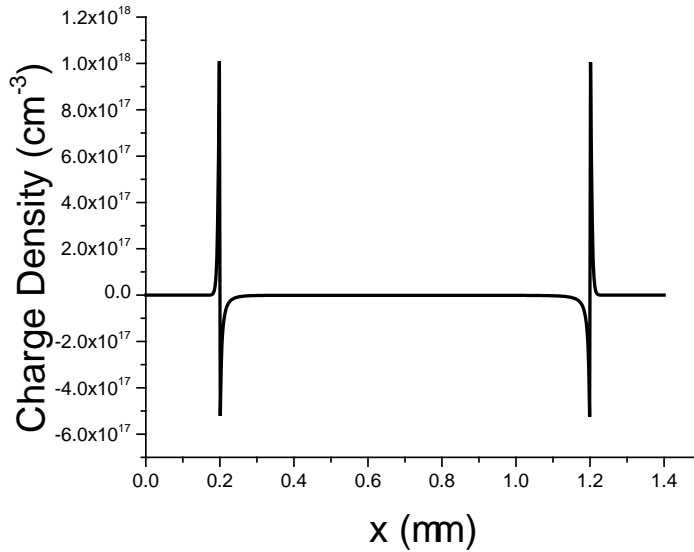


Fig. 7.2: Charge density plot for the structure in Fig. 7.1 at 0.1V

7.4 Experimental Work

In order to predict the effect of this space charge region on the device performance, a series of DWELL devices with identical active regions and spacer regions placed near two different contacts were grown. Fig. 7.3 shows the schematics of the three DWELL detectors. All the devices consist of seven stacks of 5.3 nm $\text{In}_{0.15}\text{Ga}_{0.85}\text{As}$ QW with 2.0 ML InAs quantum dots embedded in them, separated by 50 nm $\text{Al}_{0.08}\text{Ga}_{0.92}\text{As}$ barriers. The active region structures are same as CE DWELL 1 device described in chapter 5.

Confinement enhancing barriers [127] consisting of 2 nm $\text{Al}_{0.22}\text{Ga}_{0.78}\text{As}$ layers on both sides of QW regions have been included. InAs quantum dots are n-doped (Si) with a sheet density of $1.6 \times 10^{11} \text{ cm}^{-2}$. Quantum wells and barriers are undoped. Top (200 nm) and bottom (500 nm) GaAs contacts are n-doped, with doping density of $\sim 2 \times 10^{18} \text{ cm}^{-3}$ to form ohmic contacts with Ge/Au/Ni/Au metal layers. In the control device with no spacer, 50nm $\text{Al}_{0.08}\text{Ga}_{0.92}\text{As}$ barriers are incorporated between each of the contacts and DWELL regions. In the structure 'Top Spacer', 50nm $\text{Al}_{0.08}\text{Ga}_{0.92}\text{As}$ barrier near the top contact is replaced by 200 nm $\text{Al}_{0.08}\text{Ga}_{0.92}\text{As}$ barrier keeping the bottom barrier same, while in the 'Bottom Spacer' structure, 50 nm $\text{Al}_{0.08}\text{Ga}_{0.92}\text{As}$ barrier near the bottom contact is replaced by 200 nm $\text{Al}_{0.07}\text{Ga}_{0.93}\text{As}$ barrier keeping the top barrier same. All the other growth parameters were kept identical, within the growth tolerances.

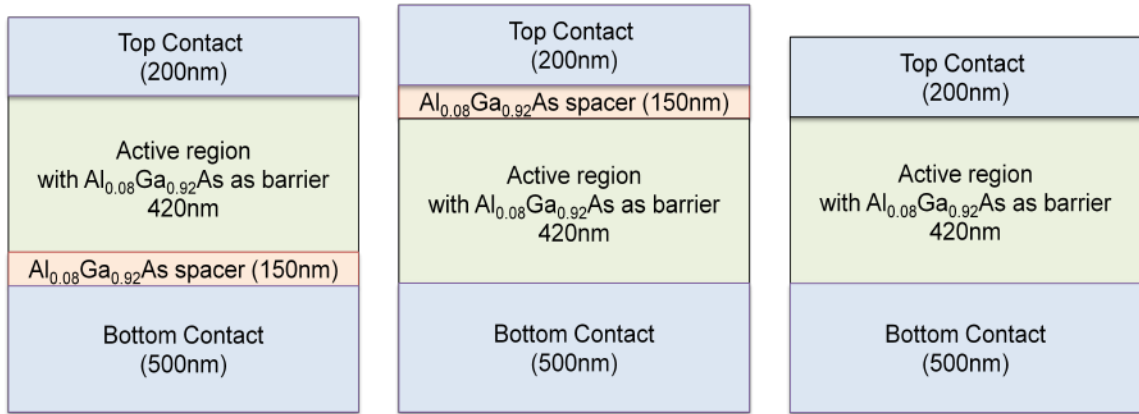


Fig. 7.3: Schematics of structures used for experimental study. Active regions are same as those used in CE DWELL 1 device. (a) 'Bottom Spacer' device (b) 'Top Spacer' device (c) Control device.

The detectors were processed in $410 \times 410 \mu\text{m}^2$ square mesas with standard dry etching technique and contact metal was deposited. The spectral response measured with Fourier

Transform spectroscopy were similar to reported previously with CE DWELL 1 [127] device, with a broad spectrum from 4 μm to 9 μm . Excellent signal to noise ratio with high detectivity values obtained at 77 K were desirable for reducing the measurement uncertainties. Fig. 7.4 (a) and (b) show comparisons between the dark currents of the control device with that of 'Bottom Spacer' and the 'Top Spacer' devices, respectively. A very clear trend is obtained. For 'Bottom Spacer' device, since the bottom PN junction is reverse biased in the negative bias, the majority of electric field falls across the spacer region, thus reducing the dark current, as compared to the control device. In the positive bias, since very small electric field drops across the forward biased PN junction near the bottom contact and active region interface, the effect of spacer is minimized. It is important to note that even though the active region thicknesses are vastly different for the two devices (420 nm for the control device and 570 nm for the 'Bottom Spacer' and 'Top Spacer' devices), the dark current is same for a same bias! This proves that very small electric field is falling across the bottom spacer region in the positive bias. Same trend is obtained for the comparison between the control device and 'Top Spacer' device, thus validating the experiment.

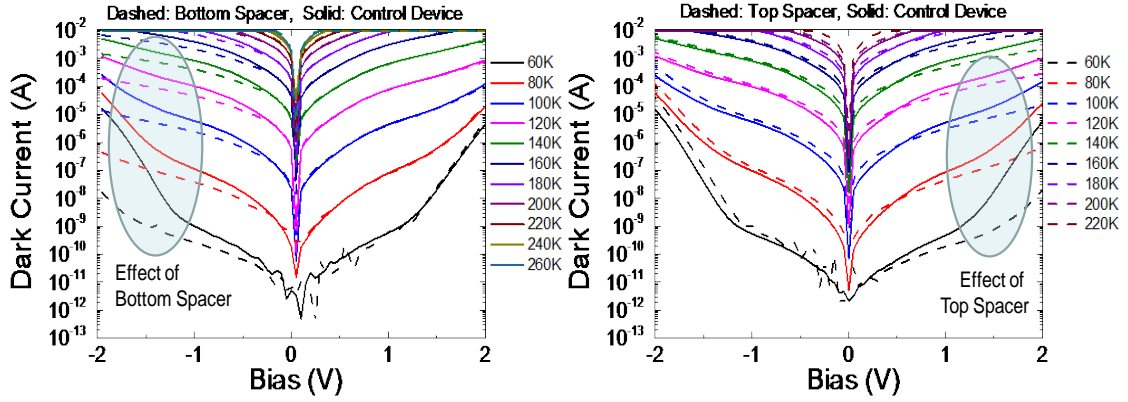


Fig. 7.4: Comparison of dark currents between (a) Bottom Spacer and the control device, showing same dark current levels in positive bias and a bias and temperature dependent reduction for the spacer device in negative bias. (b) Top Spacer device and the control device, showing the same trend in other bias polarity.

Fig. 7.5 (a) shows the ratio of dark currents from the control device to 'Bottom Spacer' device, as a function of bias at various temperatures. As expected, the ratio is close to unity for all the temperatures in the positive bias. In the negative bias, on the other hand, the ratio increases with increase in bias and decreases with the increase in temperature. As the negative bias increases, more field drops across the bottom spacer, thus reducing the dark current further, as compared to the control device. It is to be noted that this strong, faster than exponential, bias dependence for the ratios of the dark current with and without the spacer layer cannot be explained with the existing self consistent model [157], as the model focuses on the carrier capture and reemission from the first quantum well, with a constant electric field in each barrier. As the temperature increases, the thermal generation and diffusion of dark current carriers becomes more effective, thus reducing the importance of drift component of the dark current. Fig. 7.5 (b) compares the activation energies of all the three devices at different biases. The systematic differences in activation energies cannot be explained by simple emission-capture models.

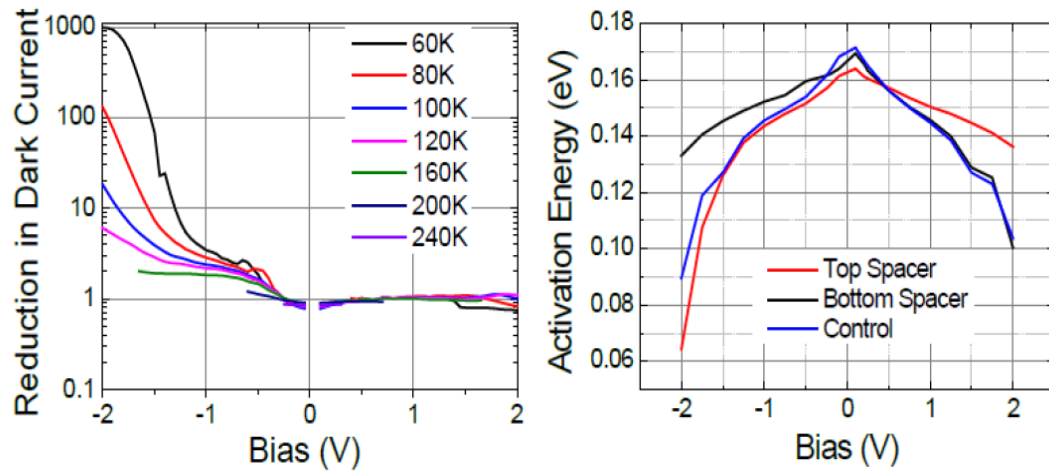


Fig. 7.5: (a) Ratio of dark current between the control device and bottom spacer device, showing huge reduction in the dark current, which reduces with reduction in negative bias and increase in temperature. (b) Comparison of activation energy between the three devices showing similar activation energy for top spacer and control device in the negative bias and bottom spacer and control device in the positive bias.

Due to bias drop across the spacer region, the photocurrent signal also reduces along with the dark current, as shown in Fig. 7.6. However, the reduction in photocurrent strength is much smaller than reduction in the dark currents, especially at higher bias, leading to substantially higher signal to noise ratios at higher bias for the side with spacer action (negative bias for bottom spacer and positive bias for top spacer). This is because dark current has much stronger dependence on applied electric field as compared to photocurrent. Note that for the other bias, there is almost no change in the signal strength, within experimental error.

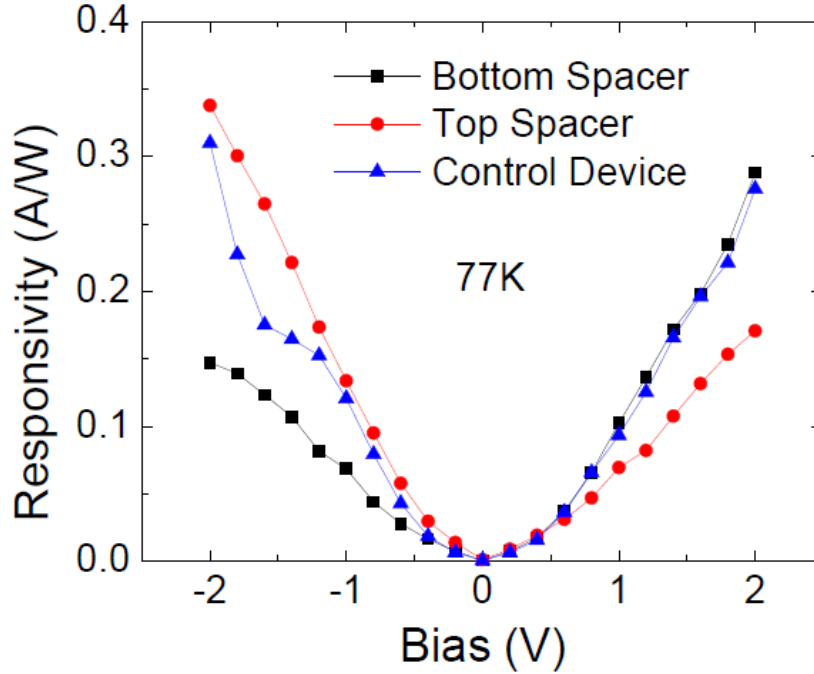


Fig. 7.6: Comparison of responsivity for all the three devices showing similar responsivity between the control device and bottom spacer device in positive bias, while reduced responsivity for spacer device in the negative bias. Same trend is observed for top spacer for the other bias polarity. It is to be noted that this reduction in responsivity is much smaller than the reduction in dark current.

7.5 Comparison with Theoretical Results

The experimental results described above suggest a formation of space charge region with high electric field drop at the boundary between the contact layer and the barrier layer. This picture indeed emerges from qualitative simulations that we have undertaken. The calculated electric field with the top spacer and with no spacer for different bias regions has been plotted in Fig. 7.7 (a)-(d). Doping in the barriers was assumed to be $4 \times 10^{14} \text{ cm}^{-3}$ (p-type), which was obtained from Hall measurements on non-intentionally doped layers. Doping in the quantum wells was taken to be $1.6 \times 10^{16} \text{ cm}^{-3}$, which is same as the nominal doping in the DWELL structures used in the experiments. Quantum effects have not been considered for these bulk simulations. As it can be seen from Fig.

7.7, there are space charge regions forming near the contact layer boundaries, leading to high electric fields in these regions.

- Significant electric field drops across the spacer, in the positive bias, while very low electric field drops across the spacer in the negative bias, making all the applied bias available in the quantum well regions.
- The electric field in the individual barrier, especially near the contact region is not linear. The electric field dropped across the spacer in positive bias leads to smaller field drop across the quantum well region as compared to the control device, as shown. This results in exponentially decreasing dark current, reduced signal strength and higher activation energy, as observed in experimental results, only in the positive bias for the top spacer device, as compared to the control device.
- Negligible change in field drop across the quantum well region in the negative bias, as suggested by the electric field simulations, is consistent with observed experimental properties.
- Similar results were obtained for the case of bottom spacer.

Fig. 7.8 (a) shows the band bending for top spacer device at two biases. It is clear that the band bending for the first quantum well is higher in positive bias than negative bias. Fig. 7.8 (b) shows the charge density in the device at 0.1V. It can be seen that the space charge regions near the contact regions are much bigger than those near the individual quantum well regions. This can be compared with spacer charge region for NPN device shown in Fig. 7.2.

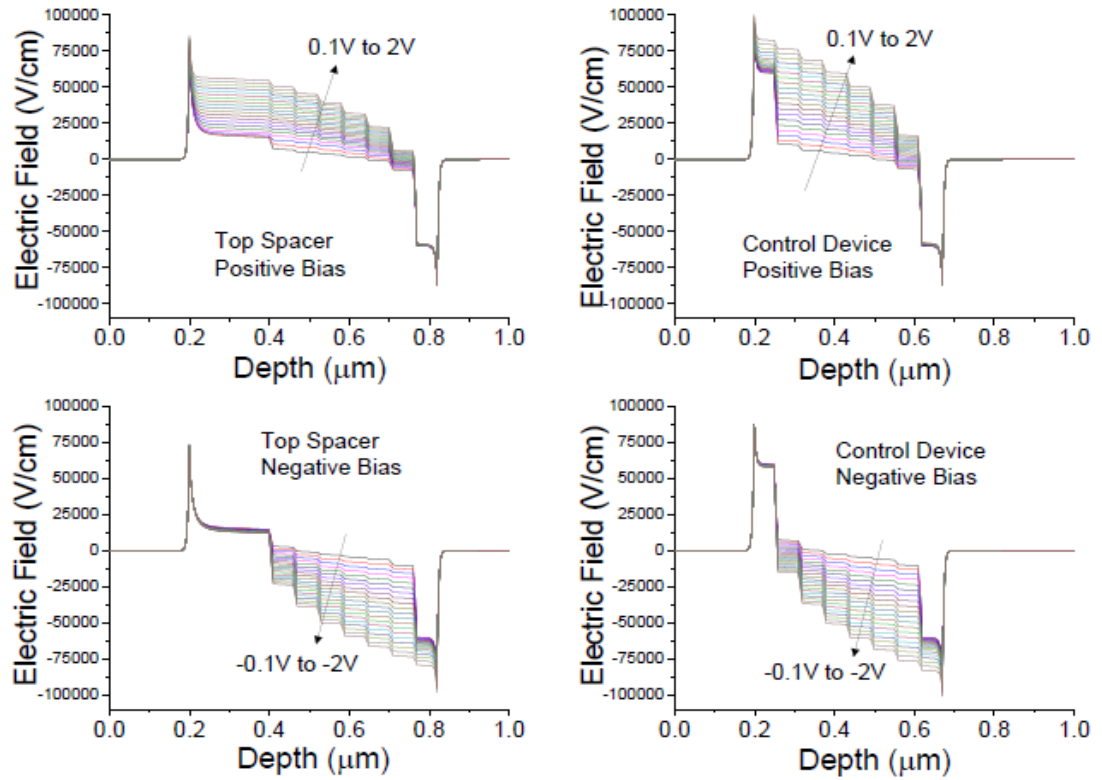


Fig. 7.7: Simulated electric field for top spacer and control device for different bias polarities. In positive bias, increasing electric field drops across the top spacer, while in the negative bias, the field drop across the spacer region is small.

In conclusion, experimental evidences of band bending due to the formation of p-n junctions between the n-doped contact regions and non-intentionally doped barrier regions, are presented. A simple drift diffusion based model, which solves the nonlinear Poisson equation simultaneously with current continuity equations, has been used. The simulations suggest that in a particular polarity of bias, positive bias for top spacer and negative bias for the bottom spacer, significant electric field drops across the spacer region, leading to lower dark current, lower signal strength and higher activation energies, as compared to the control device, which is consistent with experimental observations. In the other bias polarity, since negligibly small change in electric field dropping across the spacer region, these properties remain same between the device with

the spacer and the control device, even though the thickness of active region is drastically different. This band bending has significant importance in device designs and would be more significant for QDIPs than for QWIPs due to smaller n-doping in the absorber region.

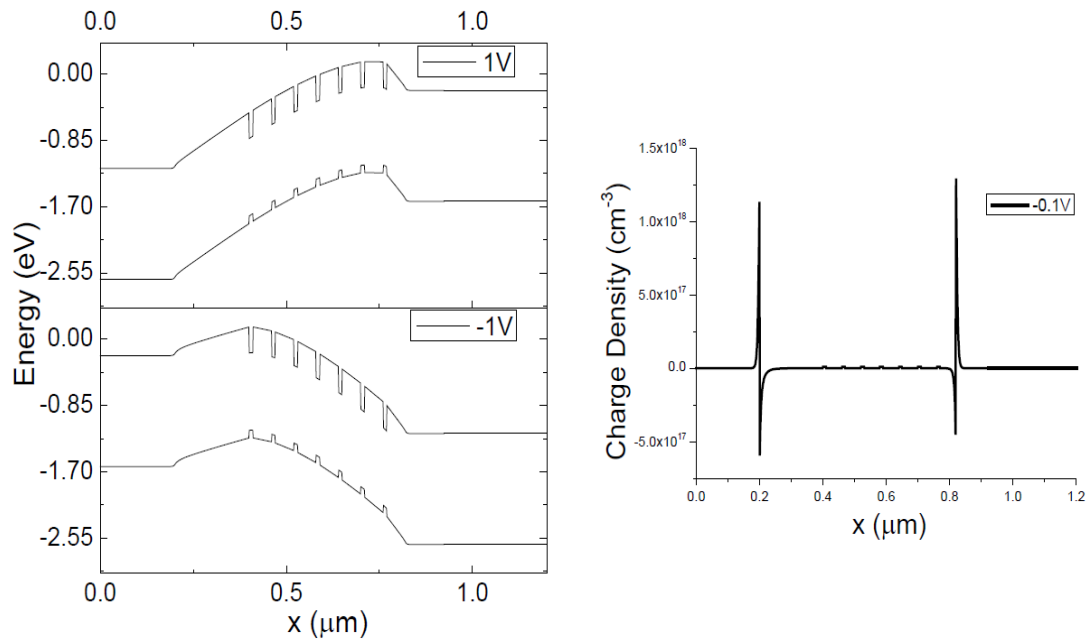


Fig. 7.8 (a): Band diagram for top spacer structure for +1V and -1V, showing higher band bending for first QW in positive bias. (b) Charge density as a function of distance, showing that the spacer charge regions near the contact regions are much bigger than those near the individual quantum well regions.

8 Discussions and Future Directions

8.1 Conclusions

Since their conceptualization and initial demonstrations, the DWELL detectors have made tremendous progress towards becoming a competitive technology for the third generation infrared focal plane arrays. The key requirements, such as high operating temperature, multicolor operation and large format arrays can be successfully achieved by DWELL detectors owing to their zero dimensional confinement, richness of electronic states in quantum dots and the mature GaAs growth and processing technology. Even though the low dark current levels mean that the signal to noise ratios are comparable or better than several other technologies, the major hurdle in commercialization of DWELL detectors has been the absorption quantum efficiency, which is currently lower than that of QWIPs. This work attempts to identify the key areas of improvement for making the DWELL detectors suitable for high operating temperature FPAs. Three important aspects of the DWELL devices were looked at:

1. Material improvements from device point of view. Effect of quantum dot doping, dot thicknesses, compositions, growth temperatures and materials were studied for detector optimization.
2. Designing the DWELL structure and the barrier to optimize each stack for the given design requirement based on dark current, photocurrent, peak wavelength, and

FWHM of the spectral response. Interplay between various structural parameters and device response were studied.

3. Modeling and experimental optimization of the entire active region (macro-engineering). Understanding the transport mechanism in intersubband photoconductive detectors both theoretically and experimentally. A photovoltaic detector, with quantum dot quantum cascade detection, allowing for zero bias operation in a traditional n-i-n architecture was proposed and implemented.

As discussed in chapter 3, the electronic structure modeling for DWELL detectors is a challenging process, mostly due to the difficulty in obtaining the structural parameters for the quantum dot ensemble. Atomistic strain modeling in DWELL detectors with valence force field method has been successfully implemented. The results highlight the fact that the strain distribution inside the quantum dot is highly nonlinear in space, leading to different confinements for different types of carriers, such as heavy holes and light holes. A k.p formulation of electronic band structures, with the appropriate strain effects added to the confinement potential in the modified Hamiltonian, should eventually lead to predictive design of devices, rather than the semi-empirical procedure currently used.

A systematic study of different transitions in DWELL detectors, such as bound to continuum, bound to quasibound and bound to bound has been conducted by gradually changing the quantum well thickness to vary the energy of the excited state in the quantum well, with respect to the barrier. For B-C transitions, since the photoexcited electron is above the barrier energy, very little electric field is needed to collect the photocurrent. On the other hand, since field assisted tunneling involved for the escape of

photocarriers from DWELLs for B-B transition, high electric fields are needed. However, the absorption quantum efficiency is higher in B-B transitions, due to a better confinement of excited state wavefunction, thus increasing the transition matrix for absorption. Thus, different types of transitions give optimized performance in different bias ranges, with B-Q types of transitions combining the advantages of both B-B and B-C transitions. These transitions can be characterized based on the spectral width, which decreases from B-C ($>25\%$), B-Q (12-25%) to B-B ($<12\%$). Interestingly, these transitions can also be observed in a single detector with multiple energy levels in the DWELL region, as shown in Fig. 2.9. This gives rise to bias tunable multicolor detection, with a broad midwave output (B-C) for low bias and narrow longwave output (B-B) at higher bias. High performance FPAs were made from B-C type detectors which show imaging of human face up to 100 K, which is the highest reported for QD based detectors.

Two types of barrier structures were studied to improve the performance of DWELL detectors. With resonant tunneling barriers, discussed in chapter 4, 2-3 orders of magnitude reduction in the dark current, while only a factor of 4-5 reduction in photocurrent helps in increasing the overall detectivity and hence the maximum operating temperatures, for the same peak wavelength. Record high detectivity values were obtained with the use of resonant tunneling barriers on optimized quantum dots in double well detectors. Varying the passband of the resonant tunneling barrier, it is possible to change the peak wavelength of RT-DWELL detector from otherwise identical control detector. This feature was demonstrated for RT-DWELL as well as RT-DDWELL

detectors. For RT-DDWELL detectors, in order to extract the long wavelength component, a novel 'split barrier' configuration was successfully used.

Confinement enhancing barrier devices aim at improving the photocurrent by optimizing the product of absorption quantum efficiency and the escape probability, while simultaneously reducing the dark current. This was successfully achieved with CE DWELL detector, which shows markedly improved performance over an optimized B-Q type of detector. CE barriers combine the advantages of low barrier structures, such as small operating bias suitable for FPA operation, long wavelength response, better QD material quality, higher responsivity with the advantages of high energy barrier, such as low dark current to obtain high SNR at low bias. Detailed analysis of the effect of barrier on the performance of DWELL detectors was performed by dividing the barrier region in two parts, 'proximity barrier' adjacent to the DWELL region and the 'remote barrier', which is between two DWELL stacks. It is shown that the proximity barrier is responsible for properties such as the cutoff wavelength, responsivity, while the remote barrier has a strong influence on the dark current, responsivity, and the activation energy. The dependence of activation energy on different barriers is further highlighted by looking at Fig 4.17, which shows that the activation energy for the RT-Split detector is similar to DDWELL detectors (with $\text{Al}_{0.1}\text{Ga}_{0.9}\text{As}$ barriers) for smaller biases while it becomes comparable to DWELL devices (with GaAs barriers) at higher biases. This is because at higher biases, the band bending due to electric field prevents carrier from seeing the taller $\text{Al}_{0.1}\text{Ga}_{0.9}\text{As}$ barriers, which is as designed.

Based on CE DWELL 1 structure as the absorption region, a quantum cascade detector based on InAs quantum dot has been introduced for the first time. These structures

exploit the increased excited state lifetime in the DWELL region for making the extraction process more efficient than their quantum well counterpart. The quantum cascade barriers transport the photoexcited carriers back to the ground state of the quantum dot in the next stack, by the action of effective electric field generated by the 'energy ladder'. This design, due to photovoltaic action, shows excellent characteristics at zero bias, with the responsivity and detectivity values higher than those in optimized QW based QCDs. Designing a QD QCD is a challenging process due to the requirement of precise knowledge of energy levels in DWELL stacks and each of the QW in the cascade region. This was achieved through the knowledge of PL and spectral characteristics of the parent CE DWELL structure and through the solution of one dimensional Schrödinger equation in the cascade region. The energy levels were designed to be separated by close to 36 meV, which is a LO phonon energy of GaAs, for efficient extraction of carriers.

Coupling the electrons into the quantum dot is also a challenging process, due to highly compressive nature adding a large cumulative compressive strain per stack. This was achieved by coupling to a known excited state in the quantum dot through a strained InGaAs quantum well. The first generation QD QCD shows a successful photovoltaic operation with a large photovoltaic shift in the photocurrent, especially at low temperatures, where the photocurrent at zero bias is more than 2 orders of magnitude higher than the dark current. Photoconductive gain of less than unity (~ 0.36) proves that this coupling process is successful in coupling the quantum dots into the quantum well. This lower PC gain, along with a zero bias operation is very attractive for FPA operation with higher sensitivity at high temperatures.

Although traditionally all the barrier devices are designed with a flat band approximation, in chapter 7 we saw that the non intentional doping in the barriers cause space charge regions near the contact regions, which lead to substantial band bending. The existence of these regions was proved by drift diffusion simulations which show high electric field regions near the boundary between the contact layer and the active region. To experimentally verify this, a series of structures with identical active regions, but with spacer layers of different thicknesses were grown and fabricated. Due to a large component of electric field falling across the spacer region, the electric field inside the active region is decreased, leading to a large decrease in dark current, and some decrease in photocurrent. The dark current reduction is bias dependent, with larger reduction for the larger absolute bias. It also reduces with the increase in temperature, because the drift component of the current is less dominant at higher temperatures. These observations can be qualitatively explained by the theoretical simulations on similar QWIP structures.

8.2 Discussions and Future Work

Although all the above conclusions have been supported by successful implementation of devices, there is still a scope for improvements in various structures and simulations. In this section, we will discuss some of these improvements.

8.2.1 RT DWELL Devices

In resonant tunneling devices, the thickness of RT barriers used was limited to 2 nm for the proof of the concept. Thicker barriers lead to a sharper transfer function for RT barrier, which means lower dark current, but also mean that it is harder to align the passband of the barrier to the excited state of the DWELL region. However, after

demonstrating the performance improvements with RT barriers, a lot more knowledge about types of transitions, energy levels in DWELL detectors has been added. Using this knowledge, along with the development in QD energy structure modeling, it is now possible to improve the RT structures for high temperature operation and for different wavelength regions. Following improvements are achievable:

1. By growing thicker RT barriers, such as 3 nm barriers used in Su et al [65], it is possible to achieve further reduction in the dark current.
2. RT barriers below the quantum dots can be designed more predictably, as their distance from the QD layer can be better controlled than those above the QD. In the original designs, since the effect of added compressive strain on QDs was not known, the barriers were placed above (in the growth direction) of the quantum dots. However, as we saw with QD QCD devices, placing the InGaAs QW below the QD actually improves the structural properties of QDs.
3. RT barriers can be used to extract very longwavelength response from QD ground state to QD excited state, such as in Su et al [21]. This VLW or THz signal extraction would require large biases in traditional DWELL designs, but with RT DWELL designs this can be done at lower biases. The knowledge gained in the conduction band energy levels for CE DWELL 1 and QD QCD devices can be utilized for this purpose.

8.2.2 CE DWELL Devices

It is possible to take the advantage of DWELL geometry, in which the QD ground state and QD excited state can be controlled independently of each other, to implement CE DWELL designs for different wavelengths. For example, going towards MWIR is

possible by increasing the barrier height or increasing the size of quantum dots. LWIR response can be obtained by reducing the size of QD, or growing quantum dots with InGaAs or AlInAs, instead of InAs.

8.2.3 QD QCD Devices

The device shown in chapter 6 for QD QCD was only the first design for it. The encouraging results were obtained from this unoptimized device, such as zero bias operation, strong photovoltaic shift, low photoconductive gain etc. This gives a lot of motivation for trying to further optimize the detector. Following improvements are possible:

1. As described in chapter 6, the doping in the quantum dots can be further increased in order to increase the responsivity. Higher doping would help in supplying more electrons in the conduction band excited state in QDs, which is the most important state for QD QCD design.
2. A design with a larger number of quantum wells in a cascade region will probably make the cascade action more efficient and reduce the design tolerance. One such design is shown below in Fig. 8.1 (a), which is a modified version of QD QCD device presented in chapter 6.
3. The thickness of barriers in the cascade region can be improved much further in order to maximize the transfer coefficient between the two cascade states and minimize the coupling between unwanted states and higher lying excited states. This will reduce the leakage of current by a long range resonant tunneling processes. For example [158], in QW based QCDs, the barriers can be as thick as 6 nm, as opposed to 2 nm used in this

work. Thicker barriers, however, present stricter design requirements, so more rigorous modeling is required for designing the QCD detectors.

4. For going towards VLWIR and THz operation with QD QCD devices, which is a popular wavelength choice for QW QCD detectors, it is imperative to use AlInAs quantum dots. This is because using InAs QDs, the cascade between QD excited state and QD ground state will need highly compressively strained InGaAs QWs, which is not a viable solution. With AlInAs QDs, it is possible to increase the bandgap to make it comparable to GaAs band gap. This can then be efficiently used to design QCDs working in VLWIR. One such variation is shown in Fig. 8.1 (b) for LWIR applications. Tensile strained InGaP layers can also be used for barriers in order to increase the number of stacks by strain compensation.

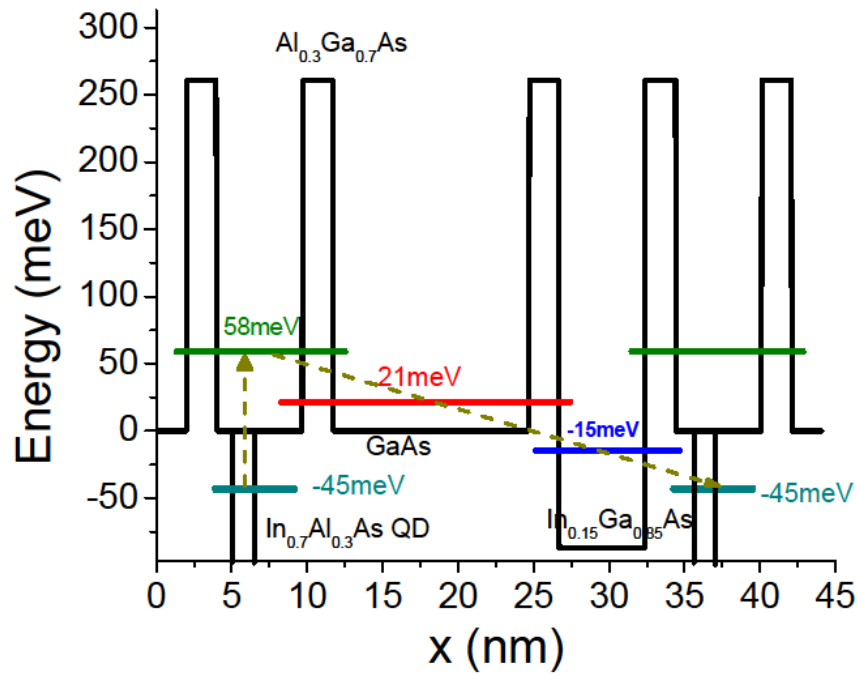
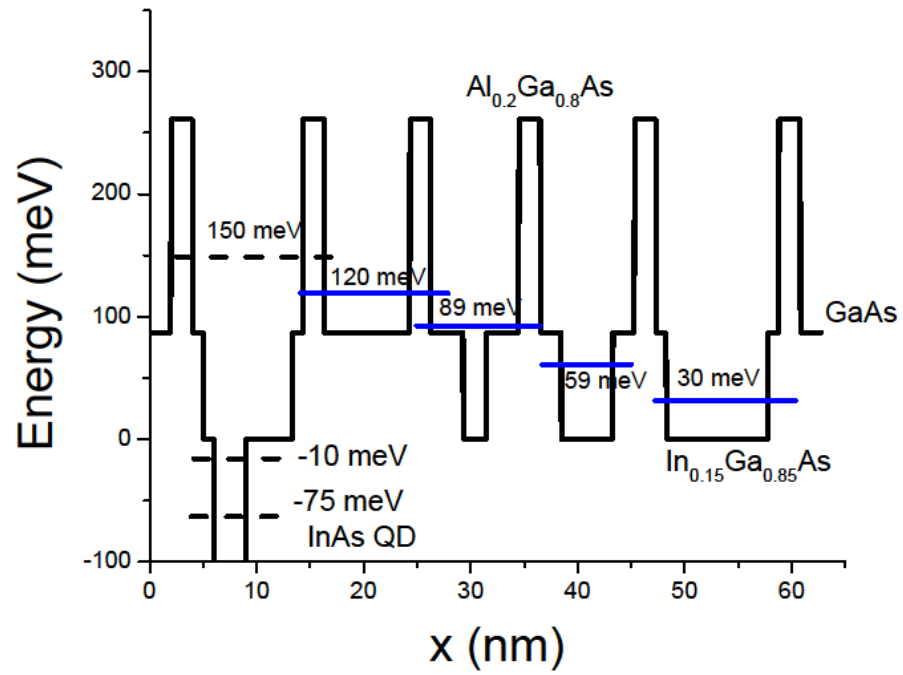


Fig. 8.1: (a) QD QCD design for same wavelengths as in QD QCD 1, but with 4 quantum wells in the cascade region. (b) QD QCD design with $\text{In}_{0.7}\text{Al}_{0.3}\text{As}$ quantum dots, for LWIR detection.

8.2.4 Higher Normal Incidence Absorption

As it can be seen from various TEMs presented here, SK quantum dots tend to be 'pan cake' shape, with the base of 15-20 nm and height of 5-7 nm. Since the normal incidence absorption (s-polarized light) depends on the confinement in lateral direction, this leads to poor s/p polarization ratio in these devices. For example, the s/p polarization ratio measured for B-Q2 device discussed in chapter 4 and CE DWELL 1 device in chapter 5, is shown in Fig. 8.2 (a) and (b), respectively. Both of them show s/p' polarization ratio to be around 21%. It is to be noted that p' polarization contains component of s and p polarization, so the actual s/p polarization ratio is close to 12%.

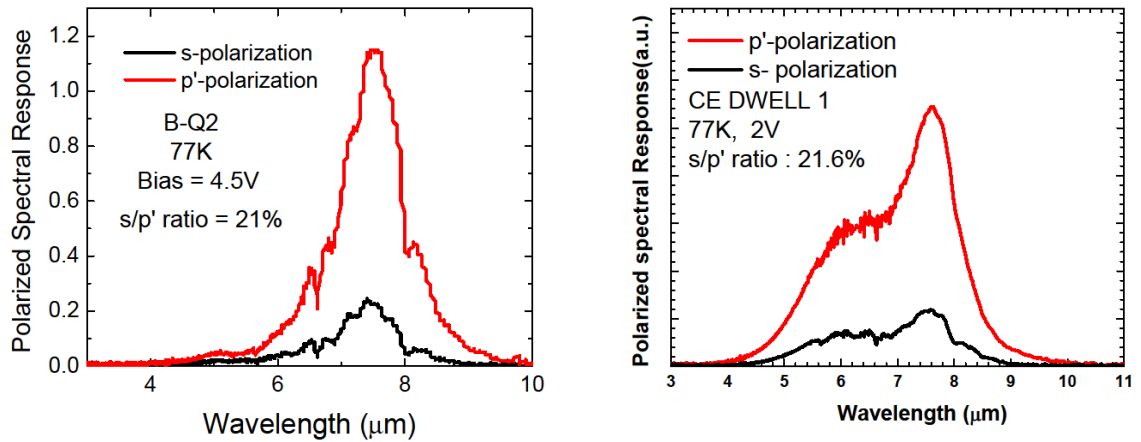


Fig. 8.2: Polarization dependent spectral response for (a) B-Q2 device (measurements by Dr. Jiayi Shao) and (b) CE DWELL 1 device (measurements by Dr. Jun Oh Kim) showing 21% s/p' polarization ratio.

This shows the huge potential for improvement in the QD growth in order to decrease the QD base diameter and interdiffusion of materials at QD interfaces. This is possible by changing the capping materials with Al containing strained layers, such as InAlGaAs. With InAlGaAs capping layer, an s/p' polarization ratio of 50% has been obtained [159]. The key is to find a balance between lowering the interdiffusion and at the same time not

increasing the QW energy too much, so that carriers can be extracted at smaller bias. Another approach is to use submonolayer (SML) quantum dots, in which the base dimension and the height of the quantum dot can be independently controlled to increase the s/p polarization ratio. However, care needs to be taken to not increase the dot density too high in order to avoid the quantum mechanical coupling between the quantum dots, reducing the confinement in the lateral direction. Another way of tapping into high p-polarization absorption is the use of gratings to diffract the s-polarized light into p-polarized components. Such 2D gratings are very mature for QWIPs based on GaAs processing technology, so it does not pose any significant technological challenge.

The low s/p polarization ratio also makes substrate scattering an important issue. As a semi-insulating GaAs substrate which is transparent to the infrared wavelengths of interest is used in all of the measurements reported in this work, the substrate scattering is present. Substrate scattering refers to the scattering of light by the substrate which artificially increases the collection area of a single pixel detector used for the measurement of responsivity. Two separate measurements, one with covering the sidewalls of the dice with silver paint, and other with a hybrid chip configurations, resulted in the conclusion that the substrate scattering enhances responsivity by a factor between 2 to 3. The results shown for QD QCD in chapter 6 have already been corrected for this effect.

8.2.5 Transport Modeling

Although some progress has been made to explain the behavior of DWELL devices qualitatively, using the drift diffusion model, there is a vast scope of improvement in the

model to get more accurate results. Following features need to be added for accurate dark current models

1. Thermionic emission and capture of electrons in quantum wells and quantum dots. The self consistent nature of emission and capture would alter the space charge formation near the QD/QWs.
2. Although classical formulation for drift diffusion is sufficient for macroscopic simulations, in order to get detailed information about the band bending near the QW/QD region, the current formulation needs to be self consistently coupled with Schrödinger equation.
3. For simulations involving tunneling junctions and high electric field regions, Fermi Dirac distribution is preferred.
4. Generation recombination mechanisms, such as Shockley Reed Hall (SRH) recombination, trap assisted recombination etc, and optical generation can be added to make it more suitable for SLS devices.

In conclusion, this work utilizes 'barrier engineering' at various levels, such as for materials, DWELL heterostructures and device designs to achieve high performance infrared detectors suitable for integrating into third generation focal plane arrays. High operating temperature imaging, as well as highly sensitive imaging at low temperatures has been demonstrated. Various barrier designs such as resonant tunneling barriers, confinement enhancing barriers, and device architectures such as quantum dot quantum cascade detectors have been successfully implemented. There is a vast scope of improvement in the performance of DWELL detectors by the use of gratings, suitable

capping materials and improved barrier designs. This work attempted to tap into this improvement by providing a systematic way of *choosing* device parameters such as spectral response position and shape, photoconductive gain, response, signal to noise ratio, dark current levels, activation energies etc.

There are 4 group III sources, Ga30, GaSUMO, Al30 and In; two group V sources equipped with a valved cracker, As and P; and two dopant sources, Si for n-doping and Be for p-doping. The sources used in each layer are listed in column 'materials'. The first column is the name of the layer, second gives the growth temperature. Fourth column gives the temperature of Si doping used in that particular layer. Other columns are thickness of each layer, unit, growth rate, growth time for the layer, number of repetition and total growth time for the layer. Several growth parameters are chosen as follows:

1. Sources and Growth Rates

For Ga source, two crucibles are available to choose from. Since GaSUMO cell has a larger SUMO crucible, this cell is used for higher growth rate, while Ga30 with a smaller crucible is used for smaller growth rate. This is done to maximize the time before depleting the source. Growth rates are chosen based on the alloy composition needed. Indium growth rate is determined by the desired growth rate for QD. Ga30 growth rate is determined by the composition of the quantum well in DWELL stack. GaSUMO growth rate is typically determined by the composition of AlGaAs layer in the barrier. Care is taken not to exceed the growth rate above 1.0 ML/s to minimize growth defects. However, in this particular structure, since two compositions of AlGaAs (7% and 22%) are needed, GR of $\text{Al}_{0.07}\text{Ga}_{0.93}\text{As}$ is set at 1.18ML/s.

2. Growth Temperatures

Growth temperature plays an important role in the crystalline quality. In a DWELL detector, since the QD and QW region is grown at lower temperature and barriers are growth at higher temperatures, several temperature changing cycles are present. The

temperatures are first calibrated with respect to a pyrometer, which gives accurate values over 450 °C. Buffer layer, etch stop layer, barrier layers and contact layers are grown at a temperature equal to or higher than 590 °C. DWELL region is grown at a temperature lower than 510 °C and higher than 460 °C. It has been observed that Aluminum containing layers should be grown at higher temperatures in order to minimize the defects.

3. Growth Interruptions:

In order to facilitate the temperature changes, growth is interrupted under the supply of group V element. Typically, 180s to 300s growth interruption is enough for the desired change in substrate temperatures. The substrate temperature increase on In or Al containing layers should be avoided. This is because of Indium desorption during temperature increase and Al attracting residual impurities from the chamber. To achieve this, GaAs spacer layers are added above and below the QW layer, as shown.

4. Floating Layer

For minimizing the Indium segregation during the InGaAs QW growth, a floating layer of InAs is used. This layer is deposited before the growth of strain bed of InGaAs QW, and it gradually floats up as the growth progresses, even at low temperatures. This layer then gets added to the nominal deposition of InAs to grow quantum dots. Thus, nominal thickness of QD for the structure shown in table A.1 is $(0.716 + 1.086 + 0.21) \text{ ML} = 2.01 \text{ ML}$. This can be confirmed by observing the RHEED pattern during the growth of QD, which shows streak to chevron pattern transformation at 1.7 ML of InAs deposition.

Appendix B: Processing

QDIP FPA Process Flow

WAFER PRECLEAN			
Date/ Time	1	Solvent Clean p Solvent Hood	Acetone/IPA/DI rinse (2-5 minute) Nitrogen dry 6 minute dehydration bake @ 150°C
MESA ETCH			
Date/ Time	1.1	Solvent Clean p Solvent Hood	(Required if etch does not immediately follow metal lift-off) Acetone/IPA/DI rinse (2-5 minute) Nitrogen dry 6 minute dehydration bake @ 150°C
	1.2	Etch Photolithography p Spinner p Hot plate p Spinner p Hot plate p Mask Aligner p Develop hood p Profilometer p Inspection Microscope p Quality gate	HMDS, 5k rpm, 30 sec 150°C / 30 sec AZp4330, 4k rpm, 30 sec 90°C / 90 sec Mask Exposure time = 7sec, Cl2 setting Develop AZ 400k (1:4), time ~50 sec Center Resist Thickness _____ Check smallest feature _____ C Pass C Fail: Hold, contact Engineering. Sign off: _____ (Engr) _____ (Fab)
	1.3	Semiconductor Etch p ICP p Profilometer	Etch recipe: H ₂ ANNEAL Etch Rate -0.2µm/min to 0.3µm/min Pumpdown time: _____ (min) Etch time: _____ Center Thickness: _____

	1.4	Photolithography Strip p Solvent Hood p Profilometer p ICP p Quality gate	Acetone/ IPA / DI rinse RIE with Oxygen plasma at 100mTorr, 100W for 2min for residual PR descum. Center Thk. _____ Update ICP logbook 1.125 μm < target etch depth < 1.375 μm (e.g) C Pass C Fail: Hold, contact Engineering. Sign off: _____ (Engr) _____ (Fab)	
<u>Si₃N₄ Deposition</u>				
Date/ Time	2.1	Solvent Clean p Solvent Hood	Acetone/IPA/DI rinse (2-5 minute) Nitrogen dry 6 minute dehydration bake @ 150°C	
	2.2	SAMCO PECVD Deposition	N2 15 SCCM 488mT + NH3 50SCCM 431mT + SiH4 SILANE 30 SCCM 540mT set ; TOTAL PROCESS PRESSURE 635mT RF power 50W Total time: ~7 min Temperature = 300°C Color: Dark Blue.	
COMMON OHMIC METAL LIFTOFF				
Date/ Time	3.1	Solvent Clean p Solvent Hood	Acetone/IPA/DI rinse (2-5 minute) Nitrogen dry 6 minute dehydration bake @ 150°C	
	3.2	Liftoff Photolithography p Spinner p Hot plate p Spinner p Hot plate p Mask Aligner p Hot plate p Mask Aligner p Develop hood p Inspection Microscope p Quality gate	HMDS, 5k rpm, 30 sec 150°C / 30 sec AZ5214E-IR, 5k rpm, 30 sec 90°C / 90 sec Mask Exposure time = 3.5 sec, Cl2 setting 112°C / 60 sec (image reverse bake) Flood exposure time = 60 sec, Cl2 setting Develop AZ400K 1:5, DI water, time = ~45 sec Mesa fully covered? C Pass C Fail: Hold, contact Engineering. Sign off: _____ (Engr) _____ (Fab)	
	3.3	Surface Preparation p Acid/Base Hood	30 sec, , HCl:H ₂ O;1:10 30 sec, N ₂ Blow Dry	

	3.4	n-Metal Deposition Evaporator p Metal I p Metal II p Record Deposition Currents and rates	Roughing pumpdown time: _____. Ge (Pocket #1): 260 Å @ 1 Å/sec (tooling: 100%) Au (Pocket 3): 540 Å @ 1 Å/sec (tooling: 96%) Ni (Pocket #2): 150 Å @ 1 Å/sec (tooling: 92%) Au (Pocket #3): 3,000 Å @ 2.5 Å/sec Ge: _____ mA Å/s Au: _____ mA Å/s Ni: _____ mA Å/s Au: _____ mA Å/s	
	3.5	Metal Liftoff p Solvent Hood p Profilometer p Quality gate	Acetone / Methanol / DI rinse Center Thickness. _____ 3555 Å < metal thickness < 4345 Å C Pass C Fail: Hold, contact Engineering. Sign off: _____ (Engr) _____ (Fab)	
RAPID THERMAL ANNEAL				
Date/ Time	3.6	Ohmic Anneal p RTA p Print Run Graph	Recipe: 360°C/60 sec Check contact resistance with a probe station Also inspect integrity of Si ₃ N ₄ layer.	

UNDERBUMP METAL LIFTOFF				
Date/ Time	4.1	Liftoff Photolithography p Spinner p Hot plate p Spinner p Hot plate p Mask Aligner p Hot plate p Mask Aligner p Develop hood p Inspection Microscope p Quality gate	HMDS, 5k rpm, 30 sec 150°C / 30 sec AZ5214E-IR, 4k rpm, 30 sec 90°C / 90 sec Mask Exposure time = 1.9 sec, Cl2 setting 112°C / 60 sec (image reverse bake) Flood exposure time = 20 sec, Cl2 setting Develop AZ400K 1:5, DI water, time = ~25 sec Smallest Features O.K.? C Pass C Fail: Hold, contact Engineering. Sign off: _____ (Engr) _____ (Fab)	
	4.2	Surface Preparation p Acid/Base Hood	30 sec, , HCl:H ₂ O;1:10 30 sec, N ₂ Blow Dry	

4.3	n-Metal Deposition Evaporator p Metal I p Metal II p Record Deposition Currents and rates	Roughing pumpdown time: _____. Ti (Pocket #1): 500 Å @ 1 Å/sec (tooling: 100%) Ni (Pocket #2): 1500 Å @ 2.5 Å/sec (tooling: 92%) Au (Pocket #3): 500 Å @ 2 Å/sec Ti: _____ mA Å/s Ni: _____ mA Å/s Au: _____ mA Å/s	
4.4	Metal Liftoff p Solvent Hood p Profilometer p Quality gate	Acetone / IPA / DI rinse Center Thickness _____ 2000 Å < metal thickness < 4000 Å C Pass C Fail: Hold, contact Engineering. Sign off: _____ (Engr) _____ (Fab)	

INDIUM METAL LIFTOFF			
Date/ Time	5.1	Liftoff Photolithography p Spinner p Hot plate p Spinner p Oven p Mask Aligner p Develop hood p Inspection Microscope p Quality gate	HMDS, 5k rpm, 30 sec 150°C / 30 sec AZ4620, 2k rpm, 60 sec, Remove edge bead. Air bake for 5 min, 95°C oven for 12 min. Mask Exposure time = 30 sec, Cl2 setting Develop AZ400K 1:4, DI water, time = ~3 min 45 sec Smallest Features O.K.? Walls vertical? Resist Thickness should be above 10µm. C Pass C Fail: Hold, contact Engineering. Sign off: _____ (Engr) _____ (Fab)
	5.2	Indium Thermal Deposition Thermal Evaporator IV p Record Deposition Currents and rates	Roughing pumpdown time: _____. In (Source #1): 30,000 Å @ 5 Å/sec (tooling: 100%) In: _____ mA Å/s
	5.3	Metal Liftoff p Solvent Hood p Profilometer p Quality gate	Acetone / IPA / DI rinse May need Acetone spray gun. Center Thickness _____ 2500Å < metal thickness < 3500 Å C Pass C Fail: Hold, contact Engineering. Sign off: _____ (Engr) _____ (Fab)

After Indium deposition, following steps are involved for individual FPA fabrication

1.Dicing individual dies: Use designated dicing lines.

Use 1-2mil blade, 100 mil/sec cutting rate.

2.Indium reflow:

- Use reflow flux on top of individual dice.
- Set on a hot plate at 180°C, make sure that the flux spreads uniformly over the dice
- Observe the color change to a darker color, indicating that Indium has reflowed.
- Rinse the flux off with acetone/IPA/DI water rinse.
- Inspect under microscope to see the uniformity across the FPA.
- Grade the FPA based on number of working pixels.

3. Hybridization with Si ROIC.

- Remove surface oxides with HCl:H₂O (1:10) dip for 30sec.
- Hybridization is done at FC 150 flip chip bonder with low force bonding arm.

- Temperature = 180°C.

4. Underfil epoxy application

- Set a drop of Trabond epoxy at a smaller edge of FPA (on the edge without any test pixels).
- Wait at room temperature for 5 min for the underfil to spread across the smaller edge
- Set it on a 70°C hotplate for uniform spread of the underfil epoxy.
- Observe the coverage of epoxy and cleanliness of pads under the microscope.
- Bake the epoxy in 130°C oven for 20 min.

5. Substrate removal

Substrate removal is currently the most challenging step in the entire process flow for FPA. The most popular approach is a combination of mechanical polishing and a selective dry etching.

Mechanical Polish:

- Load the dice on the glass chuck, along with 4 spacer GaAs samples, with crystal bond.
- Cover the ROIC exposed area with crystal bond
- Use 9µm polishing suspension on glass plate at Logitech polisher

- For typical conditions such as full load, 30 rpm, the polish rate is ~45 $\mu\text{m}/\text{min}$
- For the last 60 μm , switch to chemical mechanical polishing with chemlox solution, 70 rpm.
- Stop when the remaining substrate is ~20 μm thick.
- Rinse thoroughly in DI water to remove residual Chemlox. Acetone gun may also need to be used.
- Measure the thickness with profilometer after stripping the crystal bond.

Selective Dry Etching

- Protect ROIC pads with a negative PR
- Use a combination of BCl_3 and SF_6 for achieving high selectivity between GaAs and AlAs etch stop layer.
- Clean the dice and mount it on 84 pin leadless chip carrier (LCC).

6. Testing

Use pour filled dewar or a closed cycled dewar to cool the FPA down to 60K or 80K.

Perform two point non uniformity correction with a blackbody, after optimizing the dynamic range by adjusting the video gain and offset values.

Record images and perform radiometric characterization to estimate noise equivalent temperature difference (NETD)

$$NETD = v_n \left(\frac{\Delta T}{\Delta V} \right) \quad A.1$$

where v_n is noise voltage in rms, ΔV is the voltage difference measured for the temperature change ΔT . Typically V is collected over a constant temperature scene for several blackbody temperatures to measure NETD in linear range.

References

- [1] E. L. Dereniak and G. D. Boreman, *Infrared detectors and systems*: Wiley, 1996.
- [2] A. Rogalski, "Infrared detectors: an overview," *Infrared Physics & Technology*, vol. 43, pp. 187-210, Jun-Oct 2002.
- [3] A. Rogalski, "Infrared detectors: status and trends," *Progress in Quantum Electronics*, vol. 27, pp. 59-210, 2003 2003.
- [4] E. A. Dauler, B. S. Robinson, A. J. Kerman, J. K. W. Yang, E. K. M. Rosfjord, V. Anant, B. Voronov, G. Gol'tsman, and K. K. Berggren, "Multi-Element Superconducting Nanowire Single-Photon Detector," *Applied Superconductivity, IEEE Transactions on*, vol. 17, pp. 279-284, 2007.
- [5] A. V. Barve and S. Krishna, "Quantum Dot Infrared Photodetectors," in *Advances in Infrared Photodetectors*. vol. 84, S. D. Gunapala, D. R. Rhiger, and C. Jagadish, Eds., ed San Diego: Elsevier Academic Press Inc, 2011, pp. 153-193.
- [6] C. T. Elliott, "New infrared and other applications of narrow-gap semiconductors," San Diego, CA, USA, 1998, pp. 763-775.
- [7] A. W. Hoffman, P. J. Love, and J. P. Rosbeck, "Megapixel detector arrays: visible to 28 μm ," San Diego, CA, USA, 2004, pp. 194-203.
- [8] D. L. Smith and C. Mailhot, "Proposal for strained type II superlattice infrared detectors," *Journal of Applied Physics*, vol. 62, pp. 2545-2548, 1987.
- [9] E. Plis, J. B. Rodriguez, H. S. Kim, G. Bishop, Y. D. Sharma, L. R. Dawson, S. Krishna, S. J. Lee, C. E. Jones, and V. Gopal, "Type II InAs/GaSb strain layer superlattice detectors with p-on-n polarity," *Applied Physics Letters*, vol. 91, pp. 133512-3, 2007.
- [10] B.-M. Nguyen, D. Hoffman, Y. Wei, P.-Y. Delaunay, A. Hood, and M. Razeghi, "Very high quantum efficiency in type-II InAs/GaSb superlattice photodiode with cutoff of 12 μm ," *Applied Physics Letters*, vol. 90, pp. 231108-3, 2007.
- [11] M. Kinch, "Fundamental physics of infrared detector materials," *Journal of Electronic Materials*, vol. 29, pp. 809-817, 2000.
- [12] R. Antoni, "Infrared detectors: an overview," *Infrared Physics & Technology*, vol. 43, pp. 187-210, 2002.
- [13] A. Rogalski, "Third-generation infrared photon detectors," *Optical Engineering*, vol. 42, pp. 3498-3516, 2003.
- [14] P. Martyniuk, S. Krishna, and A. Rogalski, "Assessment of quantum dot infrared photodetectors for high temperature operation," *Journal of Applied Physics*, vol. 104, Aug 1 2008.

- [15] P. Martyniuk and A. Rogalski, "Quantum-dot infrared photodetectors: Status and outlook," *Progress in Quantum Electronics*, vol. 32, pp. 89-120, 2008.
- [16] A. V. Barve, S. J. Lee, S. K. Noh, and S. Krishna, "Review of current progress in quantum dot infrared photodetectors," *Laser & Photonics Reviews*, vol. 4, pp. 738-750, 2010.
- [17] J. C. Campbell and A. Madhukar, "Quantum-Dot Infrared Photodetectors," *Proceedings of the IEEE*, vol. 95, pp. 1815-1827, 2007.
- [18] S. Tsao, H. Lim, H. Seo, W. Zhang, and M. Razeghi, "InP-based quantum-dot infrared photodetectors with high quantum efficiency and high-temperature imaging," *Ieee Sensors Journal*, vol. 8, pp. 936-941, May-Jun 2008.
- [19] H. Lim, S. Tsao, W. Zhang, and M. Razeghi, "High-performance InAs quantum-dot infrared photodetectors grown on InP substrate operating at room temperature," *Applied Physics Letters*, vol. 90, Mar 26 2007.
- [20] P. Bhattacharya, X. H. Su, S. Chakrabarti, G. Ariyawansa, and A. G. U. Perera, "Characteristics of a tunneling quantum-dot infrared photodetector operating at room temperature," *Applied Physics Letters*, vol. 86, May 9 2005.
- [21] X. H. Su, J. Yang, P. Bhattacharya, G. Ariyawansa, and A. G. U. Perera, "Terahertz detection with tunneling quantum dot intersublevel photodetector," *Applied Physics Letters*, vol. 89, pp. 031117-3, 2006.
- [22] D. Z. Y. Ting, S. V. Bandara, S. D. Gunapala, J. M. Mumolo, S. A. Keo, C. J. Hill, J. K. Liu, E. R. Blazejewski, S. B. Rafol, and Y.-C. Chang, "Submonolayer quantum dot infrared photodetector," *Applied Physics Letters*, vol. 94, pp. 111107-3, 2009.
- [23] B. Levine, "Quantum well infrared photodetectors," *J. Appl. Phys.*, vol. 74, p. R1, 1993.
- [24] S. D. Gunapala, S. V. Bandara, J. K. Liu, C. J. Hill, S. B. Rafol, J. M. Mumolo, J. Thang, M. Z. Tidrow, and P. D. LeVan, "MWIR and LWIR megapixel QWIP focal plane arrays," Denver, CO, USA, 2004, pp. 141-148.
- [25] H. C. Liu, J. Y. Duboz, R. Dudek, Z. R. Wasilewski, S. Fafard, and P. Finnie, "Quantum dot infrared photodetectors," *Physica E-Low-Dimensional Systems & Nanostructures*, vol. 17, pp. 631-633, Apr 2003.
- [26] A. Rogalski, "Quantum well photoconductors in infrared detector technology," *J. Appl. Phys.*, vol. 93, p. 4355, 2003.
- [27] J. Urayama, T. B. Norris, J. Singh, and P. Bhattacharya, "Observation of Phonon Bottleneck in Quantum Dot Electronic Relaxation," *Physical Review Letters*, vol. 86, pp. 4930-4933, 2001.
- [28] H. C. Liu, R. Dudek, A. Shen, E. Dupont, C. Y. Song, Z. R. Wasilewski, and M. Buchanan, "High absorption ([greater-than] 90%) quantum-well infrared photodetectors," *Applied Physics Letters*, vol. 79, pp. 4237-4239, 2001.
- [29] Y. Arakawa and H. Sakaki, "Multidimensional quantum well laser and temperature dependence of its threshold current," *Applied Physics Letters*, vol. 40, pp. 939-941, 1982.

- [30] M. Asada, Y. Miyamoto, and Y. Suematsu, "Gain and the threshold of three-dimensional quantum-box lasers," *Quantum Electronics, IEEE Journal of*, vol. 22, pp. 1915-1921, 1986.
- [31] D. Leonard, K. Pond, and P. M. Petroff, "Critical layer thickness for self-assembled InAs islands on GaAs," *Physical Review B*, vol. 50, pp. 11687-11692, 1994.
- [32] Q. Xie, P. Chen, A. Kalburge, T. R. Ramachandran, A. Nayfonov, A. Konkar, and A. Madhukar, "Realization of optically active strained InAs island quantum boxes on GaAs(100) via molecular beam epitaxy and the role of island induced strain fields," *Journal of Crystal Growth*, vol. 150, Part 1, pp. 357-363, 1995.
- [33] G. S. Solomon, J. A. Trezza, and J. J. S. Harris, "Substrate temperature and monolayer coverage effects on epitaxial ordering of InAs and InGaAs islands on GaAs," *Applied Physics Letters*, vol. 66, pp. 991-993, 1995.
- [34] H. Drexler, D. Leonard, W. Hansen, J. P. Kotthaus, and P. M. Petroff, "Spectroscopy of Quantum Levels in Charge-Tunable InGaAs Quantum Dots," *Physical Review Letters*, vol. 73, pp. 2252-2255, 1994.
- [35] R. Heitz, M. Veit, N. N. Ledentsov, A. Hoffmann, D. Bimberg, V. M. Ustinov, P. S. Kop'ev, and Z. I. Alferov, "Energy relaxation by multiphonon processes in InAs/GaAs quantum dots," *Physical Review B*, vol. 56, pp. 10435-10445, 1997.
- [36] H. Jiang and J. Singh, "Strain distribution and electronic spectra of InAs/GaAs self-assembled dots: An eight-band study," *Physical Review B*, vol. 56, pp. 4696-4701, 1997.
- [37] A. Franceschetti and A. Zunger, "Free-standing versus AlAs-embedded GaAs quantum dots, wires, and films: The emergence of a zero-confinement state," *Applied Physics Letters*, vol. 68, pp. 3455-3457, 1996.
- [38] K. W. Berryman, S. A. Lyon, and M. Segev, "Mid-infrared photoconductivity in InAs quantum dots," *Applied Physics Letters*, vol. 70, pp. 1861-1863, 1997.
- [39] S. Maimon, E. Finkman, G. Bahir, S. E. Schacham, J. M. Garcia, and P. M. Petroff, "Intersublevel transitions in InAs/GaAs quantum dots infrared photodetectors," *Applied Physics Letters*, vol. 73, pp. 2003-2005, 1998.
- [40] D. Pan, E. Towe, and S. Kennerly, "Normal-incidence intersubband (In, Ga)As/GaAs quantum dot infrared photodetectors," *Applied Physics Letters*, vol. 73, pp. 1937-1939, 1998.
- [41] J. Phillips, K. Kamath, and P. Bhattacharya, "Far-infrared photoconductivity in self-organized InAs quantum dots," *Applied Physics Letters*, vol. 72, pp. 2020-2022, 1998.
- [42] J. Phillips, "Evaluation of the fundamental properties of quantum dot infrared detectors," *Journal of Applied Physics*, vol. 91, pp. 4590-4594, 2002.
- [43] V. Ryzhii, "The theory of quantum-dot infrared phototransistors," *Semiconductor Science and Technology*, vol. 11, p. 759, 1996.
- [44] W. Zhang, H. Lim, M. Taguchi, S. Tsao, B. Movaghar, and M. Razeghi, "High-detectivity InAs quantum-dot infrared photodetectors grown on InP

- by metal--organic chemical--vapor deposition," *Applied Physics Letters*, vol. 86, pp. 191103-3, 2005.
- [45] E. T. Kim, A. Madhukar, Z. M. Ye, and J. C. Campbell, "High detectivity InAs quantum dot infrared photodetectors," *Applied Physics Letters*, vol. 84, pp. 3277-3279, Apr 26 2004.
 - [46] S. Chakrabarti, A. D. Stiff-Roberts, X. H. Su, P. Bhattacharya, G. Ariyawansa, and A. G. U. Perera, "High-performance mid-infrared quantum dot infrared photodetectors," *Journal of Physics D-Applied Physics*, vol. 38, pp. 2135-2141, Jul 7 2005.
 - [47] Z. Mi and P. Bhattacharya, "Molecular-beam epitaxial growth and characteristics of highly uniform InAs/GaAs quantum dot layers," *Journal of Applied Physics*, vol. 98, pp. 023510-5, 2005.
 - [48] A. Stintz, G. T. Liu, A. L. Gray, R. Spillers, S. M. Delgado, and K. J. Malloy, "Characterization of InAs quantum dots in strained In_xGa_{1-x}As quantum wells," Banff (Canada), 2000, pp. 1496-1501.
 - [49] Z. Chen, O. Baklenov, E. T. Kim, I. Mukhametzhanov, J. Tie, A. Madhukar, Z. Ye, and J. C. Campbell, "Normal incidence InAs/Al_xGa_{1-x}As quantum dot infrared photodetectors with undoped active region," *Journal of Applied Physics*, vol. 89, pp. 4558-4563, 2001.
 - [50] E.-T. Kim, Z. Chen, and A. Madhukar, "Tailoring detection bands of InAs quantum-dot infrared photodetectors using In_xGa_{1-x}As strain-relieving quantum wells," *Applied Physics Letters*, vol. 79, pp. 3341-3343, 2001.
 - [51] L. Fu, H. H. Tan, I. McKerracher, J. Wong-Leung, C. Jagadish, N. Vukmirovic, and P. Harrison, "Effects of rapid thermal annealing on device characteristics of InGaAs/GaAs quantum dot infrared photodetectors," *Journal of Applied Physics*, vol. 99, pp. 114517-8, 2006.
 - [52] E. C. Le Ru, P. Howe, T. S. Jones, and R. Murray, "Strain-engineered InAs/GaAs quantum dots for long-wavelength emission," *Physical Review B*, vol. 67, p. 165303, 2003.
 - [53] S. Chakrabarti, A. D. Stiff-Roberts, P. Bhattacharya, and S. W. Kennerly, "Heterostructures for achieving large responsivity in InAs/GaAs quantum dot infrared photodetectors," *Journal of Vacuum Science & Technology B*, vol. 22, pp. 1499-1502, May-Jun 2004.
 - [54] H. S. Ling, S. Y. Wang, C. P. Lee, and M. C. Lo, "High quantum efficiency dots-in-a-well quantum dot infrared photodetectors with AlGaAs confinement enhancing layer," *Applied Physics Letters*, vol. 92, May 12 2008.
 - [55] A. Amtout, S. Raghavan, P. Rotella, G. von Winckel, A. Stintz, and S. Krishna, "Theoretical modeling and experimental characterization of InAs/InGaAs quantum dots in a well detector," *Journal of Applied Physics*, vol. 96, pp. 3782-3786, 2004.
 - [56] S. Krishna, D. Forman, S. Annamalai, P. Dowd, P. Varangis, T. Tumolillo, A. Gray, J. Zilko, K. Sun, M. G. Liu, J. Campbell, and D. Carothers, "Demonstration of a 320x256 two-color focal plane array using

- InAs/InGaAs quantum dots in well detectors," *Applied Physics Letters*, vol. 86, May 9 2005.
- [57] S. Raghavan, P. Rotella, A. Stintz, B. Fuchs, S. Krishna, C. Morath, D. A. Cardimona, and S. W. Kennerly, "High-responsivity, normal-incidence long-wave infrared ($\lambda \sim 7.2 \mu\text{m}$) InAs/In_{0.15}Ga_{0.85}As dots-in-a-well detector," *Applied Physics Letters*, vol. 81, pp. 1369-1371, 2002.
 - [58] P. Aivaliotis, S. Menzel, E. A. Zibik, J. W. Cockburn, L. R. Wilson, and M. Hopkinson, "Energy level structure and electron relaxation times in InAs/In_xGa_{1-x}As quantum dot-in-a-well structures," *Applied Physics Letters*, vol. 91, pp. 253502-3, 2007.
 - [59] P. Aivaliotis, E. A. Zibik, L. R. Wilson, J. W. Cockburn, M. Hopkinson, and R. J. Airey, "Tuning the photoresponse of quantum dot infrared photodetectors across the 8--12 μm atmospheric window via rapid thermal annealing," *Applied Physics Letters*, vol. 91, pp. 143502-3, 2007.
 - [60] G. Ariyawansa, A. G. U. Perera, G. S. Raghavan, G. v. Winckel, A. Stintz, and S. Krishna, "Effect of well width on three-color quantum dots-in-a-well infrared detectors," *Photonics Technology Letters, IEEE*, vol. 17, pp. 1064-1066, 2005.
 - [61] X. Han, J. Li, J. Wu, G. Cong, X. Liu, Q. Zhu, and Z. Wang, "Intersubband optical absorption in quantum dots-in-a-well heterostructures," *Journal of Applied Physics*, vol. 98, pp. 053703-5, 2005.
 - [62] L. Hoglund, C. Asplund, Q. Wang, S. Almqvist, H. Malm, E. Petrini, J. Y. Andersson, P. O. Holtz, and H. Pettersson, "Origin of photocurrent in lateral quantum dots-in-a-well infrared photodetectors," *Applied Physics Letters*, vol. 88, pp. 213510-3, 2006.
 - [63] G. Jolley, L. Fu, H. H. Tan, and C. Jagadish, "Effects of well thickness on the spectral properties of In_{0.5}Ga_{0.5}As/GaAs/Al_{0.2}Ga_{0.8}As quantum dots-in-a-well infrared photodetectors," *Applied Physics Letters*, vol. 92, pp. 193507-3, 2008.
 - [64] M. A. Naser, M. J. Deen, and D. A. Thompson, "Spectral function and responsivity of resonant tunneling and superlattice quantum dot infrared photodetectors using Green's function," *Journal of Applied Physics*, vol. 102, pp. 083108-12, 2007.
 - [65] X. H. Su, S. Chakrabarti, P. Bhattacharya, G. Ariyawansa, and A. G. U. Perera, "A resonant tunneling quantum-dot infrared photodetector," *Ieee Journal of Quantum Electronics*, vol. 41, pp. 974-979, Jul 2005.
 - [66] A. V. Barve, S. Y. Shah, J. Shao, T. E. Vandervelde, R. V. Shenoi, W. Y. Jang, and S. Krishna, "Reduction in dark current using resonant tunneling barriers in quantum dots-in-a-well long wavelength infrared photodetector," *Applied Physics Letters*, vol. 93, Sep 29 2008.
 - [67] A. Barve, J. Shao, Y. D. Sharma, T. E. Vandervelde, K. Sankalp, S. J. Lee, S. K. Noh, and S. Krishna, "Resonant Tunneling Barriers in Quantum Dots-in-a-Well Infrared Photodetectors," *Ieee Journal of Quantum Electronics*, vol. 46, pp. 1105-1114, Jul 2010.

- [68] S. Chakrabarti, A. D. Stiff-Roberts, P. Bhattacharya, and S. W. Kennerly, "High responsivity AlAs/InAs/GaAs superlattice quantum dot infrared photodetector," *Electronics Letters*, vol. 40, pp. 197-198, 2004.
- [69] P. Boucaud and S. Sauvage, "Infrared photodetection with semiconductor self-assembled quantum dots," *Comptes Rendus Physique*, vol. 4, pp. 1133-1154, Dec 2003.
- [70] N. Vukmirovic and S. Tomic, "Plane wave methodology for single quantum dot electronic structure calculations," *Journal of Applied Physics*, vol. 103, May 15 2008.
- [71] O. Stier, M. Grundmann, and D. Bimberg, "Electronic and optical properties of strained quantum dots modeled by 8-band k-p theory," *Physical Review B*, vol. 59, pp. 5688-5701, 1999.
- [72] L. Hoglund, C. Asplund, Q. Wang, S. Almqvist, H. Malm, E. Petrini, J. Y. Andersson, P. O. Holtz, and H. Pettersson, "Origin of photocurrent in lateral quantum dots-in-a-well infrared photodetectors," *Applied Physics Letters*, vol. 88, May 22 2006.
- [73] A. J. Williamson and A. Zunger, "InAs quantum dots: Predicted electronic structure of free-standing versus GaAs-embedded structures," *Physical Review B*, vol. 59, pp. 15819-15824, 1999.
- [74] T.-M. Hwang, W.-W. Lin, W.-C. Wang, and W. Wang, "Numerical simulation of three dimensional pyramid quantum dot," *Journal of Computational Physics*, vol. 196, pp. 208-232, 2004.
- [75] S. D. Gunapala, S. V. Bandara, C. J. Hill, D. Z. Ting, J. K. Liu, S. B. Rafol, E. R. Blazejewski, J. M. Mumolo, S. A. Keo, S. Krishna, Y. C. Chang, and C. A. Shott, "640 x 512 pixels long-wavelength infrared (LWIR) quantum-dot infrared photodetector (QDIP) imaging focal plane array," *Ieee Journal of Quantum Electronics*, vol. 43, pp. 230-237, Mar-Apr 2007.
- [76] A. V. Barve, J. Montaya, Y. Sharma, T. Rotter, J. Shao, W.-Y. Jang, S. Meesala, S. J. Lee, and S. Krishna, "High temperature operation of quantum dots-in-a-well infrared photodetectors," *Infrared Physics & Technology*, vol. 54, pp. 215-219, May 2011.
- [77] T. E. Vandervelde, M. C. Lenz, E. Varley, A. Barve, J. Shao, R. V. Shenoi, D. A. Ramirez, W. Jang, Y. D. Sharma, and S. Krishna, "Quantum dots-in-a-well focal plane arrays (Invited paper)," *Ieee Journal of Selected Topics in Quantum Electronics*, vol. 14, pp. 1150-1161, Jul-Aug 2008.
- [78] P. Bhattacharya, S. Ghosh, and A. D. Stiff-Roberts, "Quantum dot optoelectronic devices," *Annual Review of Materials Research*, vol. 34, pp. 1-40, 2004 2004.
- [79] D. Pal and E. Towe, "Uniformity assessment of key characteristics of quantum-dot infrared detectors: A prerequisite for focal plane arrays," *Journal of Applied Physics*, vol. 100, Oct 15 2006.
- [80] S. Krishna, "Quantum dots-in-a-well infrared photodetectors," *Journal of Physics D-Applied Physics*, vol. 38, pp. 2142-2150, Jul 7 2005.
- [81] M. A. Herman and A. Sitter, "Molecular beam epitaxy—fundamentals and current status," *Springer*, 1989.

- [82] D. Bimberg, M. Grundmann, and N. N. Ledentsov, "Quantum Dot Heterostructures," Wiley, 1999.
- [83] E. Placidi, F. Arciprete, M. Fanfoni, F. Patella, E. Orsini, and A. Balzarotti, "InAs/GaAs(001) epitaxy: kinetic effects in the two-dimensional to three-dimensional transition," *Journal of Physics: Condensed Matter*, vol. 19, p. 225006, 2007.
- [84] P. Kratzer, Q. K. K. Liu, P. Acosta-Diaz, C. Manzano, G. Costantini, R. Songmuang, A. Rastelli, O. G. Schmidt, and K. Kern, "Shape transition during epitaxial growth of InAs quantum dots on GaAs(001): Theory and experiment," *Physical Review B*, vol. 73, p. 205347, 2006.
- [85] R. S. Attaluri, S. Annamalai, K. T. Posani, A. Stintz, and S. Krishna, "Influence of Si doping on the performance of quantum dots-in-well photodetectors," *Journal of Vacuum Science & Technology B*, vol. 24, pp. 1553-1555, May-Jun 2006.
- [86] S. Chakrabarti, A. D. Stiff-Roberts, P. Bhattacharya, S. Gunapala, S. Bandara, S. B. Rafol, and S. W. Kennerly, "High-temperature operation of InAs-GaAs quantum-dot infrared photodetectors with large responsivity and detectivity," *Photonics Technology Letters, IEEE*, vol. 16, pp. 1361-1363, 2004.
- [87] J. Y. Duboz, H. C. Liu, Z. R. Wasilewski, M. Byloss, and R. Dudek, "Tunnel current in quantum dot infrared photodetectors," *Journal of Applied Physics*, vol. 93, pp. 1320-1322, 2003.
- [88] K. Drozdowicz-Tomsia, E. M. Goldys, L. Fu, and C. Jagadish, "Doping effect on dark currents in In_{0.5}Ga_{0.5}As/GaAs quantum dot infrared photodetectors grown by metal-organic chemical vapor deposition," *Applied Physics Letters*, vol. 89, Sep 11 2006.
- [89] H. Lim, B. Movaghar, S. Tsao, M. Taguchi, W. Zhang, A. A. Quivy, and M. Razeghi, "Gain and recombination dynamics of quantum-dot infrared photodetectors," *Physical Review B*, vol. 74, p. 205321, 2006.
- [90] V. Ryzhii and et al., "Device model for quantum dot infrared photodetectors and their dark-current characteristics," *Semiconductor Science and Technology*, vol. 16, p. 331, 2001.
- [91] N. Vukmirovic, Z. Ikonc, I. Savic, D. Indjin, and P. Harrison, "A microscopic model of electron transport in quantum dot infrared photodetectors," *Journal of Applied Physics*, vol. 100, Oct 1 2006.
- [92] M. Ershov, "Photoconductivity nonlinearity at high excitation power in quantum well infrared photodetectors," *Appl. Phys. Lett.*, vol. 70, p. 414, 1997.
- [93] A. V. Barve, T. Rotter, Y. Sharma, S. J. Lee, S. K. Noh, and S. Krishna, "Systematic study of different transitions in high operating temperature quantum dots in a well photodetectors," *Applied Physics Letters*, vol. 97, Aug 9 2010.
- [94] T. Shiang-Feng, C. Cheng-Der, W. Ping-Kuo, G. Yau-Tang, L. Jiunn-Jye, Y. San-Te, S. Chih-Chang, S. Y. Lin, and L. Si-Chen, "High-temperature operation normal incident 256×256 InAs-GaAs quantum-dot infrared

- photodetector focal plane array," *Photonics Technology Letters, IEEE*, vol. 18, pp. 986-988, 2006.
- [95] B. Kochman, A. D. Stiff-Roberts, S. Chakrabarti, J. D. Phillips, S. Krishna, J. Singh, and P. Bhattacharya, "Absorption, carrier lifetime, and gain in InAs-GaAs quantum-dot infrared photodetectors," *Ieee Journal of Quantum Electronics*, vol. 39, pp. 459-467, Mar 2003.
 - [96] T. B. Bahder, "Eight-band k-p model of strained zinc-blende crystals," *Physical Review B*, vol. 41, pp. 11992-12001, 1990.
 - [97] R. Veprek, S. Steiger, and B. Witzigmann, "Reliable band structure calculation for nanostructures using finite elements," *Journal of Computational Electronics*, vol. 7, pp. 521-529, 2008.
 - [98] N. Vukmirovic, D. Indjin, Z. Ikonic, and P. Harrison, "Origin of detection wavelength tuning in quantum dots-in-a-well infrared photodetectors," *Applied Physics Letters*, vol. 88, pp. 251107-3, 2006.
 - [99] C. Pryor, "Eight-band calculations of strained InAs/GaAs quantum dots compared with one-, four-, and six-band approximations," *Physical Review B*, vol. 57, pp. 7190-7195, 1998.
 - [100] M. A. Cusack, P. R. Briddon, and M. Jaros, "Electronic structure of InAs/GaAs self-assembled quantum dots," *Physical Review B*, vol. 54, pp. R2300-R2303, 1996.
 - [101] P. N. Keating, "Effect of Invariance Requirements on the Elastic Strain Energy of Crystals with Application to the Diamond Structure," *Physical Review*, vol. 145, pp. 637-645, 1966.
 - [102] M. Grundmann, O. Stier, and D. Bimberg, "InAs/GaAs pyramidal quantum dots: Strain distribution, optical phonons, and electronic structure," *Physical Review B*, vol. 52, pp. 11969-11981, 1995.
 - [103] J. Singh, *Electronic and Optoelectronic Properties of Semiconductor Structures*: Cambridge University Press, 2003.
 - [104] S. L. Chuang, *Physics of Photonic Devices*, 2nd Ed. ed.: John Wiley, 2009.
 - [105] L. Landou and E. Lifshitz, *Theory of Elasticity*, 1959.
 - [106] C. Pryor, J. Kim, L. W. Wang, A. J. Williamson, and A. Zunger, "Comparison of two methods for describing the strain profiles in quantum dots," *Journal of Applied Physics*, vol. 83, pp. 2548-2554, 1998.
 - [107] R. M. Martin, "Elastic Properties of ZnS Structure Semiconductors," *Physical Review B*, vol. 1, pp. 4005-4011, 1970.
 - [108] J. R. Shewchuk, "An introduction to the conjugate gradient method without the agonizing pain," Carnegie Mellon University, Technical Report CMU-CS-94-125, 1994.
 - [109] S. Meesala, "Microscopic electronic structure modeling of self-assembled InAs/GaAs quantum dots," *B. Tech. Project Stage I Report, Department of Electrical Engineering, IIT Bombay*, 2011.
 - [110] P. Enders, A. Bärwolff, M. Woerner, and D. Suisky, "k-p theory of energy bands, wave functions, and optical selection rules in strained tetrahedral semiconductors," *Physical Review B*, vol. 51, pp. 16695-16704, 1995.
 - [111] D. Gershoni, C. H. Henry, and G. A. Baraff, "Calculating the optical properties of multidimensional heterostructures: Application to the modeling

- of quaternary quantum well lasers," *Quantum Electronics, IEEE Journal of*, vol. 29, pp. 2433-2450, 1993.
- [112] O. Stier and D. Bimberg, "Modeling of strained quantum wires using eight-band k·p theory," *Physical Review B*, vol. 55, pp. 7726-7732, 1997.
 - [113] Z. Ye, J. C. Campbell, Z. Chen, E.-T. Kim, and A. Madhukar, "InAs quantum dot infrared photodetectors with In_{0.15}Ga_{0.85}As strain-relief cap layers," *Journal of Applied Physics*, vol. 92, pp. 7462-7468, 2002.
 - [114] P. Bhattacharya, X. Su, G. Ariyawansa, and G. U. Perera, "High-temperature tunneling quantum-dot intersublevel detectors for mid-infrared to terahertz frequencies," *Proceedings of the IEEE*, vol. 95, pp. 1828-1837, Sep 2007.
 - [115] G. Ariyawansa, V. Apalkov, A. G. U. Perera, S. G. Matsik, G. Huang, and P. Bhattacharya, "Bias-selectable tricolor tunneling quantum dot infrared photodetector for atmospheric windows," *Applied Physics Letters*, vol. 92, pp. 111104-3, 2008.
 - [116] G. Huang, W. Guo, P. Bhattacharya, G. Ariyawansa, and A. G. U. Perera, "A quantum ring terahertz detector with resonant tunnel barriers," *Applied Physics Letters*, vol. 94, pp. 101115-3, 2009.
 - [117] A. D. Stiff-Roberts, X. H. Su, S. Chakrabarti, and P. Bhattacharya, "Contribution of field-assisted tunneling emission to dark current in InAs-GaAs quantum dot infrared photodetectors," *Photonics Technology Letters, IEEE*, vol. 16, pp. 867-869, 2004.
 - [118] R. Tsu and L. Esaki, "Tunneling in a finite superlattice," *Applied Physics Letters*, vol. 22, pp. 562-564, 1973.
 - [119] J. H. Davies, *The Physics of Low Dimensional Semiconductors*: Cambridge University Press, 1998.
 - [120] I. H. Tan, G. L. Snider, L. D. Chang, and E. L. Hu, "A self-consistent solution of Schrödinger-Poisson equations using a nonuniform mesh," *Journal of Applied Physics*, vol. 68, pp. 4071-4076, 1990.
 - [121] K. Kawano and T. Kitoh, "Introduction to Optical Waveguide Analysis," Wiley, pp. 117-160, 2001.
 - [122] S. Adachi, "Properties of Group-IV, III-V and II-VI Semiconductors," Wiley, 2005.
 - [123] K. K. Choi, S. V. Bandara, S. D. Gunapala, W. K. Liu, and J. M. Fastenau, "Detection wavelength of InGaAs/AlGaAs quantum wells and superlattices," *Journal of Applied Physics*, vol. 91, pp. 551-564, 2002.
 - [124] S. J. Lee, Z. Ku, A. Barve, J. Montoya, W.-Y. Jang, S. R. J. Brueck, M. Sundaram, A. Reisinger, S. Krishna, and S. K. Noh, "A monolithically integrated plasmonic infrared quantum dot camera," *Nat Commun*, vol. 2, p. 286, 2011.
 - [125] M. S. Kiledjian, J. N. Schulman, and K. L. Wang, "Absorption in GaAs/Ga_(1-x)Al_(x)As quantum wells with resonant barriers for improved responsivity," *Physical Review B*, vol. 44, pp. 5616-5621, 1991.

- [126] G. Jolley, L. F. H. H. Tan, and C. Jagadish, "Influence of quantum well and barrier composition on the spectral behavior of InGaAs quantum dots-in-a-well infrared photodetectors," *Applied Physics Letters*, vol. 91, Oct 22 2007.
- [127] A. V. Barve, S. Sengupta, J. O. Kim, Y. D. Sharma, S. Adhikary, T. J. Rotter, S. J. Lee, Y. H. Kim, and S. Krishna, "Confinement enhancing barriers for high performance quantum dots-in-a-well infrared detectors," *Applied Physics Letters*, vol. 99, pp. 191110-3, 2011.
- [128] A. Kastalsky, "Photovoltaic detection of infrared light in a GaAs/AlGaAs superlattice," *Appl. Phys. Lett.*, vol. 52, p. 1320, 1988.
- [129] D. Pan, "Photovoltaic quantum-dot infrared detectors," *Appl. Phys. Lett.*, vol. 76, p. 3301, 2000.
- [130] L. Nevou, "Asymmetric heterostructure for photovoltaic InAs quantum dot infrared photodetector," *Appl. Phys. Lett.*, vol. 97, p. 023505, 2010.
- [131] H. Schneider, "Photovoltaic quantum well infrared photodetectors: The four-zone scheme," *Appl. Phys. Lett.*, vol. 71, p. 246, 1997.
- [132] H. Schneider, M. Walther, C. Schönbein, R. Rehm, J. Fleissner, W. Pletschen, J. Braunstein, P. Koidl, G. Weimann, J. Ziegler, and W. Cabanski, "QWIP FPAs for high-performance thermal imaging," *Physica E: Low-dimensional Systems and Nanostructures*, vol. 7, pp. 101-107, 2000.
- [133] F. R. Giorgetta, E. Baumann, M. Graf, Y. Quankui, C. Manz, K. Kohler, H. E. Beere, D. A. Ritchie, E. Linfield, A. G. Davies, Y. Fedoryshyn, H. Jackel, M. Fischer, J. Faist, and D. Hofstetter, "Quantum Cascade Detectors," *Quantum Electronics, IEEE Journal of*, vol. 45, pp. 1039-1052, 2009.
- [134] F. R. Giorgetta, "InGaAs/AlAsSb quantum cascade detectors operating in the near infrared," *Appl. Phys. Lett.*, vol. 91, p. 111115, 2007.
- [135] D. Hofstetter, "Midinfrared quantum cascade detector with a spectrally broad response," *Appl. Phys. Lett.*, vol. 93, p. 221106, 2008.
- [136] M. Graf, "InP-based quantum cascade detectors in the mid-infrared," *Appl. Phys. Lett.*, vol. 88, p. 241118, 2006.
- [137] A. Buffaz, "Quantum cascade detectors for very long wave infrared detection," *Appl. Phys. Lett.*, vol. 96, p. 172101, 2010.
- [138] L. Gendron, "Quantum cascade photodetector," *Appl. Phys. Lett.*, vol. 85, p. 2824, 2004.
- [139] M. Graf, "Terahertz range quantum well infrared photodetector," *Appl. Phys. Lett.*, vol. 84, p. 475, 2004.
- [140] E. A. Zibik, T. Grange, B. A. Carpenter, N. E. Porter, R. Ferreira, G. Bastard, D. Stehr, S. Winnerl, M. Helm, H. Y. Liu, M. S. Skolnick, and L. R. Wilson, "Long lifetimes of quantum-dot intersublevel transitions in the terahertz range," *Nat Mater*, vol. 8, pp. 803-807, 2009.
- [141] S. Sauvage, P. Boucaud, R. P. S. M. Lobo, F. Bras, G. Fishman, R. Prazeres, F. Glotin, J. M. Ortega, and J. M. Gérard, "Long Polaron Lifetime in InAs/GaAs Self-Assembled Quantum Dots," *Physical Review Letters*, vol. 88, p. 177402, 2002.
- [142] A. Buffaz, M. Carras, L. Doyennette, V. Trinite, X. Marcadet, and V. Berger, "Long range resonant tunneling in quantum cascade structures," *Appl. Phys. Lett.*, vol. 96, p. 162103, 2010.

- [143] M. S. Lundstrom and R. J. Schuelke, "Numerical analysis of heterostructure semiconductor devices," *Electron Devices, IEEE Transactions on*, vol. 30, pp. 1151-1159, 1983.
- [144] H. Liu, "Photoconductive gain mechanism of quantum well intersubband infrared detectors," *Appl. Phys. Lett.*, vol. 60, p. 1507, 1992.
- [145] T. Asano, A. Madhukar, K. Mahalingam, and G. J. Brown, "Dark current and band profiles in low defect density thick multilayered GaAs/InAs self-assembled quantum dot structures for infrared detectors," *Journal of Applied Physics*, vol. 104, Dec 1 2008.
- [146] T. Hickmott, "Negative charge, barrier heights, and the conduction band discontinuity in Al_xGa_{1-x}As capacitors," *J. Appl. Phys.*, vol. 57, p. 2844, 1985.
- [147] B. Laikhtman, "Effect of high unintentional doping in AlGaAs barriers on scattering times in accumulation layers," *Appl. Phys. Lett.*, vol. 57, p. 1557, 1990.
- [148] R. Leavitt, "Quantitative model for photocurrent spectroscopy of quantum well diodes including transit time and background doping effects," *J. Appl. Phys.*, vol. 75, p. 2215, 1994.
- [149] A. Saar, C. Mermelstein, H. Schneider, C. Schoenbein, and M. Walther, "Space charge buildup in quantum-well infrared photodetectors leading to low-power nonlinear photoresponse," *Photonics Technology Letters, IEEE*, vol. 10, pp. 1470-1472, 1998.
- [150] D. A. Ramirez, J. Shao, M. M. Hayat, and S. Krishna, "Midwave infrared quantum dot avalanche photodiode," *Applied Physics Letters*, vol. 97, pp. 221106-3, 2010.
- [151] N. Gautam, H. S. Kim, M. N. Kutty, E. Plis, L. R. Dawson, and S. Krishna, "Performance improvement of longwave infrared photodetector based on type-II InAs/GaSb superlattices using unipolar current blocking layers," *Applied Physics Letters*, vol. 96, pp. 231107-3, 2010.
- [152] D. L. Scharfetter and H. K. Gummel, "Large-signal analysis of a silicon Read diode oscillator," *Electron Devices, IEEE Transactions on*, vol. 16, pp. 64-77, 1969.
- [153] "nanohub.org/resources/9093/download/Drift_Diffusion_Modeling.ppt".
- [154] D. Vasileska, "Drift-Diffusion Modeling and Numerical Implementation Details," ed, 2010.
- [155] Wikipedia, "Tridiagonal matrix algorithm," http://en.wikipedia.org/w/index.php?title=Tridiagonal_matrix_algorithm&oldid=466973736.
- [156] I. D. Mayergoyz, "Solution of the nonlinear Poisson equation of semiconductor device theory," *Journal of Applied Physics*, vol. 59, pp. 195-199, 1986.
- [157] L. Thibaudau, "A self-consistent model for quantum well infrared photodetectors," *J. Appl. Phys.*, vol. 79, p. 446, 1996.
- [158] D. Hofstetter, M. Graf, T. Aellen, J. Faist, L. Hvozdar, and S. Blaser, "23 GHz operation of a room temperature photovoltaic quantum cascade

- detector at $5.35 \mu\text{m}$," *Applied Physics Letters*, vol. 89, pp. 061119-3, 2006.
- [159] J. Shao, T. E. Vandervelde, A. Barve, W.-Y. Jang, A. Stintz, and S. Krishna, "Enhanced normal incidence photocurrent in quantum dot infrared photodetectors," vol. 29, p. 03C123, 2011.